

Magnetic, Magnetocaloric and Magneto- Transport Properties of Heusler Alloys

A thesis submitted for the award of the degree of

Doctor of Philosophy

in

Physics (Experimental)

by

Arup Ghosh

September, 2015

Department of Physics

University of Calcutta

Kolkata, India

Dedicated to my beloved parents.....

Acknowledgements

I would like to acknowledge the following people who helped me in many aspects that made me possible to write this thesis.

At first, I address a special thanks to my supervisor, *Professor Kalyan Mandal* for his continuous supports, effortless helps, valuable discussions and humble guidance. He always encourages my work and allows me to think and execute my plans independently. I really feel so lucky to have him as my supervisor.

I would like to thank *Defense Research Development Organization (DRDO), India*, for providing the financial supports during the first two and half years of my Ph.D. through a project, "*Study of Magnetocaloric Effect (ERIPR/ER/0902182/M/01/1296)*". I am also grateful to *S. N. Bose National Centre for Basic Sciences (SNBNCBS), Kolkata*, and *Department of Science and Technology (DST), India*, for providing a beautiful campus, wonderful research environment and financial supports.

I am thankful to *Dr. Dipankar Das, Scientist-G, Dr. Souvik Chatterjee, Scientist-D, UGC-DAE Consortium for Scientific Research, Kolkata* and *Dr. Pintu Sen, Scientist-H, Professor Sujit Kumar Bandyopadhyay, Variable Energy Cyclotron Centre (VECC), Kolkata* for providing their PPMS facility and helping throughout the measurements.

I am also thankful to *Distinguished Professor (Emeritus) A. K. Raychaudhuri, S. N. Bose National Centre for Basic Sciences, Kolkata*, for his continuous involvement in motivating students to enjoy the research. Some of the other faculties and non-academic staffs of this institute are also acknowledged for their helps.

I must acknowledge all the technical staffs including *Shakti Da, Surojit da, Piyali, Samik, Dipankar, Indra, Urmi* and *Amit* of *S. N. Bose National Centre for Basic Sciences* for their effortless help during samples' characterization and measurements.

I would like to thank all my lab mates: *Madhuri Di, Arka Da, Shyam Da, Debasish Da, Rajasree Di, Gobinda Da, Ashutosh, Rupali, Monalisa, Maheeb, Keshab, Sourav, Souvanik* and *Indranil* for providing such wonderful and friendly environment inside the lab. They are always very helpful regardless of their own busy schedules.

I am grateful to some of my school, college and university teachers (*Subhashis Sir, Barakat Sir, J. R. C. Sir, Arunava Sir and Bibhas Sir*) who motivated me throughout my student life. Specially, *Arunava Sir*, whom I use to call at any time for any queries or suggestions, and he helps me all the time as much as he can with a big smile in his face. He always treats me like a son and I feel myself blessed for the same.

I would like to give my gratitude to some of my friends from the childhood since now: *Sampad, Mithun, Partho, Arpita, Sauren, Tanmay and Ransell*, who helped me in every possible ways and made my life more enjoyable with their presence.

I must address my special thanks to *GoGo Da (Gobinda Da), Shyam Da, Debasish Da* and *Ashu (Ashutosh)*. These people are my best lab mates, very good friends and brothers. Their unconditional support and the most enjoyable company made me able to easily cross so many hurdles during my Ph.D. life. Specially *Ashu*, he is my best friend, my brother and always will be.

I would love to give my special gratitude to my brothers and sisters from the college days since now: *Sajal Da, Pinki Di, Samrat, Tapas, Anup, Archana, Anshu, Poonam, Vibhuti, Neha and Ravi (Ravindra)*. You people have filled my life with so many colors and happiness. Specially, to *Vibhuti, Neha and Ravi*; I might have not been able to resume myself if you three were not by my side.

Above everything, I am highly grateful to my beloved parents for all the sacrifices they have made to make my future better. Their continuous support, unconditional love, so much faith and endless freedom always boost me to work even harder. They are the most important people in my life and I dedicate my thesis to them. They are the best parents that the luckiest person can have. I also thank my cousins, their spouses and children for all the love, support and enjoyable company.

Arup Ghosh

List of publications related to thesis work

- [1] **A. Ghosh** and K. Mandal, "Large inverse magnetocaloric effect in $\text{Ni}_{48.5-x}\text{Co}_x\text{Mn}_{37}\text{Sn}_{14.5}$ ($x = 0, 1$ and 2) with negligible hysteresis", *Journal of Alloys and Compounds*, 579, 295–299 (2013).
 - [2] **A. Ghosh** and K. Mandal, "Large magnetoresistance associated with large inverse magnetocaloric effect in Ni-Co-Mn-Sn alloys", *European Physical Journal B*, 86, 378 (2013).
 - [3] **A. Ghosh** and K. Mandal, "Large magnetic entropy change and magnetoresistance associated with a martensitic transition of Mn-rich $\text{Mn}_{50.5-x}\text{Ni}_{41}\text{Sn}_{8.5+x}$ alloys", *Journal of Physics D: Applied Physics*, 46, 435001 (2013).
 - [4] **A. Ghosh** and K. Mandal, "Effect of structural disorder on the magnetocaloric properties of Ni-Mn-Sn alloy", *Applied Physics Letters*, 104, 031905 (2014).
 - [5] **A. Ghosh** and K. Mandal, "A comparative study of magnetocaloric properties between Ni-rich and Mn-rich Ni-Mn-Sn alloys", *IEEE Transactions on Magnetics*, 50, no. 11, 1-4 (2014).
 - [6] **A. Ghosh** and K. Mandal, "Tuning of magnetocaloric potential in disordered Ni-Mn-Sn alloy", *Physics Procedia*, 54, 10–15 (2014).
 - [7] **A. Ghosh** and K. Mandal, "Effect of Fe substitution on the magnetic and magnetocaloric properties of Mn-rich Mn-Ni-Fe-Sn off-stoichiometric Heusler alloys", *Journal of Applied Physics*, 117, 093909 (2015).
 - [8] **A. Ghosh** and K. Mandal, "Magnetocaloric Effect in Mn-rich Mn-Fe-Ni-Sn alloys", *AIP Conference Proceedings*, 1665, 030015 (2015).
 - [9] **A. Ghosh**, S. Misra, P. Sen, S. K. Bandyopadhyay and K. Mandal, "Measurement protocol dependent magnetocaloric properties in Mn-rich Si-doped Mn-Ni-Sn-Si off-stoichiometric Heusler alloy", 2015 (Communicated).
-

List of publications apart from thesis work

- [1] S. Ghosh, G. G. Khan, **A. Ghosh**, S. Varma and K. Mandal, "Zinc vacancy-induced high- T_C ferromagnetism and photoluminescence in group-1 alkali-metal substituted p-type ZnO thin films", *Crystal Engineering and Communication*, 15, 7748 (2013).
- [2] D. Pal, **A. Ghosh** and K. Mandal, "Large inverse magnetocaloric effect and magnetoresistance in nickel rich $Ni_{52}Mn_{34}Sn_{14}$ Heusler alloy", *Journal of Magnetism and Magnetic Materials*, 360, 183-187 (2014).
- [3] D. Sarkar, **A. Ghosh**, R. Rakshit, and K. Mandal, "Magnetic properties of Fe_3O_4 nano hollow spheres", *Journal of Magnetism and Magnetic Materials*, 393, 192-198 (2015).
-

List of attended conferences and schools

International:

- [1] International Conference on Material Science and Technology (ICMST-2012), St. Thomas College, Pala, Kottayam, Kerala, India, 10-14 June 2012.
- [2] International Conference on Magnetic Materials and Applications (ICMagMA-2013), Indian Institute of Technology, Guwahati, India, 05-07 December 2013.
- [3] 7th IEEE Magnetics Society Summer School, Centro Brasileiro de Pesquisas Fisicas, Urca, Rio de Janeiro, Brazil, 10-15 August 2014.

National:

- [1] DST-SERC School on "Advanced Functional Magnetic Materials", Goa University, Taleigao Plateau, Goa, India 03-21 February 2014.
 - [2] National Conference on "Current Trends in Advanced Materials", Variable Energy Cyclotron Centre, Kolkata, India, 19-21 November 2014.
 - [3] 59th DAE-Solid State Physics Symposium-2014, VIT University, Vellore, Tamilnadu, India, 16-20 December 2014.
 - [4] 33rd Young Physicists' Colloquium (YPC 2015), Saha Institute of Nuclear Physics, Kolkata, India, 20-21 August 2015.
-

List of abbreviations

ac	alternating current
A_f	austenite finish temperature
AMR	anisotropic magnetoresistance
A_s	austenite start temperature
CMR	colossal magnetoresistance
dc	direct current
ΔM_{sat}	difference in saturation magnetization
DOS	density of states
DSC	differential scanning calorimetry or calorimeter
ΔS_M	isothermal magnetic entropy change
ΔT	transition width
ΔT_{ad}	adiabatic temperature change
ΔT_{hys}	thermal hysteresis
EAF	electric arc-melting furnace
EB	exchange bias
EDAX	energy dispersive X-ray analysis
EDS	energy dispersive spectroscopy
FC	field cooled
fcc	face centered cubic
FESEM	field emission scanning electron microscope
FIMST	field induced magneto-structural transition
FOMST	first order magneto-structural transition
FOMT	first order magnetic transition
FOPT	first order phase transition
FWHM	full width at half maxima
G_A	Gibb's free energy of the austenite phase
G_M	Gibb's free energy of the martensite phase
GMR	giant magnetoresistance

H_C	coercivity
H_{EB}	exchange bias field
HF	heat flow
HL	hysteresis loss
IMCE	inverse magnetocaloric effect
MCE	magnetocaloric effect
M_f	martensite finish temperature
MR	magnetoresistance
MRAM	magnetoresistive random access memory
M_S	martensite start temperature
M_{sat}	saturation magnetization
M_{sat}^A	saturation magnetization in the austenite phase
M_{sat}^M	saturation magnetization in the martensite phase
MSME	magnetic shape memory effect
PPMS	physical property measurement system
RC	Refrigerant capacity
SEM	scanning electron microscope
SMA	shape memory alloys
SME	shape memory effect
SOMT	second order magnetic transition
SOPT	second order phase transition
T_A	martensite to austenite transition temperature
T_C	Currie temperature
T_C^A	Currie temperature of the austenite phase
T_C^M	Currie temperature of the martensite phase
T_{EB}	exchange bias blocking temperature
T_M	austenite to martensite transition temperature
VSM	vibrating sample magnetometer
XRD	X-ray diffraction or diffractometer
ZFC	zero field cooled

List of symbols

a	lattice constant
B	magnetic flux density
C	heat capacity
d	inter-planner separation
e	elementary charge ($= 1.602 \times 10^{-19}$ C)
e/a	valence electron concentration
G	Gibb's free energy
g	gyromagnetic ratio
H	magnetic field
I	Current
k_B	Boltzmann constant ($= 1.3806488 \times 10^{-23}$ J/K)
χ	susceptibility
χ'	real part of the ac susceptibility
χ''	imaginary part of the ac susceptibility
λ	wave length
M	magnetization
μ_B	Bohr magnetron ($= 9.274096 \times 10^{-24}$ J/T)
μ_0	permeability of free space
φ	phase shift
Φ	magnetic flux
R	resistance
r	Radius
ρ	electrical resistivity
S	Entropy
T	temperature
t	Time
θ	Angle
V	Voltage

CONTENTS

List of publications related to thesis work	I
List of publications apart from thesis work	II
List of attended conferences and schools	III
List of abbreviations	IV
List of symbols	VI
1. Introduction	1 - 33
1.1. Preamble	1
1.2. Thermodynamics of magnetocaloric effect	2
1.2.1. Maxwell's relation for determining magnetocaloric effect	3
1.2.2. Condition for obtaining large magnetocaloric effect	4
1.2.3. Conventional and inverse magnetocaloric effect	5
1.3. Thermodynamic cycle of magnetic cooling	6
1.3.1. Magnetic Ericsson cycle	7
1.3.2. Magnetic Brayton cycle	7
1.4. Measurement techniques for magnetocaloric effect	8
1.4.1. Direct measurement of MCE	8
1.4.2. Indirect measurement of MCE	8
1.4.3. Refrigerant capacity	9
1.5. Magnetic refrigeration and its importance	10
1.6. History of magnetocaloric effect	11
1.7. Magnetocaloric materials	12
1.7.1. Rare earth based magnetocaloric materials	13
1.7.2. Transition element based magnetocaloric materials	13
1.7.3. Mixed rare earth and transition element based materials	13
1.7.4. Some other MCE materials and an overall comparison	14
1.8. Heusler alloys	15
1.8.1. Structural properties of Heusler alloys	16
1.8.2. Martensitic transition in Heusler alloys	16

1.8.3. Field induced effect on the martensitic transition	18
1.8.4. Exchange bias effect in Heusler alloys	19
1.8.5. Magnetoresistance in Heusler alloys	21
1.9. Motivation and objectives of thesis	22
1.10. Organization of the thesis	24
<i>Bibliography</i>	26
2. Experimental details	34 - 55
2.1. Preamble	34
2.2. Sample preparation technique	34
2.2.1. Electric Arc-Melting Furnace	35
2.3. Structural and compositional characterization techniques	37
2.3.1. X-ray Diffractometer	37
2.3.2. Scanning Electron Microscope	38
2.3.3. Energy Dispersive Analysis of X-rays	40
2.4. Thermal characterization technique	41
2.4.1. Differential Scanning Calorimeter	41
2.5. AC Magnetic characterization technique	42
2.5.1. Basic design and theory for determining the ac susceptibility	43
2.5.2. Block diagram and an overview of the setup	45
2.5.3. Designing and fabrication of the coils	46
2.5.4. The complete setup	47
2.5.5. To convert voltage into susceptibility	48
2.5.6. Limitations	49
2.6. DC Magnetic and magneto-transport characterization techniques	50
2.6.1. Vibrating Sample Magnetometer	50
2.6.2. Physical Property Measurement System	52
<i>Bibliography</i>	55

3. Magnetocaloric and magneto-transport properties in Co-doped Ni-rich Ni-Co-Mn-Sn off-stoichiometric Heusler alloys	56 – 84
3.1. Preamble	56
3.2. Experimental	58
3.3. Results and discussions	58
3.3.1. MCE in $\text{Ni}_{48.5-x}\text{Co}_x\text{Mn}_{37}\text{Sn}_{14.5}$ alloys with negligible hysteresis	58
3.3.1.1. Structural, thermal and electrical properties	58
3.3.1.2. Structural and magnetic phase transitions	60
3.3.1.3. Exchange bias	63
3.3.1.4. Magnetic hysteresis	64
3.3.1.5. Magnetocaloric effect	67
3.3.2. MCE and MR in $\text{Ni}_{47.5-y}\text{Co}_y\text{Mn}_{37.5}\text{Sn}_{15}$ alloys	68
3.3.2.1. Structural and magnetic phase transitions	68
3.3.2.2. Magnetic properties	73
3.3.2.3. Magnetocaloric properties	75
3.3.2.4. Resistivity and magnetoresistance	77
3.4. Conclusions	81
<i>Bibliography</i>	83
4. Tuning of magnetocaloric properties in Ni-rich disordered Ni-Mn-Sn off-stoichiometric Heusler alloy	85 – 101
4.1. Preamble	85
4.2. Experimental	87
4.3. Results and discussions	88
4.3.1. Structural characterization and phase transition	89
4.3.2. Temperature dependent magnetic properties	90
4.3.3. Exchange bias	93
4.3.4. Field dependent magnetic properties	95
4.3.5. Magnetocaloric properties	98
4.4. Conclusions	99

<i>Bibliography</i>	100
5. Magnetocaloric and magneto-transport properties of Mn-rich Mn-Ni-Sn and Mn-Fe-Ni-Sn off-stoichiometric Heusler alloys	102 – 131
5.1. Preamble	102
5.2. Experimental	104
5.3. Results and discussions	105
5.3.1. Martensitic transition in Mn-rich $\text{Mn}_{50.5-x}\text{Ni}_{41}\text{Sn}_{8.5+x}$ alloys and its associated MCE and MR	105
5.3.1.1. Structural characterization	105
5.3.1.2. Temperature dependent magnetic properties	106
5.3.1.3. Field dependent magnetic properties	109
5.3.1.4. Magnetocaloric properties	111
5.3.1.5. Magneto-transport properties	112
5.3.2. Effect of Fe substitution on the phase diagram and MCE in Mn-rich Mn-Fe-Ni-Sn off-stoichiometric Heusler alloys	114
5.3.2.1. Structural Characterization	114
5.3.2.2. Temperature dependent magnetic properties and phase diagram	116
5.3.2.3. Field dependent magnetic properties	120
5.3.2.4. Magnetocaloric properties	124
5.4. Conclusions	127
<i>Bibliography</i>	129
6. Measurement protocol dependent magnetocaloric effect in a Mn-rich Si doped Mn-Ni-Sn-Si off-stoichiometric Heusler alloy and its magnetoresistance	132 – 152
6.1. Preamble	132
6.2. Experimental	134
6.3. Results and discussions	135
6.3.1. Temperature dependent structural, magnetic properties and phase transitions	135

6.3.2. Exchange Bias	137
6.3.3. Isofield M - T curves and MCE	139
6.3.4. Field dependent magnetic properties in heating and cooling protocol	140
6.3.5. Isothermal magnetic entropy change	142
6.3.6. Universal curve fitting of MCE	144
6.3.7. Refrigerant capacity	146
6.3.8. Magnetoresistance	147
6.4. Conclusions	149
<i>Bibliography</i>	151
7. Conclusion and scope for future work	153 - 157
7.1. Epilogue	153
7.2. Scope for future work	156

Chapter 1 | Introduction

In this chapter we have discussed about the magnetocaloric effect and its importance. A literature review on the magnetocaloric materials has been described. The properties of Heusler alloys and an outline of the thesis have been also discussed.

1.1. Preamble

Magnetic materials have always been a great interest to the mankind because of their various interesting physical properties and applications in large scale [1-4]. Till date, the investigations on these materials helped to discover exciting new physics and to develop new technologies to make our life easier [3, 5-8]. From bulk to the nanostructures, magnetic materials have evolved in times with their increasing interests and multifunctionalities [9-12]. Although, recent research has a major focus on nano materials, the bulk materials still hold the ground as they can be handled easily and applied to the simple daily used devices.

In recent times, the cost of energy is increasing significantly due to the increased demand of electricity, fuels and crisis of their resources [13]. A major portion of research is thus focused to improve the applicability of the unlimited resources of natural energies like solar energy [14-16], wind power [17, 18], hydroelectric power [19, 20], geothermal energy [21, 22], etc. We consume majority portion of the total energy by using cooling devices like freezers, air conditioners, etc. in regular basis. Previously, these cooling devices used to contain hazardous gases as refrigerant materials that are suspected to deplete the ozone layer of the upper atmosphere [23, 24]. Although, these refrigerants are now replaced by the harmless gases, the low efficiency of vapor compression refrigerators is still an issue. In this scenario, the use of magnetic refrigerators that works on the principle of magnetocaloric effect (MCE) might be an alternative and energy efficient cooling technology as their efficiency can be enhanced up to 30% higher than that of the gas refrigerators [25-30].

MCE is a magneto-thermodynamic phenomenon that results in a change in temperature in adiabatic process and occurs due to the alignment or dis-alignment of spins under a magnetic field variation [30]. After the discovery of MCE in 1881 [31], lot of efforts have been given by many researchers to understand the effect and extract the benefits out of it [32-34]. Since 1930s, magnetic refrigeration has been a standard technique to cool down a system to the millikelvin temperatures by adiabatically demagnetizing the paramagnetic salts [35-37]. In 1997, the

demonstration of a room temperature magnetic refrigeration unit with Gd as a refrigerant material, gave a major breakthrough [38]. Since then, a large number of investigations have been done by many research groups on the costly rare earth based materials [39-46]. Although, rare earth based materials are found to be very effective magnetocaloric material, their high cost has become a major limitation. Therefore, other materials have been also studied, but either their MCE values are not so high or the working temperature region is not favorable for room temperature applications [30, 47-50]. In this context, transition metal based Heusler alloys are found to be an alternative as they are cheaper in cost, show large MCE [51-56] along with other interesting magneto-coupled multifunctional properties like magnetic shape memory effect (MSME) [52, 57-59], magnetoresistance (MR) [60-62], magnetothermal conductivity (MC) [63, 64], exchange bias (EB) effect [65, 66], etc. Moreover, their working temperature can be easily tuned for suitable room temperature applications. In this thesis, we have studied the magnetic, magnetocaloric and magneto-transport properties of Ni-Mn based Ni-Mn-Sn off-stoichiometric Heusler alloys to improve their aforementioned multifunctional properties [67-74].

In this chapter, we have discussed about the basic thermodynamics of MCE, its importance, history and the literature review of magnetocaloric materials. The properties of Heusler alloys, motivation of the thesis along with its objectives and a brief outline of the thesis chapters have been also discussed.

1.2. Thermodynamics of magnetocaloric effect

The entropy of a magnetic solid can be written as [75],

$$S(T, H) = S_M(T, H) + S_{\text{Lat}}(T) + S_{\text{El}}(T) \quad (1.1)$$

where $S_M(T, H)$, $S_{\text{Lat}}(T)$ and $S_{\text{El}}(T)$ are respectively the magnetic, lattice and electronic part of the total entropy of the material. T is the temperature and H is the applied external magnetic field. When a magnetic material is subjected to an external magnetic field, its $S_M(T, H)$ decreases due to the increase in ordering of the magnetic

sublattices. If the process is adiabatic, the released heat increases $S_{\text{Lat}}(T)$ which results in an increase in temperature. This magneto-thermodynamic phenomenon is known as MCE. Fig. 1.1 depicts the typical entropy versus temperature diagram ($S - T$ diagram) of a magnetic solid in the presence of zero and non-zero magnetic field. The adiabatic line gives the temperature change ($\Delta T_{\text{ad}}(\Delta H)$) and the isothermal line represents the magnetic entropy change ($\Delta S_{\text{M}}(T, \Delta H)$).

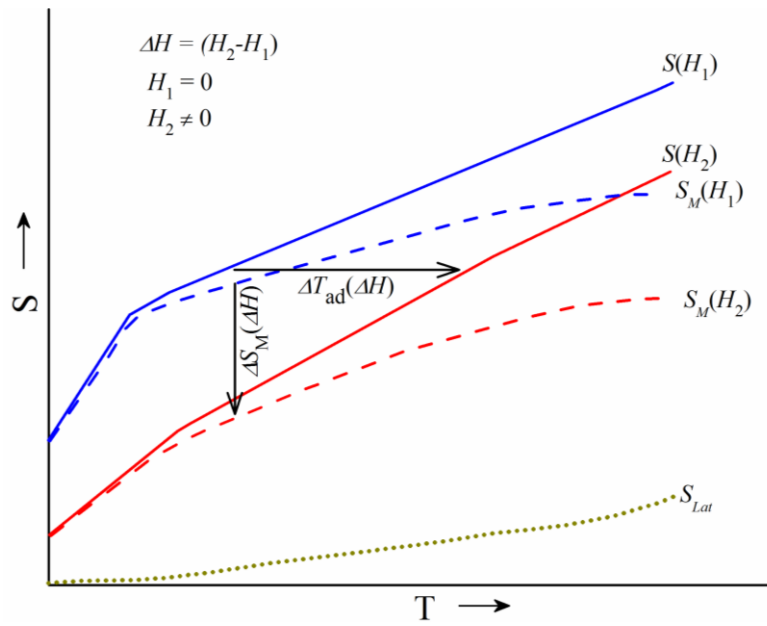


Fig. 1.1: Schematic diagram of the entropy (S) of a magnetic solid as a function of temperature (T) in presence of a zero and non-zero magnetic field.

1.2.1. Maxwell's relation for determining magnetocaloric effect

The total entropy can be written in differential form as,

$$dS(T, H) = \left(\frac{\partial S(T, H)}{\partial T} \right)_H dT + \left(\frac{\partial S(T, H)}{\partial H} \right)_T dH \quad (1.2)$$

Using,

$$C(T, H) = T \left(\frac{\partial S(T, H)}{\partial T} \right)_H \quad (1.3)$$

and the following Maxwell's relation,

$$\left(\frac{\partial S(T, H)}{\partial H} \right)_T = \mu_0 \left(\frac{\partial M(T, H)}{\partial T} \right)_H \quad (1.4)$$

equation (1.2) can be written as,

$$dS(T, H) = \frac{C(T, H)}{T} dT + \mu_0 \left(\frac{\partial M(T, H)}{\partial T} \right)_H dH \quad (1.5)$$

where $C(T, H)$, $M(T, H)$ and μ_0 are respectively the specific heat, magnetization of the material and the permeability of free space. For isothermal process, $dT = 0$. Thus, for a field changes from H_1 to H_2 , the integral form of equation (1.5) becomes,

$$\Delta S_M(T, \Delta H) = \int_{H_1}^{H_2} dS(T, H) = \mu_0 \int_{H_1}^{H_2} \left(\frac{\partial M(T, H)}{\partial T} \right)_H dH \quad (1.6)$$

In the case of adiabatic process, $dS = 0$ and equation (1.5) gives,

$$\frac{C(T, H)}{T} dT + \mu_0 \left(\frac{\partial M(T, H)}{\partial T} \right)_H dH = 0 \quad (1.7)$$

$$dT = -\mu_0 \frac{T}{C(T, H)} \left(\frac{\partial M(T, H)}{\partial T} \right)_H dH \quad (1.8)$$

For a field changes from H_1 to H_2 ,

$$\Delta T_{ad}(T, \Delta H) = \int_{H_1}^{H_2} dT = -\mu_0 \int_{H_1}^{H_2} \frac{T}{C(T, H)} \left(\frac{\partial M(T, H)}{\partial T} \right)_H dH \quad (1.9)$$

The equation (1.6) and (1.9) give the measure of MCE and well known as the Maxwell's relations for determining the ΔS_M and ΔT_{ad} .

1.2.2. Condition for obtaining large magnetocaloric effect

Although, MCE is an intrinsic property to the all magnetic materials, it is necessary to find out the criterion for obtaining larger MCE. It helps us to choose better magnetocaloric materials and standardize them for possible applications. The Currie-Weiss law under low magnetic field and at high temperatures takes the following form [76]:

$$\chi = \frac{M(T, H)}{H} \quad (1.10)$$

$$= \frac{Ng^2J(J+1)\mu_B^2}{3Ak_B(T-T_C)} \quad (1.11)$$

where N , g , J , μ_B , A , k_B and T_C are respectively the number of magnetic atoms per unit volume, gyromagnetic ratio, total angular momentum quantum number, Bohr magneton, atomic weight, Boltzmann constant and Currie temperature. Therefore,

$$\left(\frac{\partial M(T,H)}{\partial T}\right)_H = -\frac{Ng^2J(J+1)\mu_B^2H}{3Ak_B(T-T_C)^2} \quad (1.12)$$

Using equation (1.12), the equations (1.6) and (1.9) become,

$$\Delta S_M(T, \Delta H) = -\mu_0 \int_{H_1}^{H_2} \left(\frac{Ng^2J(J+1)\mu_B^2H}{3Ak_B(T-T_C)^2}\right) dH \quad (1.13)$$

and,

$$\Delta T_{ad}(T, \Delta H) = \mu_0 \int_{H_1}^{H_2} \frac{T}{C(T,H)} \left(\frac{Ng^2J(J+1)\mu_B^2H}{3Ak_B(T-T_C)^2}\right) dH \quad (1.14)$$

From equations (1.13) and (1.14), we can see that in the expressions for ΔS_M and ΔT , there is a $J(J+1)$ term in the numerator and a $(T-T_C)^2$ term in the denominator. Therefore, the isothermal magnetic entropy change, ΔS_M , and adiabatic temperature change, ΔT_{ad} , will be the maximum for a material near its Currie temperature, T_C and having larger J value. In this context, rare earth elements can be very effective. For the application of MCE near room temperature, the T_C of a material should be very close to the same temperature. In addition to that, the specific heat, C , of the material should be low so that its temperature can be changed easily. Moreover, there is a term, $(\partial M/\partial T)_H$, in both the expressions for ΔS_M and ΔT_{ad} . This predicts that any kind of phase transition is desirable for MCE study if it accompanies significant change in magnetic properties.

1.2.3. Conventional and inverse magnetocaloric effect

There are two types of MCE we would like to mention. Fig. 1.2(a) represents a magnetization versus temperature plot for a typical ferromagnet across its T_C . The magnetization here decreases noticeably with increasing the temperature across the phase transition. This makes $\partial M/\partial T$ negative (Fig. 1.2.(b)) and thus ΔS_M also. It is known as the conventional magnetocaloric effect. It can be observed across the Currie temperature of a ferromagnet, Néel temperature of an antiferromagnet (T_N) and any other magnetic phase transitions where magnetization decreases with increasing the temperature [47-50].

In some phase transitions, the magnetization increases with increasing the temperature across the transition point (Fig. 1.2(c)). It makes $\partial M/\partial T$ positive (Fig.

1.2(d)) and thus ΔS_M also. It is called as the inverse magnetocaloric effect (IMCE). The materials exhibiting antiferro-ferro transition can show IMCE. Other types of phase transitions like any structural phase change from a weakly magnetic structure to a magnetically more sensitive structure on heating are also very effective to obtain IMCE [51-56]. Although, the MCE is defined in these two types, they do not differ from each other largely when we talk about the materials' application possibilities. In order to obtain magnetic cooling, the conventional MCE materials are needed to be taken out from the external magnetic field, where IMCE materials are required to be subjected to the same.

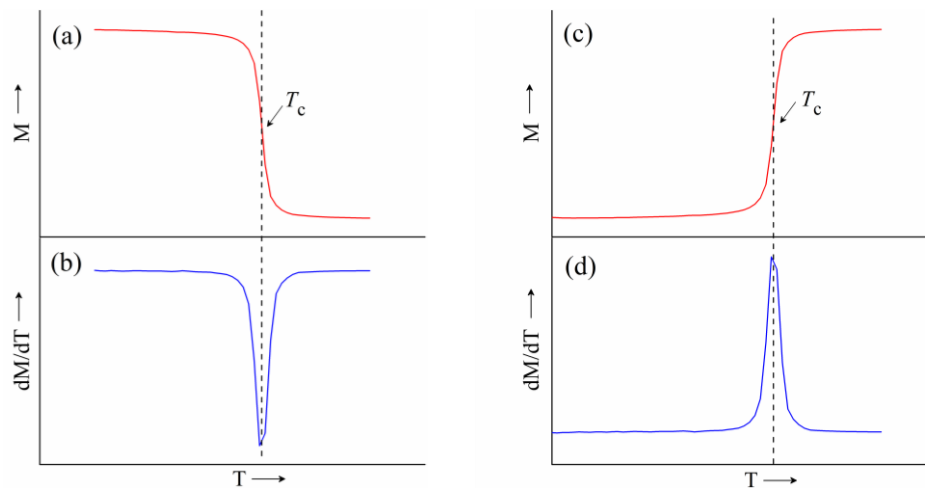


Fig. 1.2: Schematic representation of the temperature dependence of magnetization for a magnetic material across its (a) magnetic phase transition and (c) phase transition that accompanies an increase in magnetization with increasing the temperature. (b) and (d) show the corresponding $\partial M/\partial T$.

1.3. Thermodynamic cycle of magnetic cooling

The refrigeration cycle using the magnetic field is very similar to the vapor compression cycle [77]. The major difference is, for gas refrigerators, the external stimulus is the pressure, but in the case of magnetic refrigerators, it is the magnetic field. In general, magnetic refrigeration cycle consists of four processes [78]. Two of them are magnetization and demagnetization. Among all the basic magnetic refrigeration cycles, Ericsson and Brayton cycles are well applicable for room temperature refrigeration. A representative schematic form of magnetic Brayton cycle is shown in Fig. 1.3.

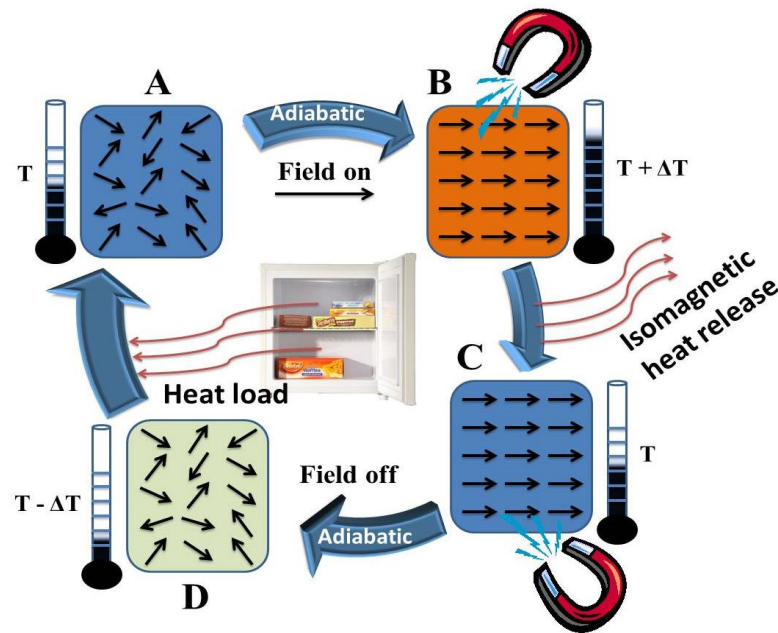


Fig. 1.3: Schematic representation of magnetic Brayton cycle.

1.3.1. Magnetic Ericsson cycle

This cycle consists of two isothermal and two isofield processes. It works as follows:

- Isothermal magnetization (A→B):** The refrigerant material is magnetized isothermally and the released heat is transferred to the regenerator fluid.
- Isomagnetic heat rejection (B→C):** During this process the applied field remains unchanged and the released heat is rejected to the sink. Both the entropy and temperature decreases.
- Isothermal demagnetization (C→D):** The applied field is now removed isothermally and the refrigerant absorbs heat form the regenerator fluid.
- Isomagnetic heat absorption (D→A):** Now, the regenerator fluid is allowed to absorb heat from the environment that is needed to cool.

After the completion of the above mentioned cycle, heat can be extracted from the refrigerator and rejected to the outside. Therefore, a continuous repetition of the same cycle results in a monotonic decrease in temperature.

1.3.2. Magnetic Brayton cycle

It consists of two adiabatic and two isofield processes. Its principle is described as follows:

- a) *Adiabatic magnetization (A→B)*: The refrigerant is first magnetized adiabatically and its temperature increases. The regenerator fluid absorbs the amount of heat released by the refrigerant.
- b) *Isomagnetic heat rejection (B→C)*: The heat is now rejected isomagnetically to the sink by the regenerator fluid and the regenerator comes back to its initial temperature.
- c) *Adiabatic demagnetization (C→D)*: An adiabatic demagnetization causes a decrease in temperature and the heat from the regenerator fluid is absorbed and its temperature also decreases.
- d) *Isomagnetic heat load (D→A)*: At this point, the heat can be extracted from the interior of the refrigerator through the regenerator fluid.

1.4. Measurement techniques for magnetocaloric effect

There are two ways to measure the MCE of a material; direct and indirect methods [52, 53, 56, 79, 80].

1.4.1. Direct measurement of MCE

Direct measurement of MCE can be done by adiabatically measuring the temperature changes and thus no further calculations are required [45]. For better measurement, the sample needs to be isolated properly so that no heat can be exchanged between the sample and the surroundings. The thermal conductivity of the sample should be high; otherwise, the instantaneous change in temperature will be measured incorrectly during the period of field sweeping.

1.4.2. Indirect measurement of MCE

The MCE of a material can be measured indirectly by using two different approaches. Firstly, the temperature dependent heat capacity is measured in presence of zero and non-zero magnetic field [80]. Equation (1.3) can be written as,

$$S(T, 0) = \int_0^T \frac{C(T,0)}{T} dT + S(0,0) \quad (1.15)$$

and,

$$S(T, H) = \int_0^T \frac{C(T, H)}{T} dT + S(0, H) \quad (1.16)$$

where $S(0, 0)$ and $S(0, H)$ are respectively the entropies under zero and non-zero field at the absolute zero. Both are the same for a condensed system. Therefore, subtracting equation (1.15) from (1.16), we have the ΔS_M as,

$$\Delta S_M(T, \Delta H) = \int_0^T \frac{C(T, H) - C(T, 0)}{T} dT \quad (1.17)$$

On the other hand, ΔS_M can also be measured by taking the isothermal field dependence of magnetization (M - H curves) data at different temperatures around the temperature of interest (across the phase transition) with a small temperature interval ($\Delta T \sim 1 \text{ K} - 3 \text{ K}$) and using a numerical approximation of equation (1.6) as,

$$\Delta S_M(T, \Delta H) = \mu_0 \sum_i \frac{(M(T + \frac{\Delta T}{2}, H_i) - M(T - \frac{\Delta T}{2}, H_i))}{\Delta T} \Delta H_i \quad (1.18)$$

To measure the adiabatic temperature change indirectly, we need field dependent heat capacity data along with the M - H curves. ΔT_{ad} can be calculated from equation (1.9) as,

$$\Delta T_{ad}(T, \Delta H) = -\mu_0 \sum_i \frac{T}{C(T, H_i)} \frac{(M(T + \frac{\Delta T}{2}, H_i) - M(T - \frac{\Delta T}{2}, H_i))}{\Delta T} \Delta H_i \quad (1.19)$$

For the materials with second order magnetic phase transition the use of equations (1.17), (1.18) and (1.19) remain valid. But, for the materials with first order transitions, use of the aforementioned relations may over or underestimate the MCE values due to the field induced metamagnetic effect [52-54]. The possible ways to deal with this problem are discussed later in this chapter (subsection 1.8).

1.4.3. Refrigerant capacity

For indirect measurement of MCE, the isothermal magnetic entropy change and adiabatic temperature change are not sufficient to characterize any refrigerant material. Its refrigerant capacity (RC) is required to be estimated also [55, 81, 82]. RC is defined as the amount of thermal energy that can be extracted from a colder source and transferred to a hotter sink in one ideal thermodynamic cycle. Figs. 1.4(a)

and b) represent typical temperature dependent curves of ΔS_M near a magnetic phase transition. Usually, it shows a peak function like behavior and the area under the curve gives us the measure of RC. It can be evaluated by using the following formula [81]:

$$RC = \int_{T_1}^{T_2} |\Delta S_M(T, \Delta H)| dT \quad (1.20)$$

where T_1 and T_2 are respectively the lower (colder source) and upper (hotter sink) temperatures of the full width at half maxima (FWHM) of the $\Delta S_M - T$ curve as depicted in Figs. 1.4(a and b). A good refrigerant material should have high RC. Therefore, the criteria will be like; the peak value of ΔS_M should be high and the width of the phase transition should be broad.

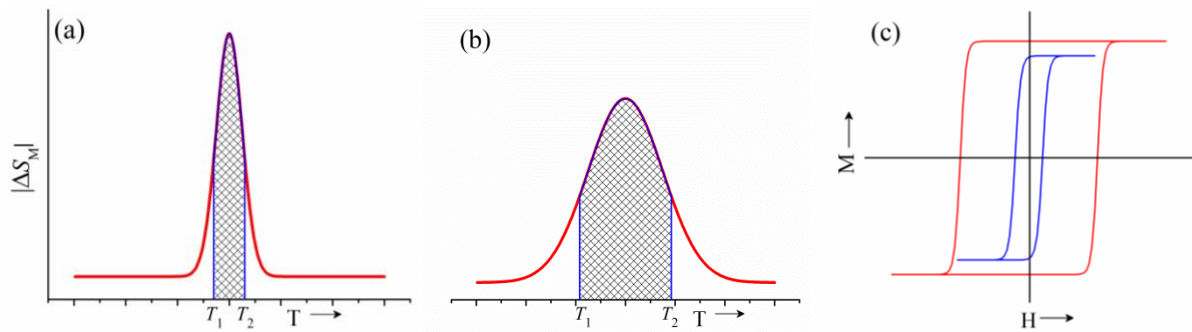


Fig. 1.4: Temperature dependent magnetic entropy change across a (a) sharp and (b) broad phase transition. (c) Magnetic hysteresis loops showing the losses.

Along with the above mentioned conditions, the magnetic hysteresis losses (HL) should also be small. In this context, soft magnetic materials can be effective. The energy consumed by the material itself during the magnetization process can be estimated using the formula [83],

$$HL = \mu_0 \oint M(T, H) dH \quad (1.21)$$

This loss is required to be subtracted from the total RC to obtain its net value.

1.5. Magnetic refrigeration and its importance

Using the above mentioned thermodynamic cycles, a heat pump can be constructed which may be used for refrigeration purposes. This technology is known as the magnetic refrigeration. It is an environmentally clean refrigeration technique

as the refrigerant materials are solid and non-toxic. Water can be used as the regenerator fluid. Till date, the vapor compression refrigerators are the maximally used cooling devices. But, its refrigerant gas, the chemical called “Freon” contains chloro-fluoro-carbons (CFCs), which are suspected of causing damage to the ozone layer of stratosphere. The harmful ultraviolet rays coming from the Sun that cause different types of biological disorder and skin cancer are absorbed by the ozone gas. Hence, the use of such refrigerant gases may be unsafe for the living beings. Although, CFCs are now replaced by harmless gases like tetrafluoroethane, there are still some issues like energy consumptions and the unattainability of millikelvin temperatures using the gas refrigerators.

The magnetic refrigerators are expected to consume almost 30% less energy as compared to the gas refrigerators. A large amount of energy is consumed by our daily used cooling devices. We use freezer, air conditioner (AC), dehumidifier, air conditioned car, etc. for our personal comforts. The cold storages and supermarkets are one of the most consuming candidates of electricity for using the centralized ACs. In recent times, we are running out of the easily available energy sources and thus the cost of energy is increasing day by day. Therefore, a major amount of recent research is focused on the search for alternative naturally available energy resources like solar energy, wind power, geothermal energy, etc. [14-22]. In this scenario, if it is possible to replace the current cooling devices by the above mentioned magnetic cooling prototypes and save 30% of such energy that we are consuming in present days, it can not only save our money, but at the same time it can also solve the current energy crisis up to some extent [25-30].

1.6. History of magnetocaloric effect

Although, MCE is an interesting and very active field of research, it was discovered a long time ago. In 1881, Emil Warburg observed the change in temperature due to the application of magnetic field in pure Fe for the first time [31]. Almost 45 years later, in 1926 and 1927 Debye [32] and Giauque [33] independently understood the phenomena and explained the process of cooling using magnetic

field variation. The process of magnetic cooling was demonstrated for the first time in 1933 by Giauque and MacDugall [34]. They built an adiabatic demagnetization unit which was able to reach a temperature as low as 0.25 K.

Since 1930s, magnetic refrigeration became a standard technique to drop down the temperature below 1 K by adiabatically demagnetizing the paramagnetic salts [35-37]. In 1976, the first room temperature magnetic refrigeration unit was designed by Brown [84]. About 15 years later, a prototype was built by Green *et al* which actually was able to cool the load [85]. A major breakthrough occurred in 1997 in Ames Laboratory when they demonstrated a magnetic refrigeration unit in collaboration with the Astronautics Corporation that can be operated in room temperature and can be competitive with the vapor compression refrigerators [38]. They used Gd spheres as the refrigerant material. One of the major limitations of their prototype was that the used magnet was superconducting, which limited its possibilities of application. A similar prototype using permanent magnet was built in 2001 [86]. Since then, a large number of prototypes were demonstrated by many research groups [87], but to make them commercially available, extensive efforts are still required to enhance the quality of such refrigerators and as well as to find out better refrigerant materials.

1.7. Magnetocaloric materials

The MCE has been studied extensively during the last four decades to improve the quality of refrigerant materials for room temperature magnetic refrigeration [25-85]. Initially, the main interests were focused on the rare earth metals and their alloys [39-46, 88]. These materials have shown large MCE (ΔS_M and ΔT_{ad}) across their ferromagnetic ordering temperatures which is near the room temperature (~ 300 K). But, due to the high cost of rare earth based materials, the research interest on MCE has started to shift towards the relatively cheaper transition metal based alloys and compounds [47-56]. A brief overview on the effective MCE materials has been given in this subsection considering the latest literature surveys and most of the materials have been compared by plotting them in a master curve (Fig. 1.5).

1.7.1. Rare earth based magnetocaloric materials

The metallic Gd is taken as a reference MCE material which has the ability to exhibit 10 J/kg K and 10 K of respectively ΔS_M and ΔT_{ad} around its $T_C \sim 294$ K due to 50 kOe of field changes [89]. In 1997, Pecharsky and Gschneidner reported $\Delta S_M \sim 20$ J/kg K near 273 K under the same field changes in $Gd_5Si_2Ge_2$ which undergoes a first order phase transition (FOPT) [88]. As the ΔS_M value of this Gd-Si-Ge material is significantly larger as compared to the metallic Gd, the effect was named as giant MCE. The same group investigated on the series of Gd-Si-Ge alloys and also reported giant MCE in them [39-41, 46]. There are many reports showing large MCE in other rare earth based alloys and compounds like Gd-Tb, Gd-Dy-Nd, etc. [90-93].

1.7.2. Transition element based magnetocaloric materials

Although, the rare earth based materials are found to show large MCE, their cost is very high, which is not favorable for commercial applications. Therefore, lots of works on MCE have been reported in the literature on transition metal based alloys and compounds [47-60]. Mn based materials are good in that way. Mn-As based Mn-Fe-P-As-Sb and manganites have shown large MCE across their FOPT [94-98]. Ni-Mn based Heusler alloys are one of the most promising magnetocaloric candidate of recent time. These materials can exhibit large MCE across their magneto-structural transition which is first order in nature [51-56].

1.7.3. Mixed rare earth and transition element based materials

The transition elements based materials are however good refrigerant, but their MCE values fall noticeably short as compared to the Gd based giant MCE materials. Therefore, people have tried to obtain giant MCE by inter-mixing the rare earth and transition elements as the rare earth elements have larger J values, which can enhance the MCE. Many of such works have been found to be successful in this scenario. For example; La and Pr doped manganites have shown enormous enhancement in ΔS_M [99-103]. La-Fe-Si materials are also one of the most successful candidates [104-106]. The same materials have shown giant MCE across FOPT which originates due the itinerant electron metamagnetism [104].

1.7.4. Some other MCE materials and an overall comparison

In addition to the above mentioned magnetocaloric materials, the amorphous magnetic materials [107-109], nanocomposites and some molecular clusters [110-112] have been also reported. In Fig. 1.5, we have made a schematic representation of the magnetic entropy changes (normalized by the respective field change values) for the effective MCE materials as a function of temperature. Even if the ΔS_M does not changes linearly in most of the materials across their FOPT due to the field induced effect, a fair comparison can be made from such approach. It can help us to choose effective working material out of the best magnetic refrigerants.

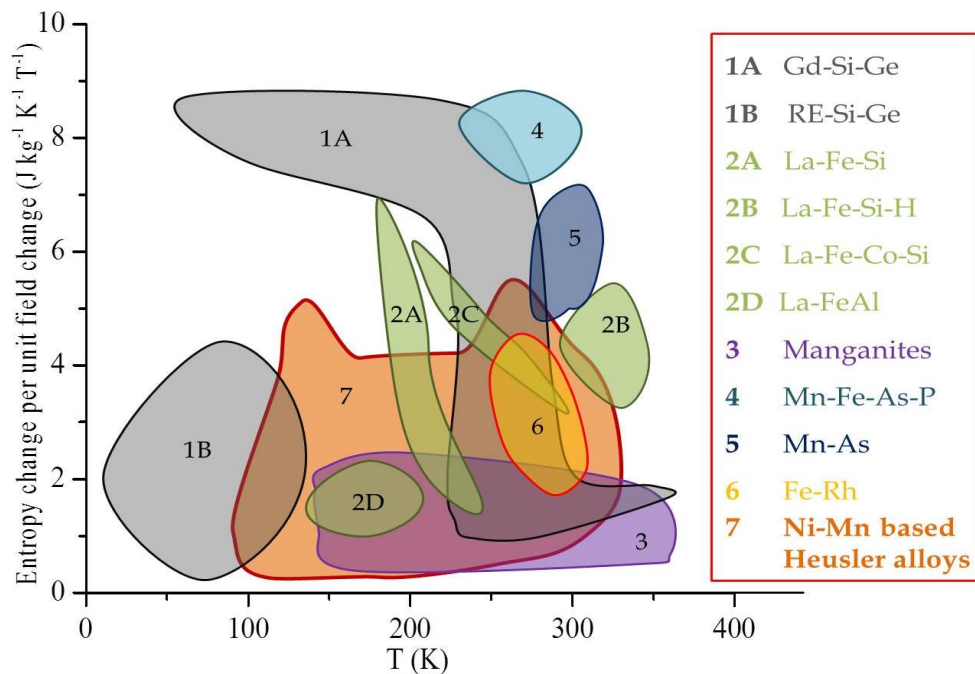


Fig. 1.5: Normalized magnetic entropy changes (per unit field change) as a function of temperature for the various classes of magnetocaloric materials.

One can observe that Gd based giant MCE materials have the largest MCE values and their working temperature range is good for room temperature magnetic refrigeration. But, their larger values of MCE are obtainable from just below room temperature (~ 300 K) to the lower temperatures and their cost is also very high. This makes them commercially unfavorable. For the other materials up to 6 (as indicated in Fig. 1.5), either their peak values of ΔS_M are low or working temperatures and its widths are not suitable for room temperature applications. The Ni-Mn based Heusler

alloys are found to be very interesting in this context. Their MCE values are large and the working temperature range is highly suitable for room temperature magnetic refrigeration. They are cheaper in cost and their transition temperatures can be easily optimized by changing the elementals' ratios or doping other agents [52, 56]. Considering all the above mentioned facts, we have realized that if the MCE of such Ni-Mn based Heusler alloys can be enhanced up to the giant values, a very efficient, environmentally clean, energy saving and low cost magnetic cooling may become possible. Therefore, we have chosen these materials to study them rigorously and find some way, so that their MCE can be improved.

1.8. Heusler alloys

Heusler alloys are a very special class of material that has cubic ($L2_1$) structure with four interpenetrating face centered cubic (fcc) sublattices. Its chemical formula is X_2YZ , where X and Y are the transition metals and Z is the post transition elements [52, 113]. The name "Heusler" came from the German mining engineer and chemist, Friedrich Heusler who studied a Cu_2MnSn alloy in 1903. He found that although, Cu-Mn alloy does not contain any ferromagnetic element, the addition of *sp* elements (Al, In, Sn, Sb or Bi) can turn it into a ferromagnetic material. In 1929, the structure of Heusler alloys was revealed when Potter did X-ray measurements on a Cu-Mn-Al alloy. It is basically an ordered combination of two binary *B2* compounds; XY and XZ. If one of the four sublattices remains unoccupied, it is called half Heusler alloys with $C1_b$ structure.

Majority number of Heusler alloys order ferromagnetically in their stoichiometric compositions. Their Currie temperature resides very close to the room temperature (~ 300 K), which is very good for various practical applications [52, 56]. Most of the Heusler alloys in their off-stoichiometric composition undergo a first order magneto-structural transition (FOMST) which is a well known martensitic transition. The observation of shape memory effect, MCE and MR in Ni-Mn based Heusler alloys across their martensitic transition has made them very interesting for active research [51-64].

1.8.1. Structural properties of Heusler alloys

In stoichiometric X_2YZ Heusler alloys, four interpenetrating fcc sublattices form a unit cell, where X atoms take $(0,0,0)$ and $(\frac{1}{2},\frac{1}{2},\frac{1}{2})$ positions. The remaining $(\frac{1}{4},\frac{1}{4},\frac{1}{4})$ and $(\frac{3}{4},\frac{3}{4},\frac{3}{4})$ positions are occupied respectively by Y and Z atoms [113]. The $(\frac{1}{2},\frac{1}{2},\frac{1}{2})$ site remains unoccupied for the half Heusler materials. In Mn-based such alloys, Mn atoms have a tendency to occupy the Y site. Therefore, in Ni-rich (Ni ~ 50 at%) Ni-Mn based Ni_2MnZ alloys, Ni atoms can easily take the X sites and form a cubic $L2_1$ structure. But, for Mn-rich (Mn ~ 50 at%) Ni-Mn based Mn_2NiZ alloys, Mn takes one of the X sites along with the Y site. This forces Ni atoms to occupy the remaining X site, which leads to a Hg_2CuTi -type cubic structure [114]. In case off-stoichiometric Heusler alloys, the excess Y elements can occupy the partially vacant Z site. The schematic representations of Heusler structures are given in Fig. 1.6. Almost all the off-stoichiometric and very few stoichiometric compositions undergo a structural phase transition from cubic austenite to a tetragonal martensite phase on cooling, which contains significant potential to show interesting multifunctionalities.

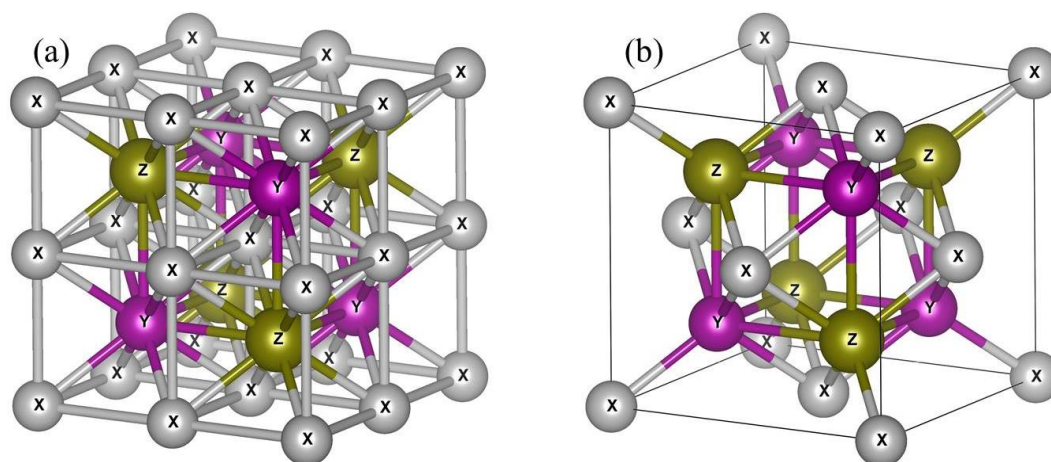


Fig. 1.6: Schematic diagram of (a) full Heusler and (b) half Heusler structures. X and Y are transition elements and Z is post transition elements.

1.8.2. Martensitic transition in Heusler alloys

The martensitic transition is a first order structural phase transformation which is displacive, but diffusionless. It means that the atoms move less than their interatomic separations and the nearest neighbors are always maintained during the phase transition. Martensitic transition was first observed in quenched steels by the

German metallurgist Adolf Martens at the end of 19th century [115]. The low temperature phase was named after him as “martensite”, whereas the gamma phase above the transition point was named after Sir William Chandler Roberts-Austen as “austenite”. In most of the cases, Heusler alloys are also found to exhibit martensitic transformation in off-stoichiometry from cubic austenite to a tetragonal martensite phase which is a FOMST. During the transformation of phase, different regions of the material transform at high speeds and therefore, the transition occurs by nucleation and growth mechanism.

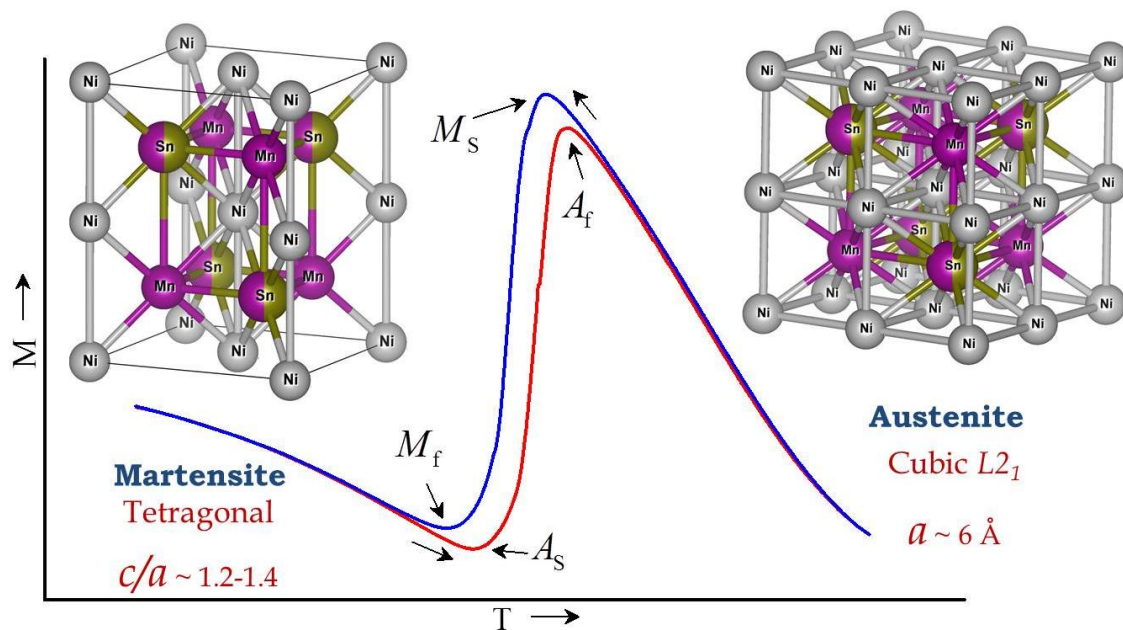


Fig. 1.7: Temperature dependent representative magnetization curves for an off-stoichiometric Ni-Mn-Sn Heusler alloy showing the existence of martensitic transition.

One of the characteristic features of the martensitic transformation is its thermal hysteresis. Fig. 1.7 shows the schematic representation of the temperature dependent magnetization curves for Ni-Mn-Sn off-stoichiometric Heusler alloys exhibiting martensitic phase transition. The change in interatomic spacing during the phase transition causes a significant variation in the magnetic correlations between the inter and intra-site X, Y elements [116]. This results in a large change in magnetization across the martensitic transition and thus large MCE is expected from these materials. During heating, the martensite to austenite transition starts at A_s and finishes at A_f . The transition temperature during heating is defined as $T_A =$

$(A_S + A_f)/2$. The reverse transition during cooling starts at M_S and finishes at M_f . The transition temperature during cooling is $T_M = (M_S + M_f)/2$. Most of these characteristic temperatures are also indicated in Fig. 1.7.

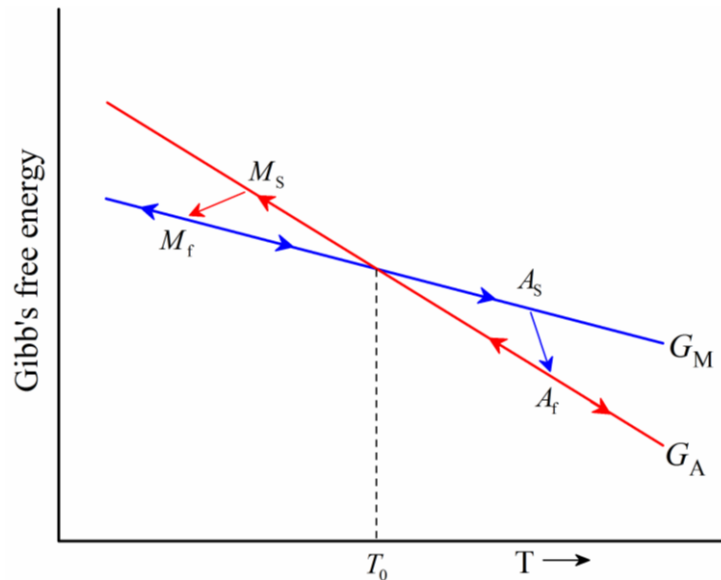


Fig. 1.8: A schematic representation of the temperature dependent Gibb's free energy of the two structures across the martensitic transition of Heusler alloys.

The temperature dependent Gibb's free energies of the martensite (G_M) and austenite (G_A) phases are schematically presented in Fig. 1.8. At the equilibrium temperature (T_0), $G_M = G_A$. For $T < T_0$, $G_M < G_A$, which indicates that the martensite phase is energetically stable below the phase transition temperature [117]. For $T > T_0$, $G_M > G_A$, and similarly the austenite phase gains the stability. The stability of these two phases can be altered by applying external thermal, mechanical, magnetic, etc. forces. In this way, the FOMST can be induced by the external field.

1.8.3. Field induced effect on the martensitic transition

The martensite phase of Ni-Mn based Heusler alloys has twinned structure with high magnetocrystalline anisotropy. When a magnetic field is applied, the magnetic moments rotate together with the structure to align the easy axis along the direction of applied field. As a result, the multi-variant martensite phase becomes single variant. A schematic illustration is given in Fig. 1.9. If the temperature is close to the A_S , the structure of the sample can be transformed from martensite to the

austenite at a constant temperature by applying high magnetic field. It is known as the field induced magneto-structural transition (FIMST). The initial phase of the sample can be regained partially after the removal of field.

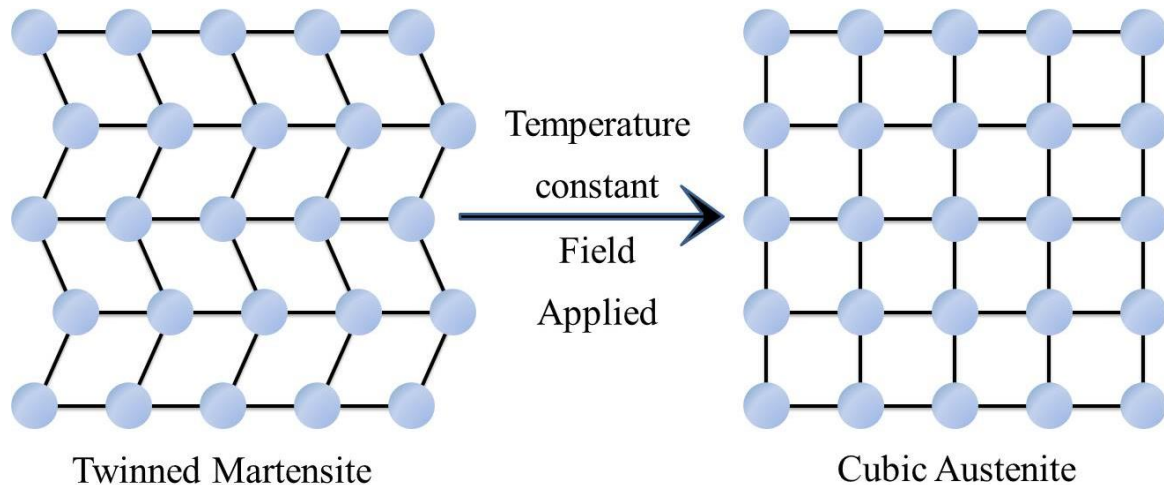


Fig. 1.9: A Schematic representation of the magnetic field induced reverse martensitic transformation.

This FIMST creates a major problem during the measurements and calculations of MCE for the Heusler alloys. The magnetization in the saturation region increases nonlinearly due to the metamagnetic transition under high magnetic field [52-54]. The history of last field sweeping affects the next $M-H$ curves across the martensitic transition due the field induced irreversibility in structural transition. All these above mentioned facts results in an overestimation of the MCE values. Some efforts can be made to overcome these difficulties and achieve better results for a fair comparison of the magnetocaloric materials. Firstly, The $M-H$ curves across the FOMST can be taken in discontinuous temperature ramping mode [118, 119]. Next, the maximum applicable field can be limited below the critical field of starting the metamagnetic transition. And finally, the net value of RC can be estimated by subtracting the field induced losses [82].

1.8.4. Exchange bias effect in Heusler alloys

Along with the MCE, these multifunctional Heusler alloys possess exchange bias (EB) effect in the martensitic phase due to the existence of inhomogeneous magnetic phases. EB effect was discovered in 1956 by Meiklejohn and Bean in Co/CoO core-shell nanoparticles [120]. The EB originates due to the unidirectional

anisotropy that develops because of the exchange interactions between the ferromagnetic and antiferromagnetic layers at their interfaces. The ferromagnetic spins near the interface get pinned along the direction of the interfacial antiferromagnetic moments. Therefore, some exchange field exists in the absence of external magnetic field. This causes a shift in the magnetic hysteresis loops. Extra amount of energy is required to unpin the ferromagnetic spins, which gives us the measure of exchange bias field (H_{EB}). Fig. 1.10 gives a schematic representation of EB behavior. H_{EB} can be measured as,

$$H_{EB} = \frac{|H_{C1} + H_{C2}|}{2} \quad (1.22)$$

where H_{C1} and H_{C2} are the coercivities during respectively field up and field down modes as illustrated in Fig. 1.10.

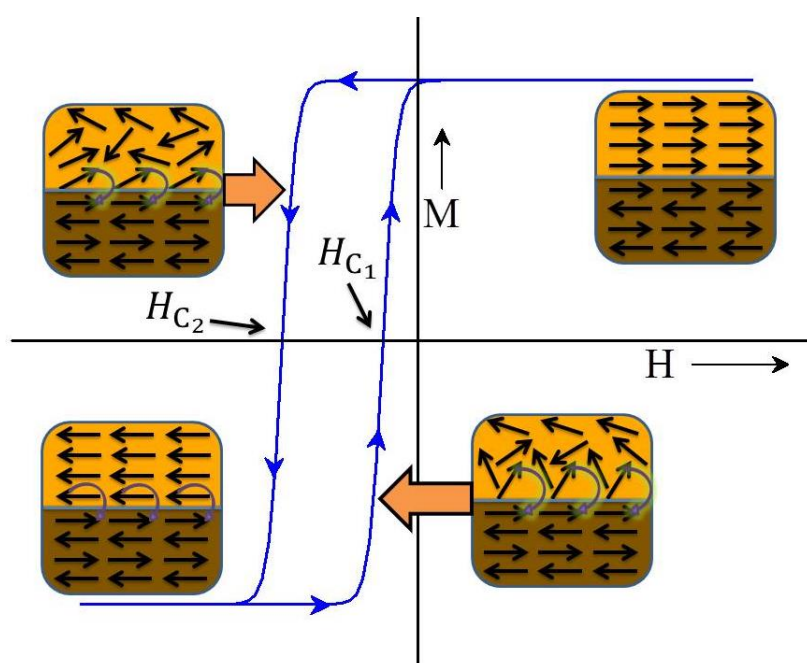


Fig. 1.10: A schematic diagram of magnetic hysteresis loop showing the exchange bias effect.

EB is generally observed in multilayered thin films and core-shells that have ordered interfaces. For Ni-Mn based Heusler alloys, the interfaces are formed between the different sites that contain ferro/antiferro correlations in the martensite phase [66, 121, 122]. EB has several technological applications in magnetic recording devices, magnetoresistive random access memories (MRAM), etc.

1.8.5. Magnetoresistance in Heusler alloys

Magnetoresistance (MR) is defined as the change in electrical resistivity in presence of a magnetic field [123]. It was discovered by William Thomson in 1856. The geometrical MR can be observed even if the material is not magnetic. The anisotropic magnetoresistance (AMR) arises from the simultaneous action of magnetization and spin-orbit interaction which alters the *s-d* scattering of electrons under the applied magnetic field. After the discovery of giant magnetoresistance (GMR) and colossal magnetoresistance (CMR) at the end of 20th century, the applications of MR in modern technologies like sensors, storage devise, MRAMs, etc. have drawn immense attention. MR can be estimated using the formula,

$$\text{MR} = \frac{(\rho_H - \rho_0)}{\rho_0} \times 100 \% \quad (1.23)$$

where ρ_0 and ρ_H are respectively the electrical resistivities under zero and non-zero magnetic field.

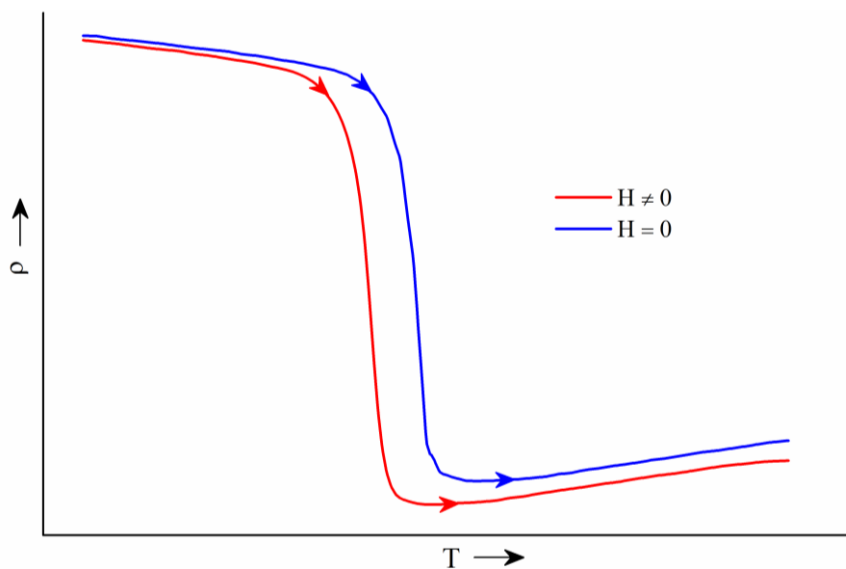


Fig. 1.11: A representative temperature dependent resistivity plot for Heusler alloys.

Fig. 1.11 illustrates the temperature dependence of electrical resistivity for a Ni-Mn-Sn off-stoichiometric Heusler alloy under zero and non-zero field. The transformation of the structure from martensite to the austenite phase accompanies a significant decrease in electrical resistivity [124, 125]. The FOMST shows large field induced shift under the application of higher magnetic field due the FIMST. The

cumulative result comes out as a very large negative MR across the martensitic transition. In the temperatures far from the FOMST, only a few % of MR can be achieved, which mainly originates due the reduction in $s-d$ scattering in presence of magnetic field.

1.9. Motivation and objectives of thesis

In the subsection 1.5, we have already discussed about the importance of magnetic refrigeration. It is desirable to find out effective materials that can exhibit large MCE and make the environment friendly energy saving cooling possible. In the subsection 1.7, we have reviewed the magnetocaloric materials and found that Ni-Mn based Heusler alloys can be a potential candidate for room temperature magnetic refrigeration. They are commercially cheap in cost and have a very good tuneability of working temperature. Ni-Mn based Heusler alloys have drawn immense attention during the last decade due to their valuable multifunctional properties like MSME, MC, MCE, MR, EB effect, etc. [51-66, 117, 121, 122, 124, 125].

Most of these properties in Heusler alloys are associated with their martensitic transition. A large number of such alloys have been studied by many groups in this context [51-66]. Ni-Mn-Ga Heusler alloys have shown the existence of FOMST in stoichiometric composition [52]. But, for other materials like Ni-Mn-In, Ni-Mn-Sb and Ni-Mn-Sn, off-stoichiometry is necessary [52, 56]. Ni-Mn-Ga and Ni-Mn-In alloys have shown large MCE and thus they have been studied extensively. Only, Ni-Mn-Ga exhibit conventional MCE across their FOMST. For other above mentioned Heusler alloys, IMCE can be observed across their martensitic phase transformation. The reports on these alloys predict that the MCE of them can be enhanced to the giant values by various treatments. We have observed that Ni-Mn-Sn off-stoichiometric alloys show very interesting structural and magnetic properties and their MCE values can be enhanced by rigorously studying them.

$\text{Ni}_{50}\text{Mn}_{50-x}\text{Sn}_x$ alloys were studied by Krenke *et al* [126] and a $\Delta S_M \sim 20$ J/kg K were reported due to a 50 kOe magnetic field change. 32 J/kg K of ΔS_M was obtained in $\text{Ni}_{47}\text{Mn}_{40}\text{Sn}_{13}$ alloy under the same field changes [127]. Co and Fe substituted Ni-

Mn-Sn alloys have shown $\Delta S_M \sim 33$ J/kg K due to 50 kOe of ΔH [128, 129]. These indicate that the addition of magnetic elements like Co and Fe can be very helpful. The martensitic transition in Mn_2NiSn alloys was predicted theoretically by Paul *et al* [130] and Ma *et al* [114] verified it experimentally. These Mn-rich systems can show larger MCE as they have maximum number of Mn-Mn inter-site pairs which controls the leading magnetic correlations in similar alloys. Considering all the above facts, we have chosen Ni-Mn-Sn off-stoichiometric Heusler alloys to study the MCE and find out the possible ways for its further improvements. Moreover, these materials exhibit EB effect and large MR also [60-62, 66, 121-125]. Therefore, detail study on their magnetic and magneto-transport properties has been carried out.

The main objectives of the thesis are summarized below:

- We have doped Co by replacing Ni in Ni-rich Ni_2MnSn off-stoichiometric alloys and successfully enhanced the MCE across their martensitic transition under a small change in magnetic field (~ 15 kOe). The undoped sample has shown negligible hysteresis losses across the martensitic transition and thus enhanced refrigerant capacity has been achieved.
- Another series of Co doped similar alloys show a monotonic increase in entropy changes, but the net refrigerant capacity starts to fall as the doping concentration exceeds 1 at%. The reasons behind such results are small transition width and large field induced hysteresis loss. One of the samples has shown large magnetoresistance with broad working temperature range.
- In order to improve the MCE potentials, we have prepared a Ni-rich Ni_2MnSn alloy and annealed it for different times. Although, the exchange bias and entropy change are found to increase as the structural ordering increases with increasing the duration of annealing, the net refrigerant capacity is the maximum for the material which is partially disordered.
- Next, we have prepared some Mn-rich Mn_2NiSn off-stoichiometric Heusler alloys and obtained noticeable increase in magnetic correlations, magneto-structural coupling, decrease in thermal hysteresis and a significantly large MCE with almost 50% higher net refrigerant capacity as compared to the

similar Ni-rich alloys. A favorable amount of magnetoresistance is also available.

- For further improvement in magnetocaloric properties, we have doped Fe independently in the place of Ni and Mn in Mn-rich Mn_2NiSn off-stoichiometric Heusler alloys. Our results conclude that smaller concentration of doping (1-2 at%) can be effective to enhance the MCE with almost double net refrigerant capacity comparative to undoped similar materials.
- Despite of all the above mentioned improvements, these materials still suffer from field induced hysteresis losses. For further investigation, we have carried out a detail MCE study on a Mn-rich Mn-Ni-Sn-Si off-stoichiometric Heusler alloy by measuring the MCE across its magneto-structural transition in both the heating and cooling mode. Finally, we have concluded that the cooling protocol can provide a better and more accurate MCE values.

1.10. Organization of the thesis

The entire thesis has been divided into seven chapters. A brief overview of all the chapters is given below:

Chapter 1 gives an introduction about the magnetocaloric effect, magnetic refrigeration and their importance in human lives. A literature review on the magnetocaloric materials has been described. The basic properties of Heusler alloys and their effectiveness for magnetic refrigeration have been also discussed. The outline of the thesis has been summarized along with the motivation of work.

Chapter 2 describes the sample preparation and characterization techniques. The basic principles of the instruments that we have used, has been discussed. The development of our home-made ac susceptibility setup has been also described.

Chapter 3 is based on the study of magnetocaloric and magneto-transport properties in Co-doped Ni-rich (Ni ~ 50 at%) Ni_2MnSn off-stoichiometric Heusler alloys. We

observed a monotonic increase in magnetic entropy changes, but the net refrigerant capacity starts to fall as the doping concentration exceeds 1 at%. One of the samples has shown large magnetoresistance within a large temperature range.

Chapter 4 discusses about the magnetocaloric parameters of a Ni-rich Ni_2MnSn alloy as a function of atomic ordering. The exchange bias and magnetic entropy changes are improved with the ordering, but a partially disordered sample has shown the maximum refrigerant capacity among others.

Chapter 5 describes the structural, magnetic and transport properties of Mn-rich (Mn \sim 50 at%) Mn_2NiSn off-stoichiometric Heusler alloys. Firstly, We have observed large magnetocaloric effect in these materials with almost 50% higher refrigerant capacity as compared to the Ni-rich similar alloys. Next, we doped Fe independently in the place of Ni and Mn in this Mn-rich system and obtained a significant increment in magnetocaloric parameters for the materials with smaller doping concentrations (1-2 at%).

Chapter 6 represents a detail study of magnetocaloric properties in a Si-doped Mn-rich Mn-Ni-Sn-Si alloy under different measurement protocols. For similar materials, the field induced losses are one of the major limitations. We have been able to minimize the losses to its negligible values by discontinuously cooling the sample and taking the isothermal field dependent magnetization data. The use of such cooling protocol has provided more consistent and better results.

Chapter 7 gives an overall conclusion of the thesis, compares our materials with other reported magnetocaloric candidates and discusses about the scope for future work in the related fields.

Bibliography

- [1] D. C. Jiles, "Introduction to Magnetism and Magnetic Materials", *Chapman & Hall/CRC, Taylor & Francis Group*, New York, USA (1998).
- [2] J. M. D. Coey, "Magnetism and Magnetic Materials", *Cambridge University Press*, New York, USA (2009).
- [3] N. A. Spaldin, "Magnetic Materials: Fundamentals and Applications", *Cambridge University Press*, New York, USA (2003).
- [4] B. D. Cullity and C. D. Graham, "Introduction to Magnetic materials", *John Wiley & Sons, Inc.*, New Jersey, USA (1972).
- [5] R. Gerber, C. D. Wright and G. Asti, "Applied Magnetism", Series E: Applied Sciences - Vol. 253, *Kluwer Academic publishers*, Netherlands (1994).
- [6] S. X. Wang and A. M. Taratorin, "Magnetic Information Storage Technology", *Academic Press, Harcourt Brace & Company*, California, USA (1999).
- [7] C. Mee, E. D. Daniel, "Magnetic Recording Technology", *McGraw Hill Professional*, USA (1996).
- [8] D. D. Tang and Y. J. Lee, "Magnetic Memory: Fundamentals and Technology", *Cambridge University Press*, New York, USA (2010).
- [9] E. Burstein, M. L. Cohen, D. L. Mills and P. J. Stiles (Series Editors), "Contemporary Concepts of Condensed Matter Science", D. L. Mills and J. A. C. Bland (Volume Editors), "Nanomagnetism: Ultrathin Films, Multilayers and Nanostructures", *Elsevier B. V.*, Netherlands (2006).
- [10] F. Nasirpour and A. Nogaret (Editors), "Nanomagnetism and Spintronics: Fabrication, Materials, Characterization and Applications", *World Scientific Publishing Co. Pte. Ltd.*, Singapore (2011).
- [11] O. Gutfleisch, M. A. Willard, E. Brück, C. H. Chen, S. G. Sankar and J. P. Liu, *Adv. Mater.* 23, 821-842 (2011).
- [12] J. Karlsson and O. Soderstrom, "Review of Magnetic Materials Along With a Study of the Magnetic Stability and Solidity of Y40", Student thesis, Uppsala University (2012).
- [13] L. P. Lombard, J. Ortiz and C. Pout, *Energy and Buildings* 40, 394 (2008).

-
- [14] W. A. Badway, *J. Adv. Res.* 6, 123 (2015).
- [15] A. Luque, A. Marti and C. Stanley, *Nat. Photonics* 6, 146 (2012).
- [16] A. Terakawa, *Sol. Energ. Mat. Sol. C.* 119, 204 (2013).
- [17] F. D. González, A. Sumpera, O. G. Bellmunta and R. V. Robles, *Renew. Sust. Energ. Rev.* 16, 2154 (2012).
- [18] M. Lei, L. Shiyang, J. Chuanwen, L. Hongling and Z. Yan, *Renew. Sust. Energ. Rev.* 13, 915 (2009).
- [19] J. P. Deane, B. P. Ó Gallachóir and E. J. McKeogh, *Renew. Sust. Energ. Rev.* 14, 1293 (2010).
- [20] B. K. Sovacool, S. Dhakal, O. Gippner and M. J. Bambawale, *Energy* 36, 3468 (2011).
- [21] J. W. Lund, D. H. Freeston and T. L. Boyd, *Geothermics* 40, 159 (2011).
- [22] S. J. Self, B. V. Reddy and M. A. Rosen, *Appl. Energ.* 101, 341 (2013).
- [23] R. C. Arora, "Refrigeration and Air Conditioning", *PHI Private Limited*, New Delhi, India (2010).
- [24] A. Cavallini, *Int. J. Refrig.* 19, 485 (1996).
- [25] J. A. Barclay, *Adv. Cryog. Eng.* 33, 719 (1988).
- [26] V. K. Pecharsky and K. A. Gschneidner Jr., *J. Magn. Magn. Mater.* 200, 44 (1999).
- [27] V. Franco, J. S. Blázquez, B. Ingale and A. Conde, *Annu. Rev. Mater. Res.* 42, 305 (2012).
- [28] S. A. Tassou, J. S. Lewis, Y. T. Ge, A. Hadawey and I. Chaer, *Appl. Therm. Eng.* 30, 263, (2010).
- [29] B. F. Yu, Q. Gao, B. Zhang, X. Z. Meng and Z. Chen, *Int. J. Refrig.* 26, 622 (2003).
- [30] K. A. Gschneidner Jr., V. K. Pecharsky and A. O. Tsokol, *Rep. Prog. Phys.* 68, 1479 (2005).
- [31] E. Warburg, *Ann. Phys.* 13, 141 (1881).
- [32] P. Debye, *Ann. Phys.* 81, 1154 (1926).
- [33] W. F. Giauque, *J. Am. Chem. Soc.* 49, 1864 (1927).
-

-
- [34] W. F. Giaque and D. P. MacDougall, *Phys. Rev.* 43, 768 (1933).
- [35] A. H. Cooke, H. Meyer and W. P. Wolf, *RSC Proceedings A* 233, 1195 (1956).
- [36] R. Sessoli, *Angewandte Chemie Int. Edition* 51, 43 (2012).
- [37] R. Li, T. Numazawa, T. Hashimoto, A. Tomoyiko, T. Goto, S. Todo, *Adv. Cryog. Eng.* 32, 287 (1986).
- [38] C. Zimm, A. Jastrab, A. Sternberg, V. K. Pecharsky, K. A. Gschneidner Jr., M. Osborne and I. Anderson, *Adv. Cryog. Eng.* 43, 1759 (1998).
- [39] V. K. Pecharsky and K. A. Gschneidner Jr., *Appl. Phys. Lett.* 70, 3299 (1997).
- [40] A. O. Pecharsky, K. A. Gschneidner Jr., V. K. Pecharsky and C. E. Schindler, *J. Alloys Compds.* 338, 126 (2002)
- [41] V. K. Pecharsky, A. O. Pecharsky and K. A. Gschneidner Jr., *J. Alloys Compd.* 344, 362 (2002).
- [42] N. P. Thuy, L. T. Tai, N. T. Hien, N. V. Nong, T. Q. Vinh, P. D. Thang, T. P. Nguyen and P. Molini'e, *Proc. 8th Asia-Pacific Physics Conf. (Taipei, Taiwan) (Singapore: World Scientific)*, p-354 (2001).
- [43] N. P. Thuy, *Solid State Sci. Technol. (Malaysia)* 10, 1 (2002).
- [44] Y. Zhuo, R. Chahine and T. K. Bose, *IEEE Trans. Magn.* 39, 3358 (2003).
- [45] A. Gigu`ere, M. Foldeaki, B. R. Gopal, R. Chahine, T. K. Bose, A. Frydman and J. A. Barclay, *Phys. Rev. Lett.* 83, 2262 (1999).
- [46] K. A. Gschneidner Jr., V. K. Pecharsky, E. Bruck, H. G. M. Duijn and E. M. Levin, *Phys. Rev. Lett.* 85, 4190 (2000).
- [47] E. Brück, O. Tegus, D. T. C. Thanh, N. T. Trung and K. H. J. Buschow, *Int. J. Refrig.* 31, 763 (2008).
- [48] M. H. Phan and S. C. Yu, *J. Magn. Magn. Mater.* 308, 325 (2007).
- [49] K. A. Gschneidner Jr. and V. K. Pecharsky, *Annu. Rev. Mater. Sci.* 30, 387 (2000).
- [50] K. A. Gschneidner Jr. and V. K. Pecharsky, *Int. J. Refrig.* 31, 945 (2008).
- [51] J. Marcos, L. Mañosa, A. Planes, F. Casanova, X. Batlle and A. Labarta, *Phys. Rev. B* 68, 094401 (2003).
- [52] A. Planes, L. Manosa and M. Acet, *J. Phys.: Condens. Matter* 21, 233201 (2009).
-

-
- [53] R. Kainuma¹, Y. Imano, W. Ito, Y. Sutou, H. Morito, S. Okamoto, O. Kitakami, K. Oikawa, A. Fujita, T. Kanomata and K. Ishida, *Nature* 439, 957 (2006).
- [54] V. Basso, C. P. Sasso, K. P. Skokov and O. Gutfleisch, *Phys. Rev. B* 85, 014430 (2012).
- [55] P. J. Shamberger and F. S. Ohuchi, *Phys. Rev. B* 79, 144407 (2009).
- [56] V. D. Buchelnikov and V. V. Sokolovskiy, *Phys. Met. Metallog.* 112, 633 (2011).
- [57] O. Söderberg, Y. Ge, A. Sozinov, S. P. Hannula and V. K. Lindroos, *Smart Mater. Str.* 14, 5 (2005).
- [58] K. Ullakko, J. K. Huang, C. Kantner, R. C. O'Handley, and V. V. Kokorin, *Appl. Phys. Lett.* 69, 1966 (1996).
- [59] K. Ullakko, J. K. Huang, V. V. Kokorin and R. C. O'Handley, *Scripta Mater.* 36, 1133 (1997).
- [60] J. Dubowik, K. Załski, I. Gościańska, H. Głowiński, and A. Ehresmann, *Appl. Phys. Lett.* 100, 162403 (2012).
- [61] S. Y. Yu, L. Ma, G. D. Liu, Z. H. Liu, J. L. Chen, Z. X. Cao, G. H. Wu, B. Zhang and X. X. Zhang, *Appl. Phys. Lett.* 90, 242501 (2007).
- [62] L. Chen, F.X. Hu, J. Wang, L.F. Bao, J.R. Sun, B.G. Shen, J.H. Yin and L.Q. Pan, *Appl. Phys. Lett.* 101, 012401 (2012).
- [63] B. Zhang and X. X. Zhang, S. Y. Yu, J. L. Chen, Z. X. Cao and G. H. Wu, *Appl. Phys. Lett.* 91, 012510 (2007).
- [64] Y. K. Kuo, K. M. Sivakumar, H. C. Chen, J. H. Su and C. S. Lue, *Phys. Rev. B* 72, 054116 (2005).
- [65] M. Wang, Y. Liu, B. Xia, P. Ren and L. Wang, *J. Appl. Phys.* 111, 043912 (2012).
- [66] S. Giri, M. Patra and S. Majumdar, *J. Phys.: Condens. Matter* 23, 073201 (2011).
- [67] A. Ghosh and K. Mandal, *J. Alloys Compd.* 579, 295 (2013).
- [68] A. Ghosh and K. Mandal, *Eur. Phys. J. B* 86, 378 (2013).
- [69] A. Ghosh and K. Mandal, *Appl. Phys. Lett.* 104, 031905 (2014).
- [70] A. Ghosh and K. Mandal, *J. Phys. D: Appl. Phys.* 46, 435001 (2013).
- [71] A. Ghosh and K. Mandal, *IEEE Trans. Magn.* 50, no. 11, 1-4 (2014).
- [72] A. Ghosh and K. Mandal, *Physics Procedia*, 54, 10-15 (2014).
-

-
- [73] A. Ghosh and K. Mandal, *J. Appl. Phys.* 117, 093909 (2015).
- [74] A. Ghosh and K. Mandal, *AIP Conference Proceedings* 1665, 030015 (2015).
- [75] N. A. de Oliveira and P. J. von Ranke, *Phys. Rep.* 489, 89 (2010).
- [76] Y. Shao, J. Zhang, J. K. L. Lai and C. H. Shek, *J. Appl. Phys.* 80, 76 (1996).
- [77] B. F. Yu, Q. Gao, B. Zhang, X. Z. Meng and Z. Chen, *Int. J. Refrig.* 26, 622 (2003).
- [78] A. Kitanovoski, U. Plaznik, J. Tusek, A. Poredos, *Int. J. Refrig.* 37, 28 (2014).
- [79] V. K. Pecharsky, K. A. Gschneidner, Jr., *Adv. Cryog. Eng. Mater.* 42, 423 (1997).
- [80] V. K. Pecharsky, K. A. Gschneidner, Jr., A. O. Pecharsky, and A. M. Tishin, *Phys. Rev. B* 64, 144406 (2001).
- [81] R. C. Flores, V. Franco, A. Conde, K. E. Knipling and M. A. Willard, *Appl. Phys. Lett.* 98, 102505 (2011).
- [82] T. L. Phan, P. Zhang, N. H. Dan, N. H. Yen, P. T. Thanh, T. D. Thanh, M. H. Phan and S. C. Yu, *Appl. Phys. Lett.* 101, 212403 (2012).
- [83] V. Provenzano, A. J. Shapiro and R. D. Shull, *Nature* 429, 853 (2004).
- [84] G. V. Brown, *J. Appl. Phys.* 47, 3673 (1976).
- [85] G. Green, W. Patton and J. Stevens, *Adv. Cryog. Eng.* 33, 777 (1988).
- [86] S. J. Lee, J. M. Kenkel, V. K. Pecharsky and D. C. Jiles, *J. Appl. Phys.* 91, 8894 (2002).
- [87] B. Yu, M. Liu, P. W. Egolf and A. Kitanovski, *Int. J. Refrig.* 33, 1029 (2010).
- [88] V. K. Pecharsky, K. A. Gschneidner Jr., *Phys. Rev. Lett.* 78, 4494 (1997).
- [89] X. Zhang, L. Yang, S. Zhou, L. Qi and Z. Liu, *Mater. Trans.* 42 2622 (2001).
- [90] A. S. Chernyshov, A. M. Tishin, K. A. Gschneidner Jr., A. O. Pecharsky, V. K. Pecharsky and T. A. Lograsso, *Adv. Cryog. Eng.* 48, 19 (2002).
- [91] W. Dai, B. G. Shen, D. X. Li and Z. X. Gao, *J. Alloys Compd.* 311, 22 (2000).
- [92] D. Wang, S. Huang, Z. Han, Z. Su, Y. Wang and Y. Du, *Solid State Commun.* 131, 97 (2004).
- [93] Y. L. Wu, A. O. Pecharsky, V. K. Pecharsky and K. A. Gschneidner Jr., *Adv. Cryog. Eng.* 48, 3 (2002).
- [94] H. Wada, K. Taniguchi and Y. Tanabe, *Mater. Trans.* 43, 73 (2002).
-

-
- [95] H. Wada, T. Morikawa, K. Taniguchi, T. Shibata, Y. Yamada and Y. Akishige, *Physica B* 328, 114 (2003).
- [96] T. Morikawa and H. Wada, *J. Magn. Magn. Mater.* 272, 583 (2004).
- [97] O. Tegus, E. Bruck, K. H. J. Buschow and F. R. de Boer, *Nature* 415, 150 (2002).
- [98] E. Bruck, O. Tegus, X. W. Li, F. R. de Boer and K. H. J. Buschow, *Physica B* 327, 431 (2003).
- [99] T. J. Zhou, Z. Yu, W. Zhong, X. N. Xu, H. H. Zhang and Y. W. Du, *J. Appl. Phys.* 85, 7975 (1999).
- [100] H. Zhu, H. Song and Y. H. Zhang, *Appl. Phys. Lett.* 81, 3416 (2002).
- [101] W. Zhong, W. Chen, H. Y. Jiang, X. S. Liu, C. T. Au and Y. W. Du, *Eur. Phys. J. B* 30, 331 (2002).
- [102] A. M. Gomes, F. Garcia, A. P. Guimaraes, M. S. Reis, V. S. Amaral and P. B. Tavares, *J. Magn. Magn. Mater.* 290, 694 (2005).
- [103] M. S. Reis, A. M. Gomes, J. P. Araujo, J. S. Amaral, P. B. Tavares, I. S. Oliveira and V. S. Amaral, *J. Magn. Magn. Mater.* 290, 697 (2005).
- [104] A. Fujita, S. Fujieda, Y. Hasegawa and K. Fukamichi, *Phys. Rev. B* 67, 104416 (2003).
- [105] T. T. M. Palstra, J. A. Mydosh, G. J. Nieuwenhuys, A. M. van der Kraan and K. H. J. Buschow, *J. Magn. Magn. Mater.* 36, 290 (1983).
- [106] K. Mandal, D. Pal, O. Gutfleisch, P. Kerschl and K. H. Müller, *J. Appl. Phys.* 102, 053906 (2007).
- [107] M. Foldeaki, R. Chahine, B. R. Gopal, T. K. Bose, X. Y. Liu and J. A. Barclay, *J. Appl. Phys.* 83, 2727 (1998).
- [108] L. Si, . Ding, Y. Li, B. Yao, H. Tan, *Appl. Phys. A* 75, 535 (2002).
- [109] F. Johnson and R. D. Shull, *J. Appl. Phys.* 99, 08K909 (2006).
- [110] R. D. McMichael, J. J. Ritter and R. D. Shull, *J. Appl. Phys.* 73, 6946 (1993).
- [111] Y. Shao, J. Zhang, J. K. L. Lai and C. H. Shek, *J. Appl. Phys.* 80, 175 (1996).
- [112] Y. I. Spichkin, A. K. Zvezdin, S. P. Gubin, A. S. Mischenko and A. M. Tishin, *J. Phys. D: Appl. Phys.* 34, 1162 (2001).
- [113] G. E. Bacon and J. S. Plant, *J. Phys. F: Metal Phys.* 1, 524 (1971).
-

-
- [114] L. Ma, S. Q. Wang, Y. Z. Li, C. M. Zhen, D. L. Hou, W. H. Wang, J. L. Chen and G. H. Wu, *J. Appl. Phys.* 112, 083902 (2012).
- [115] F. E. Wang, W. J. Buehler and S. J. Pickart, *J. Appl. Phys.* 36, 3232 (1965).
- [116] S. Aksoy, M. Acet, P. P. Deen, L. Manosa and A. Planes, *Phys. Rev. B* 79, 212401 (2009).
- [117] S. Aksoy, "Magnetic interactions in martensitic Ni-Mn based Heusler systems", Ph.D. Thesis, Department of Physics, University of Duisburg-Essen (2009).
- [118] L. Caron, Z. Q. Ou, T. T. Nguyen, D. T. C. Thanh, O. Tegus and E. Bruck, *J. Magn. Magn. Mater.* 321, 3559 (2009).
- [119] G. J. Liu, J. R. Sun, J. Shen, B. Gao, H. W. Zhang, F. X. Hu and B. G. Shen, *Appl. Phys. Lett.* 90, 032507 (2007).
- [120] W. H. Meiklejohn and C. P. Bean, *Phys. Rev.* 102, 1413 (1956).
- [121] M. Khan, I. Dubenko, S. Stadler and N. Ali, *J. Appl. Phys.* 102, 113914 (2007).
- [122] B. M. Wang, Y. Liu, B. Xia, P. Ren and L. Wang, *J. Appl. Phys.* 111, 043912 (2012).
- [123] C. L. Dennis, R. P. Borges, L. D. Buda, U. Ebels, J. F. Gregg, M. Hehn, E. Jouguelet, K. Ounadjela, I. Petej, I. L. Prejbeanu and M. J. Thornton, *J. Phys.: Condens. Matter* 14, R1175 (2002).
- [124] H. C. Xuan, Y. Deng, D. H. Wang, C. L. Zhang, Z. D. Han and Y. W. Du, *J. Phys. D: Appl. Phys.* 41, 215002 (2008).
- [125] K. Koyama, H. Okada, K. Watanabe, T. Kanomata, R. Kainuma, W. Ito, K. Oikawa and K. Ishida, *Appl. Phys. Lett.* 89, 182510 (2006).
- [126] T. Krenke, E. Duman, M. Acet, E. F. Wassermann, X. Moya, L. Manosa, and A. Planes, *Nature Mater.* 4, 450 (2005).
- [127] S. E. Muthu, N. V. R. Rao, M. M. Raja, D. M. R. Kumar, D. M. Radheep and S. Arumugam, *J. Phys. D: Appl. Phys.* 43, 425002 (2010).
- [128] T. Krenke, E. Duman, M. Acet, X. Moya, L. Mañosa and A. Planes, *J. Appl. Phys.* 102, 033903 (2007).
-

- [129] R. Y. Umetsu, A. Sheikh, W. Ito, B. Ouladdiaf, K. R. A. Ziebeck, T. Kanomata and R. Kainuma, *Appl. Phys. Lett.* 98, 042507 (2011).
- [130] S. Paul and S. Ghosh, *J. Phys.: Condens. Matter* 23, 206003 (2011).
-

Chapter 2 | Experimental details

In this chapter we have discussed about sample preparation, characterization and measurement techniques. The basic principles of the instruments that we have used have been also discussed.

2.1. Preamble

In this chapter, we have discussed about the preparation of samples using arc-melting technique. The further processing of the samples to make them ready for characterization and measurements have been also described. We have taken X-ray diffraction (XRD) patterns in Rigaku MiniFlex II using Cu- K_{α} radiation to detect the crystallographic parent phase. The final compositions of the samples have been checked by energy dispersive analysis of X-rays (EDAX, Quanta FEG 250). The thermal property measurements have been carried out in differential scanning calorimeter (DSC, TA Instruments). We have measured all the magnetic and magneto-transport properties of the samples in a self-developed ac susceptibility setup, vibrating sample magnetometer (VSM, Lake Shore model-7144) and physical properties measurement system (PPMS, Cryogenic Limited). The characterization and measurement instruments that we have used are described afterwards along with their basic principles.

2.2. Sample preparation technique

All the samples were prepared by using the conventional arc-melting technique [1]. 4N (99.99%) purity argon atmosphere was maintained in the arc-melting furnace chamber during the alloying. The Aldrich make elements were used as the raw materials for sample preparation. Their form and purity are given as follows: Ni (foils, 99.98%), Co (granules, 99.995%), Fe (granules, 99.98%), Mn (chips, 99%), Sn (shots, 99.999%) and Si (pieces, 99.95%). The maximum arcing current ~ 100 A was used for sample preparation. Firstly, all the constituents were melted in low arcing current to form a single lump, Afterwards, a relatively higher current was used to melt the whole lump and let the elements to diffuse through each other's. The prepared ingots were turned and re-melted for several times (5–6 times) to ensure homogeneity. At the same time, a very few percentage of Mn was added to the samples to compensate the Mn-loss due to its evaporation during the melting.

Each of the as prepared samples were wrapped with a Ta foil and sealed in an evacuated ($\sim 10^{-3}$ bar) quartz ampoule. These ampoules were then annealed at 1173

K. Ta foil was used to absorb the oxygen present in the sealed ampoules and protect the sample from being oxidized. After annealing for the required times, the ampoules were quenched in ice water. The annealed samples were cut in small pieces using a low speed saw and polished for characterization and measurements. An image of sealed ampoule, used furnace for annealing and low speed saw for cutting the samples are shown in Fig. 2.1.

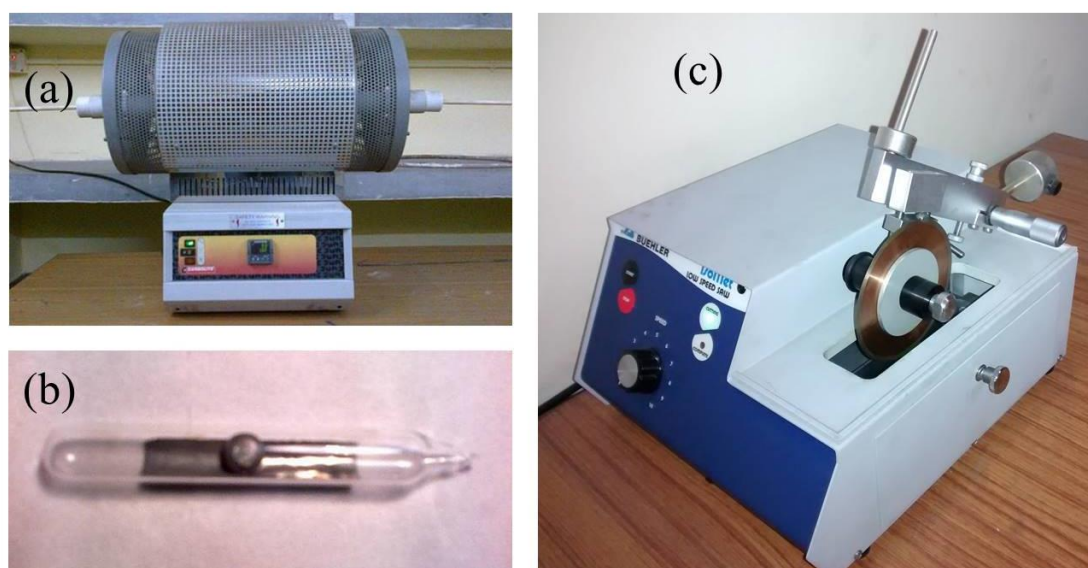


Fig. 2.1: (a) Tube furnace (Carbolite make) for annealing. (b) The sample with tantalum foil in a evacuated quartz ampoule. (c) Cutting of sample using a Buehler make IsoMet Low Speed Saw.

2.2.1. Electric Arc-Melting Furnace

An electric arc-melting furnace (EAF) is a sample preparation unit which allows us to make alloys by melting the constituent elements [2-4]. It consists of two main parts: (i) a three phase power supply and (ii) a chamber assembly along with a three phase electrode supply. In our tri-arc furnace (Cenntorr Vacuum Industries, model: 5-TA), the maximum output current of the power supply is 450 A (The whole assembly of our furnace is represented in Fig. 2.12. The furnace chamber consists of water-cooled top and bottom sections separated by a transparent pyrex tube. The top section contains three electrodes with negative polarity for striking the arcs. Each electrode consists of a copper stringer with tungsten attached at the end of it. The bottom section has a tapered opening to mount the sample on the hearth. The hearth provides a positive biasing relative to the negative electrodes. The pyrex tube keeps

2.3. Structural and compositional characterization techniques

2.3.1. X-ray Diffractometer

X-ray crystallography is used to determine the structure of crystalline materials. It is a common technique to study the crystal structure and to get detail information about the atomic spacing, inter-planer separation, crystallite size, etc. The angle and intensity of the diffracted beams give a three dimensional idea of the density of electrons within the crystal and thus the mean position of the atoms in that specified crystal can be determined.

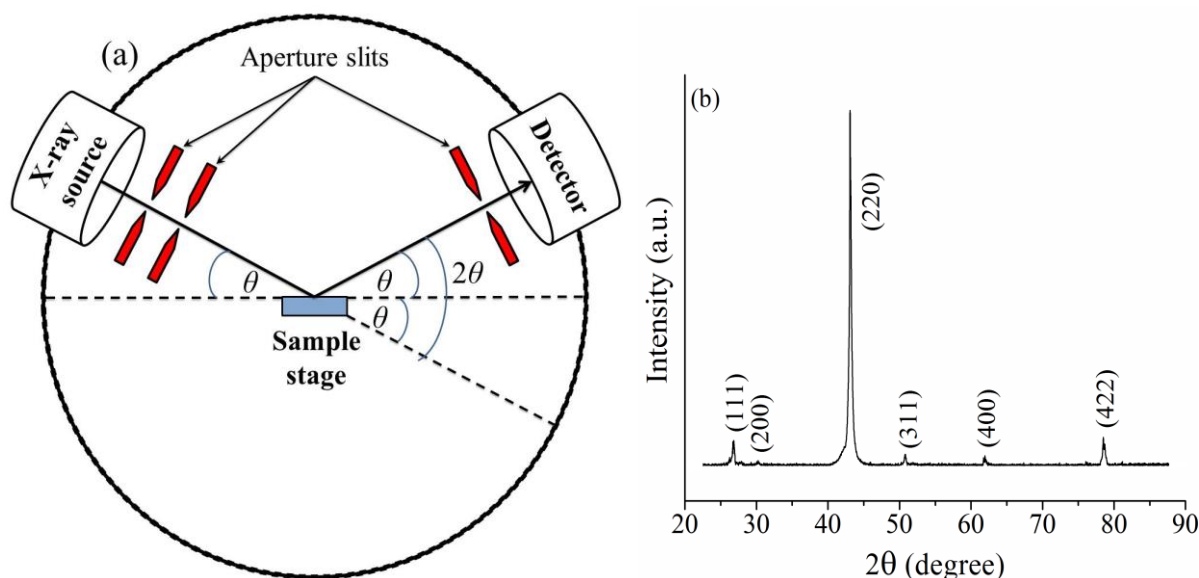


Fig. 2.3: (a) Schematic diagram of a X-ray diffractometer. (b) A representative X-ray diffraction pattern for a Ni-Mn-Sn Heusler alloy.

A schematic representation for a typical X-ray diffraction (XRD) measurement is shown in Fig. 2.3(a). A monochromatic beam of X-rays is incident on a crystalline sample. The X-rays get scattered elastically by the atomic electrons present in the planes of the material. The scattered waves interfere constructively in few specific directions that are determined by the Bragg's law which can be written as,

$$2d \sin \theta = n\lambda \quad (2.1)$$

where d is the inter-planer spacing in the crystal, θ is the angle of diffraction, n is an integer and λ is the wave length of the X-rays. The diffracted beam of X-rays in

different directions are collected by the detector and processed through software. All the possible diffraction directions of the lattice are attained by scanning the sample through a range of 2θ angles. The diffraction peaks can be identified by comparing the data with the Joint Committee on Powder Diffraction Standard (JCPDS) database. In this way, the structure, lattice parameters, disorder, etc. of the material can be revealed by performing the Reitveld analysis [5-7].

The diffraction patterns can be performed in two ways; θ - θ and θ - 2θ . In θ - θ method, the X-ray source and the detector move simultaneously. For the later one, X-ray source remains fixed and the sample's stage moves at half the angular speed of the detector to maintain the θ - 2θ relation. We have used Rigaku MiniFlex II for the initial characterization of our samples which works in the θ - 2θ mode. A representative X-ray diffraction pattern for a Ni-Mn-Sn Heusler alloy is given in Fig. 2.3(b). The target that we have used to produce monochromatic X-ray beam was Cu ($\text{Cu-K}\alpha$; $\lambda = 1.54 \text{ \AA}$).

2.3.2. Scanning Electron Microscope

In electron microscopes, a highly energetic beam of focused electrons is allowed to interact with the sample. The signals that come out from the sample, give us various important information about the material [8, 9].

Fig. 2.4(a) gives a schematic representation of a scanning electron microscope (SEM). The thermionically or field emitted electron beam from the electron gun is focused in vacuum to irradiate the sample. The beam of electrons passes through positively charged electrodes, condenser lenses, scan coils and objective lens. The objective lens does the final focusing of the beam to scan the sample's surface. These lenses are magnetic that deflect the electrons and focus them properly. SEM works on a voltage range between 2 to 50 kV. Its beam diameter varies between 5 nm to 2 μm . The highly energetic electrons interact with the material's surface and loss their energy due to the inelastic collision at the surface of the sample and also via other various mechanisms that produce variety of signals. The signals contain low energy secondary electrons (produced by inelastic scattering of incident electrons with the outer shells' electrons of the atoms of the sample), high energy backscattered

electrons, diffracted backscattered electrons, characteristic X-rays (produced by inelastic collisions of the incident electrons with the inner shells' electrons of the atoms of the sample), visible light (cathodo-luminescence) and heat. The secondary electrons can be separated from the backscattered electrons by considering their energies using the detector.

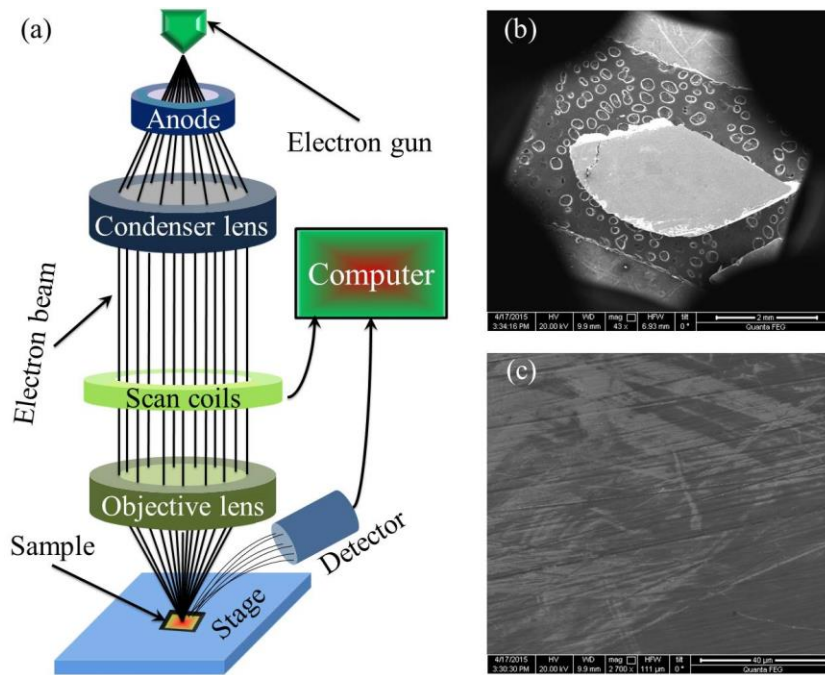


Fig. 2.4: (a) Schematic diagram of scanning electron microscope. (b) and (c) SEM micrograph of the cut surface of a Mn-Ni-Sn-Si Heusler alloy.

The displayed image in SEM is a visualization of the mapped intensities of signals as produced by the secondary electrons. A three dimensional SEM micrograph may be visualized due to the large depth of field in the narrow electron beam. The characteristic X-rays that come out from the inner shells of the atoms of the specimen are used for elemental analysis. In the case of field emission SEM (FESEM), a narrower probing of beam is possible at low as well as high energy limits. It provides improved spatial resolution and minimizes the possibility of damaging the sample during measurement. For non-conducting materials, static charges can accumulate during imaging, which is removed before the measurement by coating a very thin layer of gold on the surface of the sample. A representative FESEM image for a Mn-Ni-Sn-Si Heusler alloy's cut surface is given in Fig. 2.4(b-c).

2.3.3. Energy Dispersive Analysis of X-rays

The energy dispersive analysis of X-rays (EDAX) is a very useful tool to analyze the elemental compositions of materials [10]. A schematic representation of the fundamental process is plotted in Fig. 2.5(a). Each element's atoms have unique electronic structure with their binding energy profile in different energy levels. When the highly energetic electron interacts with the atoms of a material, it can excite an electron from the inner shells of the atoms to other higher levels or can impart the electron and take it out of the atoms. This creates a vacancy in a particular electronic level and thus an electron from relatively higher energy levels jumps to the vacant level. An electromagnetic radiation emits from the material with the energy equals to the energy difference between the two aforementioned levels.

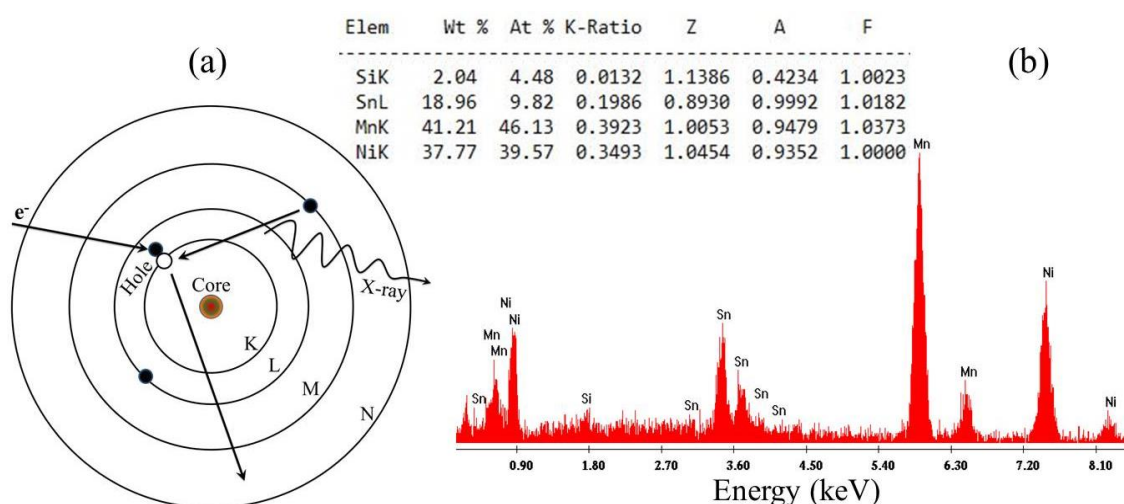


Fig. 2.5: (a) Schematic diagram for EDAX analysis. (b) EDAX spectra for a Mn-Ni-Sn-Si alloy.

The energy of the radiated electromagnetic waves falls within the range of X-rays for the innermost electronic levels of the atoms. These are characteristic X-rays and have unique energy values for a particular element. Therefore, the elements present in a sample can be identified by detecting the energies of the characteristic X-rays coming out from the same sample. For compositional analysis, the numbers of X-ray photons are counted as a function of the binding energy. A relative comparison between the different intensity peaks gives an approximate composition of the material in weight percentage (wt%) and as well as atomic percentage (at%). A representative EDAX spectra for a Mn-Ni-Sn-Si Heusler alloy is given in Fig. 2.5(b).

2.4. Thermal characterization technique

The thermal analysis allows us to get important information from a material about its thermodynamical properties like the heat capacity, phase transitions, corresponding latent heat, etc. [11, 12].

2.4.1. Differential Scanning Calorimeter

The amount of heat that is going in or coming out of a sample can be measured using a calorimeter. A differential scanning calorimeter (DSC) can measure the same relative to a reference with a linear temperature ramp. Therefore, it is necessary to know the complete thermal profile of the reference. Fig. 2.6(a) gives a schematic view of a typical DSC sample chamber. The sample is kept in a pan and an empty pan is used as the reference which is made of the same material as the sample's pan. The sample and reference are kept independently on two chromel ($\text{Ni}_{90}\text{Cr}_{10}$) wafers that are thermally connected to a relatively larger thermoelectric disc made of constantan ($\text{Cu}_{55}\text{Ni}_{45}$). Two thermocouple junctions made of alumel ($\text{Ni}_{95}\text{Mn}_2\text{Al}_2\text{Si}$) and chromel wires are kept thermally connected with the chromel discs to measure the temperature difference between the sample and reference.

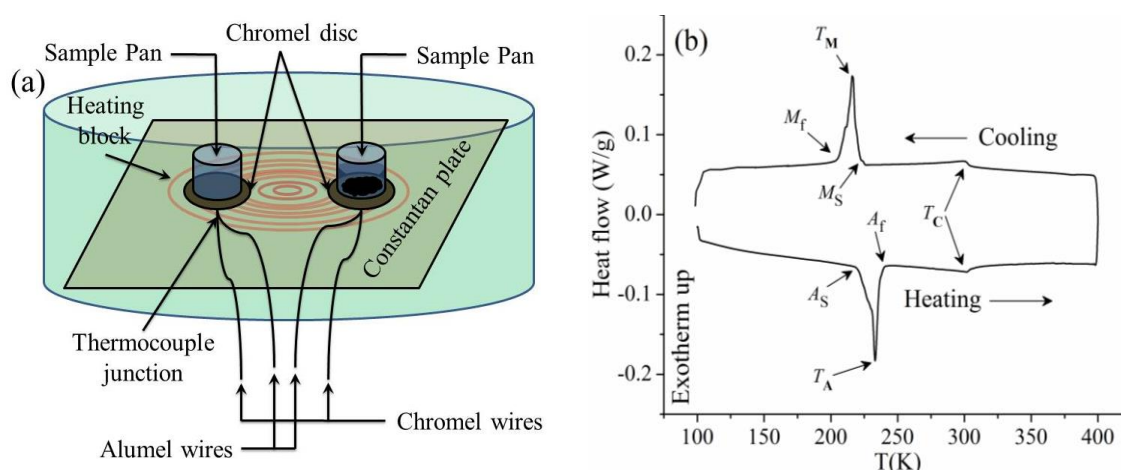


Fig. 2.6: (a) Schematic diagram of a differential scanning calorimeter. (b) Temperature dependent DSC heat flow of a Ni-Mn-Sn alloy showing the existence of structural and magnetic phase transitions.

In a DSC, the sample and the reference are allowed to have the same thermal environment. The extra amount of heat absorbed or rejected by the sample with respect to the reference pan makes a temperature difference (ΔT) between the two

thermocouple junctions which is converted to the differential heat flow (HF) assuming it is analogous to the current flow in Ohm's law [12]:

$$I = \frac{V}{R} \quad (2.2)$$

where I , V and R are respectively the current, voltage and resistance in a simple electrical circuit. Similarly we can have,

$$\text{HF} = \frac{\Delta T}{R} K_1 K_2 \quad (2.3)$$

where R represents the thermal resistance of the constantan disc. K_1 and K_2 are respectively the factory-set and user-set calibration values. Here, the ΔT is proportional to the voltage difference (ΔV) between the thermocouple junctions (between the sample and reference) which can be adjusted for the thermocouple response (S) and written as,

$$\Delta T = \frac{\Delta V}{S} \quad (2.4)$$

Using equation (2.4) in (2.3) we have the heat flow as,

$$\text{HF} = \frac{\Delta V}{RS} K_1 K_2 \quad (2.5)$$

The specific heat capacity of a material can be calculated using the heat flow data. The existence of any phase transition that accompanies changes in the thermal properties can be verified along with the latent heat of the same transition. The percentage of crystallinity and purity of a material can be estimated by comparing the experimental results with the standard data for the crystalline and pure same material. Fig. 2.6(b) depicts the DSC heat flow data showing the existence of a first order structural and a second order magnetic transition in a Ni-Mn-Sn Heusler alloy during heating (endothermic curve) and cooling (exothermic curve) cycles.

2.5. AC Magnetic characterization technique

By applying a dc magnetic field to a magnetic material, we can only study its static magnetic properties. AC magnetic measurements allow us to perform detail

dynamic magnetic analysis of a material. When the frequency of the ac field is very low, most of the results are similar to the as observed from the dc magnetometry. As the frequency of the ac field increases, the magnetization of the sample starts to lag behind the applied ac field. Therefore, the ac susceptibility, which is defined as the slope of the field dependent magnetization curve (M - H curve), contains two parameters; the magnitude of susceptibility (χ) and the phase shift (φ). In other words, the susceptibility contains an in phase (real) component, χ' , and an out of phase (imaginary) component, χ'' . The imaginary part indicates the dissipated losses in the sample [13-15].

For a conducting material, this loss may arise due the eddy currents. Spin glasses suffer from relaxation and irreversibility, that also lead to a non-zero χ'' . In the case of ferromagnetic materials, the irreversible motion of domain walls results in a hysteresis loss under dc field, which increases significantly when the driving field changes its direction very quickly (ac mode). As the ac susceptibility is proportional to the slope of the M - H curve, it is very sensitive across the phase transitions and thus can be detected easily. We have developed a temperature dependent ac susceptibility measurement setup to verify the existence of magnetic and magneto-structural transitions in Ni-Mn-Sn Heusler alloys along with their temperature dependent DSC heat flow, resistivity and dc magnetization data.

2.5.1. Basic design and theory for determining the ac susceptibility

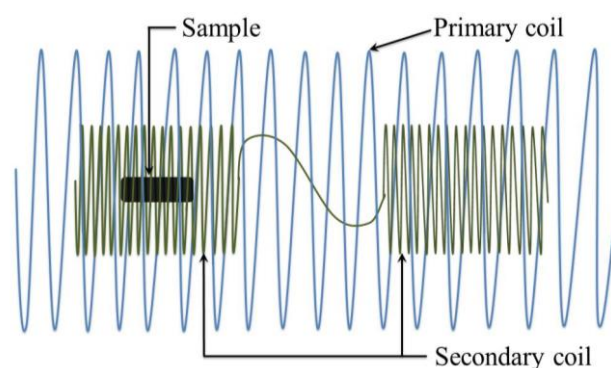


Fig. 2.7: Schematic diagram of a coil assembly for ac susceptibility measurements.

Fig. 2.7 represents a basic diagram for ac susceptibility measurement coils. In an ac susceptometer, the sample is magnetized by applying a driving ac field which is

generated by the primary coil. The flux produced by the sample due to its own magnetization is detected by the secondary coil. The secondary coil consists of two identical but oppositely wound coils that are connected in series. In the absence of sample, the flux induced by the primary coil in the secondary gets nullified. Therefore, when a sample is placed in one of the coils in secondary, the signals are generated only because of the sample's properties. The ac or dynamic susceptibility can be written as [15],

$$\chi_{ac} = \frac{dM(H,T,t)}{dH(t)} \quad (2.6)$$

where $M(H,T,t)$ and $H(t)$ are respectively the instantaneous magnetization and the applied ac magnetic field ($H(t) = H_{ac} \sin \omega t$). The time dependent magnetization can be expressed as a Fourier series of non-linear complex ac susceptibility, $\chi = \chi' + i\chi''$ as,

$$M(t) = H_{ac} \sum_n (\chi'_n \sin n\omega t + \chi''_n \cos n\omega t) \quad (2.7)$$

If $V(t)$ be the induced voltage in the secondary circuit, we have from Faraday's law:

$$V(t) = -\frac{d\Phi}{dt} \quad (2.8)$$

where $\Phi(t)$ is the total flux and can be written as,

$$\Phi(t) = (B_a(t) - B_b(t))A \quad (2.9)$$

$$= \pi r_s^2 n_s \mu_0 [(M(t) + H_a(t)) - H_b(t)] \quad (2.10)$$

where $B_a(t) = \mu_0(M(t) + H_a(t))$ and $B_b(t) = \mu_0 H_b(t)$ are respectively the magnetic flux densities linked with the detecting coil inside which the sample is loaded and the balancing coil of the secondary circuit. r_s is the radius of the secondary coils. n_s is the number of turns per unit length of the secondary coils. Now, if the two secondary coils are placed at a same distance from the center of the primary coil (along its length), then $H_a(t) = H_b(t)$, and equation (2.10) becomes:

$$\Phi(t) = \pi r_s^2 n_s \mu_0 M(t) \quad (2.11)$$

Using equations (2.7), (2.8) and (2.11), the induced voltage can be written in the following form:

$$V(t) = -\pi r_s^2 n_s \mu_0 H_{ac} \frac{d}{dt} (\sum_n (\chi'_n \sin n\omega t + \chi''_n \cos n\omega t)) \quad (2.12)$$

$$= \pi r_s^2 n_s n \omega \mu_0 H_{ac} \sum_n (\chi''_n \sin n\omega t - \chi'_n \cos n\omega t) \quad (2.13)$$

The real and imaginary components of ac susceptibility can be determined as,

$$\chi'_n = \frac{1}{\pi H_{ac}} \int_0^{2\pi} M(t) \sin n\omega t d(\omega t) \quad (2.14)$$

$$\chi''_n = \frac{1}{\pi H_{ac}} \int_0^{2\pi} M(t) \cos n\omega t d(\omega t) \quad (2.15)$$

The fundamental ac susceptibility can be obtained by putting $n = 1$. $n = 2, 3, 4 \dots$ correspond to the higher order harmonics that are associated with the non-linear terms in χ .

2.5.2. Block diagram and an overview of the setup

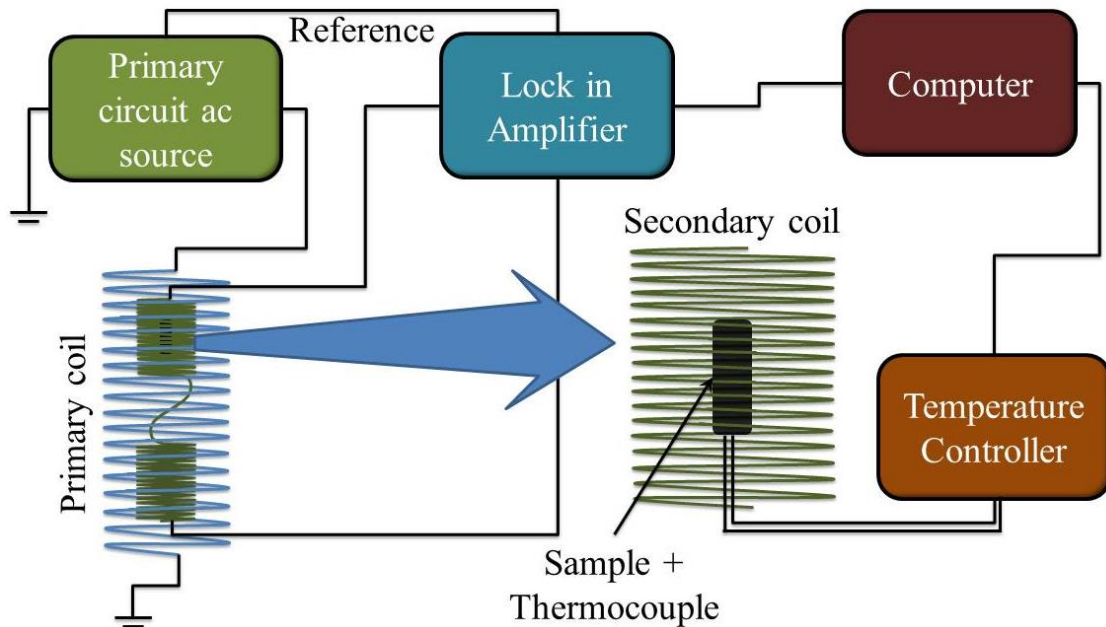


Fig. 2.8: Block diagram of an ac susceptibility setup.

Fig. 2.8 represents the schematic diagram of an ac susceptibility setup. The primary circuit consists of a solenoid (primary coil) connected with an ac source. The amplitude and the frequency of the applied current are controllable. The secondary

circuit consists of two identical but oppositely wound coils connected in series and feed to the input of the lock in amplifier. A reference signal from the ac source is given to the lock in amplifier. The sample is kept inside one of the secondary coils. The coil assembly is inserted in the sample chamber of a cryostat to perform temperature dependent study. The ac source, lock in amplifier and the temperature controller are connected with a computer to perform automated data acquisition.

When an ac current with a particular frequency is applied to the primary coil, it generates an ac magnetic field which causes an oscillation to the sample's magnetization. The time varying flux coming from the sample links with the detection coil and produce an ac signal which goes to the input of the lock in amplifier. By analyzing the signal and comparing with the reference, lock in amplifier separates the in phase and out of phase components of the complex ac susceptibility. Lock in amplifier itself has a function generator. Therefore, the ac magnetic field can also be generated by using the sine out signal of the lock in amplifier, if the required field is very small.

2.5.3. Designing and fabrication of the coils

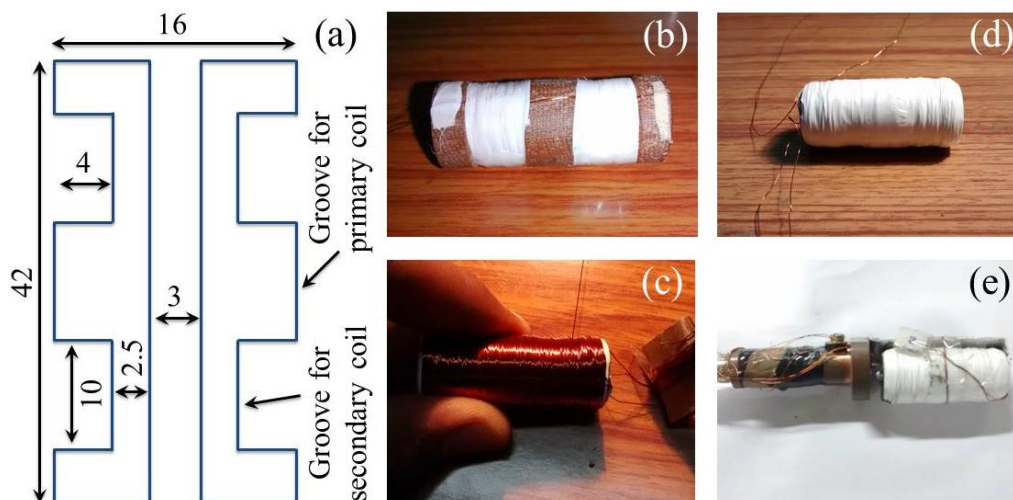


Fig. 2.9: (a) A schematic view of the coil structure (all the parameters' values are given in mm). (b-e) Cross-sectional view of the coil assembly during its fabrication.

Fig. 2.9(a) shows a schematic view of the measurement coil. We have used hylam rod to make the core. Hylam is non-magnetic and its coefficient of thermal expansion is negligible. It is electrically insulating, but a very good thermal

conductor. All these properties are very helpful for our proposed setup. Firstly, the secondary coils were wound with 850 clockwise and 850 anticlockwise turns. Figs. 2.9(b-e) show the cross-sectional view of the coils. The length and thickness of both the coils of the secondary are respectively 10 mm and 4 mm. The primary coil was wound on the secondary with 500 turns. It has a total 42 mm length and 2.5 mm thickness. In order to check the balance of the secondary coils, we connected the primary coil to the sine out and the secondary coils to the input of the lock in amplifier. 11 more turns were added to the primary on the balancing coil to achieve a proper balance. The sample can be loaded inside a cavity of 3 mm diameter.

2.5.4. The complete setup



Fig. 2.10: (a) Cryostat; inset: Lakeshore 332 temperature controller. (b) SRS830 DSP lock in amplifier and Agilent 34401A digital multimeter. (c) Sumitomo SRDK-205 cryocooler.

Fig. 2.10 represents the complete assembled setup. It consists of a cryostat, Lakeshore make model-332 temperature controller, Stanford research Systems make SRS830 DSP lock in amplifier, Agilent make 34401A multimeter and the measurement coil attached to a sample holder. The 4 K cryostat is made of a Sumitomo make SRDK-205 series cryocooler with 4 K cold head and a sample chamber attached to it. The practical limit of working temperature ranges from 6 K to 310 K. We have used the function generator of lock amplifier in as a current

source in the primary circuit. The applied current has been measured from the multimeter connected in series with the primary circuit. The real and imaginary parts of the susceptibility have been recorded from the x and y channels of the lock in amplifier.

2.5.5. To convert voltage into susceptibility

The magnetic field at the center of a solenoid can be written as,

$$H_{ac} = JaF(\alpha, \beta) \quad (2.16)$$

where $F(\alpha, \beta)$ is expressed as,

$$F(\alpha, \beta) = \beta \ln \frac{\alpha + \sqrt{\alpha^2 + \beta^2}}{\sqrt{1 + \beta^2}} \quad (2.17)$$

where α and β are respectively defined as b/a and l/a . a , b and $2l$ are respectively the inner, outer diameter and length of the solenoid as depicted in Fig. 2.11. J is the current density.

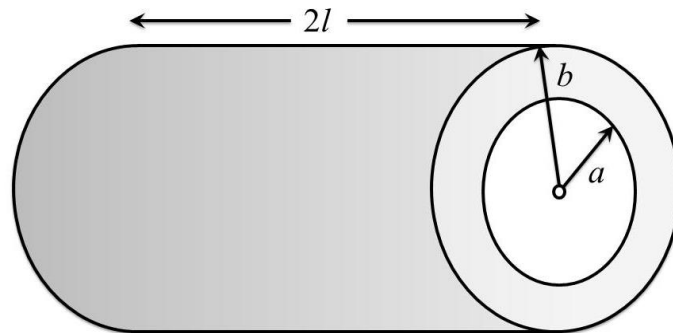


Fig. 2.11: A schematic view of the primary coil.

In this measurement setup, the primary coil has the values of $a = 8$ mm, $b = 10.5$ mm and $l = 21$ mm. Therefore, α and β becomes: $\alpha = 1.31$ and $\beta = 2.62$. By putting these values in equation (2.17) we have, $F(\alpha, \beta) = 0.29$. The applied current through the solenoid is $I = 50$ mA. J can be written as,

$$J = I/A \quad (2.18)$$

where $A = 2l(b - a) = 1.05 \times 10^{-4}$ m² is the effective cross-sectional area offered to the current flow. So, we have $J = 2.38 \times 10^5$ A/m². After putting these values in equation (2.16) the applied field has been estimated to be, $H_{ac} = 544.5$ A/m = 6.8 Oe.

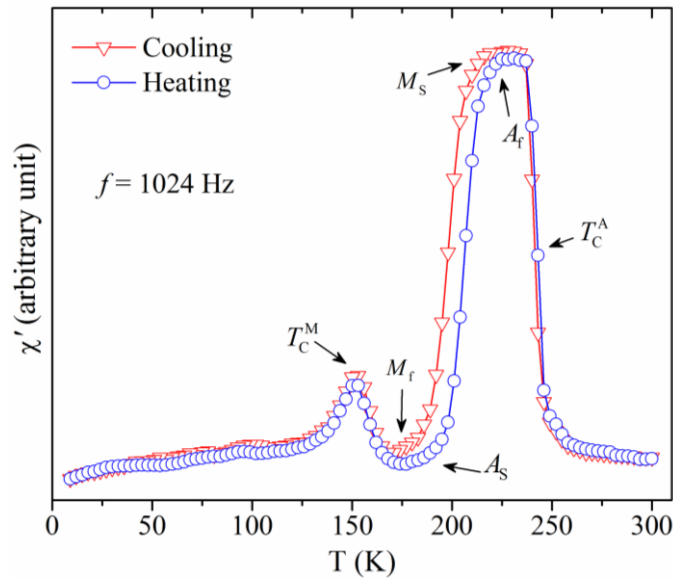


Fig. 2.12: Temperature dependent real part of the ac susceptibility for a Mn-Ni-Sn-Si Heusler alloy showing the existence of magnetic and magneto-structural phase transitions.

By considering the fundamental susceptibility ($n = 1$) and using equation (2.13), the rms value of the induced voltage (V_0) can be written as,

$$V_0 = \pi r_s^2 n_s \omega \mu_0 H_{ac} \quad (2.19)$$

Finally, the in phase and out of phase parts of the ac susceptibility can be estimated experimentally as,

$$\chi' = \frac{V(x)}{V_0} \quad (2.20)$$

and

$$\chi'' = \frac{V(y)}{V_0} \quad (2.21)$$

where $V(x)$ and $V(y)$ are respectively the real and imaginary parts of the output signal and can be recorded from the x and y channels of the lock in amplifier. Fig. 2.12 depicts a representative temperature dependent ac susceptibility plot for a Mn-Ni-Sn-Si alloy showing the existence of magnetic and magneto-structural phase transitions.

2.5.6. Limitations

For a practical temperature dependent ac susceptibility setup, the properties of the coils change with temperature. The electrical conductivity, thermal expansion, etc. affect the applied field and as well as the balancing of the secondary coils. To

resolve the problem, a compensation coil can be wound over the primary on any one of the secondary coils. By applying the required field of same frequency to the compensating coil, the balance in the secondary samples can be regained in the absence of sample for all the measurable temperatures. The process is complicated but, now a day it is available with the commercially brought ac susceptometers. Moreover, there is another way where a temperature dependent data can be recorded in absence of the sample and the same can be subtracted from the results as obtained in presence of the sample. For the materials that we have studied (Ni-Mn based Heusler alloys), the aforementioned treatment is not necessary as these materials have higher magnetic sensitivity. But, it is desirable to take care of the background errors for weak magnetic materials.

2.6. DC Magnetic and magneto-transport characterization techniques

2.6.1. Vibrating Sample Magnetometer

In a typical vibrating sample magnetometer (VSM), an electromagnet is used to apply field to the sample. Two identical but oppositely wound pickup coils are placed near the sample chamber. The sample is placed in between the two pick up coils and subjected to a sinusoidal oscillation in a particular frequency. Fig. 2.13 shows the schematic diagram of a VSM. An applied dc field magnetizes the sample and its mechanical vibration result in a change in flux density that links with the pick up coils and induce a voltage:

$$V = -NA \frac{dB}{dt} \quad (2.22)$$

where N is the number of turns in a pickup coil, A be its cross-sectional area and B is the magnetic flux density. This is the Faraday's law and we have already discussed it in equation (2.8). If M be the magnetization of the sample then the change in B can be written as,

$$\Delta B = \mu_0 M \quad (2.23)$$

Therefore, the signal takes the form:

$$V dt = -\mu_0 NAM \quad (2.24)$$

This signal is feed to the input of a lock in amplifier. The mechanical vibrator's frequency is given to the reference of the lock in amplifier to estimate the magnetization of the sample. The basic principle of the measurement for the ac and dc magnetic properties is very similar. In the case of ac measurements, the applied time varying field causes an oscillating response from the sample which induce signal to the secondary coils. But here, as the applied field is dc, the sample is required to vibrate in order to induce a signal. Although, the induced signal is proportional to the magnitude of the sample's moment, it also depends on the frequency and amplitude of the vibration. This may add error to the estimated data. In order to resolve the problem, a vibrating capacitor is used to generate reference signal which varies with the moment, vibrational frequency and its amplitude of the sample in the same way as the pick up coils' signal [16].

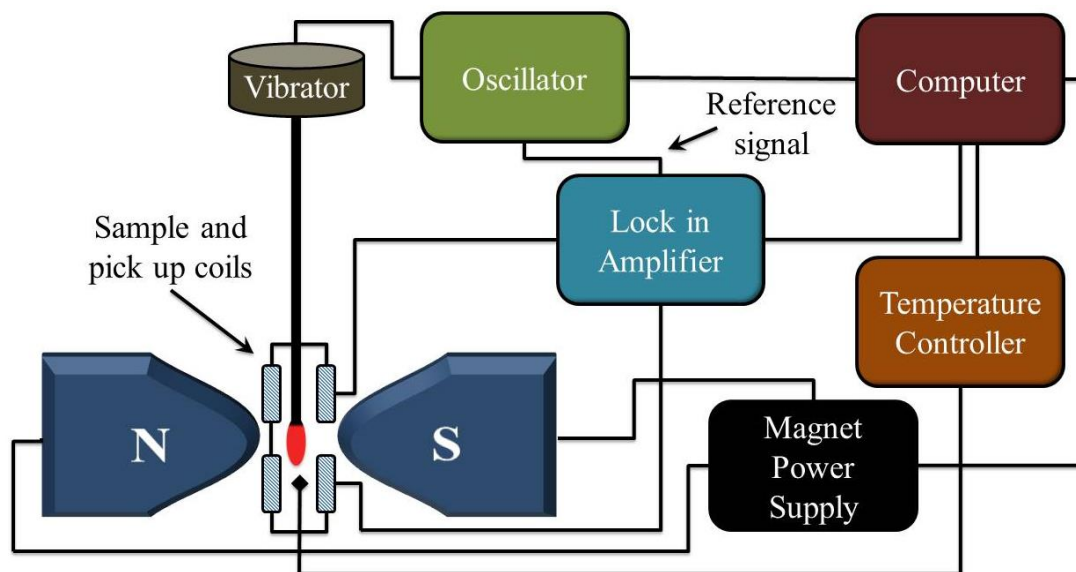


Fig. 2.13: Block diagram of a vibrating sample magnetometer.

We have used Lakeshore make model-7144 VSM for temperature and field dependent magnetic measurements. The maximum field that can be applied is 17.6 kOe with the liquid nitrogen cryostat. The low temperature measurements are limited within the temperatures between 80 K and 400 K with a temperature stability of ± 0.2 K controlled by a Lakeshore 331 temperature controller. It uses the same SRS830 DSP lock in amplifier for moment estimation which we have also used for the ac susceptibility setup. A non-magnetic sample rod is used to hold and vibrate

the sample by attaching it with the vibrator. A representative M - T curve and M - H loop for Ni-Mn-Sn alloys are depicted in Fig. 2.14.

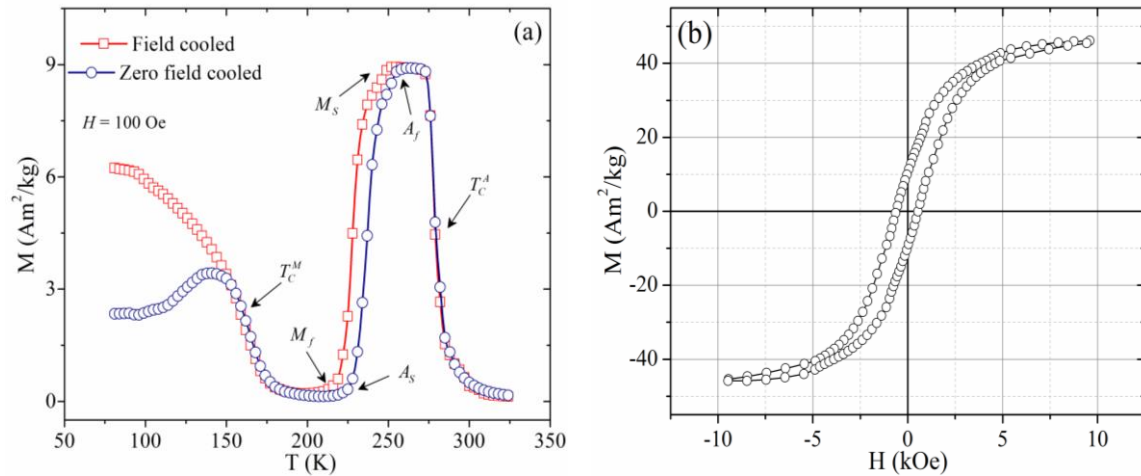


Fig. 2.14: (a) Temperature and (b) field dependent magnetization curves of a Ni-Mn-Sn Heusler alloy.

2.6.2. Physical Property Measurement System

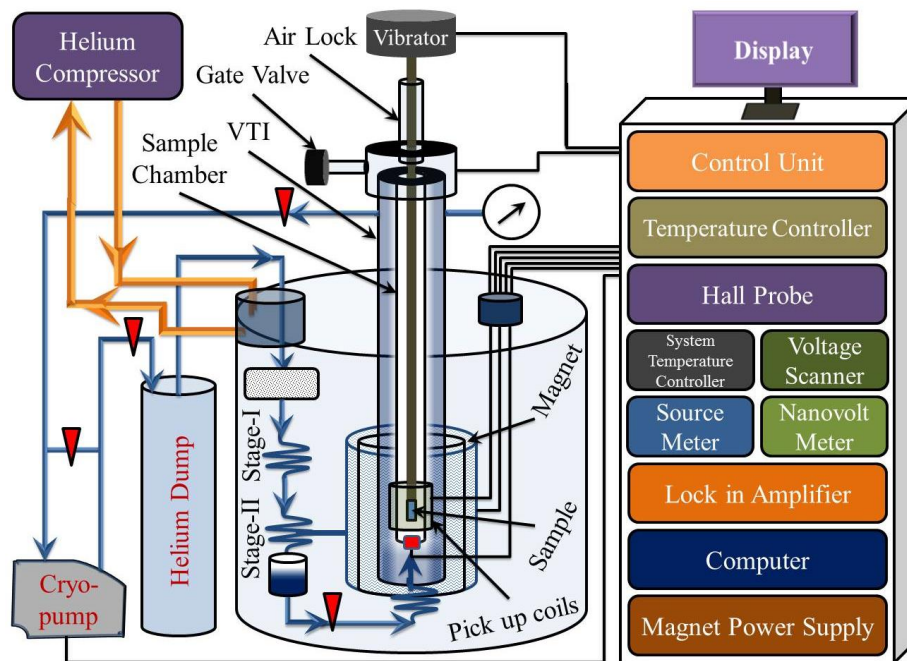


Fig. 2.15: Schematic and block representation of a physical property measurement system.

Fig. 2.15 shows the schematic diagram of a physical property measurement system (PPMS). It consists of a superconducting magnet, variable temperature insert (VTI), cryocooler, electronic rack containing all the required instruments and a workstation. It is a multipurpose measurement system where various physical properties

like magnetic, thermal, transport, etc. can be studied. We have used Cryogenic make PPMS in *UGC-DAE Consortium for Scientific Research, Kolkata, India* and *Variable Energy Cyclotron Centre (VECC), Kolkata, India* for magnetic and magneto-transport properties measurement. It has a measurement temperature limit ranging from 2 K to 320 K. It is an ever cooled system and works on two stage cooling method. The stage-I remains at 40 K. The magnet is connected to the stage-II that can attain a temperature as low as 4 K. Helium is used as exchange gas which flows in a closed path through the charcoal filter, stage-I, stage-II, helium pot, needle valve, VTI heat exchanger, cryo-pump and helium dump (as shown in Fig. 2.15) [17].

The system does the magnetic measurements based on the vibrating sample technique as discussed in the VSM part earlier. Unlike VSM, here the applied field is directed parallel to the direction of the sample's vibration and due the superconducting magnet, the maximum applicable field is very high also. Both the ac and dc magnetic measurement facilities are available in this system. The coils for ac setup are wound outside the sample chamber. It works in a very similar way as we have discussed for our self-developed ac susceptibility setup. The only difference is; the ac drive field is applied by an external source. There is a compensation coil that allows to additionally nulling the signal when required. The same secondary coils of the ac part are used as the pick coils during the dc magnetic measurements.

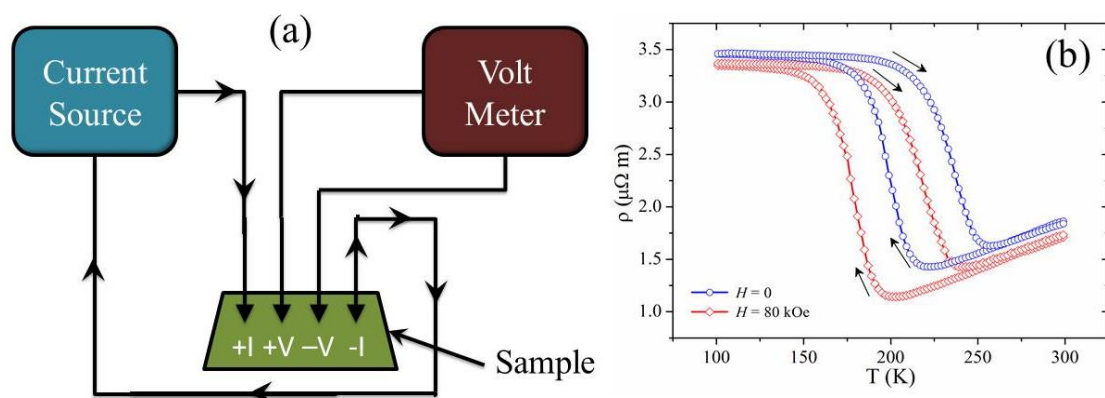


Fig. 2.16: (a) Schematic diagram of a typical four probe setup for electrical resistivity measurements. (b) Temperature dependent electrical resistivity of a Ni-Mn-Sn Heusler alloy.

It has a resistivity probe that allows us to measure the transport properties of a material. The PPMS we have used, has a Keithley make 2400 source meter,

nanovoltmeter, multi sample scanner and a hall probe. The resistivity and magnetoresistance measurements are done in standard four probe technique as depicted schematically in Fig. 2.16(a). The current is applied by the source meter through 1st and 4th probes, and the corresponding voltage drop is measured by connecting the 2nd and 3rd probes with the help of a nanovoltmeter. A representative temperature dependent resistivity data for Ni-Mn-Sn Heusler alloys is shown in Fig. 2.16(b).

Bibliography

- [1] K. Mandal, D. Pal, N. Scheerbaum, J. Lyubina and O. Gutfleisch, *J. Appl. Phys.* 105, 073509 (2009).
 - [2] B. Atcheson, F. Willi and J. Preston, "Arc-melting furnaces", *US Patent*, US2795636 A, filed September 28, 1955, and Published June 11, 1957.
 - [3] M. A. P. Alonso and, M. P. Donsion, *IEEE Trans. on* vol.19, no.1, 367-373 (2004).
 - [4] I. Ververne, K. Van Reuse and R. Belmans, *9th International Conference on* vol., no., pp.1-6, 9-11 (2007).
 - [5] B. E. Warren, "X-Ray Diffraction", *Addision Wesley Publishing Company*, USA (1969).
 - [6] H. P. Klug and L. E. Alexander, "X-Ray Diffraction Procedures", *John Wiley & Sons. Inc., Champan & Hali Limited*, USA, UK (1954).
 - [7] B. D. Cullity and S. R. Stock, "Elements of X-ray Diffraction", 3rd Edition, *Prentice Hall* (2001).
 - [8] H. Todokoro and T. Otaka, "Scanning Electron Microscope", *US Patent*, US5389787 A, filed October 19, 1993, February 14, 1995.
 - [9] M. Sato, Y. Ose, S. Fukuhara, H. Todokoro and M. Ezumi, "Scanning Electron Microscope", *US Patent*, US5608218 A, filed December 20, 1994, March 4, 1997.
 - [10] S. Koshihara, M. Sato and N. Suzuki, "Energy dispersive X-ray analyzer", *US Patent*, US5903004 A, filed August 14, 1997, May 11, 1999.
 - [11] R. E. Cavicchi, G. E. Poirier, J. S. Suehle, M. Gaitan and N. H. Tea, "Micron-scale differential scanning calorimeter on a chip", *US Patent*, US6079873 A, June 30, 1998, June 27, 2000.
 - [12] DSC 2000 manual.
 - [13] T. Parida, "AC Susceptibility Setup for 7 K Close Cycle Refrigerator", *M.Sc. Thesis*, Department of Physics, NIT, Rourkela, India (2012).
 - [14] Quantum Design manual, "Introduction to AC Susceptibility".
 - [15] M. I. Youssif, A. A. Bahgat and I. A. Ali, *Egypt. J. Sol.*, Vol. 23, No. (2), (2000).
 - [16] Lakeshore VSM 7144 manual.
 - [17] Cryogenic PPMS manual.
-

Chapter 3

Magnetocaloric and magneto-transport properties in Co-doped Ni-rich Ni-Co-Mn-Sn off-stoichiometric Heusler alloys

In this chapter we have prepared Co-doped Ni-Co-Mn-Sn alloys by varying the Ni/Co ratio and studied their magnetic, magnetocaloric and magneto-transport properties.

3.1. Preamble

Study of MCE in Ni-Mn based Ni-Mn-Z (Z = Ga, Sn, In, Sb) off-stoichiometric Heusler alloys has drawn immense attention to the research community during the last decade as they exhibit large ΔS_M around their FOMST [1-4]. It is well known that most of the functional properties like MCE, MR, MSME, etc. of these alloys are associated with their FOMST [1-8]. The variation of martensitic transition temperature in Ni-rich (Ni ~ 50 at%) Ni-Mn-Sn alloys were studied extensively by varying the ratios of Ni/Mn and Mn/Sn [3, 4, 9, 10]. For example; Ni₅₀Mn_{50-x}Sn_x alloys with $x = 13, 15$ were studied by Krenke *et al* [9] and a $\Delta S_M \sim 20$ J/kg K was reported in $x = 13$ due to a 50 kOe magnetic field change. A $\Delta S_M \sim 32$ J/kg K was obtained in Ni₄₇Mn₄₀Sn₁₃ alloy under the same field changes [10]. Ni-Mn-Sn ribbon samples also have the potential to show large $\Delta S_M \sim 4$ J/kg K due to a field change of only 20 kOe [11]. The conventional MCE was also reported for these alloys in the vicinity of their SOMT [12].

Stoichiometric Ni₅₀Mn₂₅Sn₂₅ Heusler alloys have cubic ($L2_1$) structure with four interpenetrating face centered cubic (fcc) sublattices [13]. Ni atoms take (0,0,0) and ($\frac{1}{2}, \frac{1}{2}, \frac{1}{2}$) sites and the remaining ($\frac{1}{4}, \frac{1}{4}, \frac{1}{4}$) and ($\frac{3}{4}, \frac{3}{4}, \frac{3}{4}$) sites are occupied separately by Mn and Sn atoms. In case of off-stoichiometric Ni-Mn-Sn Heusler alloys (Ni₅₀Mn_{25+x}Sn_{25-x}), the excess Mn atoms occupy the partially vacant Sn site. Recently, the substitution of Co in the Ni sites in Ni-Mn-Sn off-stoichiometric alloys is found to be an effective way to enhance the ΔS_M to the giant values. $\Delta S_M \sim 33$ J/kg K was reported in Co and Fe substituted Ni-Mn-Sn alloys due to 50 kOe of ΔH [14, 15]. Both the FOMST and SOMT of Ni-Co-Mn-Sn off-stoichiometric alloys can be tuned easily by changing the concentration of Co. Co enhances Ni-Mn exchange interaction in Ni-Mn-Z (Z = Sn, In, Sb) alloys. This exchange interaction changes various properties of Ni-Mn based alloys [16].

The magnetic correlations of these alloys also depend significantly on the inter-site Mn-Mn distances (one Mn from regular site and other one from Sn site), which is responsible for different magnetic properties in different structural phases [17]. EB behavior was also reported in many Ni-Mn-Sn off-stoichiometric alloys containing

mixture of different magnetic phases below their T_{EB} [18]. The structural transition of these alloys from the lower symmetric tetragonal martensite to a higher symmetric cubic austenite phase always accompanies some drop in electrical resistivity. Thus, MR in presence of high magnetic field was also studied by many authors [19-21]. It was reported that MR of these alloys depend on the magnetization [19]. Till date, Ni-Mn based Heusler alloys have shown up to -80 % of MR [20, 21].

It was also reported that ΔS_M in Ni-Mn-Sn alloys increases when a small percentage of Ni atoms are replaced by Mn [10]. So, a large value of ΔS_M can be achieved by taking Ni < 50 at% and then substituting Co in the Ni sites [15]. The same treatment can also help to enhance the MR in these systems. Although, some recent works reported large ΔS_M in Ni-Mn-Sn off-stoichiometric Heusler alloys, large hysteresis appears in isothermal $M-H$ curves due the FIMST. This limits the net RC of these alloys to a significant extent [1]. Therefore, it is desirable to find out such alloys those have negligible hysteresis in isothermal $M-H$ curves taken in the vicinity of the martensitic transition [22]. Moreover, large values of ΔS_M and MR in Ni-Mn-Sn alloys are usually limited in the vicinity of FOMST which restricts their working temperature range [3-6]. Hence, it might also be reasonable to find out those materials that can show large ΔS_M and MR at a distant temperature from their structural transition temperature.

In this chapter, we have prepared and studied $Ni_{48.5-x}Co_xMn_{37}Sn_{14.5}$ ($x = 0, 1$ and 2) and $Ni_{47.5-y}Co_yMn_{37.5}Sn_{15}$ ($y = 0, 1, 2$ and 3.5) alloys for their magnetocaloric and magneto-transport properties [23, 24]. Large values of ΔS_M are obtained for both the series of samples and it increases with increasing Co at%. There exists EB in all the samples of the first series. For the same series of samples, the field induced hysteresis in isothermal $M-H$ curves is absent in the undoped sample. But, the Co substituted samples show usual hysteresis nature. Hysteresis losses due to FIMST are also estimated and subtracted from total RC to obtain its net value. It is found that both the structural and magnetic transitions of the undoped sample have nearly the same potential to achieve high magnetic cooling. In the case of later series, we have observed that the net RC decreases significantly for the samples that have

higher Co concentrations. But, a large value of MR ($\sim 70\%$) has been achieved in $y = 3.5$ sample. The same sample is arrested in the austenite phase by the magnetic field during cooling cycle. It is found that this material has the capability to show large MR at a remote temperature which is far below from its FOMST.

3.2. Experimental

Ni-rich $\text{Ni}_{48.5-x}\text{Co}_x\text{Mn}_{37}\text{Sn}_{14.5}$ ($x = 0, 1$ and 2) and $\text{Ni}_{47.5-y}\text{Co}_y\text{Mn}_{37.5}\text{Sn}_{15}$ ($y = 0, 1, 2$ and 3.5) alloys were prepared by conventional arc melting technique under a 4N purity (99.99%) argon atmosphere [16]. Each of the ingots was wrapped with a Ta foil and sealed separately in highly evacuated quartz ampoules for homogenization. After a 24 h of annealing at 1173 K, the ampoules were quenched in ice water. The final compositions were confirmed by EDS. XRD patterns have been carried out using $\text{Cu-K}\alpha$ radiation to detect the crystallographic parent phase. The structural phase transitions were checked by DSC and a homemade four probe resistivity measurement setup also. Magnetic measurements were performed using a self-developed ac susceptibility setup and VSM (Lake Shore, 7144) up to 16 kOe magnetic field. Magneto-transport properties were measured in PPMS (Cryogenic Limited) up to 150 kOe field.

3.3. Results and discussions

3.3.1. MCE in $\text{Ni}_{48.5-x}\text{Co}_x\text{Mn}_{37}\text{Sn}_{14.5}$ alloys with negligible hysteresis

3.3.1.1. Structural, thermal and electrical properties

Fig. 3.1 shows the room temperature (~ 295 K) XRD patterns for $\text{Ni}_{48.5-x}\text{Co}_x\text{Mn}_{37}\text{Sn}_{14.5}$ ($x = 0, 1$ and 2) alloys. A mixed phase with martensite and austenite phase fractions is found for $x = 0$ sample which indicates that its martensitic transition temperature is close to the room temperature [10]. Cubic austenite ($L2_1$) structure is observed in $x = 1$ and 2 at room temperature. Fig. 3.2(a) represents the temperature dependent DSC heat flow during heating and cooling for all the samples across their structural phase transition. Data confirms the existence of martensitic transition in this series of samples. The endothermic peaks during

heating is for the structural transition from martensite to the austenite and the exothermic ones during cooling represent the reverse transition from austenite to the martensite. The martensitic transition shifts towards lower temperatures with increasing the Co content. The broadening of the endothermic and exothermic peaks indicates the increase in the width of martensitic transition with increasing Co.

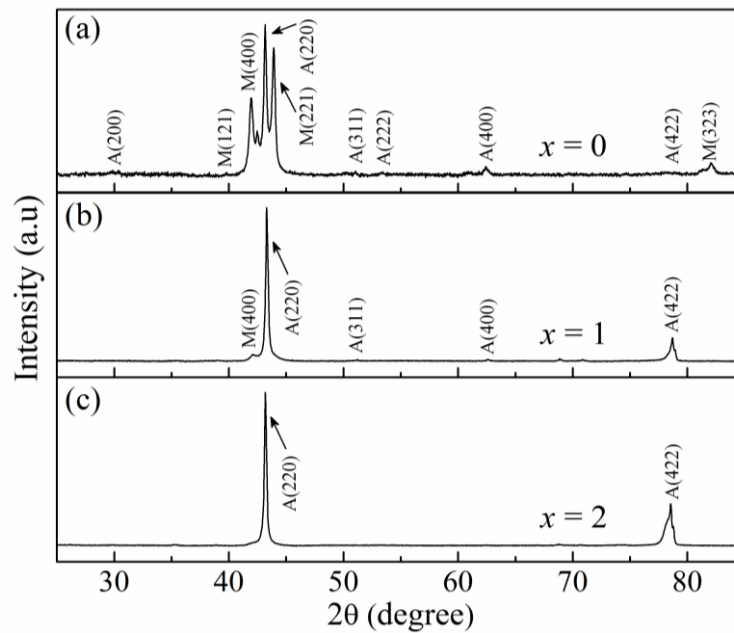


Fig. 3.1: Room temperature XRD patterns for $\text{Ni}_{48.5-x}\text{Co}_x\text{Mn}_{37}\text{Sn}_{14.5}$ alloys.

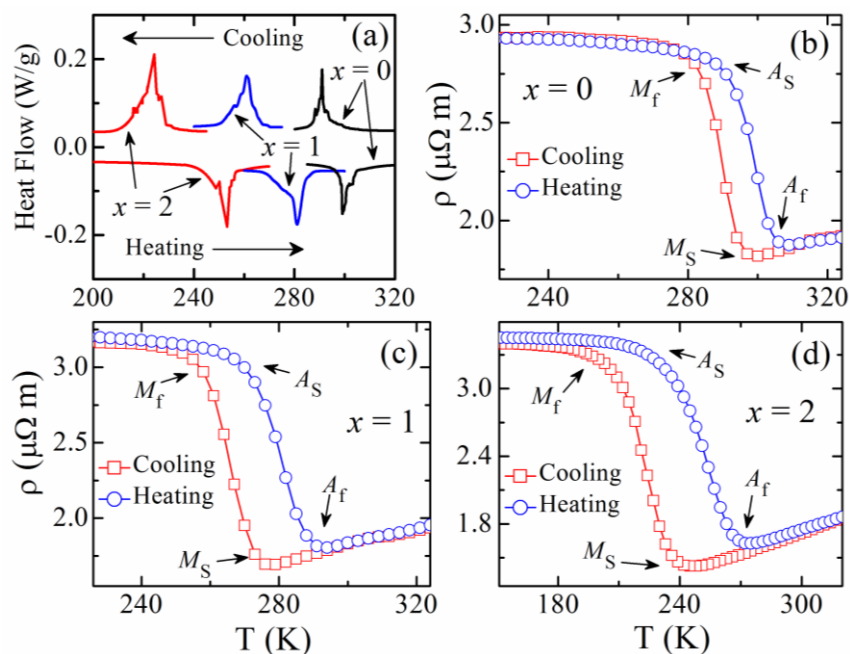


Fig. 3.2: (a) DSC heat flow as a function of temperature for $\text{Ni}_{48.5-x}\text{Co}_x\text{Mn}_{37}\text{Sn}_{14.5}$ alloys. Temperature dependence of electrical resistivity for the samples with (b) $x = 0$, (c) $x = 1$ and (d) $x = 2$.

Figs. 3.2(b-d) show the temperature dependence of electrical resistivity (ρ - T curves) for all the samples. Both the DSC and resistivity measurements agree well with each other. The characteristic transition temperatures for FOMST: A_S , A_f , T_A , M_S , M_f and T_M are given in table 3.1. An enormous change in the electrical resistivity is observed along with the martensitic and its reverse transition. The martensitic phase of these samples is found to be semi-metallic as the resistivity in that phase decreases with increasing the temperature. The resistivity decreases sharply across the structural phase transition during heating. After the structural transition, the resistivity increases monotonically with the increase of temperature in the cubic austenite parent phase, which confirms the metallic nature of that phase. As some of the Ni atoms are replaced by Co, the martensite phase becomes unstable resulting a decrease in the FOMST temperature with increasing x , which is discussed in detail in the coming parts of this chapter.

Table 3.1: Characteristic transition temperatures for $\text{Ni}_{48.5-x}\text{Co}_x\text{Mn}_{37}\text{Sn}_{14.5}$ alloys as confirmed from DSC, resistivity, ac susceptibility and magnetization data. Maximum possible error is ± 3 K.

x (at%)	A_S (K)	A_f (K)	T_A (K)	M_S (K)	M_f (K)	T_M (K)	ΔT_{hys} (K)	T_C^M (K)	T_C^A (K)
0	291	306	298.5	297	282	289.5	9	240	317
1	270	288	279	267	252	259.5	19.5	240	327
2	243	264	253.5	240	213	226.5	27	---	341

3.3.1.2. Structural and magnetic phase transitions

Fig. 3.3 depicts the temperature dependent real part of the ac susceptibility for all the samples within the temperatures between 80 K and 310 K. All the samples undergo a phase transition with thermal hysteresis. The lower temperature phase has weaker magnetic response as compared to the higher temperature phase. If we compare these data with the DSC heat flow and resistivity measurements (Fig. 3.2), the existence of a first order structural transition can be confirmed which accompanies large changes in transport and magnetic properties also.

Figs. 3.4(a-c) represent the zero field cooled (ZFC) and field cooled (FC) temperature dependence of magnetization (M - T curves) for all the samples within

the temperatures between 80 K and 400 K in the presence of 100 Oe field. The ZFC and FC M - T curves of these samples split at low temperatures and the ZFC magnetization curve shows a step like nature within the temperatures between 120 K and 140 K. A sudden drop in magnetization is observed at around 240 K for $x = 0$ and 1, which is due to their Currie temperature of the martensite phase (T_C^M). Here the samples jump from the weakly magnetic martensite to a paramagnetic like martensite state. A large change in magnetization with thermal hysteresis between ZFC and FC curves is due to the FOMST of these alloys. As the FOMST of $x = 2$ is in a relatively lower temperature, no T_C^M is observed.

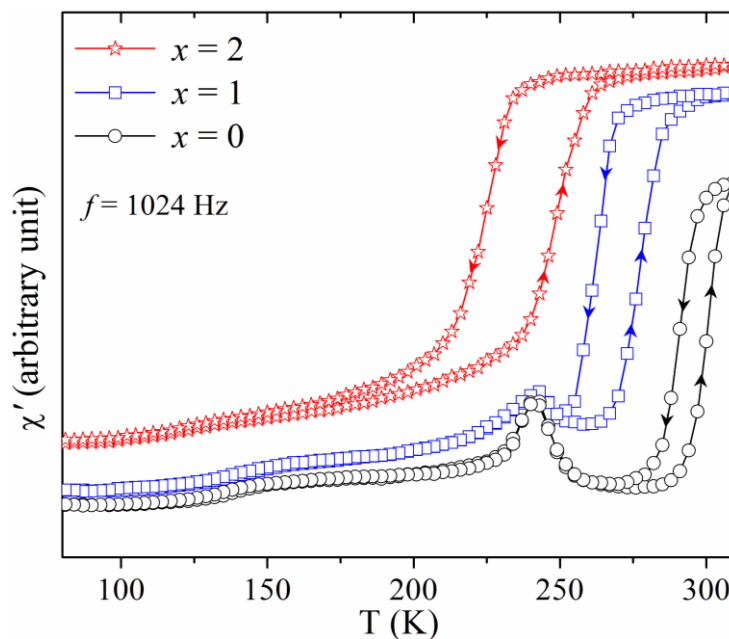


Fig. 3.3: Temperature dependence of the real part of ac susceptibility for $\text{Ni}_{48.5-x}\text{Co}_x\text{Mn}_{37}\text{Sn}_{14.5}$ alloys within the temperatures between 80 K and 300 K.

The characteristic transition temperatures for FOMST as found from the M - T curves are in good agreement with the results as obtained from DSC, resistivity and ac susceptibility data (Fig. 3.2 and Fig. 3.3). Some of these characteristic temperatures are also indicated in the temperature dependent resistivity and magnetization curves (Figs. 3.2(b-d) and Figs. 3.4(a-c)). The Currie temperature of the austenite phase (T_C^A) of these samples are given in table 3.1. It is interesting to note that FOMST and SOMT of $x = 0$ are very close to each other and occur near 300 K. The transition width (ΔT) and the thermal hysteresis (ΔT_{hys}) at FOMST increase with Co

substitution. Increase of Co content also decreases T_A and increases T_C^A . A detail phase diagram for this series of materials as a function of x is shown in Fig. 3.4(d). The temperatures above 350 K all the samples are paramagnetic in their austenite phase. A ferromagnetic austenite phase is present within the temperatures between T_C^A and M_S .

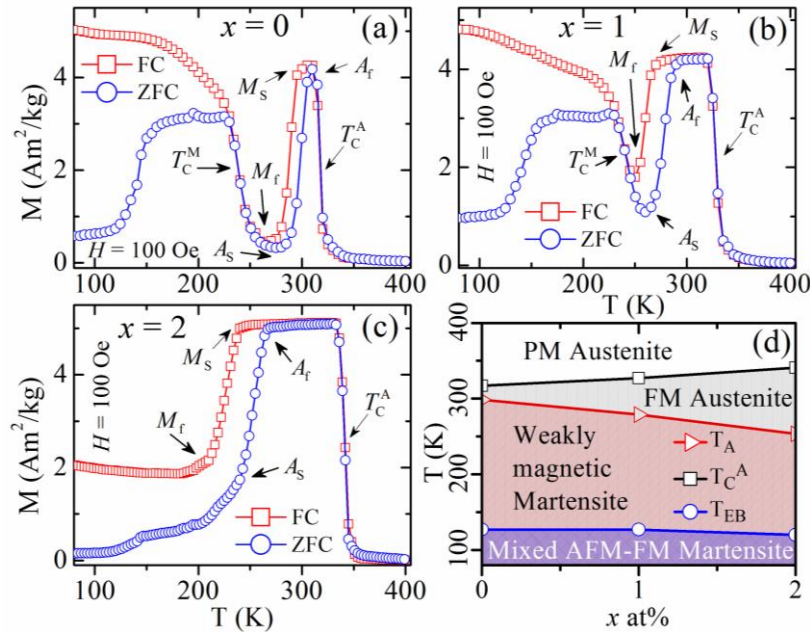


Fig. 3.4: ZFC and FC magnetization vs temperature (M - T curves) curves for $\text{Ni}_{48.5-x}\text{Co}_x\text{Mn}_{37}\text{Sn}_{14.5}$ alloys with (a) $x = 0$, (b) $x = 1$ and (c) $x = 2$ in the presence of 100 Oe magnetic field. (d) Phase diagram as a function Co concentration for $\text{Ni}_{48.5-x}\text{Co}_x\text{Mn}_{37}\text{Sn}_{14.5}$ alloys within the temperature between 80 K and 400 K.

Aksoy *et al* [17] have studied Ni-Mn-Sn and Ni-Mn-Sb alloys by neutron-polarization-analysis experiments and found that the ferromagnetic correlations are present in the cubic austenite phase in the temperatures between M_S and T_C^A . The inter-site Mn-Mn separation decreases as the structure of the sample transforms from austenite to the martensite. As a result, the ferromagnetic exchange starts to weaken and antiferromagnetic correlations become stronger. This is why the magnetization of these samples decreases during the martensitic transition on cooling. According to the recent reports the change in T_A depends on the hybridization between the $3d$ states of Mn and Ni atoms [25]. Ye *et al* [26] have theoretically investigated $\text{Ni}_2\text{Mn}_{1+x}\text{Sn}_{1-x}$ alloys and showed that the peak of total

density of states (DOS) in the minority spin $3d e_g$ states shifts systematically towards the Fermi level (E_F) with increasing x . This peak shift is attributed to the $3d$ states hybridization between Ni atoms and the excess Mn atoms in the Sn site. The Mn-Mn antiferromagnetic interaction and the Ni-Mn $3d$ states hybridization contribute significantly to stabilize the modulated martensite phase of these alloy family. Substitution of Co in the Ni site increases ferromagnetic exchange interaction, which weakens the antiferromagnetic interaction in this system and draws more stability in the ferromagnetic austenite phase [16]. This explains the reason behind the decrease in T_A and increase in T_C^A with increasing x .

3.3.1.3. Exchange bias

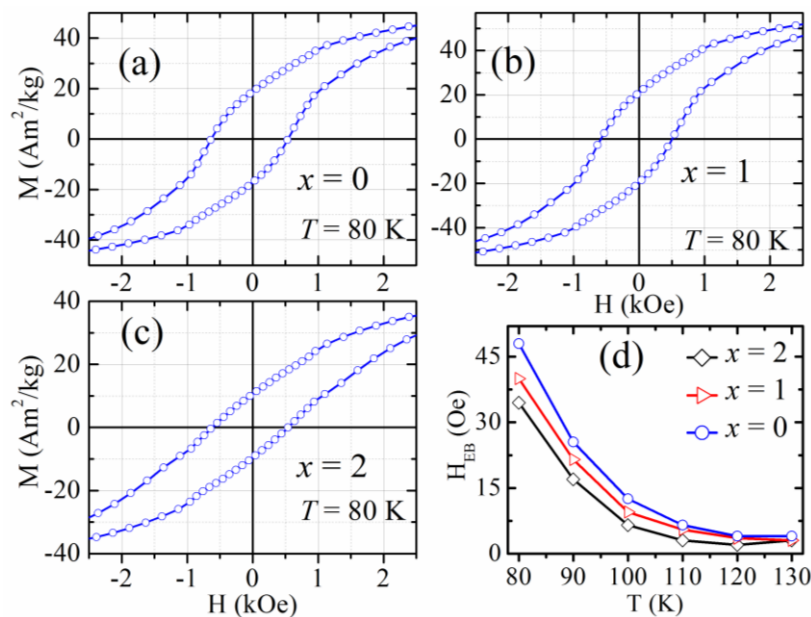


Fig. 3.5: Magnetic hysteresis loops at 80 K for Ni_{48.5-x}Co_xMn₃₇Sn_{14.5} alloys with (a) $x = 0$, (b) $x = 1$ and (c) $x = 2$ measured after cooling the samples from their respective paramagnetic phase in presence of 10 kOe field. (d) Exchange bias field (H_{EB}) as a function of temperature for Ni_{48.5-x}Co_xMn₃₇Sn_{14.5}.

Figs. 3.5(a-c) show the magnetic hysteresis loops at 80 K for the samples with $x = 0, 1$ and 2 . All the samples were first heated above their respective T_C^A and then cooled to 80 K in the presence of 10 kOe magnetic field before taking data. The field sweeping is done as follows: 10 kOe \rightarrow 0 \rightarrow -10 kOe \rightarrow 0 \rightarrow 10 kOe. A small but finite shift in the hysteresis loops is observed for all the samples which prove the existence of EB behavior in them [18]. EB is attributed to ferro-antiferro interfaces

present within a system because of the coexistence of ferromagnetic and antiferromagnetic exchange interactions [27]. Temperature dependence of H_{EB} for these alloys is plotted in Fig. 3.5(d). The H_{EB} decreases with increasing the temperature and is blocked near T_{EB} for all the samples (x dependence of T_{EB} is plotted in the phase diagram, Fig. 3.4(d)). As the temperature increases, the size of the antiferromagnetic grains decreases [28]. This is responsible for the weakening of ferro-antiferro coupling at the interfaces resulting a decrease in H_{EB} . One can observe that H_{EB} decreases with increasing x also. This result can be ascribed to the enhancement in ferromagnetic correlations due to the increase in Co content which in turn weakens the ferro-antiferro exchange interaction at the interfaces between the two (ferromagnetic and antiferromagnetic) magnetic layers.

3.3.1.4. Magnetic hysteresis

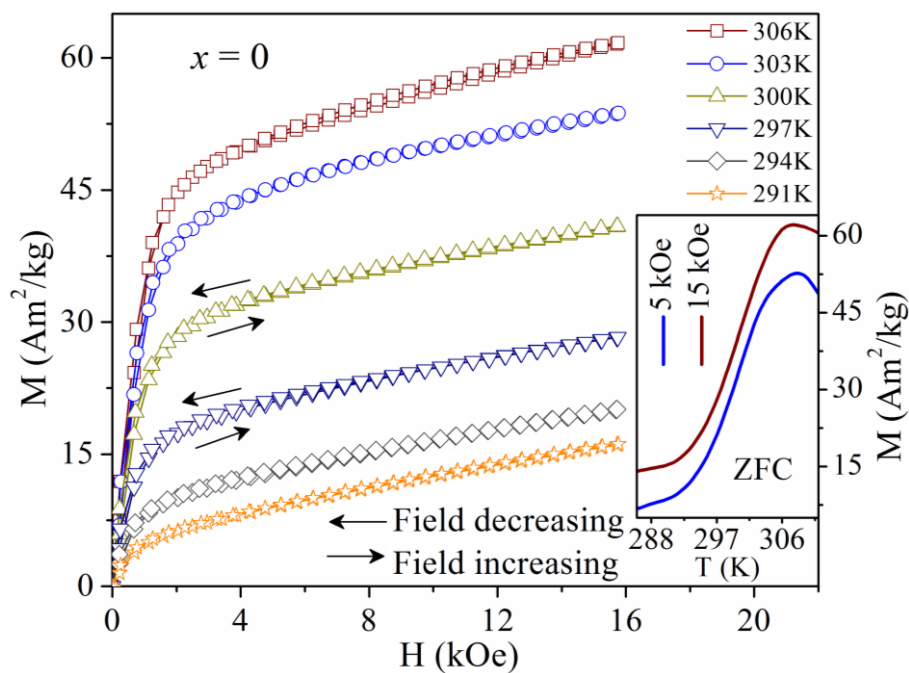


Fig. 3.6: Magnetic isotherms (M - H curves) for $x = 0$ at different temperatures near its martensitic transition. Inset: ZFC M - T curves in the vicinity of the structural transition in the presence of 5 kOe and 15 kOe magnetic field.

Magnetic isotherms (M - H curves) up to 16 kOe field near the structural transition of the samples with $x = 0$, 1 and 2 are plotted in Fig. 3.6, 3.7 and 3.8 respectively. The field sweeping is done as follows: $0 \rightarrow 16 \text{ kOe} \rightarrow 0$. The change in

saturation magnetization across the FOMST ($\Delta M_{\text{sat}} = M_{\text{sat}}^{\text{A-finish}} - M_{\text{sat}}^{\text{M-finish}}$) for all the samples are given in table 3.2. No hysteresis nature in M - H curves is observed for $x = 0$ sample. But, hysteresis between the field increasing and field decreasing M - H curves is observed for other two samples. This predicts the existence of FIMST in $x = 1$ and 2 alloys. To understand the absence of hysteresis in $x = 0$ in a better way, we performed ZFC M - T measurements in presence of 5 kOe and 15 kOe magnetic field for all the samples. From the insets of Fig. 3.6, 3.7 and 3.8 we can see that a shift between two M - T curves is visible for all the samples. The vertical shift in M - T curves of these samples is originated from the change in magnetization in the saturation region due to the application of higher magnetic field, but the horizontal shift for $x = 1$ and 2 is only due to the field induced effect on structural transition. No such horizontal shift in transition temperature is observed for $x = 0$, which implies that the structural transition of this sample is not field induced.

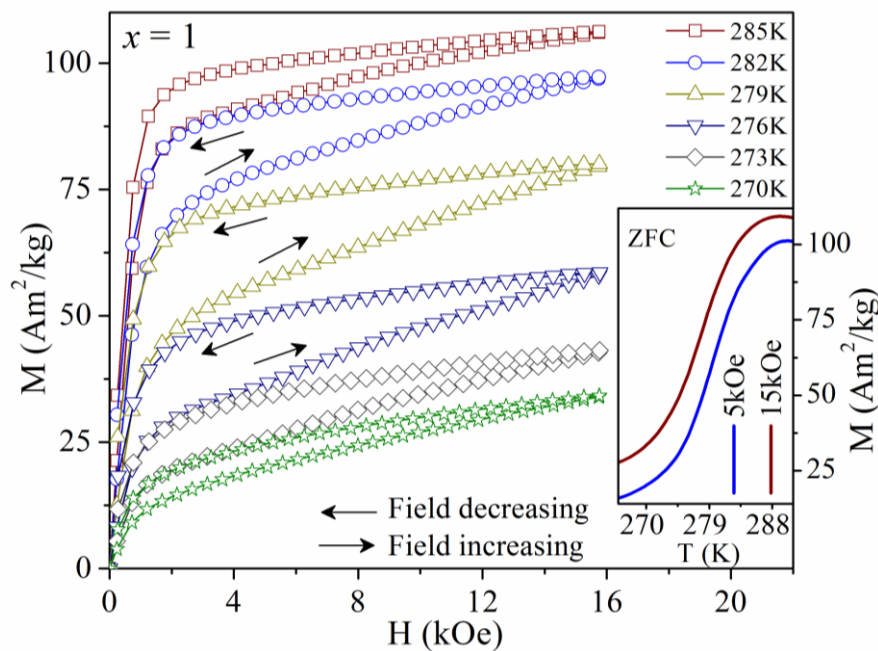


Fig. 3.7: Magnetic isotherms (M - H curves) for $x = 1$ at different temperatures near its martensitic transition. Inset: ZFC M - T curves in the vicinity of the structural transition in the presence of 5 kOe and 15 kOe magnetic field.

If we consider the Gibbs free energy of ferromagnetic shape memory alloys (FSMAs), two minima present at the two structural phases [29]. One minimum is hindered to the other by an energy barrier at the transition point. This barrier height

can be changed by both the temperature and magnetic field. When the minimum occupied by the system becomes unstable phase transition takes place. If the magnetocrystalline anisotropy energy of the sample is high, the magnetic moments rotate together with the twin boundaries to align the easy axis along the direction of applied magnetic field and as a result, a single variant is formed. When a magnetic field is applied on the sample at a temperature close to its A_S , the martensite structure starts to transform to the austenite at that single temperature. The reverse transformation occurs during the removal of field and the sample partially regains its initial phase.

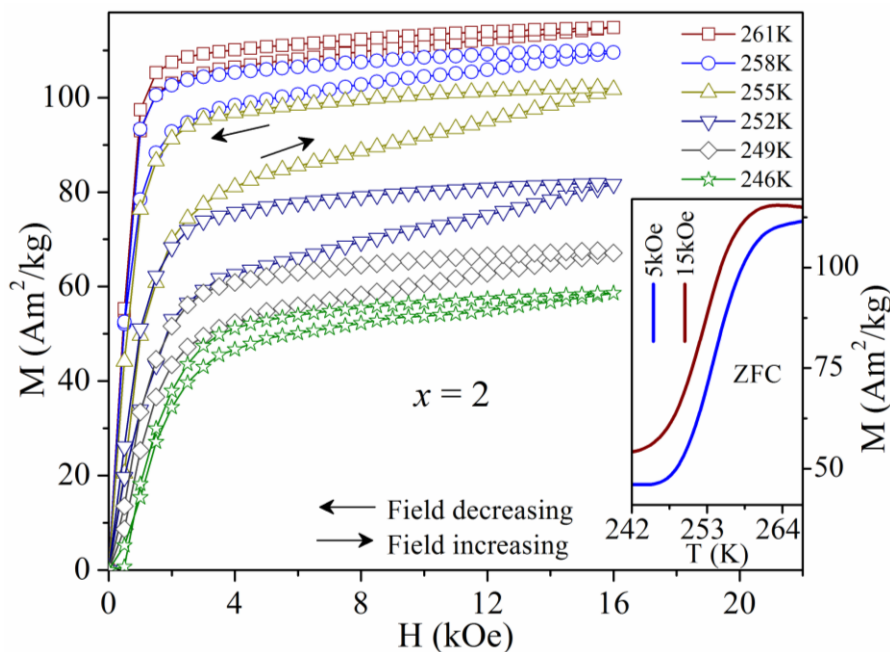


Fig. 3.8: Magnetic isotherms (M - H curves) for $x = 2$ at different temperatures near its martensitic transition. Inset: ZFC M - T curves in the vicinity of the structural transition in the presence of 5 kOe and 15 kOe magnetic field.

For $x = 0$ sample, perhaps due to smaller magnetocrystalline anisotropy, magnetization is easily changed by a magnetic field without disturbing the twinned structure. In other words, the energy barrier between austenite and martensite phases remains undisturbed under the applied magnetic field and hence no hysteresis is observed in M - H curves. On substitution of Co atoms, the magnetocrystalline anisotropy increases resulting hysteresis losses for the sample with $x = 1$ and 2.

Table 3.2: Saturation magnetization in the vicinity of structural transition and magnetocaloric parameters for $\text{Ni}_{48.5-x}\text{Co}_x\text{Mn}_{37}\text{Sn}_{14.5}$ alloys.

x (at%)	$M_{\text{sat}}^{\text{A-finish}}$ (Am ² /kg)	$M_{\text{sat}}^{\text{M-finish}}$ (Am ² /kg)	ΔM_{sat} (Am ² /kg)	ΔS_{M} (J/kg K)	RC (J/kg)	HL _{avg} (J/kg)	Net RC (J/kg)
0	62.05	13.74	48.31	6.15	50.4	---	50.4
1	109.68	26.46	83.22	10.36	88.2	14	74.2
2	115.5	53.44	62.06	9.85	68.9	14.3	54.6

3.3.1.5. Magnetocaloric effect

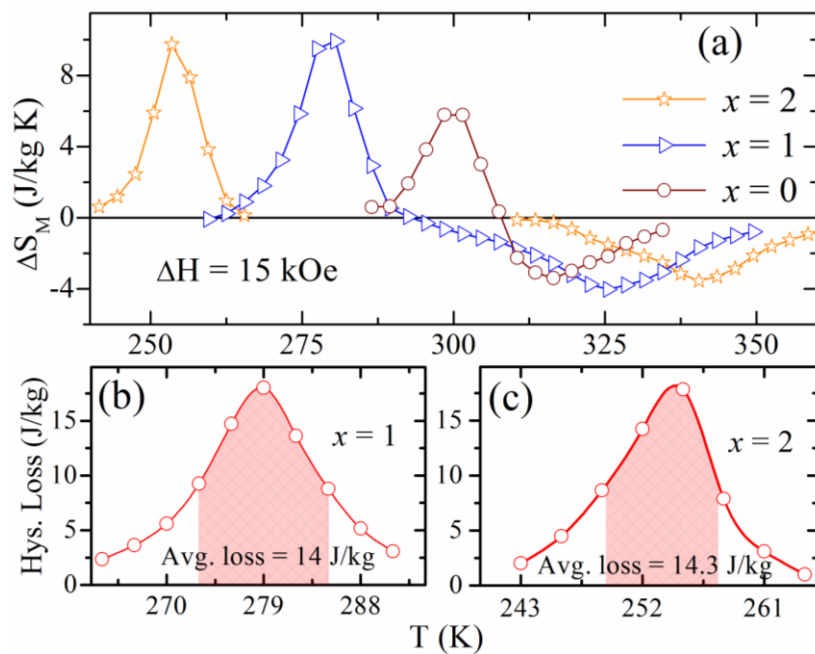


Fig. 3.9: (a) Temperature dependence of isothermal magnetic entropy changes for $\text{Ni}_{48.5-x}\text{Co}_x\text{Mn}_{37}\text{Sn}_{14.5}$ alloys due to a change of 15 kOe magnetic field. Hysteresis losses due to field induced structural transition for (b) $x = 1$ and (c) $x = 2$.

ΔS_{M} for $\text{Ni}_{48.5-x}\text{Co}_x\text{Mn}_{37}\text{Sn}_{14.5}$ alloys has been estimated using Maxwell's thermodynamic relation as represented in equation (1.18) [3]. The temperature dependence of ΔS_{M} for these alloys is plotted in Fig. 3.9(a). ΔS_{M} is found to be 6.15, 10.36 and 9.85 J/kg K at 300 K, 279.5 K and 254 K for the samples with $x = 0, 1$ and 2 respectively, due to a 15 kOe magnetic field change. All these data are given in table 3.2 also. Co atoms works here as a ferromagnetic activator, which weakens the antiferromagnetic interaction between the inter-site Mn atoms and imposes extra ferromagnetic exchange interaction in the cubic austenite phase [16]. The difference

in saturation magnetization (ΔM_{sat}) across the martensitic transition increases significantly due to the aforementioned enhancement of exchange interaction. This is the reason behind the larger ΔS_{M} for $x = 1$ and 2 compared to that for $x = 0$. As the SOMT of these samples resides near and just above room temperature, we also have calculated their ΔS_{M} near T_{C}^{A} and it is found $\sim -3.5, -4$ and -3.6 J/kg K respectively for $x = 0, 1$ and 2 under the same field change. These values are larger than the reported MCE associated with the SOMT for other reported Heusler alloys.

RC for all the samples has been estimated from the $\Delta S_{\text{M}} - T$ curves using equation (1.20) [22]. RC estimates the amount of thermal energy that can be transferred by the material between the cold source (T_1) and hot sink (T_2) in one ideal thermodynamic cycle. Estimated RC values for $x = 0, 1$ and 2 samples at FOMST under 15 kOe magnetic field are respectively, $\sim 50, 88$ and 69 J/kg. The hysteresis loss (HL) for $x = 1$ and 2 due to FIMST is plotted against temperature in Fig. 3.9(b) and Fig. 3.9(c) respectively. Integrating over the temperatures of full width at half maxima, 14 and 14.3 J/kg average hysteresis losses (HL_{avg}) is found for $x = 1$ and 2 , which lowers their effective or net RC factor to 74.2 and 54.6 J/kg.

Recently, Phan *et al* [30] showed that the FOMST shows larger ΔS_{M} compared to SOMT for Ni-Mn based Heusler alloys, but the net RC during FOMST is always smaller than that of the SOMT. This is because of the hysteresis loss in FOMST due to field induced transition. Similar result is obtained for $x = 1$ and 2 , where the RC in SOMT (~ 83 and 63 J/kg) is larger than the net RC in FOMST. But, RC ~ 50 J/kg is obtained from both the FOMST and SOMT of the sample with $x = 0$. This concludes that due to the absence of hysteresis loss efficient magnetic refrigeration can be achieved by using the materials having negligible hysteresis like $x = 0$.

3.3.2. MCE and MR in $\text{Ni}_{47.5-y}\text{Co}_y\text{Mn}_{37.5}\text{Sn}_{15}$ alloys

3.3.2.1. Structural and magnetic phase transitions

Fig. 3.10 shows the room temperature XRD patterns for $\text{Ni}_{47.5-y}\text{Co}_y\text{Mn}_{37.5}\text{Sn}_{15}$ alloys with $y = 0, 1, 2$ and 3.5 . The (220) peak is splitted for $y = 0$ sample, which signifies the existence of mixed phase with austenite and martensite phase fractions

in that sample [10]. This predicts that the martensitic transition of $y = 0$ sample may reside near room temperature. In case of other samples, cubic austenite ($L2_1$) structure is present at room temperature. The increase in intensity of (422) peak with increasing y indicates that the austenite phase of the samples becomes more stable at room temperature as the Co are added to this alloy series.

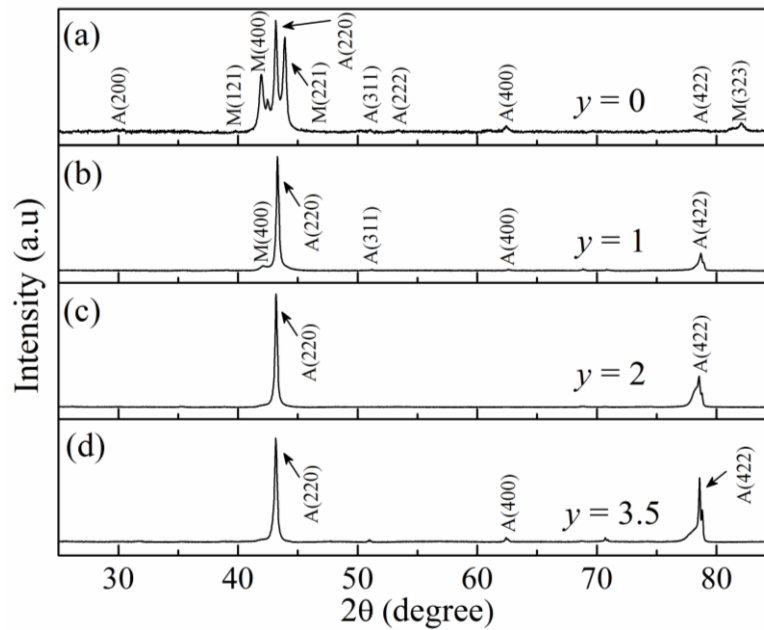


Fig. 3.10: Room temperature XRD patterns for $\text{Ni}_{47.5-y}\text{Co}_y\text{Mn}_{37.5}\text{Sn}_{15}$ alloys.

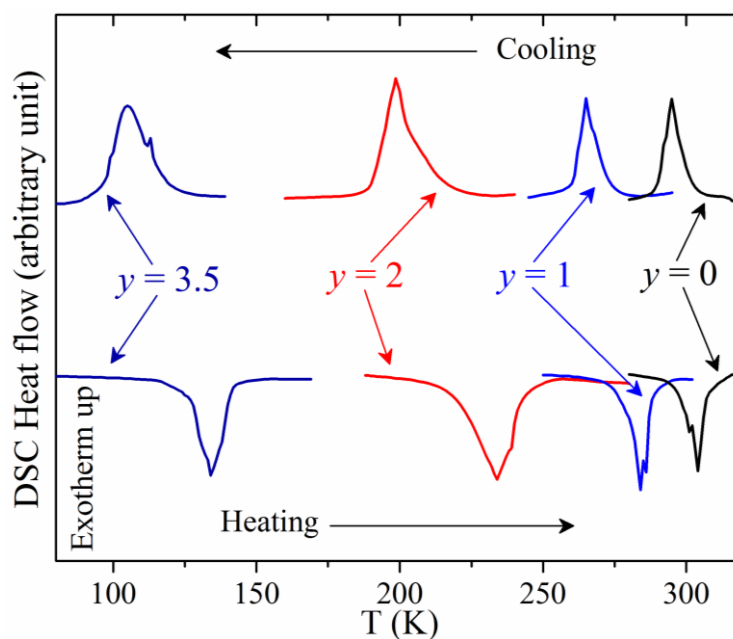


Fig. 3.11: DSC heat flow as a function of temperature across the martensitic transition of $\text{Ni}_{47.5-y}\text{Co}_y\text{Mn}_{37.5}\text{Sn}_{15}$ alloys.

The DSC heat flow data are plotted in Fig. 3.11 across the structural transition of these alloys. All the samples show the existence of FOMST. The endothermic peaks during heating and exothermic ones during cooling for the samples indicate the martensite to austenite and austenite to martensite transition respectively. The broadening of the heat flow peaks indicates that the width of the structural transition increases as Co atoms are added to the system. In addition to that, the distance between the endothermic and exothermic peaks increases with increasing y indicating the increase in thermal hysteresis.

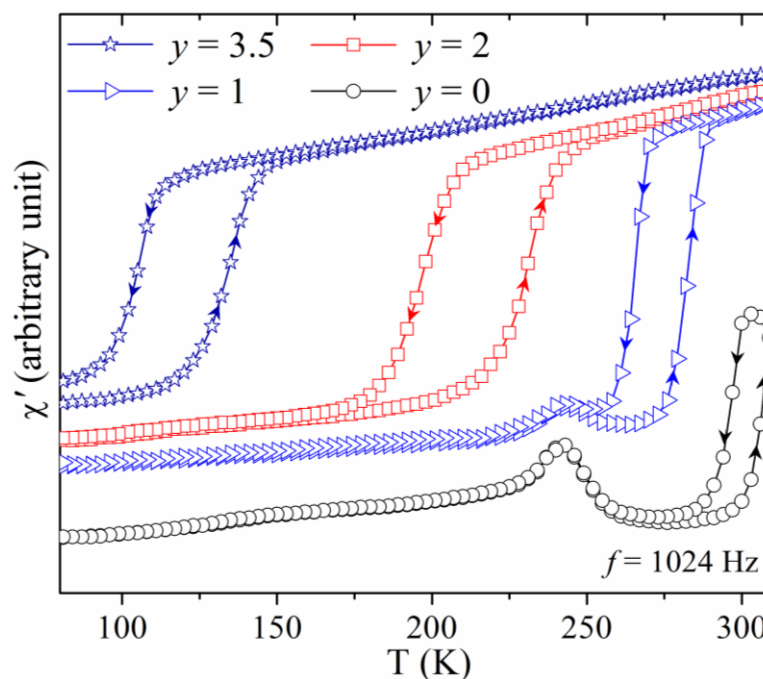


Fig. 3.12: Temperature dependent real part of the ac susceptibility for $\text{Ni}_{47.5-y}\text{Co}_y\text{Mn}_{37.5}\text{Sn}_{15}$ alloys within the temperatures between 80 K and 300 K.

The real part of the ac susceptibility is plotted in Fig. 3.12 for all the samples within the temperatures between 80 K and 300 K. The ac field frequency used is 1024 Hz. The existence of the martensitic transition can be verified from these data also. The martensite phase has a low magnetic response. The magnetic sensitivity of these samples increases significantly after the magneto-structural transition from tetragonal martensite to the cubic austenite phase. The magnetic response in both the structural phases increases with the increase in Co content. The thermal hysteresis also increases significantly as the concentration of Co increases.

Table 3.3: Characteristic transition temperatures for $\text{Ni}_{47.5-y}\text{Co}_y\text{Mn}_{37.5}\text{Sn}_{15}$ alloys as confirmed from the DSC, ac susceptibility, magnetization and resistivity data. Maximum possible error is ± 3 K.

y (at%)	A_S (K)	A_f (K)	T_A (K)	M_S (K)	M_f (K)	T_M (K)	ΔT_{hys} (K)	T_C^M (K)	T_C^A (K)
0	296	312	304	303	285	294	12	240	313
1	276	294	285	276	252	264	21	240	335
2	207	255	231	220	172	196	35	---	344
3.5	118	152	135	122	90	106	29	---	353

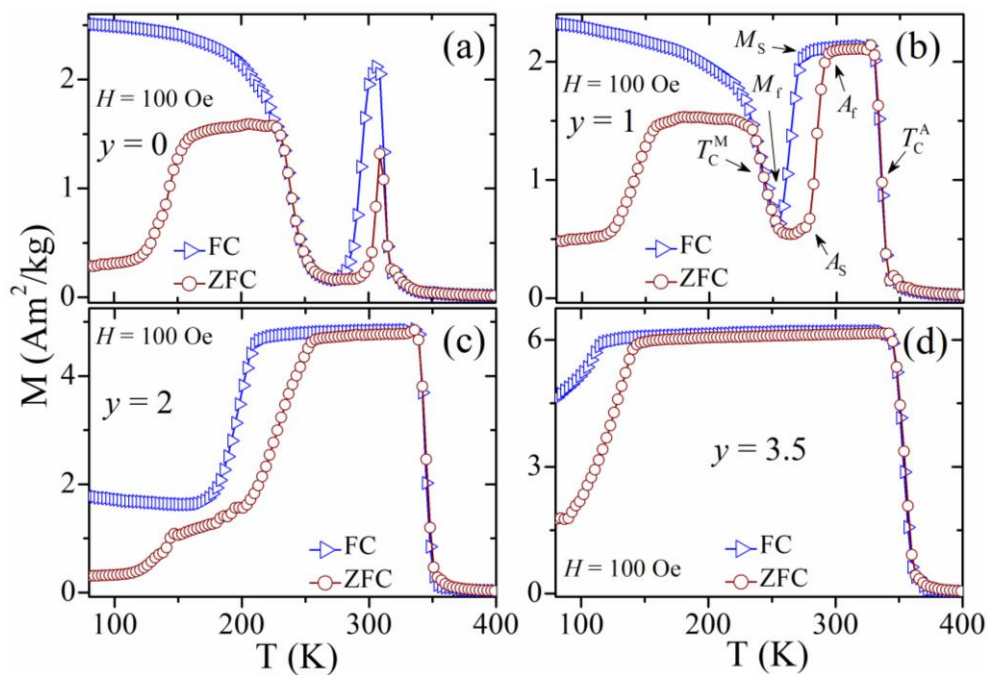


Fig. 3.13: ZFC and FC magnetization vs temperature curves for $\text{Ni}_{47.5-y}\text{Co}_y\text{Mn}_{37.5}\text{Sn}_{15}$ alloys with (a) $y = 0$, (b) $y = 1$, (c) $y = 2$ and (d) $y = 3.5$ in the presence of 100 Oe magnetic field within the temperatures between 80 K and 400 K.

Fig. 3.13 represents the ZFC and FC temperature dependence of magnetization curves for $\text{Ni}_{47.5-y}\text{Co}_y\text{Mn}_{37.5}\text{Sn}_{15}$ alloys within the temperatures between 80 K and 400 K in presence of 100 Oe field. Each sample exhibits the structural transition from the ferromagnetic austenite parent phase to a weakly magnetic or paramagnetic like martensite phase on decreasing the temperature. The martensitic transition and SOMT of the sample with $y = 0$ are very close to each other and occur near room temperature. It is observed that the FOMST of this series of alloys shifts towards the lower temperatures with increasing x . A very similar result has been obtained from

the work discussed in the previous subsection of this chapter (Chapter 3; subsection 3.3.1).

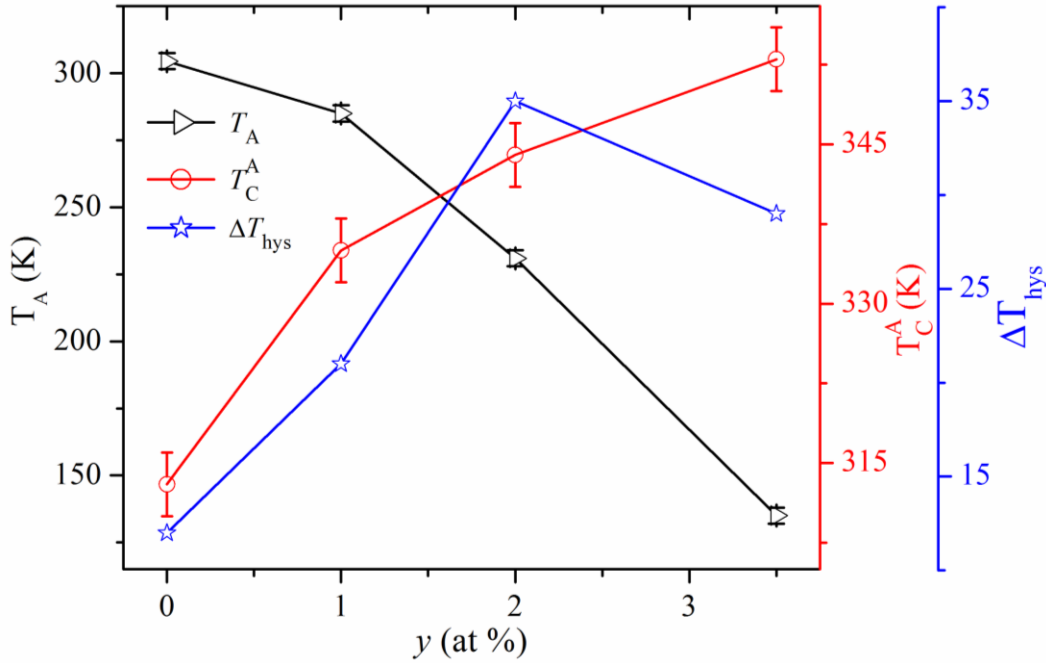


Fig. 3.14: The martensite to austenite transition temperature (T_A), Currie temperature of the austenite phase (T_C^A) and thermal hysteresis (ΔT_{hys}) at the structural transition of $\text{Ni}_{47.5-y}\text{Co}_y\text{Mn}_{37.5}\text{Sn}_{15}$ alloys as a function of Co concentration. Maximum possible error is ± 3 K.

The characteristic transition temperatures: A_S , A_f , T_A , M_S , M_f and T_M are given in table 3.3. ΔT of FOMST increases with the increase of Co content. Both the ZFC and FC M - T curves of $y = 0$ and 1 show a significant change in magnetization near 240 K, which may refer to the T_C^M of these materials. There is another phase transition above 300 K for all the samples where the magnetization decreases rapidly with increasing the temperature. This is due to the ferro-para transition of these alloys at their T_C^A . As the martensitic transition of $y = 2$ and $y = 3.5$ samples are in lower temperatures, no such T_C^M is present in their M - T curves. The dependence of T_A , T_C^A and ΔT_{hys} on the Co concentration is plotted in Fig. 3.14. T_C^A increases and T_A decreases with increasing Co at%. The ΔT_{hys} at FOMST is found to increase for $y = 0 - 2$ but, ΔT_{hys} is smaller for $y = 3.5$ than that for $y = 2$.

$\text{Ni}_2\text{Mn}_{1+x}\text{Sn}_{1-x}$ alloys were investigated by Ye *et al* [26] and it was shown that the peak of total density of states (DOS) in the minority spin $3d$ e_g states shifts

systematically towards Fermi level (E_F) with increasing x . This peak shift can be attributed to the hybridization between $3d$ states of Ni atoms in regular Ni sites and excess Mn atoms in the Sn site. Aksoy *et al* [17] have studied Ni-Mn-Sn and Ni-Mn-Sb alloys by neutron-polarization-analysis experiments and found that ferromagnetic correlations are present in the cubic austenite phase in the temperatures between M_S and T_C^A . The Mn-Mn inter-site separation decreases as the structure of the sample transforms from austenite to the martensite. As a result, ferromagnetic exchange starts to weaken and antiferromagnetic correlations become stronger. This is why the magnetization of the samples decreases due to the martensitic transition. This antiferromagnetic interaction and the above mentioned $3d$ states hybridization contribute significantly to stabilize the tetragonally distorted martensitic phase. Substitution of Co in the Ni site increases ferromagnetic exchange interaction, which weakens both the $3d$ states hybridization and Mn-Mn antiferromagnetic correlations in the system and draws more stability in ferromagnetic austenite phase. The decrease in T_A and increase in T_C^A may originate due to the aforementioned stabilization of the ferromagnetic phase as discussed in the subsection 3.3.1 in this chapter.

3.3.2.2. Magnetic properties

Fig. 3.15 represents the ZFC M - T curves respectively for $y = 0, 1, 2$ and 3.5 in the presence of 5 kOe and 15 kOe magnetic field in the vicinity of their FOMST. Unlike the undoped sample of the previous series (chapter 3; subsection 3.3.1), here, all the samples show the usual shift in the structural transition on application of high magnetic field. This shift indicates the existence of field induced metamagnetic transition in these materials. $|\Delta T/\Delta H|$ is found to be $\sim 0.12, 0.15, 0.22$ and 0.5 K/kOe for the samples with $y = 0, 1, 2$ and 3.5 respectively. The values of $|\Delta T/\Delta H|$ has also been confirmed from the resistivity data which is discussed later in this subsection. It can be observed that the $|\Delta T/\Delta H|$ increases significantly as the atomic concentration of Co increases in this alloy series. The increase in magnetocrystalline anisotropy with the addition of Co might be a reason for this. The sample with $y = 3.5$ shows a very large field induced shift which may cause significant energy consumption.

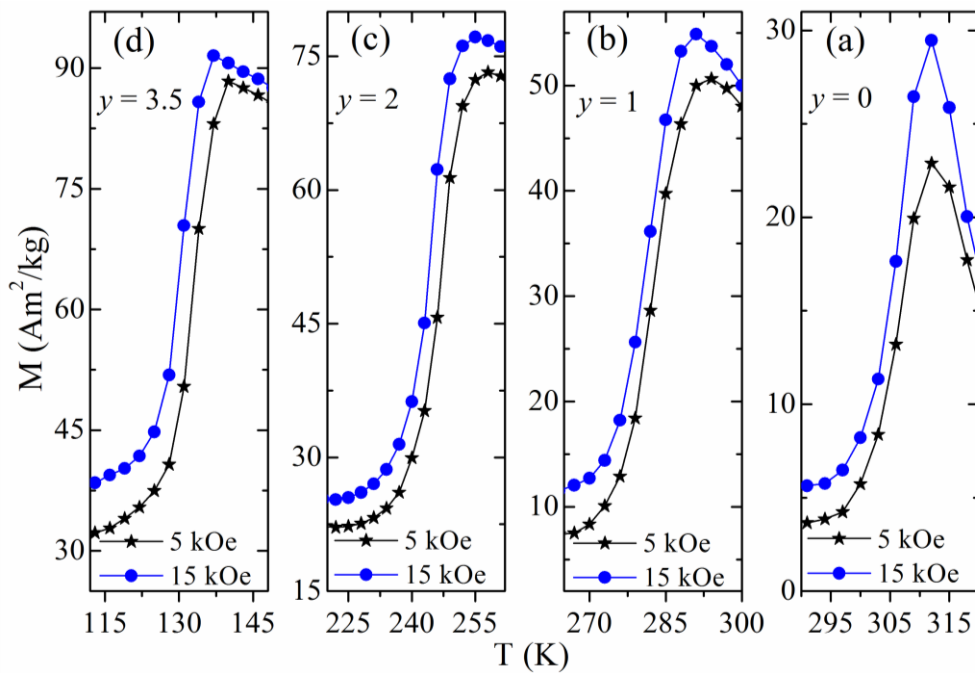


Fig. 3.15: ZFC M - T curves in the vicinity of martensitic transition for $\text{Ni}_{47.5-y}\text{Co}_y\text{Mn}_{37.5}\text{Sn}_{15}$ alloys with (a) $y = 0$, (b) $y = 1$, (c) $y = 2$ and (d) $y = 3.5$ under 5 kOe and 15 kOe magnetic field.

Fig. 3.16 shows the isothermal M - H curves near the structural transition of $\text{Ni}_{47.5-y}\text{Co}_y\text{Mn}_{37.5}\text{Sn}_{15}$ alloys. The field sweeping is done as follows: $0 \rightarrow 16 \text{ kOe} \rightarrow 0$. The saturation magnetization of the M - H curves for all the samples increases as the structure changes from martensite to the austenite with the increase of the measurement temperature. Field induced magnetic hysteresis in M - H curves is present for all the samples. Initially, this hysteresis increases with increasing y from 0 to 2. But, the magnetic hysteresis for $y = 3.5$ is less than that for the sample with $y = 2$. For the alloy with $y = 3.5$, metamagnetic transition is observed, where the magnetization suddenly starts to increase nonlinearly in the saturation region after a critical field of 12.5 kOe. The $M_{\text{sat}}^{\text{A-finish}}$ and $M_{\text{sat}}^{\text{M-finish}}$ increase significantly with the increase of Co content (values are given in table 3.4). The M - H curve at 300 K for the sample with $y = 0$ shows a paramagnetic like behavior. The T_C^{M} of this sample is near 240 K and thus its martensite phase above T_C^{M} is paramagnetic like. This type of behavior in the M - H curves near A_S of this alloy series change from paramagnetic like to ferromagnetic like as the Co concentration increases. This is due to the low T_A and enhanced ferromagnetic interaction in Co doped alloys.

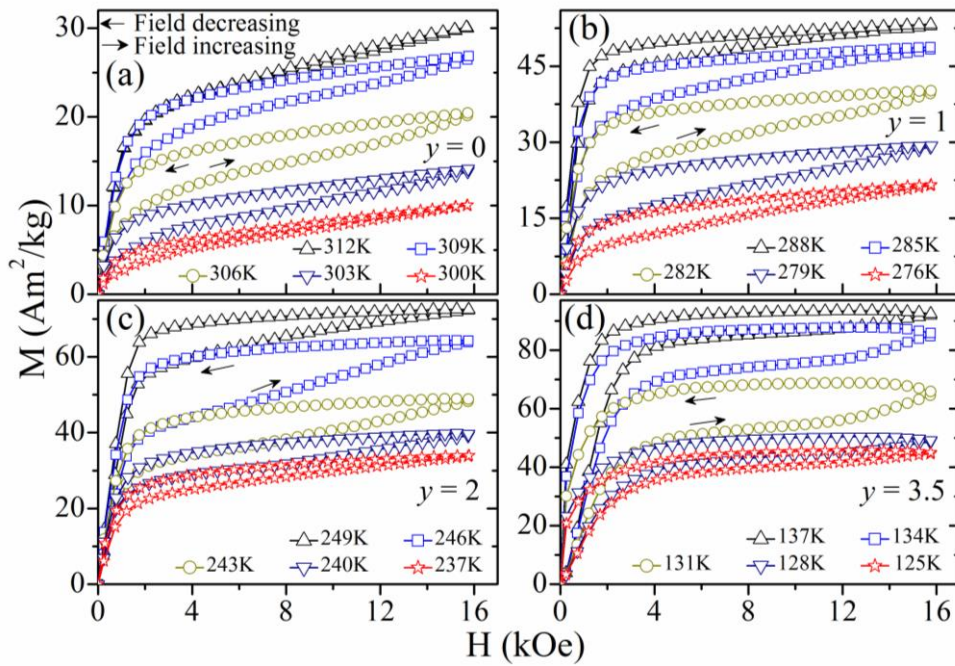


Fig. 3.16: Isothermal magnetization vs magnetic field curves for $\text{Ni}_{47.5-y}\text{Co}_y\text{Mn}_{37.5}\text{Sn}_{15}$ alloys with (a) $y = 0$, (b) $y = 1$, (c) $y = 2$ and (d) $y = 3.5$ at different temperatures in the vicinity of their structural transition.

Table 3.1: Saturation magnetization in the vicinity of structural transition and magnetocaloric parameters for $\text{Ni}_{47.5-y}\text{Co}_y\text{Mn}_{37.5}\text{Sn}_{15}$ alloys.

y (at%)	$M_{\text{sat}}^{\text{A-finish}}$ (Am ² /kg)	$M_{\text{sat}}^{\text{M-finish}}$ (Am ² /kg)	ΔM_{sat} (Am ² /kg)	ΔS_{M} (J/kg K)	RC (J/kg)	HL_{avg} (J/kg)	Net RC (J/kg)
0	29.5	5.65	23.85	3.15	21.22	3.46	17.76
1	54.84	11.91	42.93	5.1	43.84	7.36	36.48
2	77.29	25.13	52.16	6.35	45.59	12.4	33.19
3.5	91.6	37.8	53.72	9.49	46.05	19.14	26.91

3.3.2.3. Magnetocaloric properties

ΔS_{M} of the samples with $y = 0, 1, 2$ and 3.5 has been estimated using the Maxwell's thermodynamic relation (equation (1.18)) [3] and its dependence on the temperature is plotted in Fig. 3.17. ΔS_{M} is found to be $\sim 3, 5, 6.5$ and 9.5 J/kg K at 307 K, 282 K, 246 K and 132 K for $y = 0, 1, 2$ and 3.5 samples respectively, due to a field change of 15 kOe. ΔS_{M} of these alloys increases monotonically with the increase of Co content. The ΔM_{sat} is found to increase with increasing y . The role of Co atom is to enhance the ferromagnetic interaction in the system and making the

antiferromagnetic correlation between the Mn-Mn inter-site atoms weaker [16]. It stabilizes the ferromagnetic austenite phase and this is why the ΔM_{sat} increases with the increase in Co-content. One can see that the ΔM is a very important factor in the MCE equations that come from Maxwell's relations (equation (1.18)) [3, 4]. As the magnetic response across the martensitic transition increases with the increase in Co concentration, the ΔS_M increases also.

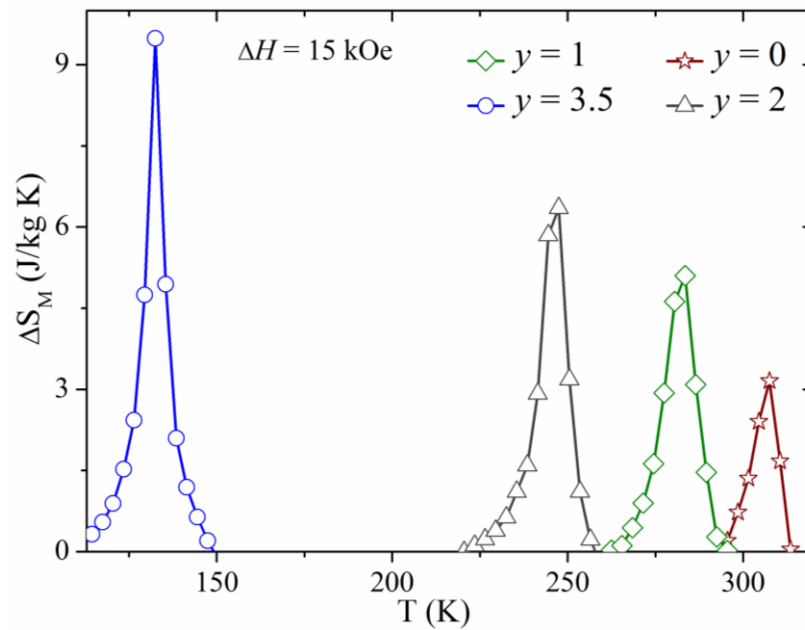


Fig. 3.17: Isothermal magnetic entropy changes as a function of temperature due to a field change of 15 kOe for $\text{Ni}_{47.5-y}\text{Co}_y\text{Mn}_{37.5}\text{Sn}_{15}$ alloys.

RC of these materials has been calculated from the temperature dependent entropy change data (equation (1.20)). In order to obtain net RC, it is necessary to subtract field induced hysteresis losses from total RC. Hysteresis loss of these samples has been calculated from the isothermal M - H curves and plotted in Fig. 3.18. The average field induced hysteresis loss is found to be 3.46, 7.36, 12.4 and 19.14 J/kg, which lowered the net RC to 17.76, 36.48, 33.19 and 26.91 J/kg for $y = 0, 1, 2$ and 3.5 samples respectively. We can see that the samples with $y = 2$ and 3.5 has shown larger ΔS_M compared to $y = 1$, but the large hysteresis loss limits their net RC. In other words, these two above mentioned samples exhibit larger MCE as compared to the others, but their cooling efficiency is not that sufficient for a better magnetic cooling.

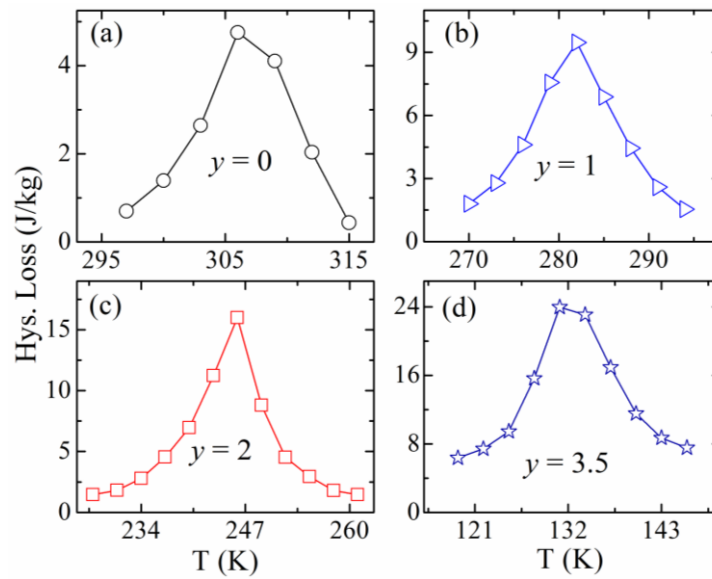


Fig. 3.18: The temperature dependence of field induced hysteresis losses under 15 kOe magnetic field for $\text{Ni}_{47.5-y}\text{Co}_y\text{Mn}_{37.5}\text{Sn}_{15}$ alloys with (a) $y = 0$, (b) $y = 1$, (c) $y = 2$ and (d) $y = 3.5$ in the vicinity of their structural transitions.

3.3.2.4. Resistivity and magnetoresistance

Fig. 3.19 shows the temperature dependence of electrical resistivity (ρ - T curves) for $\text{Ni}_{47.5-y}\text{Co}_y\text{Mn}_{37.5}\text{Sn}_{15}$ ($y = 0, 1, 2$ and 3.5) alloys during heating and cooling cycle in presence of 0 and 80 kOe magnetic field. A large drop in resistivity can be observed during the phase transition from martensite to the austenite while heating. During cooling, the aforementioned drop is even larger when the structure of a sample transforms from austenite to the martensite. The martensite phase of these alloys has a semi-metallic nature. Its resistivity decreases with the increase of temperature in that phase. In the case of austenite phase, the resistivity increases monotonically as the temperature increases. This confirms the metallic nature of these alloys in their parent phase. The phase transitions temperatures, thermal hysteresis and $|\Delta T/\Delta H|$ of FOMST as estimated from ρ - T curves agree well with the results obtained from DSC heat flow, ac susceptibility data and M - T curves of these alloys (Figs. 3.11, 3.12 and 3.13). It can be noticed that the $|\Delta T/\Delta H|$ and ΔT_{hys} in presence of magnetic field increase considerably with the increase of Co content.

MR of these alloys is obtained from the zero field and with field ρ - T curves and its dependence on the temperature (MR- T curves) during heating and cooling is

plotted in Fig. 3.20. MR at FOMST is found to be $\sim -40\%$, -46% , -57% and -69% for $y = 0, 1, 2$ and 3.5 samples respectively due to a field change of 80 kOe. It can be seen that both the MR and ΔS_M increase with increasing y in a similar manner.

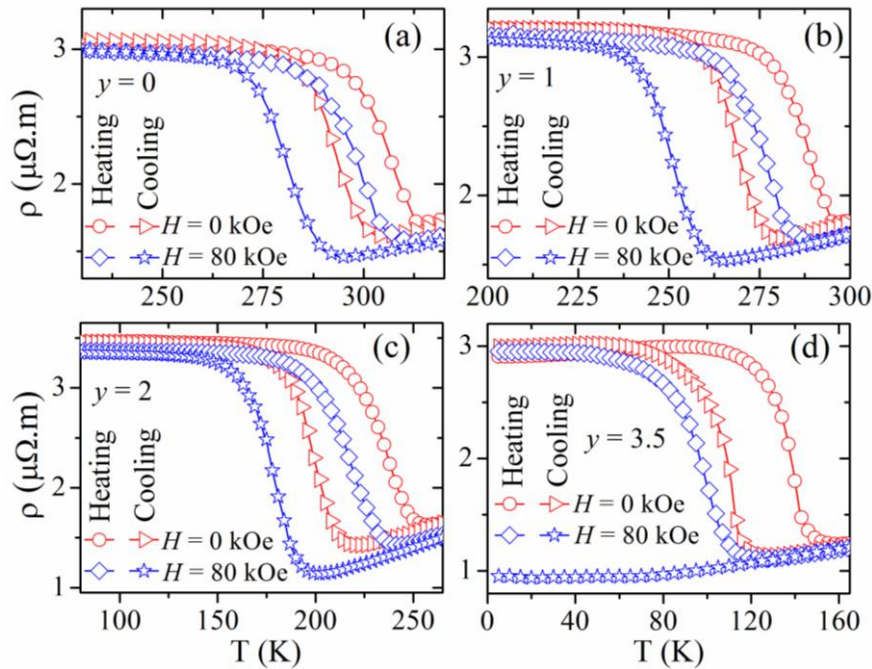


Fig. 3.19: Temperature dependence of electrical resistivity (in the presence of 0 and 80 kOe magnetic field) for $\text{Ni}_{47.5-y}\text{Co}_y\text{Mn}_{37.5}\text{Sn}_{15}$ alloys with (a) $y = 0$, (b) $y = 1$, (c) $y = 2$ and (d) $y = 3.5$.

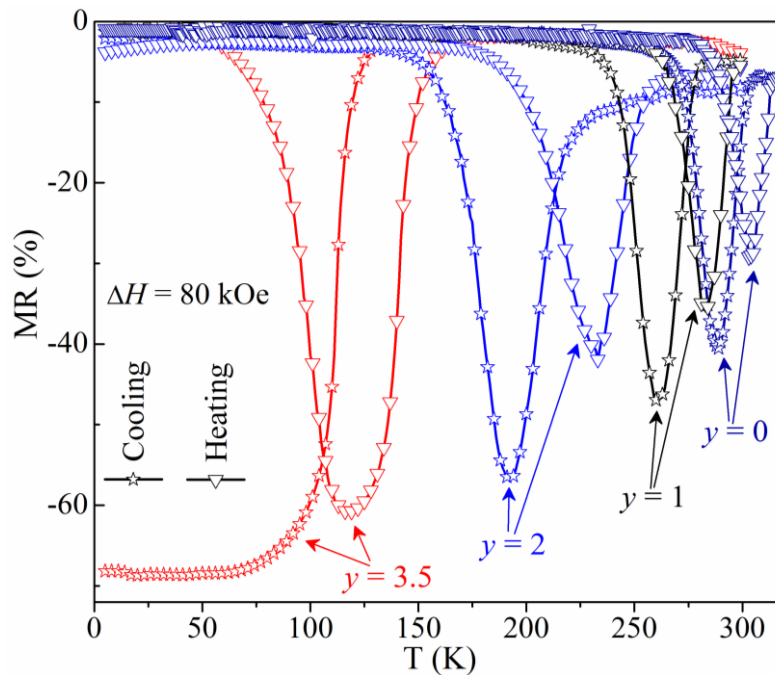


Fig. 3.20: Temperature dependence of magnetoresistance (due to application of 80 kOe field) during heating and cooling for $\text{Ni}_{47.5-y}\text{Co}_y\text{Mn}_{37.5}\text{Sn}_{15}$ alloys.

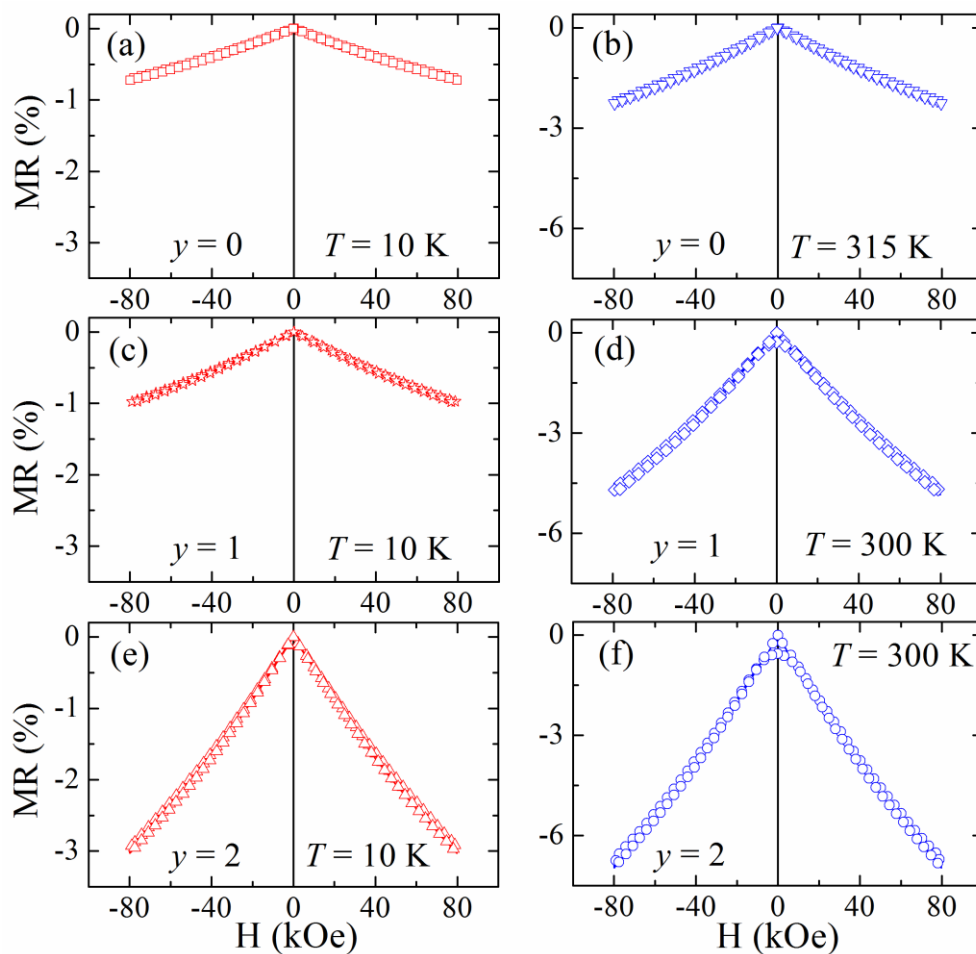


Fig. 3.21: Field dependence of magnetoresistance for the sample with (a) $y = 0$, (c) $y = 1$, (e) $y = 2$ at their martensite phase (10 K) and (b) $y = 0$, (d) $y = 1$, (f) $y = 2$ at their ferromagnetic austenite phase (300 K; 315 K for $y = 0$ only).

The field dependence of MR (MR- H curves) at the martensite (10 K) and austenite (300 K; 315 K for $y = 0$) phases for the samples with $y = 0, 1$ and 2 are plotted in Fig. 3.21. The field sweeping is done as follows: $0 \rightarrow 80 \text{ kOe} \rightarrow 0 \rightarrow -80 \text{ kOe} \rightarrow 0$. A very small percentage of MR ($\sim -0.7\%$ for $y = 0$, -1% for $y = 1$ and -3% for $y = 2$) is obtained at 10 K for these samples under 80 kOe field. But, the ferromagnetic austenite phase of these samples (at $\sim 300 \text{ K}$) shows larger MR ($\sim -2.5\%$ for $y = 0$, -5% for $y = 1$ and -7% for $y = 2$) as compared to that of at the martensite phase under the same field. The martensite phase is weakly magnetic. There exist short range interactions with ferromagnetic and antiferromagnetic couplings. So the possibilities of minimizing the s - d scattering with increasing magnetic field are small [31]. In the case of ferromagnetic austenite phase, the

scattering of conduction electrons decreases significantly as the field is increased which is responsible for such larger MR. Moreover, MR also increases in both the structural phases with increasing the concentration of Co. As the more Co atoms are added to the Ni-Mn based Heusler alloys, the ferromagnetic correlation increases and dominates largely. This leads to a decrease in *s-d* scattering when the magnetic field is applied to the sample and as a result, MR increases more.

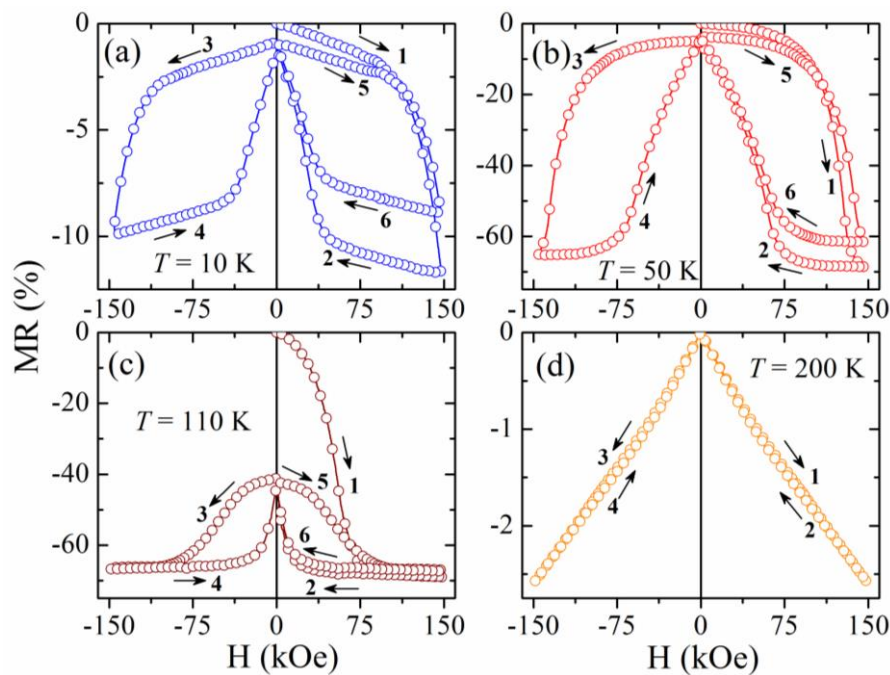


Fig. 3.22: Field dependence of magnetoresistance for the sample with $y = 3.5$ at (a) 10 K, (b) 50 K, (c) 110 K and (d) 200 K.

It can be seen from the ρ - T curves that unlike other samples, $y = 3.5$ does not experience martensitic transition during cooling in presence of 80 kOe magnetic field. The MR- H curves of the sample with $y = 3.5$ has been measured in different temperatures and plotted in Fig. 3.22. The field sweeping is done as follows: $0 \rightarrow 150$ kOe $\rightarrow 0 \rightarrow -150$ kOe $\rightarrow 0 \rightarrow 150$ kOe $\rightarrow 0$. At 10 K, $MR_{\max} \sim -12\%$ is obtained under 150 kOe magnetic field. Though 10 K is far below from the structural transition point, field induced shift in structural transition and its corresponding hysteresis is observed at that temperature. Similar behavior is observed in the MR- H curve at 50 K with $MR_{\max} \sim -69\%$. This is the saturation value of MR for $y = 3.5$. But, its martensitic transition is around 120 K. It clearly shows that the structural phase

transition of this sample can be affected by the application of high magnetic field, keeping the sample at a temperature far below from its martensitic transition point. The MR- H curve at 110 K shows the irreversibility in field induced reverse transition during the removal of magnetic field which may be ascribed as the presence of partial kinetic arrest in $y = 3.5$ [5]. The MR at this temperature saturates near 80 kOe field. By incorporating the data obtained from ρ - T , MR- T and MR- H curves, one can conclude that during cooling under magnetic field, the structure of the sample with $y = 3.5$ is arrested in the austenite phase. The sweeping of temperature cannot but, only removal of the magnetic field can give the sample's martensite phase back in the temperatures below its FOMST. So, a large MR can be obtained from the sample with $y = 3.5$ within a wide range of temperatures between ~ 50 K and 120 K. A few % MR is observed at 200 K, which originates from the s - d scattering in austenite phase.

3.4. Conclusions

In summary, we have systematically studied the magnetic, magnetocaloric and magneto-transport properties of Co doped Ni-rich $\text{Ni}_{48.5-x}\text{Co}_x\text{Mn}_{37}\text{Sn}_{14.5}$ ($x = 0, 1$ and 2) and $\text{Ni}_{47.5-y}\text{Co}_y\text{Mn}_{37.5}\text{Sn}_{15}$ ($y = 0, 1, 2$ and 3.5) alloys. Substitution of Co lowered the structural transition temperature with larger width and thermal hysteresis for both the series of samples. For the first series, all the samples show exchange bias behavior which decreases with the increase in Co content due to the enhancement in ferromagnetic part which suppresses the interfacial exchange interactions between the ferromagnetic and antiferromagnetic layers. No hysteresis is observed in the isothermal M - H curves of the undoped sample of the first series perhaps is due to a very weak coupling between the magnetic moments and twin variants. The estimated $\Delta S_M \sim 6.15, 10.36$ and 9.85 J/kg K near the martensitic transition for $x = 0, 1$ and 2 respectively, due to a field change of only 15 kOe. Incorporating hysteresis losses that originate due to field induced effect, it is found that unlike $x = 1, 2$ and other reported alloys, both the first order magneto-structural transition and second order magnetic transition of $x = 0$ contains equal potential to achieve better magnetic cooling.

In the case of later alloy series, we have shown that large value of ΔS_M does not always warrant for a magnetocaloric material to have a high cooling capacity. The working temperature range should be broad and the hysteresis loss should be small enough. In this context, the higher percentage of doping of Co may not be valuable for magnetocaloric applications. All the samples of the same series exhibit large magnetoresistance also. The structural phase of the sample with $y = 3.5$ can be changed by applying a magnetic field at a temperature far below from its structural transition point. This material can thus be used in magnetic sensors within a large working temperature range.

Bibliography

- [1] P. J. Shamberger and F. S. Ohuchi, *Phys. Rev. B* 79, 144407 (2009).
 - [2] B. Hernando, J. L. S. Llamazares, J. D. Santos, V. M. Prida, D. Baldomir, D. Serantes, R. Varga and J. González, *Appl. Phys. Lett.* 92, 132507 (2008).
 - [3] A. Planes, L. Manosa and M. Acet, *J. Phys.: Condens. Matter* 21, 233201 (2009).
 - [4] V. D. Buchelnikov and V. V. Sokolovskiy, *Phys. Met. Metallog.* 112, 633 (2011).
 - [5] H. C. Xuan, Y. Deng, D. H. Wang, C. L. Zhang, Z. D. Han and Y. W. Du, *J. Phys. D: Appl. Phys.* 41, 215002 (2008).
 - [6] K. Koyama, H. Okada, K. Watanabe, T. Kanomata, R. Kainuma, W. Ito, K. Oikawa and K. Ishida, *Appl. Phys. Lett.* 89, 182510 (2006).
 - [7] K. Ullakko, J. K. Huang, C. Kantner, R. C. O'Handley, and V. V. Kokorin, *Appl. Phys. Lett.* 69, 1966 (1996).
 - [8] K. Ullakko, J. K. Huang, V. V. Kokorin and R. C. O'Handley, *Scripta Mater.* 36, 1133 (1997).
 - [9] T. Krenke, E. Duman, M. Acet, E. F. Wassermann, X. Moya, L. Manosa, and A. Planes, *Nature Mater.* 4, 450 (2005).
 - [10] S. E. Muthu, N. V. R. Rao, M. M. Raja, D. M. R. Kumar, D. M. Radheep and S. Arumugam, *J. Phys. D: Appl. Phys.* 43, 425002 (2010).
 - [11] B. Hernando, J. L. S. Llamazares, J. D. Santos, V. M. Prida, D. Baldomir, D. Serantes, R. Varga, and J. González, *Appl. Phys. Lett.* 92, 132507 (2008).
 - [12] T. L. Phan, N. H. Duc, N. H. Yen, P. T. Thanh, N. H. Dan, P. Zhang and S.C. Yu, *IEEE Trans. on Magn.* 48, 1381 (2012).
 - [13] A. Ayuela, J. Enkovaara, K. Ullakko and R. M. Nieminen, *J. Phys. Condens. Matt.* 11, 2017 (1999).
 - [14] B. Gao, F. X. Hu, J. Shen, J. Wang, J. R. Sun and B. G. Shen, *J. Magn. Magn. Mater.* 321, 2571 (2009).
 - [15] T. Krenke, E. Duman, M. Acet, X. Moya, L. Mañosa and A. Planes, *J. Appl. Phys.* 102, 033903 (2007).
 - [16] R. Y. Umetsu, A. Sheikh, W. Ito, B. Ouladdiaf, K. R. A. Ziebeck, T. Kanomata and R. Kainuma, *Appl. Phys. Lett.* 98, 042507 (2011).
-

- [17] S. Aksoy, M. Acet, P. P. Deen, L. Mañosa and A. Planes, *Phys. Rev. B* 79, 212401 (2009).
- [18] M. Khan, I. Dubenko, S. Stadler and N. Ali, *J. Appl. Phys.* 102, 113914 (2007).
- [19] J. Dubowik, K. Załski, I. Gościańska, H. Głowiński, and A. Ehresmann, *Appl. Phys. Lett.* 100, 162403 (2012).
- [20] S. Y. Yu, L. Ma, G. D. Liu, Z. H. Liu, J. L. Chen, Z. X. Cao, G. H. Wua, B. Zhang and X. X. Zhang, *Appl. Phys. Lett.* 90, 242501 (2007).
- [21] L. Chen, F.X. Hu, J. Wang, L.F. Bao, J.R. Sun, B.G. Shen, J.H. Yin and L.Q. Pan, *Appl. Phys. Lett.* 101, 012401 (2012).
- [22] I. Titov, M. Acet, M. Farle, D. Gonzalez-Alonso, L. Manosa, A. Planes and T. Krenke, *J. Appl. Phys.* 112, 073914 (2012).
- [23] A. Ghosh and K. Mandal, *J. Alloys Compd.* 579, 295 (2013).
- [24] A. Ghosh and K. Mandal, *Eur. Phys. J. B* 86, 378 (2013).
- [25] M. Khan, J. Jung, S. S. Stoyko, A. Mar, A. Quetz, T. Samanta, I. Dubenko, N. Ali, S. Stadler and K. H. Chow, *Appl. Phys. Lett.* 100, 172403 (2012).
- [26] M. Ye, A. Kimura, Y. Miura, M. Shirai, Y. T. Cui, K. Shimada, H. Namatame, M. Taniguchi, S. Ueda, K. Kobayashi, R. Kainuma, T. Shishido, K. Fukushima, and T. Kanomata, *Phys. Rev. Lett.* 104, 176401 (2010).
- [27] S. Aksoy, O. Posth, M. Acet, R. Meckenstock, J. Lindner, M. Farle, E. F. Wassermann, *J. Phys: Confer. Series* 200, 092001 (2010).
- [28] C. Jing, J. Chen, Z. Li, Y. Qiao, B. Kang, Shixun, S. Cao and J. Zhang, *J. Alloys Compd.* 475, 1 (2009).
- [29] L. Giudicit, Magneto-structural phase transitions and magnetocaloric effect, Ph.D. thesis, Politecnico Di Torino, Turin, Italy (2009).
- [30] T. L. Phan, P. Zhang, N. H. Dan, N. H. Yen, P. T. Thanh, T. D. Thanh, M. H. Phan and S. C. Yu, *Appl. Phys. Lett.* 101, 212403 (2012).
- [31] S. Singh and C. Biswas, *Appl. Phys. Lett.* 98, 212101 (2011).
-

Chapter 4

Tuning of magnetocaloric properties in Ni-rich disordered Ni-Mn-Sn off-stoichiometric Heusler alloy

In this chapter we have prepared a Ni-Mn-Sn alloy and studied its structural, magnetic and magnetocaloric properties as a function of structural ordering.

4.1. Preamble

The Ni-Mn based off-stoichiometric Heusler alloys have become a very popular material of active research during the last few years due to their multifunctional properties like MCE, MR, EB, MC, MSME, etc. [1-12]. These materials undergo a first order phase transition which involves the changes in structural, thermal, magnetic and electrical properties [3, 4]. The MCE has a promising application in the magnetic refrigerators for room temperature refrigeration [13]. The magnetic refrigeration technology is environment friendly, gas/liquor free and energy saving also. Till date, a large number of magnetocaloric materials have been studied to check their potential for practical applications [1-4, 14-17]. For example; a giant MCE has been reported in $\text{Gd}_5\text{Si}_2\text{Ge}_2$ by Pecharsky *et al* [18].

But, Gd is expensive and it has limited the applicability of rare-earth based giant MCE materials for commercial uses. Therefore, a great portion of the scientific community has paid a special attention to the 3d transition metal based alloys and intermetallic compounds [16, 17, 19]. Among these alloys, Ni-Mn based Heusler $\text{Ni}_2\text{Mn}_{1+x}\text{Z}_{1-x}$ ($Z = \text{Ga, Sn, In, Sb}$) alloys have drawn immense attention because of their aforementioned multifunctional properties in off-stoichiometry [3, 4].

Stoichiometric $\text{Ni}_{50}\text{Mn}_{25}\text{Z}_{25}$ Heusler alloys have cubic ($L2_1$) structure with four interpenetrating face centered cubic (fcc) sublattices [20, 21]. (0,0,0) and $(\frac{1}{2}, \frac{1}{2}, \frac{1}{2})$ sites are occupied by Ni atoms. The remaining $(\frac{1}{4}, \frac{1}{4}, \frac{1}{4})$ and $(\frac{3}{4}, \frac{3}{4}, \frac{3}{4})$ sites are taken separately by Mn and Sn atoms. In the case of off-stoichiometric same alloys, the excess Mn atoms occupy the partially vacant Sn site. In practical cases, a degree of disorder always present in the specimen where some % of Ni, Mn and Sn atoms occupy the four sites randomly [22]. This disorder can be removed up to a certain level by annealing these materials at high temperatures for a long time [23]. Slow cooling or quenching is done to obtain different ordered phases [24, 25]. Annealing increases the martensitic transition temperature and as well as Currie temperature at the austenite parent phase of these materials.

Sokolovskiy *et al* [26] have theoretically studied the structural disorder in $\text{Ni}_2\text{Mn}_{1+x}\text{Sn}_{1-x}$ alloys by inter-mixing the Mn and Sn atoms in their sublattices. Their

calculations show a good agreement with the experimental values for the Curie temperature of these alloys. The match is found for $\text{Ni}_2\text{Mn}_{1-y}\text{Sn}_y\text{Mn}_{x+y}\text{Sn}_{1-x-y}$ alloys with $y = 0.25$. This corresponds to the 25 % atomic disorder where 25 % Mn atoms from regular Mn site replace the same amount of Sn atoms from regular Mn site and vice versa. This disorder can affect the structural, magnetic and transport properties of these materials. In real cases, all the constituent elements (Ni, Mn and Sn) take part in such random ordering during the preparation of these alloys by arc melting. Therefore, it is expected to observe some noticeable changes in the multifunctional properties of the same materials due to the aforementioned disorder.

Ni-rich $\text{Ni}_{50}\text{Mn}_{25+x}\text{Sn}_{25-x}$ off-stoichiometric Heusler alloys have been largely investigated by the researchers and they showed large MCE (ΔS_M) and MR associated with the FOMST of the same alloys [3, 4, 14, 15]. The dependence of the transition temperatures and ΔS_M on the constituents' ratios [14, 15], substitution of Co, Fe [27, 28] and heat treatment process at different temperatures [23, 24] has been studied in that context. ΔS_M across the structural transition increases as the transition becomes sharper. But, a sharp transition usually has smaller width. This limits the working temperature range and RC of the same sample.

In the previous chapter (chapter 3; subsection 3.3.2), we have found that a small percentage of Co doping can effectively enhance the MCE in Ni-rich Ni-Mn-Sn alloys [29, 30]. As we move towards the higher doping concentration, ΔS_M increases but, the net RC falls noticeably due to the large field induced losses. Therefore, it is desirable to do a detail systematic study on a Ni-Mn-Sn off-stoichiometric alloy by changing the heat treatment parameters so that any improvement in the magnetic, magnetocaloric and magneto-transport properties can be achieved with increasing the structural ordering during the annealing [26]. We have chosen $\text{Ni}_{50}\text{Mn}_{36.5}\text{Sn}_{13.5}$ alloy for such investigation. This composition is a new one and the reported structural transition temperatures of Ni-Mn-Sn alloys with very similar compositions indicates that the FOMST of the above mentioned sample might reside near or just below the room temperature (300 K) which can enhance its significance in the sense of practical applications [3, 14, 31].

In this work, we have prepared a series of $\text{Ni}_{50}\text{Mn}_{36.5}\text{Sn}_{13.5}$ alloy by varying the annealing time and studied their structural properties, EB and MCE [32]. EB is present in all the samples and found to increase with increasing the annealing time. ΔS_M has the maximum value for 24 h annealed sample but, the sample that annealed for 12 h shows the largest net RC among the others.

4.2. Experimental

Ni-rich $\text{Ni}_{50}\text{Mn}_{36.5}\text{Sn}_{13.5}$ alloy was prepared by conventional arc melting technique under 4N purity (99.99%) argon atmosphere. The ingot was turned and re-melted several times (at least seven to eight times) to ensure its homogeneity. The as prepared sample (sample A) was cut into five pieces and their starting compositions were checked by energy-dispersive spectroscopy (EDS) which indicated the uniformity of the sample. One of the five pieces was kept as cast sample and named as sample A. Rest of the four pieces were wrapped separately in Ta foil. Each of the wrapped pieces was sealed separately in highly evacuated quartz ampoules for annealing. These pieces were annealed at 1173 K for different time duration: 6 h (sample B), 12 h (sample C), 18 h (sample D) and 24 h (sample E) (see table 4.1). After annealing at 1173 K, the ampoules were quenched in ice water.

The final compositions were reconfirmed for all the samples (after annealing) by EDS and found the same as the starting compositions of all the pieces (before annealing). X-ray diffraction patterns were carried out at laboratory temperature (295 K) in Rigaku MiniFlex II using $\text{Cu-K}\alpha$ radiation in order to determine the crystallographic parent phase. Thermal measurements were done in DSC 2000 with a scan rate of 5 K/min. AC magnetic measurements of these samples were measured in a self-fabricated ac susceptibility setup. DC Magnetic measurements were performed using a VSM (Lake Shore, 7144) up to a field of 15 kOe. The heating and cooling rates during all the temperature dependent magnetic measurements were maintained at 1 K/min. The same preparation technique and measurements were performed on a different ingot with the same composition and the obtained data were found to be repeatable.

4.3. Results and discussions

4.3.1. Structural characterization and phase transition

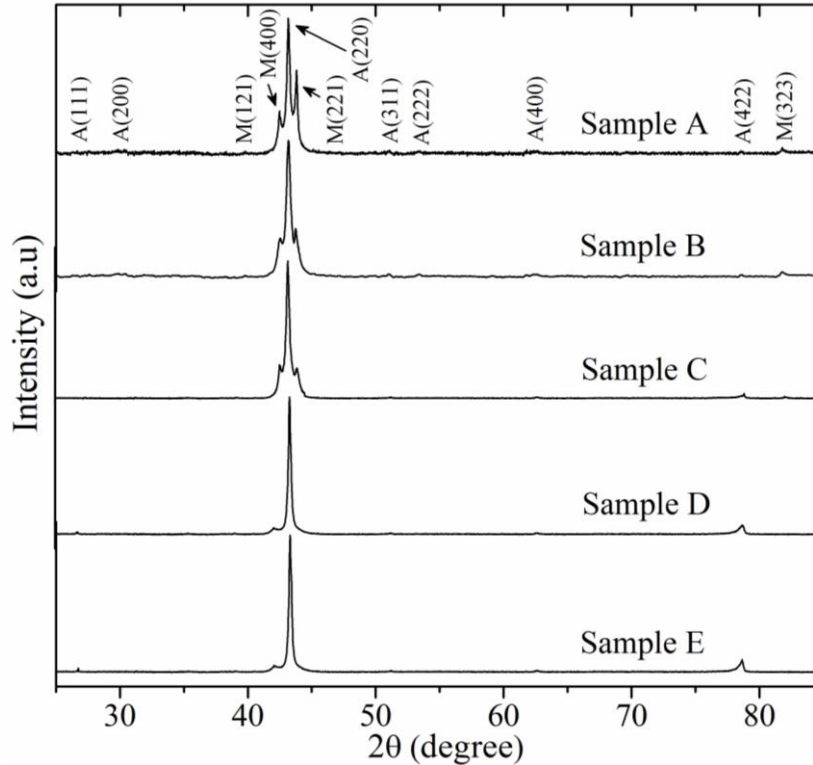


Fig. 4.1: Room temperature XRD patterns for $\text{Ni}_{50}\text{Mn}_{36.5}\text{Sn}_{13.5}$ alloys. Peak identification: 'A' for the austenite and 'M' for the martensite phase.

Fig. 4.1 shows the room temperature XRD patterns for $\text{Ni}_{50}\text{Mn}_{36.5}\text{Sn}_{13.5}$ alloy annealed for different times. The samples' name according to their annealing times is given in table 4.1. It can be seen that the main peak of the as cast alloy (sample A) is splitted in three peaks. (220) is for the cubic austenite but, (400) and (221) peaks are for the tetragonal martensite phase. The sample is thus found to be in a mixed martensite-austenite phase. The fraction of the martensite phase decreases and the cubic austenite phase becomes dominated as the time duration for heat treatment increases. The phase ratio of austenite and martensite phases has been estimated by fitting the multiple peaks and then comparing their relative intensities (see table 4.1). The superlattice diffraction peak (111) in the XRD patterns of sample D and E indicates that the atomic ordering increases as the samples are annealed for more times [15]. During annealing, the material removes stress and the atoms start to sit in

their proper sites. A relative ordering factor can be defined by taking the ratio of the intensities between (111) and (220) peaks. Although, it is impossible to achieve 100% atomic ordering experimentally, the sample annealed for 24 h (sample E) can be assumed as the maximally ordered sample. Therefore, the as cast sample (sample A) is counted as completely disordered, samples B, C and D as partially ordered and sample E as completely ordered.

Table 4.1: Name of the samples according to the duration of annealing, fractions of martensite and austenite phases present at room temperature.

Annealing time (h)	Samples' name	% of martensite phase	% of austenite phase
0	A	32	68
6	B	24.2	75.8
12	C	18.7	81.3
18	D	6.5	93.5
24	E	4.8	95.2

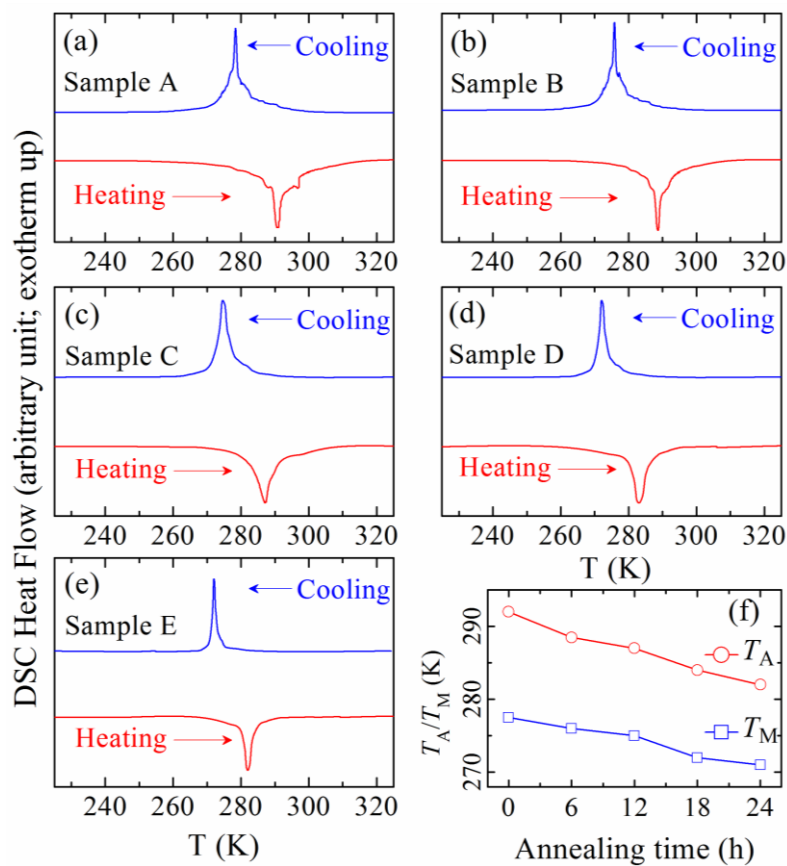


Fig. 4.2: Temperature dependence of DSC heat flow for (a) sample A, (b) sample B, (c) sample C, (d) sample D and (e) sample E. (f) Annealing time dependence of structural transition temperatures.

Figs. 4.2(a-e) show the normalized DSC heat flow vs temperature curves during heating and cooling for all the samples within the temperatures between 225 K and 325 K. The endothermic peaks during heating represent the transition from martensite to austenite structure of these samples and the exothermic peaks during cooling predict the reverse transition from austenite to the martensite. The width of the DSC heat flow peaks decreases with the increase in annealing time. This gives an indication about the increasing sharpness of the structural transition. The shift in the peaks' position towards the lower temperature with increasing the heat treatment duration is almost 10 K for heating curves (between sample A and sample E). But the same is only ~ 6 K during cooling. T_A and T_M are plotted in Fig. 4.2(f) against the annealing time. The curves indicate that the structural transition point shifts systematically towards the lower temperature with increasing the annealing time but, not similar for the forward and reverse transition. This may lead to a decrease in thermal hysteresis which is discussed in the next sub-subsection of this chapter.

Table 4.2: Characteristic transition temperatures of $\text{Ni}_{50}\text{Mn}_{36.5}\text{Sn}_{13.5}$ alloy annealed for different times. The maximum possible error is ± 3 K.

Sample	A_S (K)	A_f (K)	T_A (K)	M_S (K)	M_f (K)	T_M (K)	ΔT_{hys} (K)	ΔT (K)	T_C^A (K)
A	280	304	292	295	260	277.5	14.5	24	310
B	277	300	288.5	289	263	276	12.5	23	312
C	276	298	287	285	265	275	12	22	316
D	276	292	284	280	264	272	12	16	319
E	276	288	282	275	263	271	11	12	320

4.3.2. Temperature dependent magnetic properties

The real part of ac susceptibility as a function of temperature is plotted in Figs. 4.3(a-e) for all the samples within the temperatures between 80 K and 310 K. All the samples show the existence of a magnetic transition near 280 K accompanying thermal hysteresis between heating and cooling data. These transition temperatures match well with the DSC heat flow peaks. It confirms that the aforementioned phase transition is a magneto-structural transition of these samples from a low temperature

weakly magnetic martensite phase to a magnetically more sensitive austenite phase. There is a hump near 250 K in the curves and it becomes prominent with increasing the annealing time for $\text{Ni}_{50}\text{Mn}_{36.5}\text{Sn}_{13.5}$ alloy. This is the signature of T_C^M . Fig. 4.3(f) represents the annealing time dependence of thermal hysteresis and transition width of the martensitic transition. Both of them decrease with the increase in the duration of annealing which is discussed in the next paragraph also.

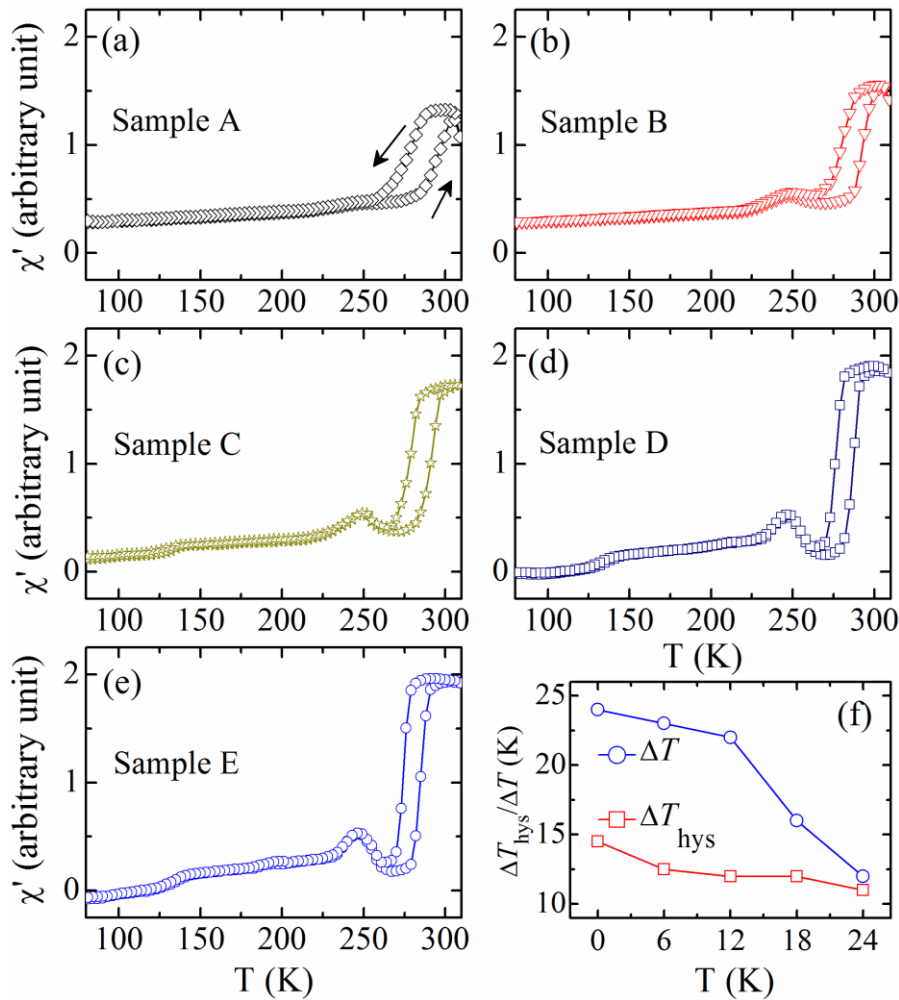


Fig. 4.3: Temperature dependence of the real part of ac susceptibility at 1024 Hz for (a) sample A, (b) sample B, (c) sample C, (d) sample D and (e) sample E. (f) Thermal hysteresis and transition width across the martensitic transition of $\text{Ni}_{50}\text{Mn}_{36.5}\text{Sn}_{13.5}$ alloy as a function of the annealing time.

The temperature dependence of magnetization (M - T curves) is also carried out for these samples in order to investigate the effect of annealing on the structural and magnetic properties of $\text{Ni}_{50}\text{Mn}_{36.5}\text{Sn}_{13.5}$ alloy. Figs. 4.4(a-e) show the M - T curves for all the samples within the temperatures between 80 K and 400 K in the presence of

100 Oe field. By following the ZFC curves of these samples, a martensite to austenite phase transition can be observed within 270 K to 300 K where the magnetization increases rapidly with increasing the temperature (also confirmed from the DSC heat flow and ac susceptibility data (Figs. 4.2(a-e) and Figs. 4.3(a-e))). The reverse phase transition can be found by following the FC curves of the same samples.

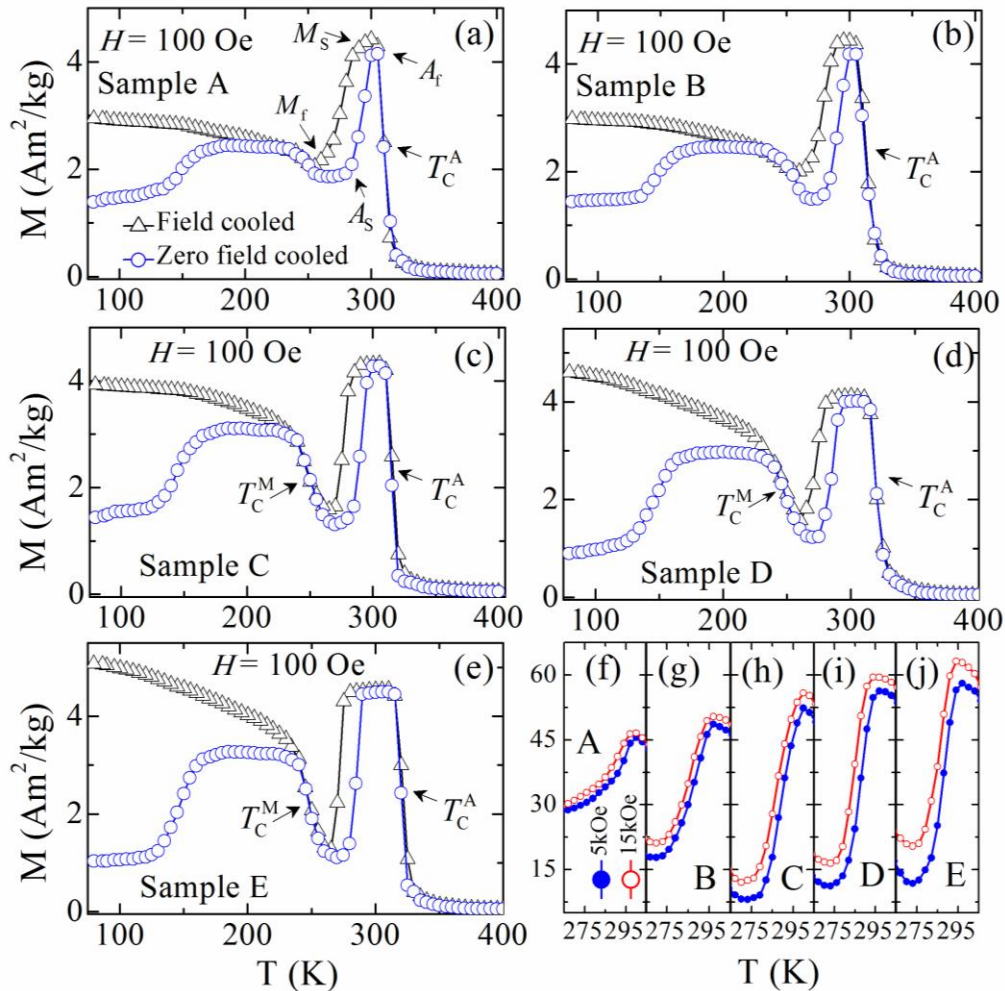


Fig. 4.4: Temperature dependence of magnetization (M - T curves) for (a) sample A, (b) sample B, (c) sample C, (d) sample D and (e) sample E in the presence of 100 Oe field. ZFC M - T curves of (f) sample A, (g) sample B, (h) sample C, (i) sample D and (j) sample E under 5 kOe and 15 kOe field.

The characteristic transition temperatures: A_S , A_f , T_A , M_S , M_f and T_M are given in table 4.2 and some of them are also indicated in the M - T curves (Fig. 4.4(a-e)). A sharp change in the magnetization is observed from all the samples within the temperatures between 300 K and 325 K, which is due to a ferro-para transition at T_C^A . The thermal hysteresis decreases with the increase in annealing time of

$\text{Ni}_{50}\text{Mn}_{36.5}\text{Sn}_{13.5}$ alloy. The transition width is also found to decrease with increasing the duration of heat treatment. The T_C^M appears clearly as the samples are annealed for higher times. This is because of the increase in the Mn-Mn inter-site interaction due to the increase in atomic ordering during heat treatment process which is discussed later in detail in this chapter.

In the temperatures below 200 K, A magnetically inhomogeneous phase is found to present in these alloys and is a possible indication of EB effect which is thought to originate from the interfacial exchange interaction between the spins of ferromagnetic and antiferromagnetic layers [7, 8]. The step like nature in the ZFC M - T curves increases with the increase of annealing time. This can be attributed to the formation of ordered interface which enhances the ferro-antiferro exchange coupling.

Figs. 4.4(f-j) show the ZFC M - T curves in the presence of 5 kOe and 15 kOe magnetic field. In the case of disordered sample (sample A), the magnetic response is very low during the structural phase transition in the presence of high magnetic field. The change in magnetization during the structural phase transition increases for the annealed samples. The field induced shift of structural transition is found to present in all the samples. It increases with the increase of the structural ordering. The annealing causes an increase in atomic ordering and the magnetocrystalline anisotropy also increases with it. When a high magnetic field is applied to these samples, their modulated multi-variant martensite structure move with the magnetic moments and tries to align along the direction of applied magnetic field and as a result, single variant is formed. Therefore, $|\Delta T/\Delta H|$ increases with the increase in atomic ordering due to the enhancement in coupling between the spins and the structure.

4.3.3. Exchange bias

Figs. 4.5(a-e) show the magnetic hysteresis loops for sample A, B, C, D and E at 80 K. The data have been taken after cooling these samples from 350 K (above their T_C^A) to 80 K in the presence of 10 kOe field [27]. The field sweeping is done as follows: 10 kOe \rightarrow 0 \rightarrow -10 kOe \rightarrow 0 \rightarrow 10 kOe. A small but finite shift in the

hysteresis loops is present in all the samples which proves the existence of EB in $\text{Ni}_{50}\text{Mn}_{36.5}\text{Sn}_{13.5}$ alloy [7, 8, 29]. Fig. 4.5(f) shows the annealing time dependence of H_{EB} and H_C of these samples at 80 K. The H_{EB} increases and H_C decrease with the increase of the duration of annealing. This may be ascribed to the change in the exchange coupling between the ferromagnetic and antiferromagnetic layers due to the annealing. The samples undergo a structural relaxation and the growths of grain size during the annealing period, which modify the degree of atomic order also. This may create more Mn-Mn inter-site pair and decrease the distance between them. Therefore, the antiferromagnetic correlation dominates across the interfaces which enhance the ferro-antiferro coupling to a significant extent [25].

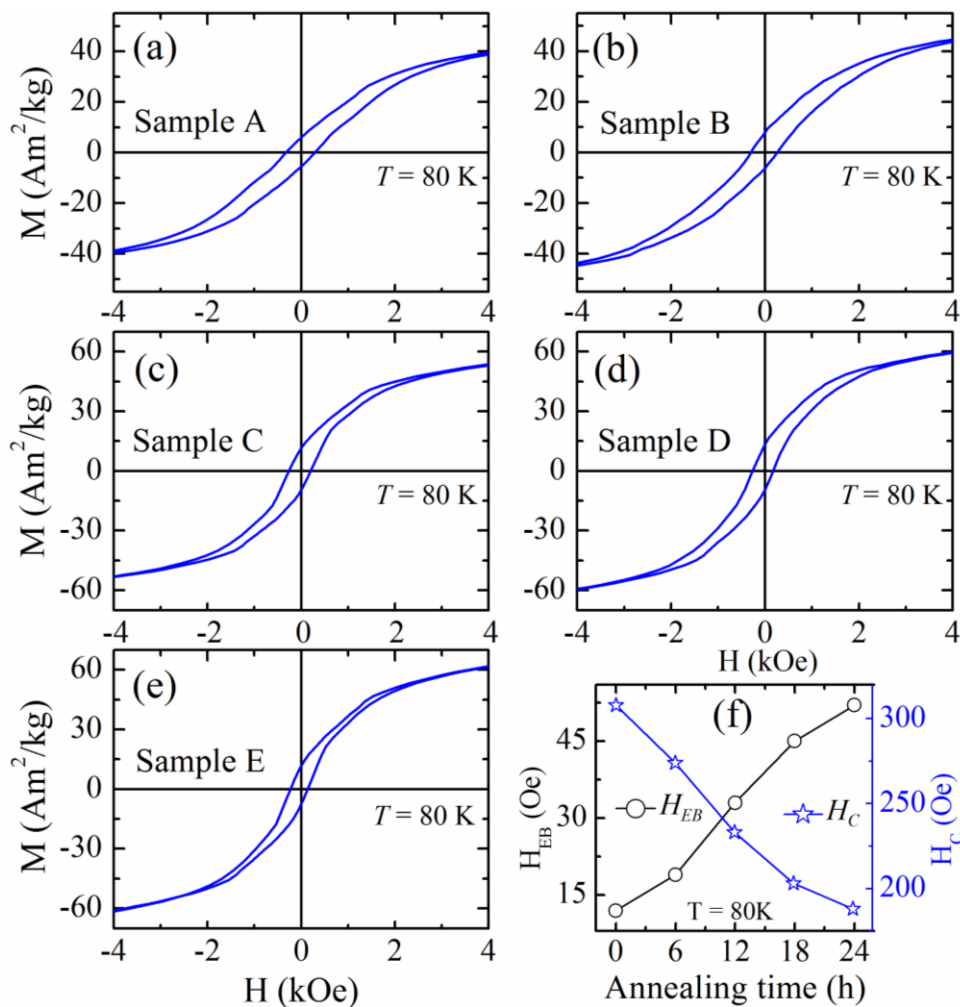


Fig. 4.5: Magnetic hysteresis loops for (a) sample A, (b) sample B, (c) sample C, (d) sample D and (e) sample E at 80 K measured after a FC under 10 kOe field. (f) The annealing time dependence of the exchange bias field and coercive field for $\text{Ni}_{50}\text{Mn}_{36.5}\text{Sn}_{13.5}$ alloy at 80 K.

4.3.4. Field dependent magnetic properties

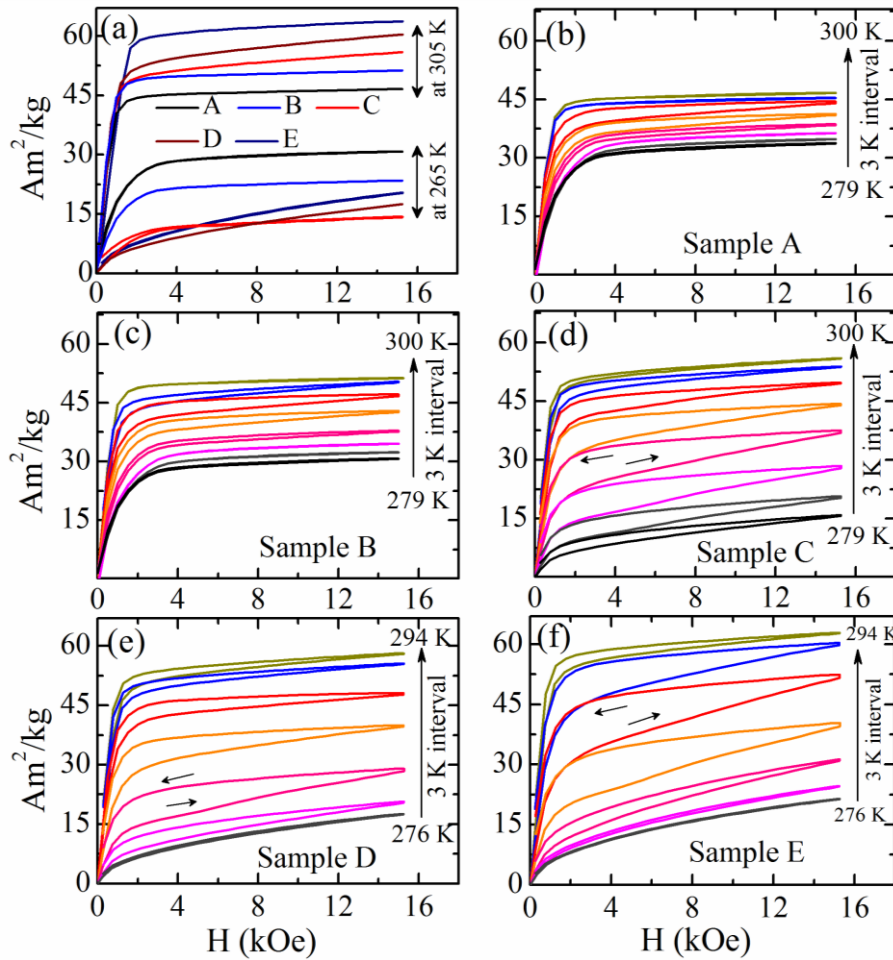


Fig. 4.6: (a) M - H curves for all the samples at 265 K and 305 K. M - H curves for (b) sample A, (c) sample B, (d) sample C, (e) sample D and (f) sample E in the vicinity of martensite-austenite phase transition.

The M - H curves at 265 K and 305 K for $\text{Ni}_{50}\text{Mn}_{36.5}\text{Sn}_{13.5}$ alloy annealed for different times are shown in Fig. 4.6(a). The field sweeping is done as follows: $0 \rightarrow 15$ kOe. The saturation magnetization (M_{sat}) in the austenite phase (at 305 K) is the maximum for the sample E. One can notice that unlike the austenite phase, the M_{sat} in the martensite phase (at 265 K) is the maximum for sample A (see table 4.3). It is also evident that the samples become paramagnetic like in the martensite phase as they are annealed for the longer time (Fig. 4.6(a) and the appearance of T_C^M in Figs. 4.4(c-e)) [25].

The heat treatment process affects the magnetic properties of both the structural phases to a significant extent. This can be explained in the context of varying

magnetic correlations in these alloy systems in different structural phases. The two Mn atoms, one from the regular Mn site and another from the Sn site order ferromagnetically in the austenite phase [33]. The increase in annealing time causes an increase in the ordering of the Mn atoms to their respective proper sites and as a result, the ferromagnetic correlation increases. The inter site Mn-Mn separation decreases as the structure of these materials transforms from austenite to martensite on cooling and antiferromagnetic interaction starts to increase. This aforementioned interaction increases as the Mn atoms in the Sn site increases. The complete structural ordering corresponds to the 25 Mn atoms (out of a total of 100 atoms including Ni, Mn and Sn) occupying the regular Mn site and the rest of the Mn atoms occupying the Sn site and it provides a maximum antiferromagnetic interaction between the Mn atoms sitting at the two different sites. The paramagnetic like $M-H$ curve for the sample D and E at 265 K indicates a very similar aspect as mentioned earlier (Fig. 4.6(a)).

Table 4.3: Saturation magnetization at 305 K, 265 K and magnetocaloric parameters for $\text{Ni}_{50}\text{Mn}_{36.5}\text{Sn}_{13.5}$ alloy.

Sample	$M_{\text{sat}}^{305\text{ K}}$ (Am ² /kg)	$M_{\text{sat}}^{265\text{ K}}$ (Am ² /kg)	ΔS_{M} (J/kg K)	RC (J/kg)	HL _{avg} (J/kg)	Net RC (J/kg)
A	46.6	30.79	1.7	18.24	2.92	15.32
B	51.32	23.5	3	25.24	4.1	21.14
C	55.9	14.38	4.23	41.97	6.46	35.51
D	60.4	17.54	4.91	38.86	9.15	29.71
E	63.7	20.34	5.15	37.14	9.84	27.3

Figs. 4.6(b-f) show the magnetic isotherms ($M-H$ curves) for sample A, B, C, D and E in the vicinity of their structural phase transition point. The field sweeping is done as follows: $0 \rightarrow 15 \text{ kOe} \rightarrow 0$. Before taking an $M-H$ curve, the sample was first cooled to 150 K (far below from the samples' structural transition temperature) in zero field and then heated back to the desired temperature to take data. After this, the sample was again cooled to 150 K in zero field and then heated back to the next desired temperature. In our case it was 3 K higher than the previous temperature.

This convention has been followed for all the M - H curves across the martensitic transition of all the samples. This measurement method is known as discontinuous heating protocol [34, 35]. Across any field induced transition, the structure of a sample is modified due to the application of high magnetic field. The structure does not completely come back to its initial state after the removal of field. So, a history of the sample's phase can affect the next M - H curve which will be taken by increasing the temperature; say +3 K (in our case). This can overestimate the values of MCE as calculated from these M - H curves. By using the aforementioned discontinuous heating protocol, we can solve this problem and get history independent isothermal M - H curves across any field induced transition. Field induced magnetic hysteresis is observed in all the samples which increase with increasing the annealing time. The difference between the M_{sat} of two consecutive M - H curves across the martensitic transition increases with the increase in the duration of annealing. This may give rise to the ΔS_{M} of the annealed samples.

4.3.5. Magnetocaloric properties

ΔS_{M} of all the samples has been estimated using Maxwell's thermodynamic relation (equation 1.18) [3]. The temperature dependence of ΔS_{M} for the sample A, B, C, D and E are plotted in Figs. 4.7(a-e). A maximum $\Delta S_{\text{M}} \sim 5.15$ J/kg K is obtained in the sample E at ~ 285 K due to a field change of only 15 kOe (see table 4.3). As compared to other samples, the larger values of ΔS_{M} for the sample D and E originate from the sharp change in magnetization during the structural transition.

RC of the materials has been calculated by integrating the $\Delta S_{\text{M}}-T$ curves within the lower and upper temperatures of the FWHM of the $\Delta S_{\text{M}}-T$ peak (equation 1.20). The value of RC for the sample C is the maximum among them (42 J/kg). In order to find out the actual magnetocaloric potential of these samples we have calculated the average losses due to the field induced hysteresis. Incorporating this, a net RC ~ 35.5 J/kg is obtained for the sample C (see table 4.3). Fig. 4.7(f) shows the dependence of ΔS_{M} and net RC of $\text{Ni}_{50}\text{Mn}_{36.5}\text{Sn}_{13.5}$ alloy on the annealing time. The values of ΔS_{M} and net RC are comparable with the results reported in the literature for the similar compositions which were annealed for similar times [14, 15, 29, 30].

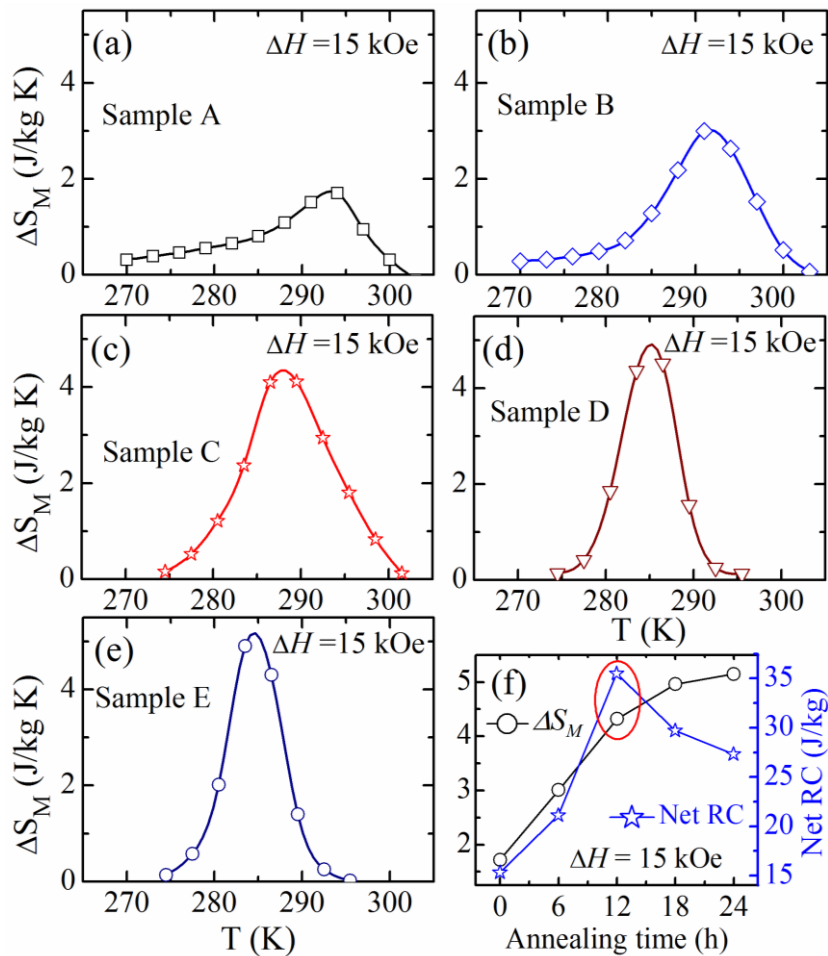


Fig. 4.7: Isothermal magnetic entropy change as a function of temperature for (a) sample A, (b) sample B, (c) sample C, (d) sample D and (e) sample E due to 15 kOe field change. (f) The annealing time dependence of ΔS_M and net RC for $\text{Ni}_{50}\text{Mn}_{36.5}\text{Sn}_{13.5}$ alloy under the same field change.

One can notice that the ΔS_M increases in a nonlinear way with the increase of annealing time and nearly saturates after 18 h but, the net RC has a peak value at the annealing time of 12 h and decreases on the both sides of increasing and decreasing the duration of annealing. There is always a competition between the values of ΔS_M and RC of a MCE material. A sharp phase transition accompanying large changes in magnetization is favorable for getting large ΔS_M . But, the experimental aspect of MCE demands that the value of ΔS_M should be high and its corresponding temperature dependence peak should be broad enough so that the same material can be used within a wide temperature range and can extract a large amount of heat from the environment that needs to cool. In the sample that annealed for 12 h (sample C), these aforementioned properties exist with satisfactorily larger values as

compared to others. This indicates that the partially disordered materials like sample C can be a better magnetic refrigerant.

4.4. Conclusions

In summary, we have systematically investigated the structural, magnetic and magnetocaloric properties of an off-stoichiometric Ni-Mn-Sn Heusler alloy by varying its annealing time. The atomic ordering increases due to the heat treatment. The exchange bias effect gets improved with the increase of the duration of annealing. The magnetic properties of $\text{Ni}_{50}\text{Mn}_{36.5}\text{Sn}_{13.5}$ change considerably due to the increase in structural ordering. In the martensite phase, strong antiferromagnetic interaction has been achieved by annealing. In case of the austenite phase, a strong ferromagnetic correlation is restored. Although, the ΔS_M is found to increase with increasing the annealing time from 0 to 24 h, the RC for the 12 h annealed sample is the maximum among the others which is due to an affordable value of ΔS_M and a broad transition width at the martensitic phase transition. Finally, one conclusion can be drawn that up to a certain degree of disorder can provide a better magnetic cooling as compared to the ordered one.

Bibliography

- [1] P. J. Shamberger and F. S. Ohuchi, *Phys. Rev. B* 79, 144407 (2009).
 - [2] B. Hernando, J. L. S. Lamazares, J. D. Santos, V. M. Prida, D. Baldomir, D. Serantes, R. Varga and J. González, *Appl. Phys. Lett.* 92, 132507 (2008).
 - [3] A. Planes, L. Manosa and M. Acet, *J. Phys.: Condens. Matter* 21, 233201 (2009).
 - [4] V. D. Buchelnikov and V. V. Sokolovskiy, *Phys. Met. Metallog.* 112, 633 (2011).
 - [5] H. C. Xuan, Y. Deng, D. H. Wang, C. L. Zhang, Z. D. Han and Y. W. Du, *J. Phys. D: Appl. Phys.* 41, 215002 (2008).
 - [6] K. Koyama, H. Okada, K. Watanabe, T. Kanomata, R. Kainuma, W. Ito, K. Oikawa and K. Ishida, *Appl. Phys. Lett.* 89, 182510 (2006).
 - [7] M. Wang, Y. Liu, B. Xia, P. Ren and L. Wang, *J. Appl. Phys.* 111, 043912 (2012).
 - [8] S. Giri, M. Patra and S. Majumdar, *J. Phys.: Condens. Matter* 23, 073201 (2011).
 - [9] B. Zhang and X. X. Zhang, S. Y. Yu, J. L. Chen, Z. X. Cao and G. H. Wu, *Appl. Phys. Lett.* 91, 012510 (2007).
 - [10] Y. K. Kuo, K. M. Sivakumar, H. C. Chen, J. H. Su and C. S. Lue, *Phys. Rev. B* 72, 054116 (2005).
 - [11] K. Ullakko, J. K. Huang, C. Kantner, R. C. O'Handley, and V. V. Kokorin, *Appl. Phys. Lett.* 69, 1966 (1996).
 - [12] K. Ullakko, J. K. Huang, V. V. Kokorin and R. C. O'Handley, *Scripta Mater.* 36, 1133 (1997).
 - [13] B. F. Yu, Q. Gao, B. Zhang, X. Z. Meng and Z. Chen, *Int. J. Refrig.* 26, 622 (2003).
 - [14] T. Krenke, E. Duman, M. Acet, E. F. Wassermann, X. Moya, L. Manosa, and A. Planes, *Nature Mater.* 4, 450 (2005).
 - [15] S. E. Muthu, N. V. R. Rao, M. M. Raja, D. M. R. Kumar, D. M. Radheep and S. Arumugam, *J. Phys. D: Appl. Phys.* 43, 425002 (2010).
 - [16] K. A. Gschneidner Jr., V. K. Pecharsky and A. O. Tsokol, *Rep. Prog. Phys.* 68, 1479 (2005).
 - [17] M. H. Phan and S. C. Yu, *J. Magn. Magn. Mater.* 308, 325 (2007).
 - [18] V. K. Pecharsky, K. A. Gschneidner Jr., *Phys. Rev. Lett.* 78, 4494 (1997).
-

-
- [19] B. G. Shen,* J. R. Sun, F. X. Hu, H. W. Zhang, and Z. H. Cheng, *Adv. Mater.* 21, 4545, (2009).
- [20] A. Ayuela, J. Enkovaara, K. Ullakko and R. M. Nieminen, *J. Phys. Condens. Matt.* 11, 2017 (1999).
- [21] R. B. Helmholdt and K. H. J. Buschow, *J. Less Common Metals* 128, 167 (1987).
- [22] V. Sa´nchez-Alarcos, V. Recarte, J. I. Pe´rez-Landaza´bala and G. J. Cuello, *Acta Mater.* 55, 3883 (2007).
- [23] S. Li, Z. Yuan, L. Y. L`u, M. Liu, Z. Huanga, F. Zhang and Y. Dub, *Mater. Sci. Engg.: A* 428, 332 (2006).
- [24] W. Ito, M. Nagasako, R. Y. Umetsu, R. Kainuma, T. Kanomata and K. Ishida, *Appl. Phys. Lett.* 93, 232503 (2008).
- [25] X. G. Zhao, C. C. Hsieh, J. H. Lai, X. J. Cheng, W. C. Chang, W. B. Cui, W. Liu and Z. D. Zhang, *Scripta Mater.* 63, 250 (2010).
- [26] V. V. Sokolovskiy, V. D. Buchelnikov, M. A. Zagrebin, P. Entel, S. Sahoo and M. Ogura, *Phys. Rev. B* 86, 134418 (2012).
- [27] B. Gao, F. X. Hu, J. Shen, J. Wang, J. R. Sun and B. G. Shen, *J. Magn. Magn. Mater.* 321, 2571 (2009).
- [28] T. Krenke, E. Duman, M. Acetc, X. Moya, L. Mañosa and A. Planes, *J. Appl. Phys.* 102, 033903 (2007).
- [29] A. Ghosh and K. Mandal, *J. Alloys Compd.* 579, 295 (2013).
- [30] A. Ghosh and K. Mandal, *Eur. Phys. J. B* 86, 378 (2013).
- [31] Z. Li, C. Jing, J. Chen, S. Yuan, S. Cao and J. Zhang, *Appl. Phys. Lett.* 91, 112505 (2007).
- [32] A. Ghosh and K. Mandal, *Appl. Phys. Lett.* 104, 031905 (2014).
- [33] S. Aksoy, M. Acet, P. P. Deen, L. Mañosa and A. Planes, *Phys. Rev. B* 79, 212401 (2009).
- [34] L. Caron, Z. Q. Ou, T. T. Nguyen, D. T. C. Thanh, O. Tegus and E. Bruck, *J. Magn. Magn. Mater.* 321, 3559 (2009).
- [35] G. J. Liu, J. R. Sun, J. Shen, B. Gao, H. W. Zhang, F. X. Hu and B. G. Shen, *Appl. Phys. Lett.* 90, 032507 (2007).
-

Chapter 5

Magnetocaloric and magneto-transport properties of Mn-rich Mn-Ni-Sn and Mn-Fe-Ni-Sn off-stoichiometric Heusler alloys

In this chapter we have investigated the structural phase transition, magnetocaloric properties and magnetoresistance in Mn-rich Mn-Ni-Sn alloys. In this context, we have varied Mn/Sn concentration and substituted Fe independently in the place of both Ni and Mn.

5.1. Preamble

Ni-rich (Ni ~ 50 at%) Ni-Mn-Sn off-stoichiometric Heusler alloys have drawn considerable attention of the research community during the last decade due to their interesting and valuable multifunctional properties like MCE [1-5] and MR [6, 7]. These properties are mainly associated with a martensitic transition which involves structural as well as magnetic changes in these alloys (henceforth termed as magneto-structural transition). This magneto-structural transition is a first order phase transition from cubic austenite to a modulated or tetragonal martensite phase [1-7]. A ΔS_M of 20 J/kg K was reported in Ni₅₀Mn₃₇Sn₁₃ alloys by Krenke *et al* under a magnetic field change of 50 kOe [8]. Koyama *et al* found ~ 50 % MR in Ni₅₀Mn₃₆Sn₁₄ alloy under a field change of 170 kOe [7].

Large values of ΔS_M in these alloys were reported extensively by many researchers by varying the Ni/Mn [5, 9], Mn/Sn [8] ratios and by replacing Ni with Co/Fe [10, 11]. A maximum ΔS_M ~ 35 J/kg K was obtained in this way under a field change of 50 kOe [10]. Some of the works are also reported in the literature those are based on the tuning of magnetocaloric properties in these materials by changing the heat treatment parameters also [12-14]. The core findings of these reports suggest that the magnetocaloric potentials (ΔS_M and net RC) of Ni-Mn-Sn alloys can be enhanced to a significant extent by increasing the at% of Mn-content [5, 8, 9]. Thus, Mn-rich Mn-Ni-Sn off-stoichiometric alloy series is desired to be a better magnetocaloric candidate where Mn is taken around 50 at%.

The stoichiometric Mn₂NiZ (Z = Ga, In, Sn and Sb) alloys have Hg₂CuTi-type cubic structure [15-17]. Mn atoms occupy (0, 0, 0) octahedral and (1/4, 1/4, 1/4) tetrahedral sites and the remaining (1/2, 1/2, 1/2) and (3/4, 3/4, 3/4) sites are occupied by Ni and Z respectively. If the stoichiometry is broken, then excess Ni occupies the partially vacant Sn site. The Mn-Mn inter-site interaction takes the leading control in these Heusler alloys to vary their magnetic properties. For such Mn-rich system, the number of inter-site Mn-Mn pair is the maximum and this may give rise to a significant change in the properties that depend on the magnetic correlations.

The existence of martensitic and magnetic transitions in Mn_2NiSn alloys has been predicted theoretically by Paul *et al* [18]. Ma *et al* [19] did an experimental investigation on Mn-rich $\text{Mn}_{50}\text{Ni}_{50-x}\text{Sn}_x$ alloys by varying the composition from $x = 0$ to 11. They reported a systematic decrease in temperature of martensitic transition with increasing the Sn content. A ferromagnetic austenite phase was available for $x \geq 9$. Large magnetization differences between the austenite and martensite phase were reported for these alloys which may give rise to large ΔS_M values also [19, 20]. These alloys possibly consume less energy as compared to Ni-rich Ni-Mn-Sn alloys due to their smaller thermal hysteresis at the FOMST.

Till date, a few investigations have been done on Mn rich Mn-Ni-Sn alloys by varying the Ni/Sn and the Mn/Ni ratios or substituting Co in the place of Ni, and some of them reported large ΔS_M and MR also [19-22]. However, the dependence of the martensitic transition temperature on the Mn/Sn concentration ratio of these alloys and its corresponding ΔS_M and MR values associated with their FOMST still need more investigation. Along with this, the substitution of Fe in the place of Ni and Mn can significantly change the magnetic correlations of these alloy family which may enhance ΔS_M the also. It is also necessary to verify their net RC after incorporating the hysteresis losses due to the FIMST to estimate their actual potential as a refrigerant material [23].

In the previous two chapters, we investigated the Ni-rich Ni-Mn-Sn alloys. Firstly, we were able to increase the ΔS_M of these alloys by introducing Co in the place of Ni [24, 25]. But, there was an issue with the net RC which starts to fall for higher doping concentration. However, we were able to achieve a very large MR along with partial kinetic arrest in a highly doped alloy. After that we tried to optimize the magnetocaloric parameters of these alloys by tuning the structural ordering with heat treatment process [26]. In both the cases, the effect of field induced hysteresis and large thermal hysteresis had a noticeable impact on affecting the MCE. Considering all these facts and some recent reports, we found that Mn-rich Mn_2NiSn off-stoichiometric Heusler alloys may come out as an effective MCE material which can solve the aforementioned problems [9, 18-20, 24-26]. Therefore,

we have chosen this Mn-rich system in this chapter for further study to improve the MCE in similar alloy family.

In this chapter, we have studied the martensitic and magnetic phase transitions of Mn-rich Mn-Ni-Sn alloys and reported large MCE in them. Firstly, we have prepared Mn-rich $\text{Mn}_{50.5-x}\text{Ni}_{41}\text{Sn}_{8.5-x}$ alloys and studied their martensitic transition, ΔS_M and MR by varying the Mn/Sn ratio [27]. We obtained a very large value of MCE in these alloys as compared to Ni-rich similar materials. A moderate value of MR is also available from these Mn-rich alloys. Next, we doped this Mn-rich system with Fe independently in the place of Ni and Mn ($\text{Mn}_{50}\text{Ni}_{40.5-y}\text{Fe}_y\text{Sn}_{9.5}$ and $\text{Mn}_{50-z}\text{Fe}_z\text{Ni}_{39.5}\text{Sn}_{10.5}$) and obtained large MCE with a significant enhancement in net RC as compared to the undoped alloys [28]. However, the enhancement in the MCE parameters was limited only in the lower level of Fe doping.

5.2. Experimental

Mn-rich $\text{Mn}_{50.5-x}\text{Ni}_{41}\text{Sn}_{8.5+x}$ ($x = 0, 1$ and 2), Mn-rich Fe-doped $\text{Mn}_{50}\text{Ni}_{40.5-y}\text{Fe}_y\text{Sn}_{9.5}$ ($y = 0, 1, 2, 3$ and 4) and $\text{Mn}_{50-z}\text{Fe}_z\text{Ni}_{39.5}\text{Sn}_{10.5}$ ($z = 0, 1, 2, 3, 4, 5$ and 6) alloys were prepared by conventional arc melting technique under 4N purity (99.99%) argon atmosphere. The ingots were turned and re-melted several times (at least seven to eight times) to ensure their homogeneity. All the ingots were wrapped separately in Ta foil. Each of them was sealed separately in highly evacuated quartz ampoules for annealing. After annealing at 1173 K for 24 h, the ampoules were quenched in ice water. The final compositions were confirmed for all the samples by EDS. X-ray diffraction patterns were carried out at laboratory temperature (295 K) in Rigaku MiniFlex II using Cu-K_α radiation in order to determine the crystallographic parent phase. AC magnetic measurements of these samples were measured in a self-fabricated ac susceptibility setup. DC Magnetic measurements were performed using a VSM (Lake Shore, 7144) up to a field of 16 kOe. Magneto-transport properties were measured in PPMS (Cryogenic Limited) up to 80 kOe field. The heating and cooling rates during all the temperature dependent magnetic and magneto-transport measurements were maintained at 1 K/min.

5.3. Results and discussions

5.3.1. Martensitic transition in Mn-rich $\text{Mn}_{50.5-x}\text{Ni}_{41}\text{Sn}_{8.5+x}$ alloys and its associated MCE and MR

5.3.1.1. Structural characterization

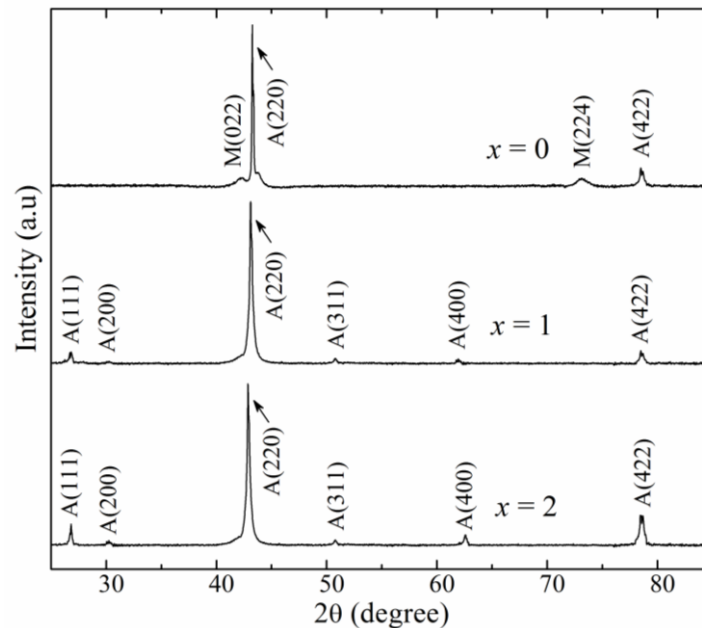


Fig. 5.1: Room temperature XRD patterns for $\text{Mn}_{50.5-x}\text{Ni}_{41}\text{Sn}_{8.5+x}$ alloys. Peak identification: 'A' for the austenite and 'M' for the martensite phase.

Fig. 5.1 shows the room temperature XRD patterns for the Mn-rich $\text{Mn}_{50.5-x}\text{Ni}_{41}\text{Sn}_{8.5+x}$ ($x = 0, 1$ and 2) alloys. For $x = 0$, the (022) and (224) peaks indicate that a very small fraction of martensite phase is present within the dominating cubic austenite phase [20]. The (220), (400) and (422) peaks for $x = 1$ and 2 confirm their Hg_2CuTi -type cubic austenite structure at room temperature. The (111), (200) and (311) super-lattice diffraction peaks suggest the existence of higher level atomic order in $x = 1$ and 2 [19, 20, 22]. The estimated values of the lattice parameter of the austenite phase are 0.5903 nm, 0.5929 nm and 0.5956 nm for $x = 0, 1$ and 2 respectively. Sn has larger atomic radius compared to that of Mn and Ni. Therefore, one can notice that the lattice parameter increases with increasing Sn-content in this alloy series. This may lead to a change in the inter-atomic spacing which in turn can alter the exchange interactions between the magnetic elements.

Table 5.1: Characteristic temperatures for $\text{Mn}_{50.5-x}\text{Ni}_{41}\text{Sn}_{8.5+x}$ alloys as confirmed from temperature dependent ac susceptibility, magnetization and resistivity data. The maximum possible error is ± 3 K.

x (at%)	A_S (K)	A_f (K)	T_A (K)	M_S (K)	M_f (K)	T_M (K)	ΔT_{hys} (K)	T_C^M (K)	T_C^A (K)
0	264	276	270	273	255	264	6	153	279
1	228	246	237	237	219	228	9	162	279
2	183	195	189	186	174	180	9	171	282

5.3.1.2. Temperature dependent magnetic properties

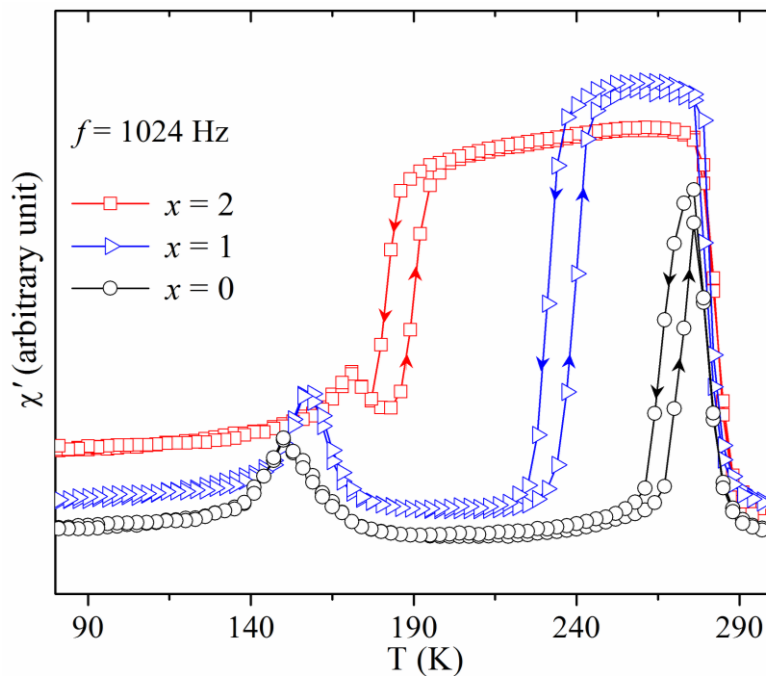


Fig. 5.2: Temperature dependence of real part of the ac susceptibility at 1024 Hz for $\text{Mn}_{50.5-x}\text{Ni}_{41}\text{Sn}_{8.5+x}$ alloys with $x = 0, 1$ and 2 .

The real part of ac susceptibility as a function of temperature is plotted in Fig. 5.2 for all the samples within the temperatures between 80 K and 300 K. All the samples show the existence of a magnetic transition at their respective T_C^A near 280 K. The existence of martensitic transition accompanying thermal hysteresis between heating and cooling data can be verified and its approximate temperatures are ~ 270 K, 230 K and 180 K respectively for the samples with $x = 0, 1$ and 2 . It is a magneto-structural transition of these types of samples from a low temperature paramagnetic like martensite phase to a magnetically more sensitive austenite phase. There is a

hump within 140 K and 180 K in the susceptibility data of all the samples which is due to their T_C^M . All these transitions have been confirmed from the dc magnetization measurements also which is discussed in the next part of this subsection.

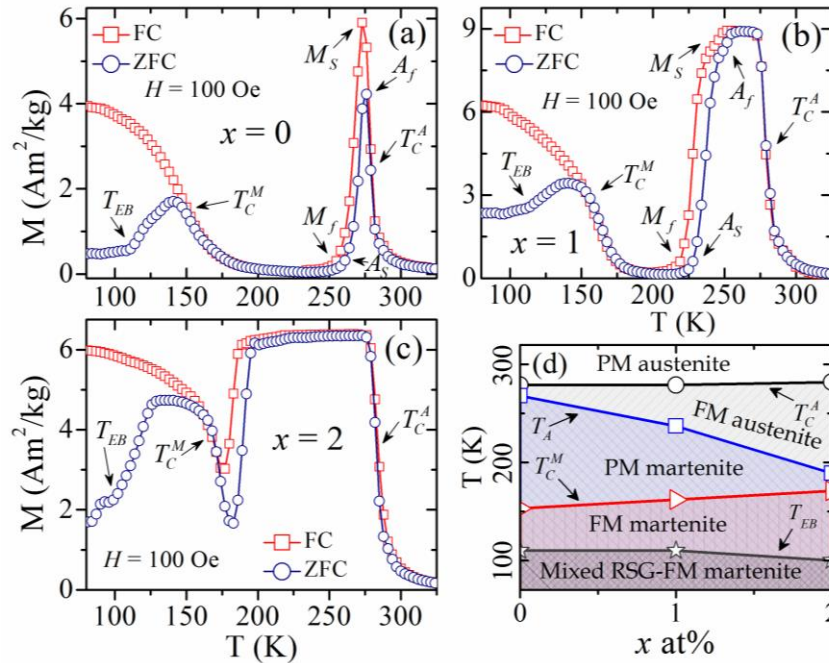


Fig. 5.3: ZFC and FC temperature dependent magnetization (M - T curves) curves for the samples with (a) $x = 0$, (b) $x = 1$ and (c) $x = 2$ in the presence of 100 Oe magnetic field. (d) Phase diagram as a function of x for $\text{Mn}_{50.5-x}\text{Ni}_{41}\text{Sn}_{8.5+x}$ alloys within the temperatures between 80 K and 350 K.

Figs. 5.3(a-c) show the ZFC and FC magnetization vs temperature curves (M - T curves) respectively for $x = 0, 1$ and 2 in the presence of a 100 Oe magnetic field. A sharp change in magnetization is observed near 280 K for all the samples, which is due to their ferro-para transition at T_C^A . T_C^A remains almost unchanged with increasing x . The further change in magnetization for $x = 0, 1$ and 2 near 270 K, 230 K and 185 K respectively indicates the presence of a FOMST in these samples. The characteristic transition temperatures for the FOMST: A_s , A_f , T_A , M_s , M_f and T_M are given in table 5.1 and some of them are also indicated in the M - T curves (Fig. 5.3(a-c)). These transition temperatures match well with as estimated from the susceptibility data. It can be seen that the structural transition of these alloys shifts towards the lower temperatures as the Mn-content decreases. It is reported that T_A of Ni-rich $\text{Ni}_{50}\text{Mn}_{50-x}\text{Sn}_x$ and Mn-rich $\text{Mn}_{50}\text{Ni}_{50-x}\text{Sn}_x$ alloys decreases with decreasing

valence electron concentration (e/a) [8, 9, 19-21]. A very similar result is obtained from our samples also. The T_A of these alloy systems is less sensitive to the Mn/Sn ratio as compared to that of Ni/Sn [19]. The thermal hysteresis near the martensitic transition is found to be very small (6 K) for $x = 0$ as compared to that of conventional Ni rich Ni-Mn-Sn alloys (~ 12 K) [1, 9]. ΔT_{hys} of these alloys increases with increasing x .

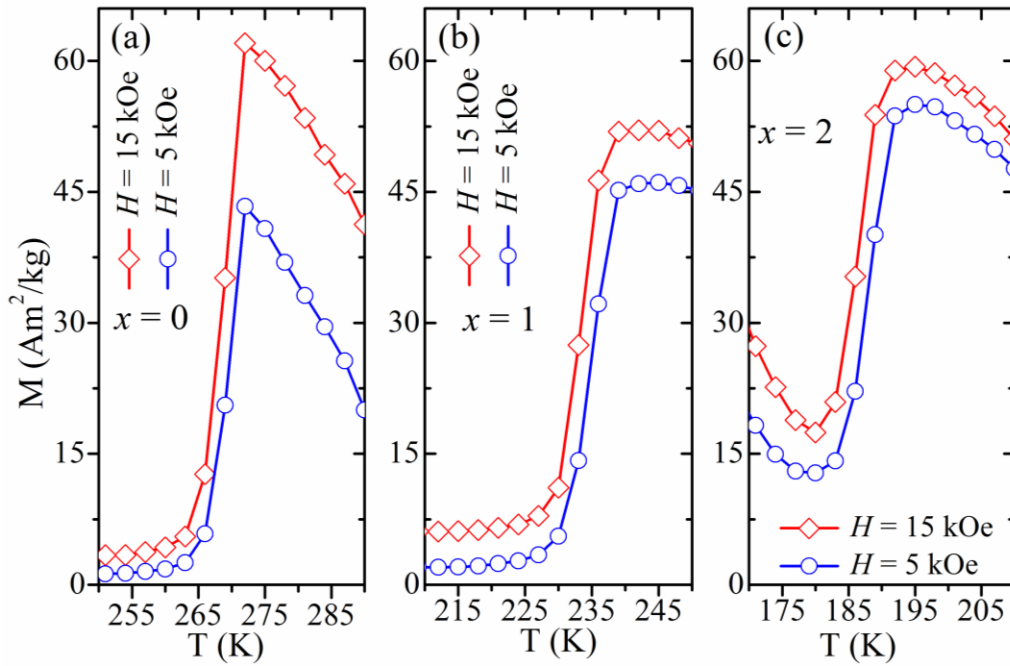


Fig. 5.4: ZFC M - T curves in the vicinity of the martensitic transition for $\text{Mn}_{50.5-x}\text{Ni}_{41}\text{Sn}_{8.5+x}$ alloys with (a) $x = 0$, (b) $x = 1$ and (c) $x = 2$ under 5 kOe and 15 kOe magnetic field.

All the samples experience another sudden change in magnetization within the temperatures between 150 K and 170 K, which is referred to the T_C^M of these samples. T_C^M increases with the decrease of Mn-content. The splitting between ZFC and FC M - T curves below 150 K may be due to the existence of exchange bias which is thought to originate from the interfacial exchange interaction between the reentrant spin glass (RSG) and the ferromagnetic martensite phases below the T_{EB} of these alloys as reported in [29]. Fig. 5.3(d) shows the phase diagram of these samples as a function of x . One can observe that the austenite phase of all the samples is paramagnetic above 280 K and ferromagnetic within their respective T_C^A and A_f . The martensite phase is found to be paramagnetic like within M_f and T_C^M of $x = 0$ and 1. In the

temperature range between T_C^M and T_{EB} the weakly ferromagnetic martensite phase is dominant, whereas below T_{EB} the phase of all the samples may be mixed RSG-ferromagnetic martensite.

Figs. 5.4(a-c) represent the ZFC M - T curves in the presence of 5 kOe and 15 kOe magnetic field in the vicinity of their martensitic transition, for $x = 0, 1$ and 2 respectively. A field induced shift of the magneto-structural transition is observed in all the samples which confirm the existence of FIMST. $|\Delta T/\Delta H|$ is found to be 0.19, 0.22 and 0.23 K/kOe for the samples with $x = 0, 1$ and 2 respectively.

5.3.1.3. Field dependent magnetic properties

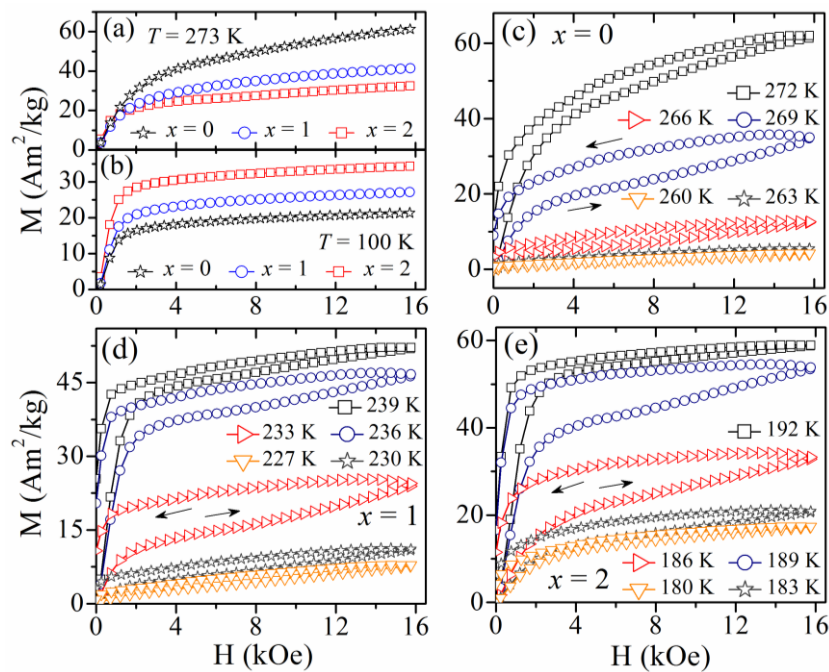


Fig. 5.5: Isothermal magnetization vs magnetic field (M - H curves) curves for $Mn_{50.5-x}Ni_{41}Sn_{8.5+x}$ alloys at (a) 273 K and (b) 100 K. M - H curves for the alloys with (c) $x = 0$, (d) $x = 1$ and (e) $x = 2$ at different temperatures in the vicinity of their magneto-structural transition.

To understand the magnetic properties of the austenite and martensite phase in a better way, the M - H curves of all the samples at 273 K and 100 K are plotted respectively in Fig. 5.5(a) and 5.5(b). The field sweeping is done as follows: $0 \rightarrow 16$ kOe. In the austenite phase, the saturation magnetization at 273 K (M_{sat}^{273K}) decreases with the increase of x . In the case of martensite phase, the saturation magnetization at 100 K (M_{sat}^{100K}) increases monotonically with increasing x . This can be explained in

the context of different types of Mn-Mn interactions in the two structural phases. The two Mn atoms, one from the octahedral and another from the tetrahedral site interact ferromagnetically in the austenite phase below T_C^A . As the samples undergo a martensitic phase transition, the Mn-Mn separation decreases and the antiferromagnetic correlations start to increase [30]. These ferro/antiferro interactions are the strongest for the samples with 50 at% of Mn. Any further change in Mn concentration weakens the aforementioned interactions. This is probably why $M_{\text{sat}}^{273\text{K}}$ decreases and $M_{\text{sat}}^{100\text{K}}$ increases with increasing x . The increase in T_C^M with the decrease in Mn-content may also enhance the $M_{\text{sat}}^{100\text{K}}$. However this effect will not be very significant as T_C^M only increases by 18 K when x changes from 0 to 2.

Table 5.2: Saturation magnetization in the vicinity of structural transition and magnetocaloric parameters for $\text{Mn}_{50.5-x}\text{Ni}_{41}\text{Sn}_{8.5+x}$ alloys.

x (at%)	$M_{\text{sat}}^{\text{A-finish}}$ (Am ² /kg)	$M_{\text{sat}}^{\text{M-finish}}$ (Am ² /kg)	ΔM_{sat} (Am ² /kg)	ΔS_M (J/kg K)	RC (J/kg)	HL _{avg} (J/kg)	Net RC (J/kg)
0	62.02	4.27	57.75	11.85	52.95	8.13	44.82
1	52.15	7.87	44.28	11.1	43.77	7.87	35.9
2	58.9	17.43	41.47	9.97	42.44	11.5	30.89

Figs. 5.5(c-e) show the isothermal M - H curves of $\text{Mn}_{50.5-x}\text{Ni}_{41}\text{Sn}_{8.5+x}$ alloys respectively with $x = 0, 1$ and 2 within the temperatures between their respective A_S and A_f . The field sweeping is done as follows: $0 \rightarrow 16 \text{ kOe} \rightarrow 0$. All these M - H curves have been taken under the discontinuous heating protocol. Every time before taking an M - H curve the sample was heated back from a temperature which was far below from its structural transition temperature. The details about this protocol are already mentioned in the previous chapter. In this way, the effect of field induced history on the consecutive M - H curves can be removed and the values of entropy change may not overshoot [31, 32]. A large magnetic hysteresis in the M - H curves of all the samples predicts the existence of FIMST in these alloys and it is confirmed from Figs. 5.4(a-c) also. The M - H curves at 260 K for $x = 0$ and at 227 K for $x = 1$ indicate that the martensite phase of them is paramagnetic like above their respective T_C^M . As the T_C^M and A_S of $x = 2$ are very close to each other, its martensite phase is weakly

ferromagnetic within these two temperatures. These results agree well with the low field M - T data also (Figs. 5.3(a-c)).

5.3.1.4. Magnetocaloric properties

ΔS_M of the $Mn_{50.5-x}Ni_{41}Sn_{8.5+x}$ alloys has been estimated from isothermal M - H curves using Maxwell's thermodynamic relation (equation (1.18)) [4] and plotted as a function of temperature in Fig. 5.6(a). The maximum value of ΔS_M is 11.85 J/kg K at 270 K for $x = 0$ due to a change of only $\Delta H = 15$ kOe. The difference in saturation magnetization between A_f and A_s (ΔM_{sat}) plays a key role in order to achieve large ΔS_M (data are given in table 5.2). One can notice that as the ΔM_{sat} decreases with decreasing Mn-content, ΔS_M also reduces.

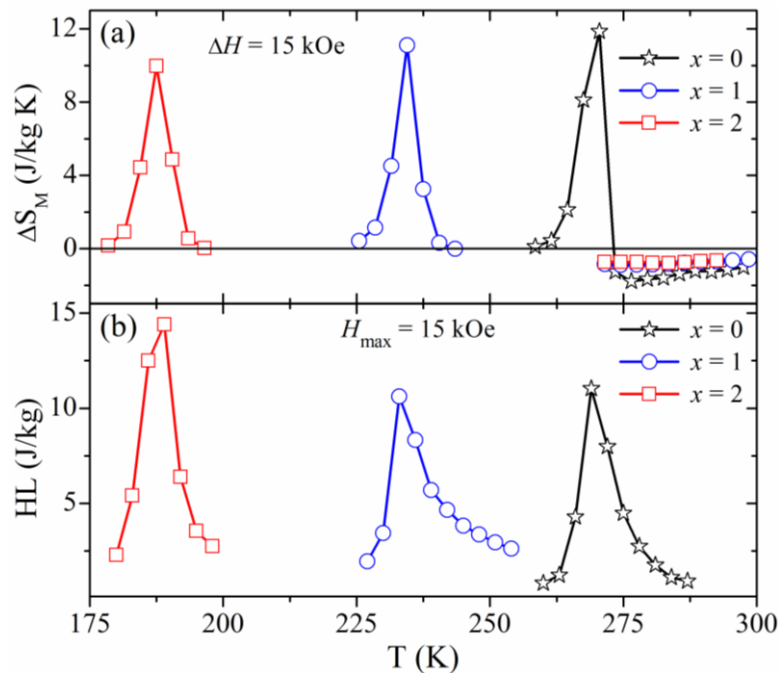


Fig. 5.6: (a) Temperature dependence of magnetic entropy changes for $Mn_{50.5-x}Ni_{41}Sn_{8.5+x}$ alloys due to 15 kOe field changes. (b) Magnetic field induced hysteresis losses of the samples as a function of temperature.

The RC of these materials has also been estimated from equation (1.20) and a RC ~ 53 J/kg is calculated for $x = 0$. In order to verify the actual potential of these alloys in the field of magnetic refrigeration, it is necessary to subtract the hysteresis loss from RC [23]. The HL during FOMST of all the samples is plotted against the temperature in Fig. 5.6(b). A maximum 14.5 J/kg HL is calculated for $x = 2$.

Integrating over the FWHM of the HL vs T curves, an avg. HL is obtained and is given in table 5.2. Incorporating field induced losses, a net RC ~ 45 J/kg is obtained for $x = 0$, which is nearly 50% higher than that for other reported Ni rich Ni-Mn-Sn alloys (the values are given in table 5.2) [1, 23]. The reported values of thermal conductivity (k) of this family of materials vary from 5 - 15 W/m K within 100 K - 300 K [33, 34]. k decreases during the phase transition from austenite to martensite.

5.3.1.5. Magneto-transport properties

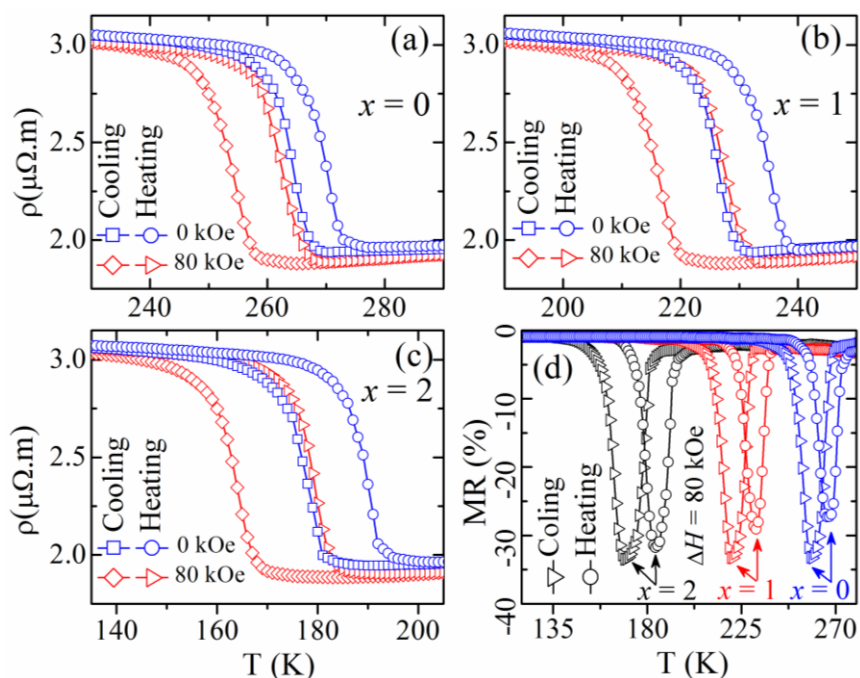


Fig. 5.7: Temperature dependence of electrical resistivity in the presence of 0 and 80 kOe magnetic field for (a) $x = 0$, (b) $x = 1$ and (c) $x = 2$. (d) Temperature dependence of magnetoresistance (due to a field change of 80 kOe) during heating and cooling for $x = 0, 1$ and 2 alloys.

Figs. 5.7(a-c) depict the electrical resistivity as a function of temperature in the presence of zero and 80 kOe magnetic field for $x = 0, 1$ and 2 respectively. All the samples show a large (30%) change in resistivity connected with the magneto-structural phase transition. In the martensite phase, the resistivity decreases with increasing temperature showing a semi-metallic nature of these alloys, while resistivity increases linearly in the austenite phase with the increase of temperature, which confirms the metallic behavior in that phase [6, 21]. The electrical conductivity (σ) of these materials has been estimated to nearly 0.53 MS/m and 0.33 MS/m in the

austenite and martensite phases respectively. The characteristic transition temperatures (given in table 5.1) and ΔT_{hys} as obtained from the ρ - T curves (in the absence of an H -field) are in well agreement with the temperature dependent ac susceptibility and magnetization data as shown in Fig. 5.2 and Figs. 5.3(a-c). Note that ΔT_{hys} becomes larger in the presence of an applied magnetic field for all the samples.

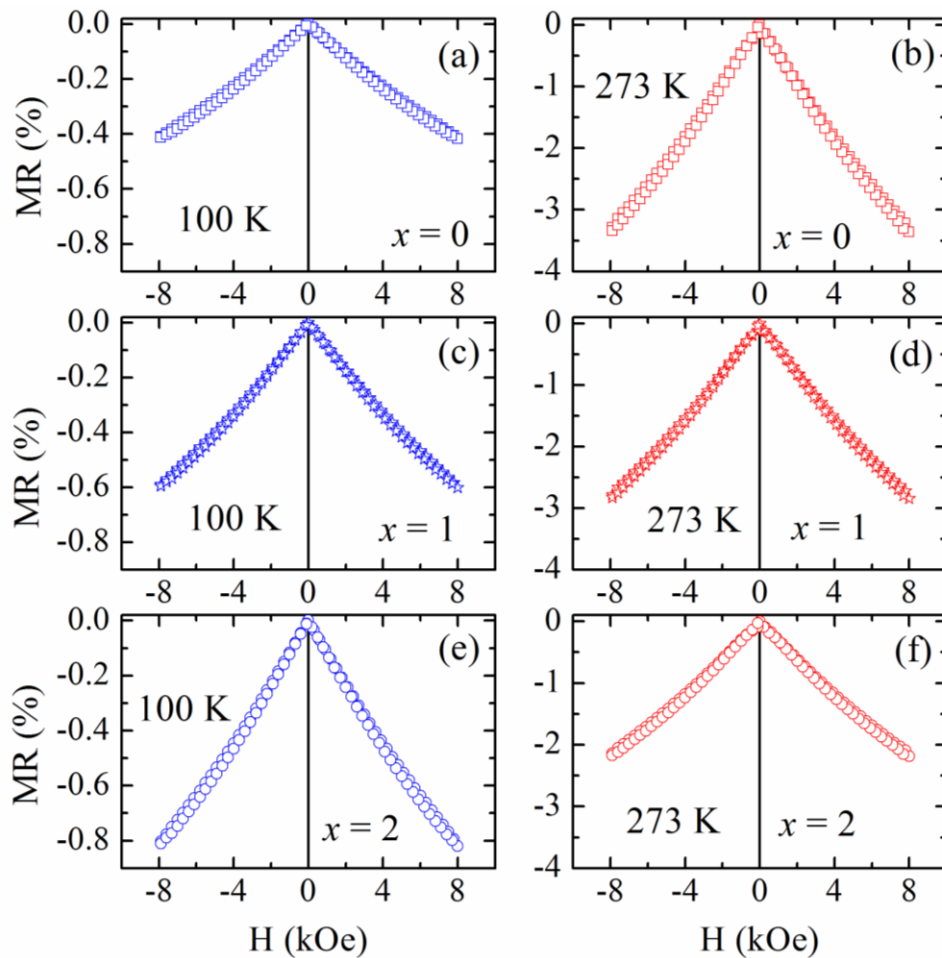


Fig. 5.8: Field dependence of magnetoresistance for the sample with (a) $x = 0$, (c) $x = 1$, (e) $x = 2$ at their martensite phase (100 K) and (b) $x = 0$, (d) $x = 1$, (f) $x = 2$ at their austenite phase (273 K).

The MR of these materials has been obtained from the temperature dependent resistivity data and plotted as a function of temperature in Fig. 5.7(d) for all the samples. A maximum $\sim 33\%$ of MR is obtained from all the three samples for a field change of 80 kOe. In order to study the field dependence of MR of these samples, the MR vs H measurements up to 80 kOe field were carried out and plotted in Fig. 5.8.

The field sweeping is done as follows: $0 \rightarrow 80 \text{ kOe} \rightarrow 0 \rightarrow -80 \text{ kOe} \rightarrow 0$. Figs. 5.8(a, c and e) represent the MR- H curves at the martensite phase (100 K) for the samples with $x = 0, 1$ and 2 respectively. Figs. 5.8(b, d and f) depict the same at the ferromagnetic austenite phase (273 K) for all the samples in the similar manner. It can be observed that the MR at martensite phase is smaller compared to that at austenite phase [35]. In the martensite phase, the magnetic sensitivity of the samples is significantly low. Therefore, the scattering of the conduction electrons by the d spins does not decrease noticeably in the presence of magnetic field. From Figs. 5.8(a, c and e) we can see that the MR at martensite phase increases with the decrease in Mn-content. Decrease in Mn at% reduces the total number of Mn-Mn antiferromagnetically coupled inter-site pairs. As a result, ferromagnetic part enhances which increase the MR also. In the case of austenite phase, MR decreases with decreasing the Mn-content. Mn atoms carry most of the moments in the austenite phase of this alloy family. So, decrease in Mn at% weakens the ferromagnetic correlations in the austenite phase and MR decreases due to the increase in s - d scattering.

5.3.2. Effect of Fe substitution on the phase diagram and MCE in Mn-rich Mn-Fe-Ni-Sn off-stoichiometric Heusler alloys

5.3.2.1. Structural Characterization

Fig. 5.9 and Fig. 5.10 represent the room temperature (295 K) XRD patterns for Mn-rich $\text{Mn}_{50}\text{Ni}_{40.5-y}\text{Fe}_y\text{Sn}_{9.5}$ and $\text{Mn}_{50-z}\text{Fe}_z\text{Ni}_{39.5}\text{Sn}_{10.5}$ alloys. All the samples of the former series are found to be in cubic austenite phase. This predicts that their martensitic transition may reside near or below the room temperature. The super lattice diffraction peaks ((111) and (311)) signify the existence of high level of atomic ordering in these alloys [9]. In the case of later alloy series, the structural phase of the samples with $z = 0, 1, 2, 3$ and 4 is austenite at room temperature. The $z = 5$ sample is in mixed phase with the phase fractions of both the phases. This indicates that the martensitic transition of this sample may reside near room temperature. The sample with $z = 6$ is found to be in the martensite phase at room temperature.

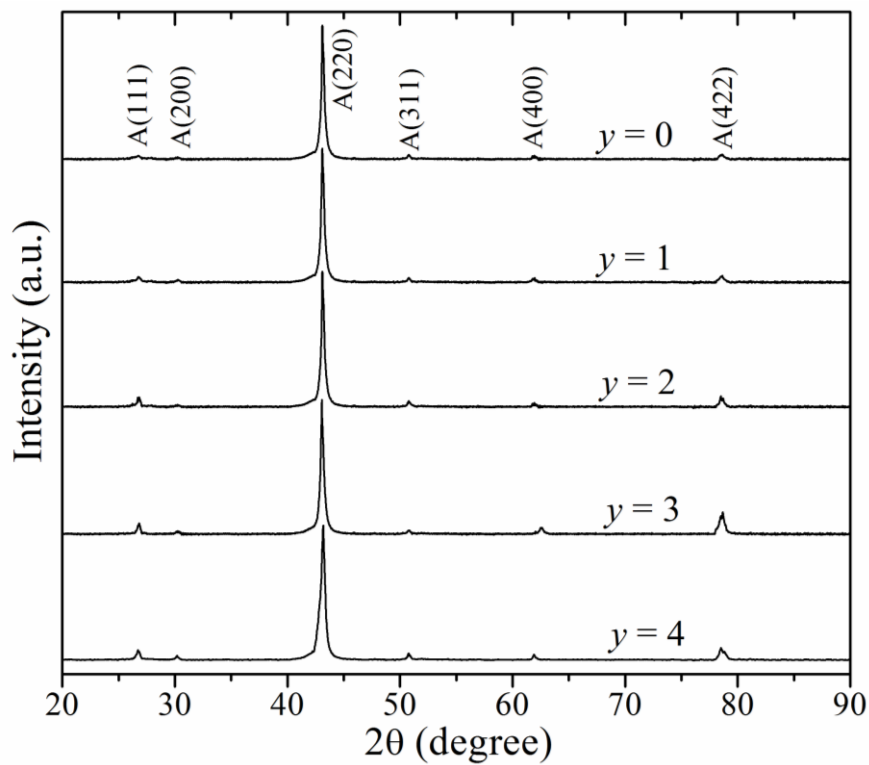


Fig. 5.9: Room temperature (295 K) XRD patterns for Mn₅₀Ni_{40.5-y}Fe_ySn_{9.5} alloys.

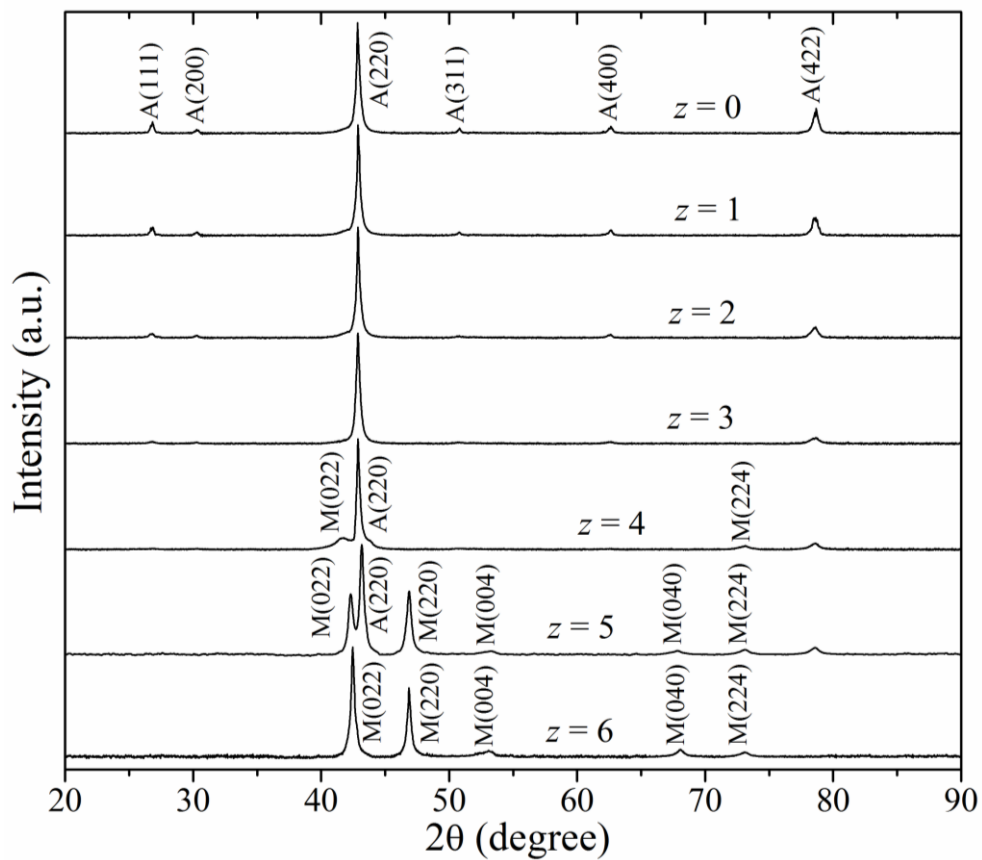


Fig. 5.10: Room temperature (295 K) XRD patterns for Mn_{50-z}Fe_zNi_{39.5}Sn_{10.5} alloys.

5.3.2.2. Temperature dependent magnetic properties and phase diagram

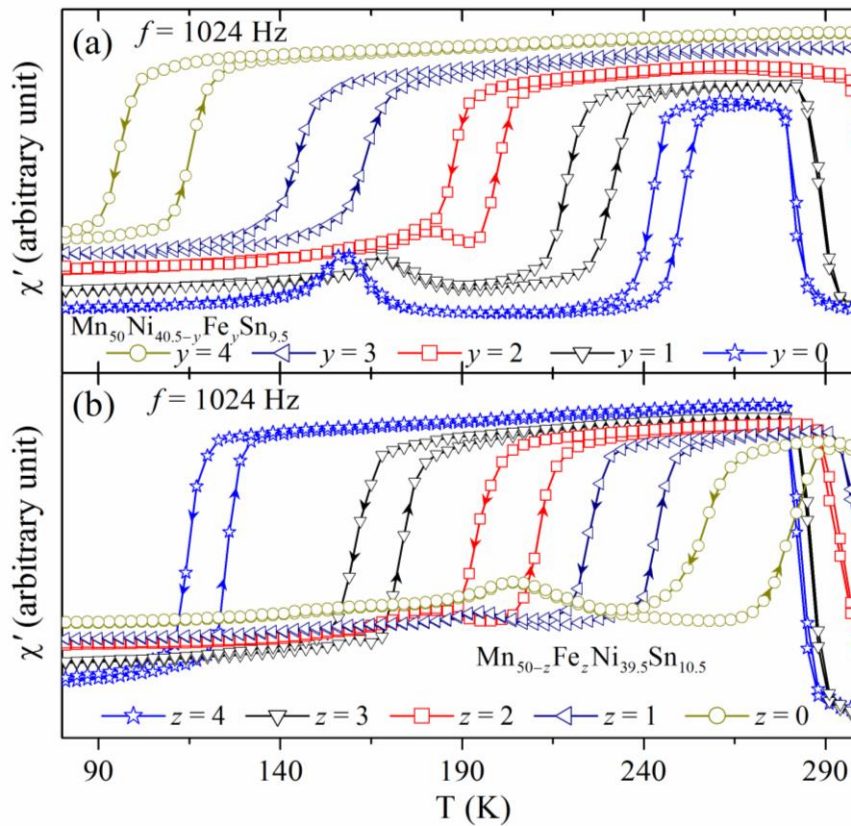


Fig. 5.11: Temperature dependent real part of the ac susceptibility for (a) $\text{Mn}_{50}\text{Ni}_{40.5-y}\text{Fe}_y\text{Sn}_{9.5}$ and (b) $\text{Mn}_{50-z}\text{Fe}_z\text{Ni}_{39.5}\text{Sn}_{10.5}$ alloys.

Figs. 5.11(a and b) represent the temperature dependence of real part of the ac susceptibility within the temperatures between 80 K and 300 K for respectively $\text{Mn}_{50}\text{Ni}_{40.5-y}\text{Fe}_y\text{Sn}_{9.5}$ and $\text{Mn}_{50-z}\text{Fe}_z\text{Ni}_{39.5}\text{Sn}_{10.5}$ alloys. As the structural transition of $z = 5$ and 6 does not fall below 300 K, their susceptibility plots are not shown here. The structural transition temperature of the first series decreases with increasing Fe content but, the same increases in the case of later series as the Fe are doped. For the first series, the magnetic response is found to increase in both the structural phases as the Fe replaces some Ni atoms. In the case of later series, the magnetic sensitivity at the martensite phase also increases with increasing the Fe (replacing Mn) content, but the same decreases in the austenite phase. These results originate from the varying magnetic correlations with the increase in Fe which decreases Ni/Mn content in these alloy systems. A detail discussion on this observation has been made in the later part in this subsection.

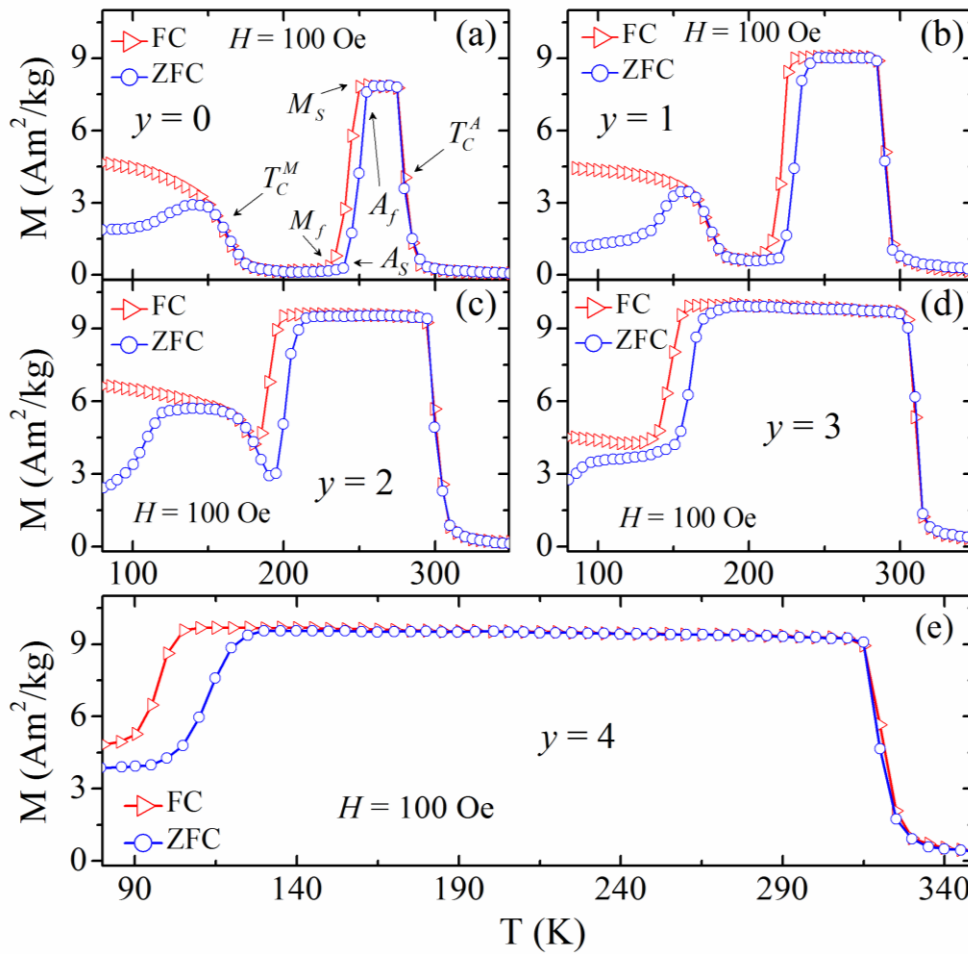


Fig. 5.12: Temperature dependent magnetization (M - T curves) for $\text{Mn}_{50}\text{Ni}_{40.5-y}\text{Fe}_y\text{Sn}_{9.5}$ alloys with (a) $y = 0$, (b) $y = 1$, (c) $y = 2$, (d) $y = 3$ and (e) $y = 4$ in the presence of 100 Oe field.

The ZFC and FC temperature dependent magnetization (M - T curves) in the presence of 100 Oe field for $\text{Mn}_{50}\text{Ni}_{40.5-y}\text{Fe}_y\text{Sn}_{9.5}$ and $\text{Mn}_{50-z}\text{Fe}_z\text{Ni}_{39.5}\text{Sn}_{10.5}$ alloys are plotted in Fig. 5.12 and Fig. 5.13 respectively. Except $z = 6$, all the samples undergo a para-ferro transition at their respective T_C^A near room temperature where the magnetization increases abruptly with the decrease of temperature. A phase transition with thermal hysteresis between the ZFC and FC curves can be found in all the samples. The magnetization here decreases significantly as the temperature of a sample is decreased. As there is no ferromagnetic austenite phase exists in $z = 6$ alloy, no such change in magnetization is found for the same material. But, its DSC data (Fig. 5.13(g): inset) clearly shows the existence of a first order phase transition. This is known as the martensitic transition of these alloys which is a FOMST. The structural phase above this transition is austenite and below is the martensite. The

characteristic transition temperatures for FOMST: A_S , A_f , T_A , M_S , M_f and T_M are given in table 5.3 and some of them are indicated in one of the M - T curve also (Fig. 5.12(a)). These temperatures match well with the temperatures as estimated from the ac susceptibility data (Fig. 5.11). The transition width for martensite to austenite phase transition increases with the increase in Fe content for both alloy series. Another phase transition can be found in these materials at their respective T_C^M where the magnetization in the martensite phase starts to increase with the decrease in temperature. The substitution of Fe in this Heusler system has a significant influence in varying the martensitic transition temperature which is discussed afterwards.

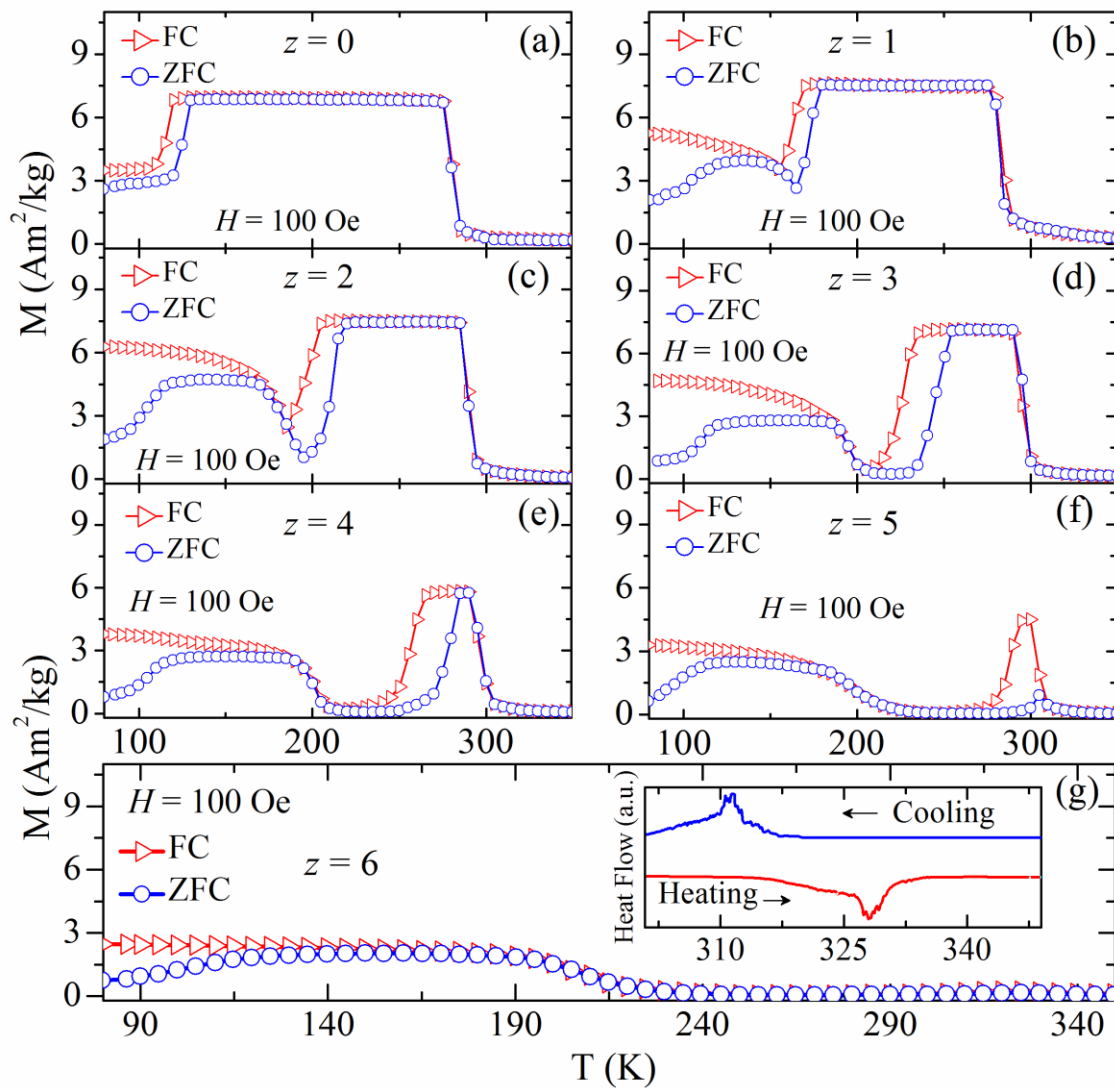


Fig. 5.13: Temperature dependent magnetization (M - T curves) for $\text{Mn}_{50-z}\text{Fe}_z\text{Ni}_{39.5}\text{Sn}_{10.5}$ alloys with (a) $z = 0$, (b) $z = 1$, (c) $z = 2$, (d) $z = 3$, (e) $z = 4$, (f) $z = 5$ and (g) $z = 6$. (g) Inset: DSC heat flow vs temperature curves for $z = 6$ sample.

Table 5.3: The characteristic temperatures of Mn-rich $\text{Mn}_{50}\text{Ni}_{40.5-y}\text{Fe}_y\text{Sn}_{9.5}$ and $\text{Mn}_{50-z}\text{Fe}_z\text{Ni}_{39.5}\text{Sn}_{10.5}$ alloys. Maximum possible error is ± 3 K.

Sample	A_S (K)	A_f (K)	T_A (K)	M_S (K)	M_f (K)	T_M (K)	T_C^A (K)	T_C^M (K)	ΔT (K)
$y = 0$	239	254	246	250	230	240	280	161	15
$y = 1$	219	240	229	230	210	220	289	172	21
$y = 2$	195	214	204	200	180	190	300	176	19
$y = 3$	145	175	160	160	130	145	311	---	30
$y = 4$	95	130	112	110	80	95	319	---	35
$z = 0$	120	130	125	120	110	115	279	---	10
$z = 1$	164	179	171	169	154	161	283	---	15
$z = 2$	196	219	207	206	187	196	289	185	23
$z = 3$	231	256	243	242	205	223	296	194	25
$z = 4$	255	288	271	271	233	252	299	199	33
$z = 5$	285	321	303	297	261	279	305	203	36
$z = 6$	311	345	328	293	329	312	---	210	35

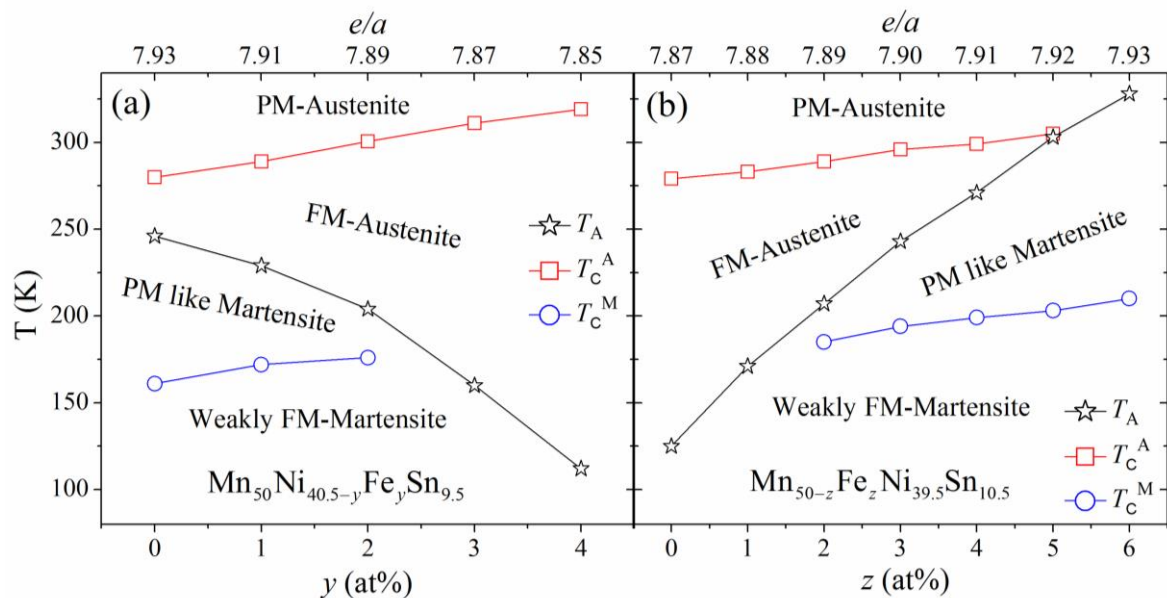


Fig. 5.14: Phase diagram for (a) $\text{Mn}_{50}\text{Ni}_{40.5-y}\text{Fe}_y\text{Sn}_{9.5}$ and (b) $\text{Mn}_{50-z}\text{Fe}_z\text{Ni}_{39.5}\text{Sn}_{10.5}$ alloy series.

The phase diagram of these two Mn-rich Heusler series can be found in Figs. 5.14(a and b). For $\text{Mn}_{50}\text{Ni}_{40.5-y}\text{Fe}_y\text{Sn}_{9.5}$ alloys, T_A decreases as Ni are replaced by Fe. On the other hand, the same increases with the replacement of Mn by Fe in

$\text{Mn}_{50-z}\text{Fe}_z\text{Ni}_{39.5}\text{Sn}_{10.5}$ alloys. The valence electron concentration (e/a ratio) of these alloys are calculated and shown in Fig. 5.14. The conventional dependence of T_A on the e/a ratio is such that they are proportional. There are few reports where T_A decreases with the increase of e/a ratio and its reason are supposed to be the hybridization between $3d$ states of Ni and Mn [36, 37]. In our series of samples, the conventional relationship is maintained. In the case of T_C^A and T_C^M , they increase with the increase of Fe in both the alloy series. This in turn signifies the increase in ferromagnetic interaction in these materials as the Fe atoms are doped.

5.3.2.3. Field dependent magnetic properties

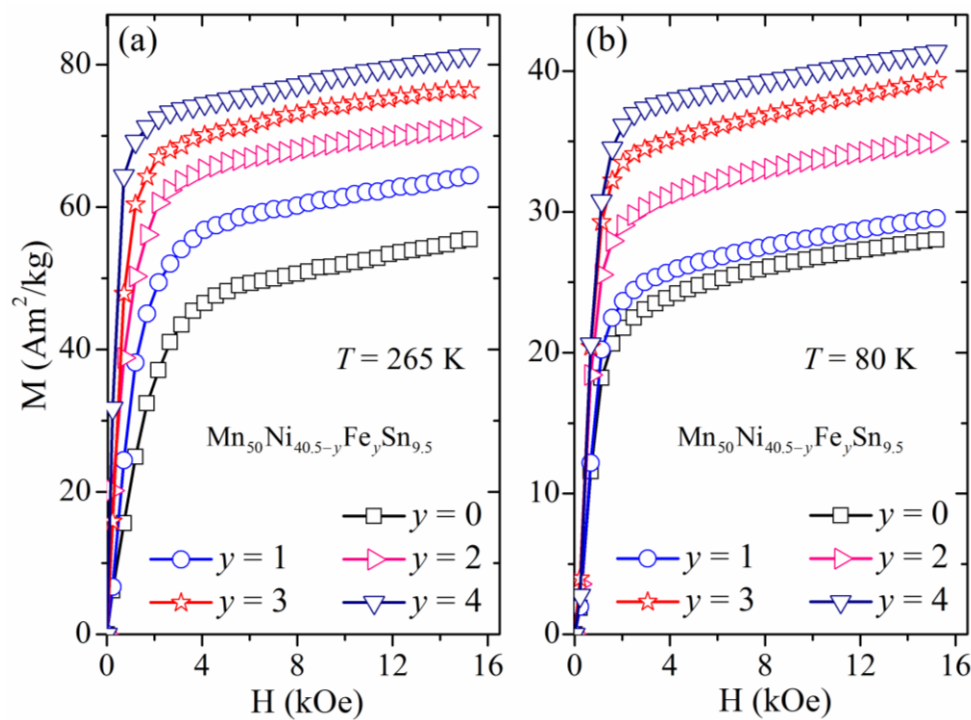


Fig. 5.15: Isothermal field dependence of magnetization (M - H curves) for $\text{Mn}_{50}\text{Ni}_{40.5-y}\text{Fe}_y\text{Sn}_{9.5}$ alloys at (a) austenite (265 K) and (b) martensite (80 K) phase.

The M - H curves at martensite and austenite phase of all the samples are plotted in Fig. 5.15 and Fig. 5.16. The field sweeping is done as follows: $0 \rightarrow 16 \text{ kOe}$. As the complete saturation is not obtained under 16 kOe field, we have calculated the saturation values of magnetization (M_{sat}) from M - H curves using a simple approach as $M_{\text{sat}} = M(H \rightarrow \infty)$. This is just an estimate and it allows us to compare the magnetic properties of the samples in their structural phases. The obtained values of

M_{sat} at the martensite and austenite phase are given in table 5.4. Figs. 5.15(a and b) represent the M - H curves in respectively austenite (at 265 K) and martensite (at 80 K) phase of $\text{Mn}_{50}\text{Ni}_{40.5-y}\text{Fe}_y\text{Sn}_{9.5}$ alloys. The M_{sat} in both the structural phases increases as the Ni atoms are replaced by Fe. This is due to the enhancement in ferromagnetic exchange interaction with the increase in Fe content in the place of Ni. The M_{sat} at the martensite phase ($M_{\text{sat}}^{80\text{K}}$) is much lower as compared to the austenite phase ($M_{\text{sat}}^{265\text{K}}$). This is because the structural phase transition from austenite to martensite accompanies some decrease in the inter-site Mn-Mn distance which causes change in the electronic band structure of these alloys and this in turn modifies the Mn-Mn magnetic correlations [30].

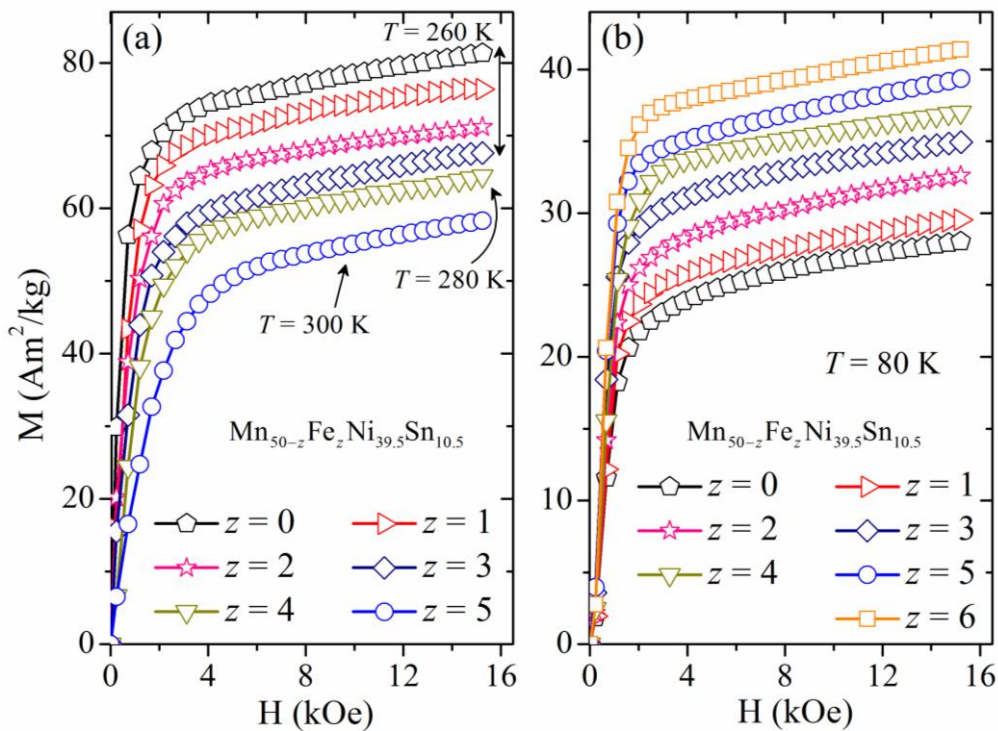


Fig. 5.16: Isothermal M - H curves for $\text{Mn}_{50-z}\text{Fe}_z\text{Ni}_{39.5}\text{Sn}_{10.5}$ alloys at (a) austenite (260 K for $z = 0, 1, 2$ and 3; 280 K for $z = 4$; 300 K for $z = 5$) and (b) martensite (80 K) phase.

On the other hand, Figs. 5.16(a and b) show the M - H curves in the austenite phase (at 260 K for $z = 0, 1, 2$ and 3; at 280 K for $z = 4$ and at 300 K for $z = 5$) and martensite phase (at 80 K) for $\text{Mn}_{50-z}\text{Fe}_z\text{Ni}_{39.5}\text{Sn}_{10.5}$ alloys. Here, the observations are something different from the previous series. M_{sat} at the austenite phase decreases with the increase in Fe. As the Mn atoms carry most of the magnetic moments for

Ni-Mn based Heusler alloy family, the obtained results predict that the decrease in Mn concentration actually cause the decrease in total moment at the austenite phase. In the case of martensite phase, the inter-site Mn-Mn interaction is strongly antiferromagnetic. If some of the Mn atoms are partially replaced by Fe, the aforementioned antiferromagnetic interaction in the martensite phase of $Mn_{50-z}Fe_zNi_{39.5}Sn_{10.5}$ alloys becomes weaker due to the reduction in the number of Mn-Mn inter-site pair. As a result, the M_{sat}^{80K} in the martensite phase increases with the addition of Fe by replacing Mn.

Table 5.4: Saturation magnetization at austenite phase (260 K for $y = 0, 1, 2, 3$ and 4; $z = 0, 1, 2$ and 3; 280 K for $z = 4$; 300 K for $z = 5$) and martensite (80 K) phase and magnetocaloric parameters for Mn-rich $Mn_{50}Ni_{40.5-y}Fe_ySn_{9.5}$ and $Mn_{50-z}Fe_zNi_{39.5}Sn_{10.5}$ alloys.

Sample	M_{sat}^{265K} (Am ² /kg)	M_{sat}^{80K} (Am ² /kg)	ΔS_M (J/kg K)	RC (J/kg)	HL _{avg} (J/kg)	Net RC (J/kg)
$y = 0$	58.30	29.48	10.7	49.2	9.1	40.1
$y = 1$	66.98	30.88	11.9	65.7	13.6	52.1
$y = 2$	73.13	36.03	9.5	75.2	15.8	59.4
$y = 3$	79.14	40.35	7.3	69	21.2	47.8
$y = 4$	83.82	42.23	5.9	67.3	22.8	44.5
$z = 0$	83.40	29.52	9	56.4	12.3	44.1
$z = 1$	79.25	30.72	10.3	78.9	15.6	63.3
$z = 2$	73.20	34.10	12.8	94.2	20.9	73.3
$z = 3$	70.53	36.19	8.2	83.9	21.2	62.7
$z = 4$	66.72	38.01	7.1	80.1	24.3	55.8
$z = 5$	61.32	40.57	5.3	41.3	19.1	22.2
$z = 6$	---	42.42	---	---	---	---

The M - H curves across the martensitic transition of $Mn_{50}Ni_{39.5}Fe_1Sn_{9.5}$ and $Mn_{48}Fe_2Ni_{39.5}Sn_{10.5}$ alloys are plotted in Fig. 5.17 and Fig. 5.18 respectively, as representatives of other samples' M - H curves across their respective FOMST. The field sweeping is done as follows: $0 \rightarrow 16$ kOe $\rightarrow 0$. The existence of field induced metamagnetic phase transition can be found in these materials. This transition starts near ~ 12 kOe where the magnetization starts to increase nonlinearly. These M - H

isotherms are measured using the discontinuous heating protocol [31]. For the each M-H measurement, the sample is first cooled to a temperature which is well below from its T_A . After that, the sample is heated to the targeted temperature without overshooting it. The temperature step used for these isotherms is 3 K. The effect of field history on the samples due to the field induced effect on the first order phase transition is removed by using the aforementioned measurement protocol which is discussed earlier in this chapter (subsection 5.3.1) and in the previous chapter also (chapter 4).

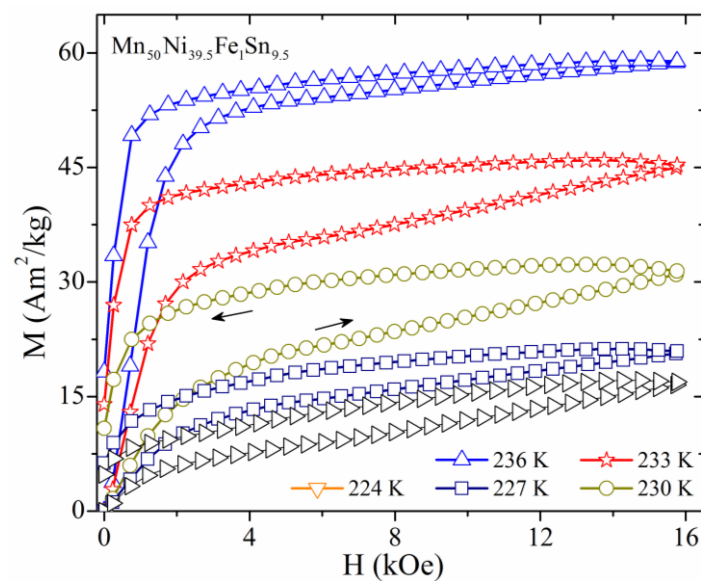


Fig. 5.17: M - H curves across the martensitic transition of $\text{Mn}_{50}\text{Ni}_{39.5}\text{Fe}_1\text{Sn}_{9.5}$ alloy.

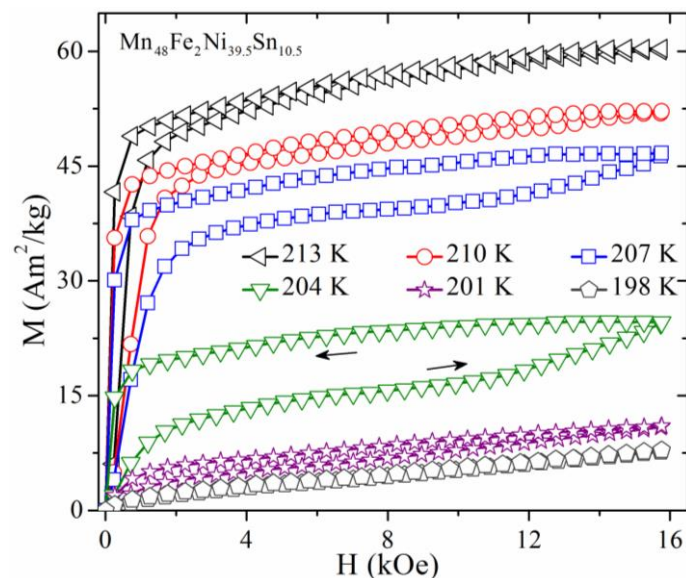


Fig. 5.18: M - H curves across the martensitic transition of $\text{Mn}_{48}\text{Fe}_2\text{Ni}_{39.5}\text{Sn}_{10.5}$ alloy.

5.3.2.4. Magnetocaloric properties

The ΔS_M of these alloys has been estimated from the isothermal $M-H$ curves across the martensitic transition using the Maxwell's relation [4]. It is reported that the use of Maxwell's relation for the first order phase transitions may show unexpected spikes in ΔS_M-T curves and thus can provide overestimated values of entropy change and RC also [32]. It is also reported that the aforementioned problem can be solved by using the discontinuous heating or cooling protocol during the isothermal $M-H$ measurements across such field induced phase transition [31]. The values of magnetocaloric parameters that we have calculated are thus reasonable under our measurement protocol.

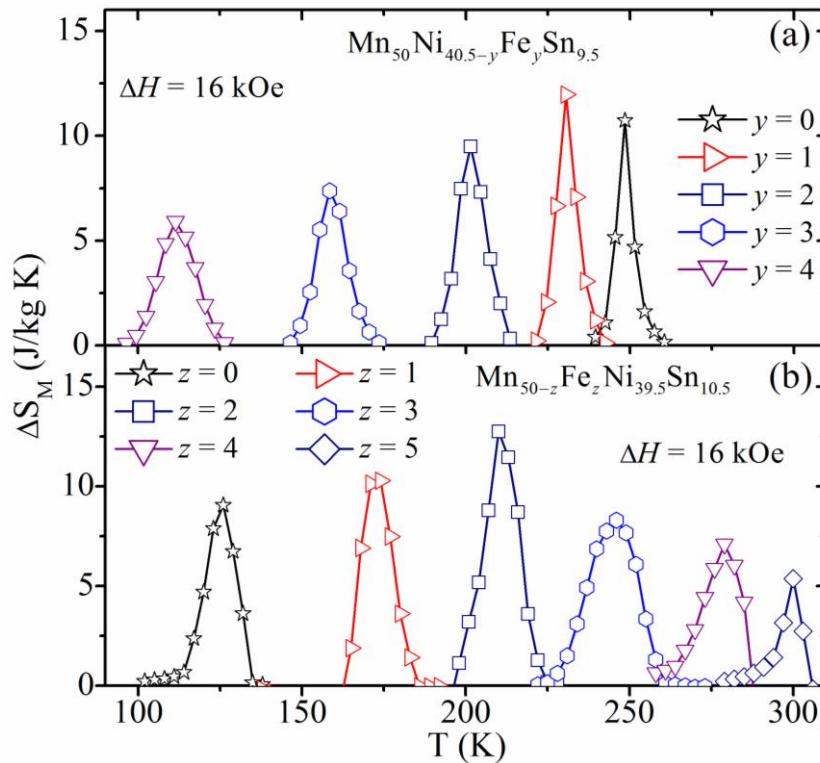


Fig. 5.19: Temperature dependent magnetic entropy change in the vicinity of martensitic transition of (a) $\text{Mn}_{50}\text{Ni}_{40.5-y}\text{Fe}_y\text{Sn}_{9.5}$ and (b) $\text{Mn}_{50-z}\text{Fe}_z\text{Ni}_{39.5}\text{Sn}_{10.5}$ alloy series due to a field change of 16 kOe.

Figs. 5.19(a and b) represent the temperature dependent curves of ΔS_M for $\text{Mn}_{50}\text{Ni}_{40.5-y}\text{Fe}_y\text{Sn}_{9.5}$ and $\text{Mn}_{50-z}\text{Fe}_z\text{Ni}_{39.5}\text{Sn}_{10.5}$ alloys respectively. For the first series, ΔS_M increases for the sample with 1 at% of Fe (~ 12 J/kg K due to 16 kOe field changes) and then it decreases monotonically as the Fe is increased further. In the case of other series, ΔS_M is found to be the maximum for the sample with 2 at% of Fe

(~ 13 J/kg K due to the same field change) and decreases on both the side of increasing and decreasing Fe-content. Although, entropy change is a very useful and well used parameter for magnetocaloric effect, RC of a material allows us to estimate its actual potential as a magnetic refrigerant. In addition to that, it is also necessary to take care of the magnetic hysteresis loss that comes due to the field induced transition of these alloys. RC and HL have been calculated and the obtained average losses subtracted from the RC values to estimate the net RC of these alloys. All these values are given in table 5.4 for all the samples. Fig. 5.20 shows the dependence of net RC of these two alloy series on the atomic concentration of Fe. Maximum value of net RC is achieved for the sample with 2 at% of Fe for both the series (~ 60 J/kg for $y = 2$ and ~ 73 J/kg for $z = 2$ under 16 kOe field change) and it is noticeably higher than similar undoped alloys as we have achieved in $\text{Mn}_{50.5-x}\text{Ni}_{41}\text{Sn}_{8.5+x}$ alloys, which is reported in the previous subsection of this chapter [27].

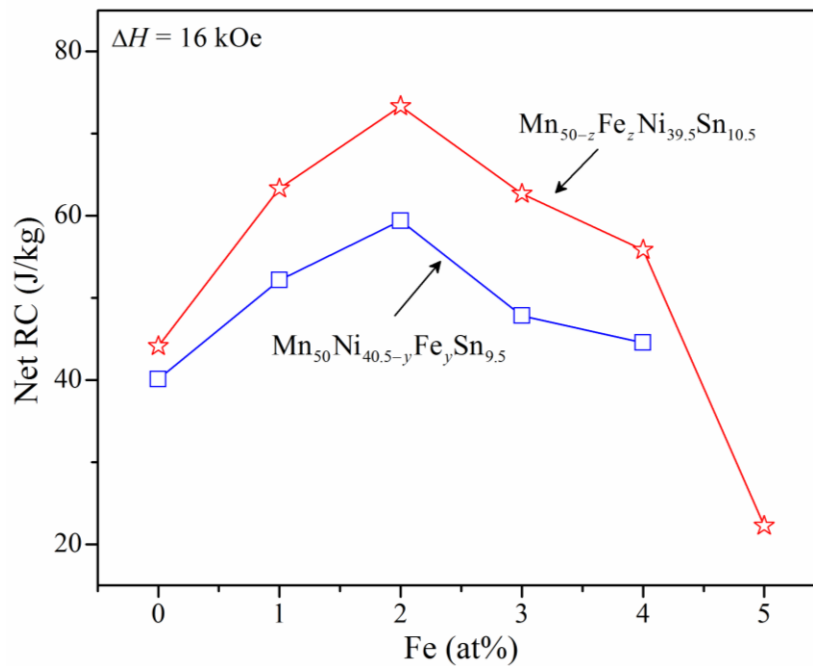


Fig. 5.20: Net RC as a function of Fe concentration for Mn-Fe-Ni- Sn alloys.

Such enhancement in net RC originates from the increased ΔT and enhanced ΔS_M in the samples with small percentages of Fe. In the case of highly doped samples, the ΔT is larger, but the value of ΔS_M is smaller and the hysteresis loss is larger as compared to the lowly doped samples. This is why their net RC is low. The

replacement of Ni by Fe enhances the ferromagnetic interaction and thus increases M_{sat} in both the martensite and austenite phases of $\text{Mn}_{50}\text{Ni}_{40.5-y}\text{Fe}_y\text{Sn}_{9.5}$ alloys. In addition to that, the increase in ΔT significantly affects $(dM/dT)_H$ across the martensitic transition. Now, this factor is an important term for the calculation of ΔS_M . Higher the $(dM/dT)_H$, larger the ΔS_M .

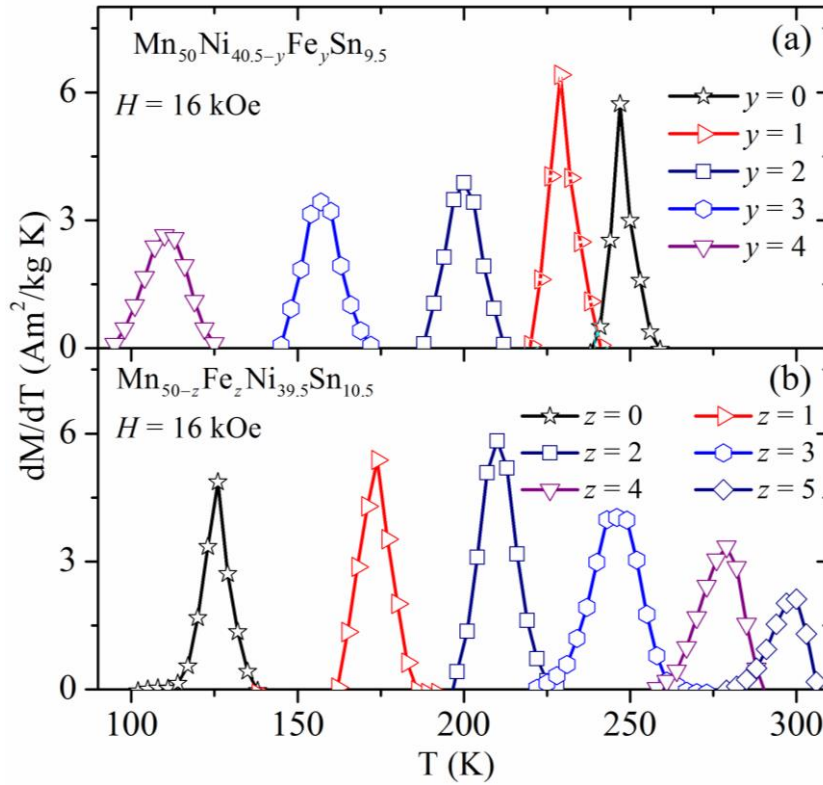


Fig. 5.21: $(dM/dT)_H$ (as calculated from isofield M - T measurements) across the martensitic transition of (a) $\text{Mn}_{50}\text{Ni}_{40.5-y}\text{Fe}_y\text{Sn}_{9.5}$ and (b) $\text{Mn}_{50-z}\text{Fe}_z\text{Ni}_{39.5}\text{Sn}_{10.5}$ alloy series under 16 kOe field.

Fig. 5.21 represents the temperature dependence of $(dM/dT)_H$ under 16 kOe field for all the samples across their martensitic phase transition. $(dM/dT)_H$ has been calculated from isofield M - T measurement data. One can notice that the nature of ΔS_M - T (as calculated from isothermal measurement data) and (dM/dT) - T (as calculated from isofield measurement data) curves are almost similar for all the samples. For the sample with $y = 1$, A_S resides above T_C^M and thus the magnetization difference between A_f and A_S (ΔM) is high and ΔT of martensitic transition is also not so wide (Fig. 5.12(b)). So, the $(dM/dT)_H$ across the martensitic transition is high and this is why the ΔS_M for $y = 1$ is the largest among that series. For

$\text{Mn}_{50-z}\text{Fe}_z\text{Ni}_{39.5}\text{Sn}_{10.5}$ alloy series, A_S resides just above the T_C^M for $z = 2$ sample (Fig. 5.13(c)). Thus, its magnetization value near A_S is very low as compared to the samples with $z = 0$ and 1. Although, the M_{sat} at the austenite phase of $z = 2$ is lower as compared to that for $z = 0, 1$ and ΔT is larger, $(dM/dT)_H$ across T_A is high. As a result, a large value of ΔS_M is obtained for the same sample which is the largest among both series of samples. In the case of highly doped samples, ΔT is larger than that of for undoped and lowly doped samples of both the series. This in turn reduces $(dM/dT)_H$ and the martensitic transition becomes magnetically less sensitive. The average field induced loss in the highly doped samples is large also. This is why the ΔS_M and net RC start to fall after the increase in doping concentration beyond a certain level (~ 2 at%).

5.4. Conclusions

In summary, we have successfully enhanced the magnetocaloric properties in Ni-Mn based Heusler alloys by making them Mn-rich. In the first subsection in this chapter, we have measured a large isothermal magnetic entropy change in Mn-rich $\text{Mn}_{50.5-x}\text{Ni}_{41}\text{Sn}_{8.5+x}$ ($x = 0, 1$ and 2) alloys in the vicinity of their martensitic phase transition. As these materials dissipate only a small amount of energy due to their smaller thermal hysteresis and exhibit a large refrigerant capacity, they can be used in magnetic refrigerators to achieve a good cooling efficiency. The shift of the magneto-structural phase transition of these alloys is less sensitive to the Mn/Sn ratio, which provides a better tuneability to their phase transition temperatures for various practical applications. A magnetoresistance of up to 33% is also available from these alloys. In the temperatures far away from the structural transition point, the obtained magnetoresistance is negligible but, it depends on the s - d scattering mechanism which is mediated by the varying magnetic correlations present in these alloys.

In the case of later part, the detail magnetic properties and magnetocaloric effect of Mn-rich Mn-Fe-Ni-Sn alloys have been studied. The martensitic transition temperature of these alloys follows the conventional e/a ratio dependence

(proportional). The ferromagnetic correlations in the austenite phase increases when Ni is replaced by Fe, but decreases when Mn is replaced by the same element. This is because of the weakening of ferromagnetic interaction in the austenite phase due to the decrease in Mn-content. In the case of martensite phase, antiferromagnetic interaction is found to reduce with increasing Fe concentration for both alloy series. Large values of magnetic entropy change have been observed with high refrigerant capacities in these Fe-doped (with small at%) samples which can make them good magnetic refrigerant for the possible use in environment friendly refrigeration technology.

Bibliography

- [1] P. J. Shamberger and F. S. Ohuchi, *Phys. Rev. B* 79, 144407 (2009).
 - [2] B. Hernando, J. L. S. Lamazares, J. D. Santos, V. M. Prida, D. Baldomir, D. Serantes, R. Varga and J. González, *Appl. Phys. Lett.* 92, 132507 (2008).
 - [3] A. Planes, L. Manosa and M. Acet, *J. Phys.: Condens. Matter* 21, 233201 (2009).
 - [4] V. D. Buchelnikov and V. V. Sokolovskiy, *Phys. Met. Metallog.* 112, 633 (2011).
 - [5] Z. D. Han, D. H. Wang, C. L. Zhang, H. C. Xuan, B. X. Gu and Y. W. Du, *Appl. Phys. Lett.* 90, 042507 (2007).
 - [6] H. C. Xuan, Y. Deng, D. H. Wang, C. L. Zhang, Z. D. Han and Y. W. Du, *J. Phys. D: Appl. Phys.* 41, 215002 (2008).
 - [7] K. Koyama, H. Okada, K. Watanabe, T. Kanomata, R. Kainuma, W. Ito, K. Oikawa and K. Ishida, *Appl. Phys. Lett.* 89, 182510 (2006).
 - [8] T. Krenke, E. Duman, M. Acet, E. F. Wassermann, X. Moya, L. Manosa, and A. Planes, *Nature Mater.* 4, 450 (2005).
 - [9] S. E. Muthu, N. V. R. Rao, M. M. Raja, D. M. R. Kumar, D. M. Radheep and S. Arumugam, *J. Phys. D: Appl. Phys.* 43, 425002 (2010).
 - [10] C. Jinga, Z. Li, H. L. Zhang, J. P. Chen, Y. F. Qiao, S. X. Cao and J. C. Zhang, *Eur. Phys. J. B* 67, 193 (2009).
 - [11] T. Krenke, E. Duman, M. Acet, X. Moya, L. Mañosa and A. Planes, *J. Appl. Phys.* 102, 033903 (2007).
 - [12] S. Li, Z. Yuan, L. Y. L'u, M. Liu, Z. Huang, F. Zhang and Y. Dub, *Mater. Sci. Engg.: A* 428, 332 (2006).
 - [13] W. Ito, M. Nagasako, R. Y. Umetsu, R. Kainuma, T. Kanomata and K. Ishida, *Appl. Phys. Lett.* 93, 232503 (2008).
 - [14] X. G. Zhao, C. C. Hsieh, J. H. Lai, X. J. Cheng, W. C. Chang, W. B. Cui, W. Liu and Z. D. Zhang, *Scripta Mater.* 63, 250 (2010).
 - [15] G. D. Liu, X. F. Dai, S. Y. Yu, Z. Y. Zhu, J. L. Chen and G. H. Wu, *Phys. Rev. B* 74, 054435 (2006).
 - [16] H. Luo, G. Liu, Z. Feng, Y. Li, L. Ma, G. Wu, X. Zhu, C. Jiang and H. Xu, *J. Magn. Magn. Mater.* 321, 4063 (2009).
-

- [17] Z. Wu, Z. Liu, H. Yang, Y. Liu and G. Wu, *Appl. Phys. Lett.* 98, 061904 (2011).
- [18] S. Paul and S. Ghosh, *J. Phys.: Condens. Matter* 23, 206003 (2011).
- [19] L. Ma, S. Q. Wang, Y. Z. Li, C. M. Zhen, D. L. Hou, W. H. Wang, J. L. Chen and G. H. Wu, *J. Appl. Phys.* 112, 083902 (2012).
- [20] Q. Tao, Z. D. Han, J. J. Wang, B. Qian, P. Zhang, X. F. Jiang, D. H. Wang and Y. W. Du, *AIP Adv.* 2, 042181 (2012).
- [21] H. C. Xuan, Y. X. Zheng, S. C. Ma, Q. Q. Cao, D. H. Wang and Y. W. Du, *J. Appl. Phys.* 108, 103920 (2010).
- [22] Z. Han, J. Chen, B. Qian, P. Zhang, X. Jiang, D. Wang and Y. Du, *Scripta Mater.* 66, 121 (2012).
- [23] T. L. Phan, P. Zhang, N. H. Dan, N. H. Yen, P. T. Thanh, T. D. Thanh, M. H. Phan and S. C. Yu, *Appl. Phys. Lett.* 101, 212403 (2012).
- [24] A. Ghosh and K. Mandal, *J. Alloys Compd.* 579, 295 (2013).
- [25] A. Ghosh and K. Mandal, *Eur. Phys. J. B* 86, 378 (2013).
- [26] A. Ghosh and K. Mandal, *Appl. Phys. Lett.* 104, 031905 (2014).
- [27] A. Ghosh and K. Mandal, *J. Phys. D: Appl. Phys.* 46, 435001 (2013).
- [28] A. Ghosh and K. Mandal, *J. Appl. Phys.* 117, 093909 (2015).
- [29] L. Ma, W. H. Wang, J. B. Lu, J. Q. Li, C. M. Zhen, D. L. Hou and G. H. Wu, *Appl. Phys. Lett.* 99, 182507 (2011).
- [30] S. Aksoy, M. Acet, P. P. Deen, L. Mañosa and A. Planes, *Phys. Rev. B* 79, 212401 (2009).
- [31] L. Caron, Z. Q. Ou, T. T. Nguyen, D. T. C. Thanh, O. Tegus and E. Bruck, *J. Magn. Magn. Mater.* 321, 3559 (2009).
- [32] G. J. Liu, J. R. Sun, J. Shen, B. Gao, H. W. Zhang, F. X. Hu and B. G. Shen, *Appl. Phys. Lett.* 90, 032507 (2007).
- [33] B. Zhang, X. X. Zhanga, S. Y. Yu, J. L. Chen, Z. X. Cao and G. H. Wu, *Appl. Phys. Lett.* 91, 012510 (2007).
- [34] Y. K. Kuo, K. M. Sivakumar, H. C. Chen, J. H. Su and C. S. Lue, *Phys. Rev. B* 72, 054116 (2005).
- [35] S. Singh and C. Biswas, *Appl. Phys. Lett.* 98, 212101 (2011).
-

- [36] L. H. Yang, H. Zhang, F. X. Hu, J. R. Sun, L. Q. Pan and B. G. Shen, *J. Alloys Compd.* 588, 46 (2014).
- [37] M. Khan, J. Jung, S. S. Stoyko, A. Mar, A. Quetz, T. Samanta, I. Dubenko, N. Ali, S. Stadler, K. H. Chowl, *Appl. Phys. Lett.* 100, 172403 (2012).
-

Chapter 6

Measurement protocol dependent magnetocaloric effect in a Mn-rich Si doped Mn-Ni-Sn- Si off-stoichiometric Heusler alloy and its magnetoresistance

In this chapter we have investigated the magnetocaloric properties of a Mn-rich Si doped Mn-Ni-Sn-Si alloy under discontinuous heating and cooling protocols across its structural phase transition. Its exchange bias and magnetoresistance have been studied also.

6.1. Preamble

MCE has a large influence in the modern society due to its promising applications in room temperature magnetic refrigerators for environment friendly and energy saving cooling [1-4]. After the discovery of giant MCE in Gd-Si-Ge in 1997 [5], scientists have paid considerable attention in order to find out even better magnetocaloric materials with larger MCE values as compared to the Gd-Si-Ge [1-3, 6, 7]. In this context, large numbers of magnetocaloric materials have been studied during the last two decades [1-3, 6-10]. Initially, the major efforts have been given to study the MCE in magnetic materials across their second order ferro-para transition [2, 3, 10]. But, the same transition becomes remote under the application of higher magnetic field, which limits the ΔS_M in them.

During the last decade, researchers have shifted their interest towards the materials with first order magnetic and magneto-structural transition as these materials are expected to show large MCE [1, 6-8]. Ni-Mn based Ni-Mn-Sn off-stoichiometric Heusler alloys are found to be very effective in this context as they can exhibit interesting and valuable multifunctional properties like MCE [6, 8, 11-15], MR [16, 17] and EB [18, 19]. They show a structural phase transition from the cubic austenite to a tetragonal martensite phase on cooling which accompanies an enormous change in the magnetic and transport properties also. Recently, Mn-rich (Mn ~50 at%) Mn-Ni-Sn alloys have drawn special attention due to its stronger magnetic correlations and large variation of the same with varying the structural phase, which shows significant enhancement in the magnetocaloric properties also [20-27].

Calculation of MCE is generally done from the isothermal $M-H$ curves taken across any magnetic phase transition by using the Maxwell's relations [1, 6, 8, 28]. Although, it is found to be a good treatment for the materials having SOMT, the FOMST suffers due to the overestimation problem, which questions about the validity of calculated results [28, 29]. The first order transitions mostly have field induced effect, where the magnetization changes nonlinearly in the saturation region (under high field) showing the existence of metamagnetic transition. Therefore, the

calculation of ΔS_M using the Maxwell's relation may show unwanted spikes in the $\Delta S_M - T$ curve [29].

This turns out as a debate if the Maxwell's relation is valid for estimating the ΔS_M in the materials exhibiting FOMST. Researchers have come up with some solution for the aforementioned problems: (1) One can subtract the field induced hysteresis losses from the total RC of a material across its FOMST to obtain the net RC [11, 30]. (2) The highest applicable field can be restricted below the critical field of starting the metamagnetic transition [24, 25, 31-33]. (3) Moreover, instead of continuously changing the temperature in step across the FOMST and taking the $M-H$ curves, one can measure a $M-H$ curve at some temperature near the phase transition (say, T) and ramp back the sample from a temperature which is far away from the transition region and then take another $M-H$ measurement at the next targeted temperature (say, $T \pm \Delta T$) [34, 35]. In this way, the effect of field history on the sample's structure and $M-H$ curves can be minimized. But, under high magnetic field the metamagnetic transition will still be induced which may provide improper data and large hysteresis losses. Therefore, it is desirable to do a detail study on the MCE parameters in such structural materials across their forward and reverse FOMST by varying the discontinuous temperature ramping protocol (heating and cooling) to find out the possibilities of getting more reliable and error free MCE.

In the previous three chapters, firstly, we investigated on Ni-Mn based Ni-rich Ni-Mn-Sn off-stoichiometric Heusler alloys and were able to increase the ΔS_M of these alloys by doping Co replacing Ni [31, 32]. We obtained large MCE in these materials but, higher doping concentrations were found to be not effective in that way. Then, we studied the magnetocaloric properties in a single Ni-Mn-Sn alloy by varying its annealing time to tune the MCE parameters with structural disorder [33]. The results showed that the partially disordered alloys can be an effective magnetocaloric candidate. In the last chapter, we studied the Mn-rich Mn-Ni-Sn alloys and showed an enormous enhancement in both the ΔS_M and net RC [24]. Moreover, we doped these Mn-rich systems with Fe by replacing Ni and Mn independently. ΔS_M increased for lower doping concentration, but net RC became

almost the double for the same doping level with respect to the similar undoped materials [25]. Although, the MCE of these materials were measured using the discontinuous heating protocol and under 16 kOe field, the loss induced by field is still an issue. For the compositions with Mn < 50 at%, the thermal hysteresis also increases [24, 25]. Addition of non-magnetic elements with relatively smaller atomic radius may decrease the inter-atomic spacing and induce more magneto-structural coupling, which can decrease the thermal hysteresis across the martensitic transition of these alloys. Considering all the above facts, we have planned to study the MCE in a Mn-rich Si-doped Mn-Ni-Sn-Si off-stoichiometric Heusler alloy across its both the forward and reverse structural transition during heating and cooling respectively.

In this chapter, we have prepared a Mn-rich Si-doped $\text{Mn}_{46}\text{Ni}_{39.5}\text{Sn}_{10}\text{Si}_{4.5}$ alloy and studied its MCE, EB and MR. The T_C^A is found to decrease significantly as compared to the similar undoped compositions. The sample has shown the existence of EB in ZFC mode at very low temperatures. We have tried to calculate the ΔS_M from the isofield $M-T$ curves and it is found to be fairly close to the isothermal results. The isothermal $M-H$ curves across the martensitic transition have been taken in both the discontinuous heating and cooling mode. Cooling mode is found to be more effective for getting better and error free MCE value, which has been checked by comparing the $\Delta S_M - T$ curves, plotting the normalized ΔS_M against rescaled temperature axis, fitting the normalized curves universally and estimating the net RC values. A good amount of MR is also available in this sample.

6.2. Experimental

Mn-rich $\text{Mn}_{46}\text{Ni}_{39.5}\text{Sn}_{10}\text{Si}_{4.5}$ alloy was prepared by conventional arc melting technique under 4N purity (99.99%) argon atmosphere. The as prepared ingot was turned and re-melted several times (at least seven to eight times) to ensure its homogeneity. The ingot was then wrapped in Ta foil and sealed in a highly evacuated quartz ampoule for annealing. After 24 h of annealing at 1173 K, the ampoule was quenched in ice water. The final composition was confirmed by EDS.

X-ray diffraction pattern was taken at laboratory temperature (295 K) in Rigaku MiniFlex II using Cu- K_{α} radiation to determine the crystallographic parent phase. AC magnetic measurement was carried out in a self-fabricated ac susceptibility setup. All the dc Magnetic and magneto-transport properties measurements were performed in PPMS (Cryogenic Limited) up to 80 kOe field. The heating and cooling rates during all the temperature dependent magnetic and magneto-transport measurements were maintained at 1 K/min.

6.3. Results and discussions

6.3.1. Temperature dependent structural, magnetic properties and phase transitions

Fig. 6.1 shows the room temperature XRD pattern for Mn-rich $Mn_{46}Ni_{39.5}Sn_{10}Si_{4.5}$ alloy. The sample is found to be in cubic austenite phase at the above mentioned temperature. The super lattice diffraction peaks, (111) and (311) indicate the existence of higher level of atomic ordering in this alloy [22]. The temperature dependent real part of the ac susceptibility is plotted in Fig. 6.2. The existence of martensitic transition around 200 K can be well confirmed from these data. The Currie temperatures in the two different phases can be identified also. The detail discussions have been made in the next part of this chapter.

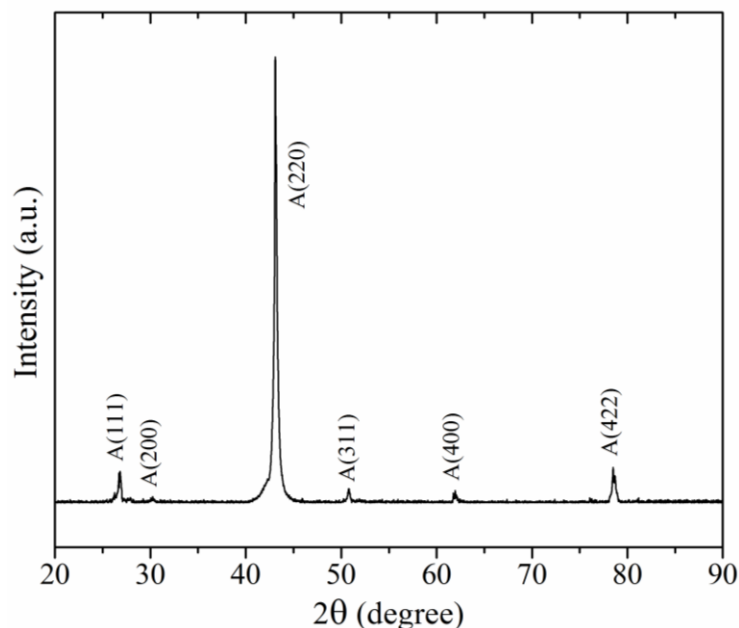


Fig. 6.1: Room temperature XRD patterns for $Mn_{46}Ni_{39.5}Sn_{10}Si_{4.5}$ alloy.

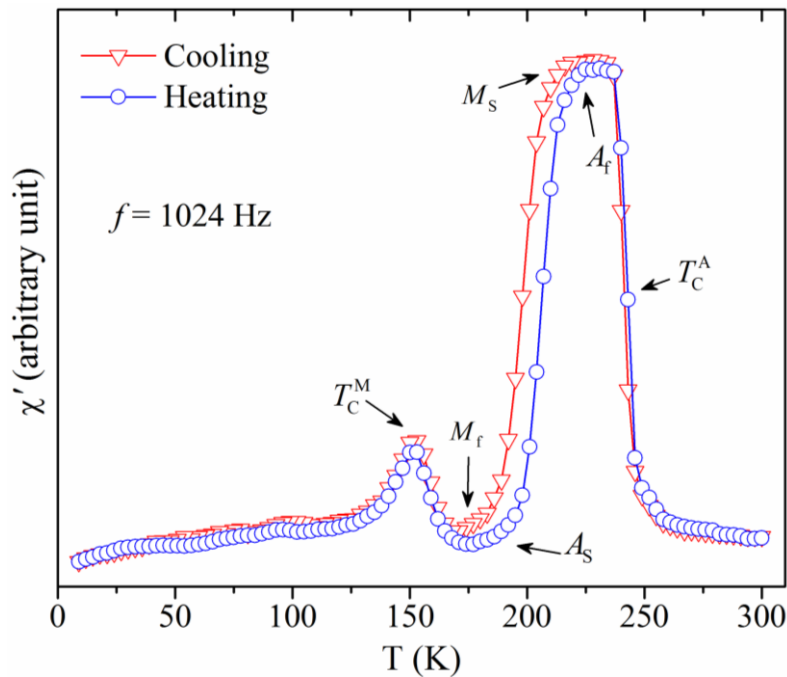


Fig. 6.2: Temperature dependence of real part of the ac susceptibility at 1024 Hz for $\text{Mn}_{46}\text{Ni}_{39.5}\text{Sn}_{10}\text{Si}_{4.5}$ alloy.

The temperature dependent magnetization curves (M - T curves) in the presence of 100 Oe field are plotted in Fig. 6.3 within the temperatures between 5 K and 300 K. The blue curve represents the data taken during ZFC mode and the red one is for FCC mode. In the ZFC curve, an increase in magnetization can be observed after 100 K which may be due to the freezing of moments in lower temperatures. In addition to that, the presence of inhomogeneous magnetic phases may also result this type of nature in the ZFC curve. Near 150 K, the magnetization decreases rapidly with temperature. This is known as the T_C^M , where the sample becomes weakly magnetic or paramagnetic like. At the temperature very close to 200 K the martensite to austenite transition starts to occur at A_S and the magnetization of the sample increases sharply with the increase in temperature. It finishes near A_f . Another phase transition can be identified near 250 K where the magnetization decreases rapidly. This is due to a ferro-para transition at the T_C^A . Above the 250 K the sample is in completely paramagnetic phase.

By following the FC curve near 200 K, one can observe the reverse transition from austenite to the martensite phase with a thermal hysteresis. The M_S and M_f are indicated in Fig. 6.3. These temperatures agree well with the values as estimated

from the ac susceptibility measurement (Fig. 6.2). If we compare this data with our previous work as reported in the last chapter [24], the martensitic transition temperature here increased due to the addition of Si atoms. Si has a smaller atomic radius compared to the other elements present in the sample of our present study. This actually decreases the lattice parameter of the sample which comes up with a shorter Mn-Mn inter-site distance and hence enhances the Mn-Mn inter-site interactions. This stabilizes the weakly magnetic or paramagnetic like martensite phase and as a result, the martensitic transition temperature increases. The same reason is also responsible for the significant decrease in T_C^A (~ 250 K) with respect to the similar reported alloys (~ 280 K) [22-24].

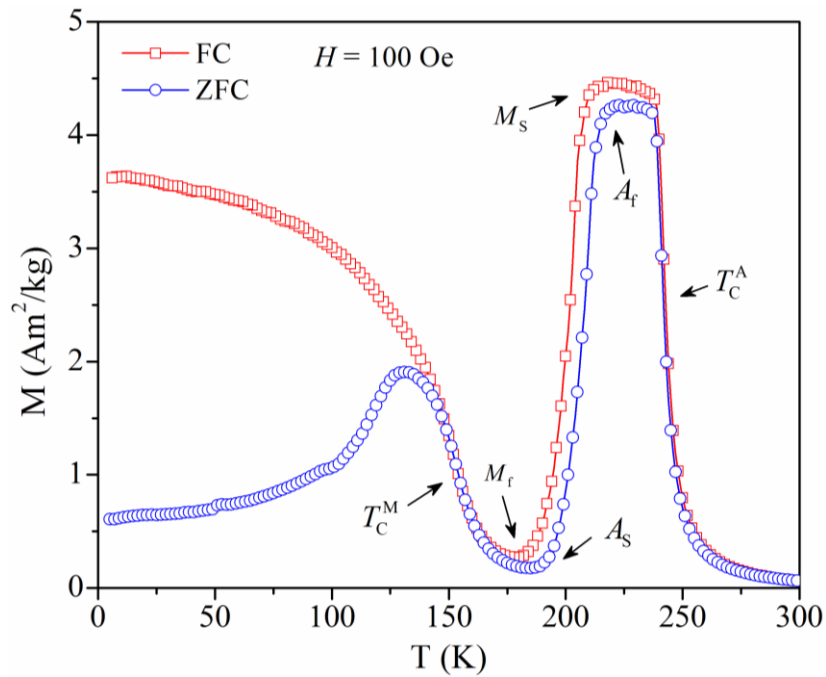


Fig. 6.3: ZFC and FC temperature dependent magnetization (M - T curves) curves for $\text{Mn}_{46}\text{Ni}_{39.5}\text{Sn}_{10}\text{Si}_{4.5}$ alloy.

6.3.2. Exchange Bias

Figs. 6.4(a-d) depict the M - H hysteresis loops for $\text{Mn}_{46}\text{Ni}_{39.5}\text{Sn}_{10}\text{Si}_{4.5}$ alloy respectively at 5 K, 20 K, 40 K and 50 K within the field ranges from -20 kOe to 20 kOe. The field sweeping is done as follows: $0 \rightarrow 50$ kOe $\rightarrow 0 \rightarrow -50$ kOe $\rightarrow 0 \rightarrow 50$ kOe. The sample was cooled from 300 K to the targeted temperature in ZFC mode before measuring each of the hysteresis loops. A finite shift in the hysteresis loop can

be found at 5 K, which decreases with increasing the temperature. This loop shift is an indication of the existence of EB in this alloy.

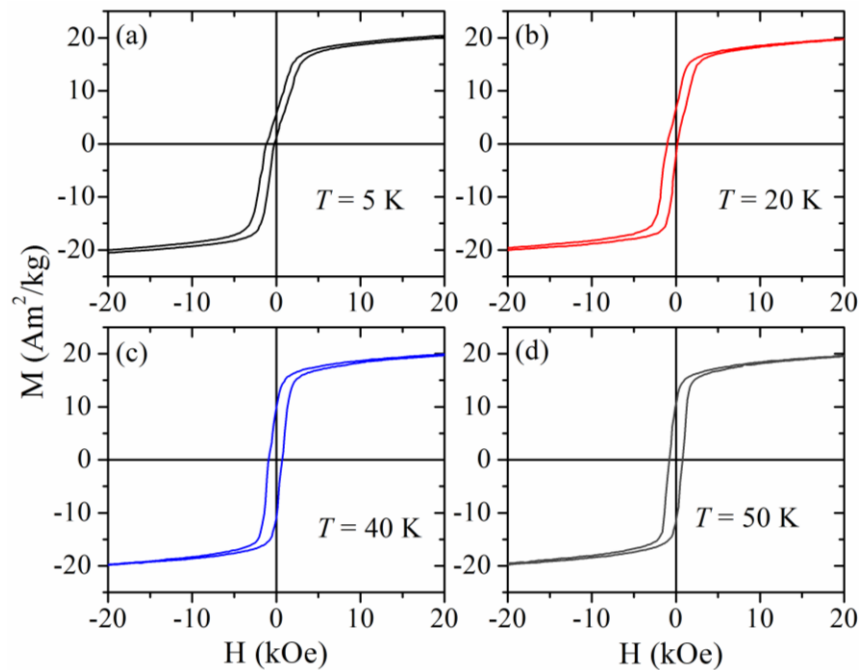


Fig. 6.4: Magnetic hysteresis loops for $\text{Mn}_{46}\text{Ni}_{39.5}\text{Sn}_{10}\text{Si}_{4.5}$ alloy at (a) 5 K, (b) 20 K, (c) 40 K and (d) 50 K measured up to 50 kOe field in ZFC mode.

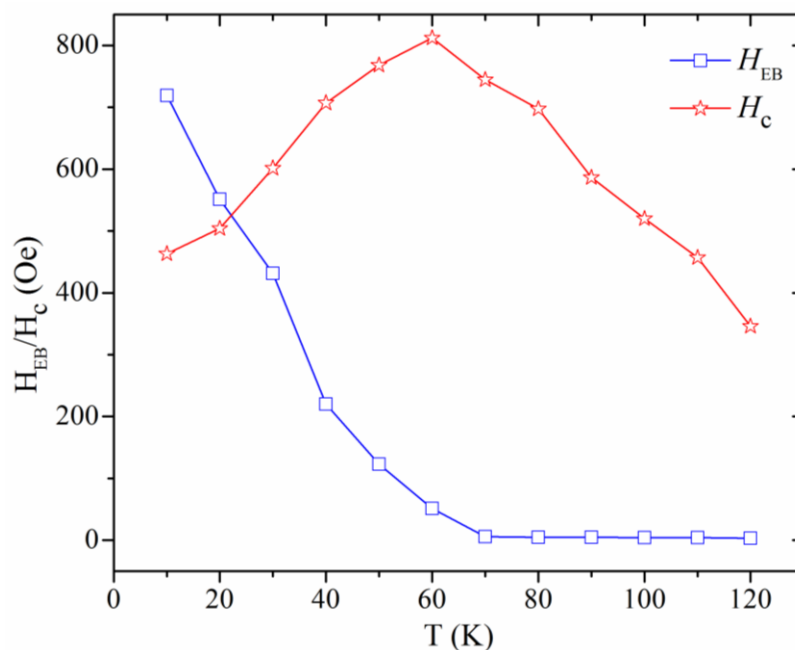


Fig. 6.5: Temperature dependent exchange bias field and coercivity for $\text{Mn}_{46}\text{Ni}_{39.5}\text{Sn}_{10}\text{Si}_{4.5}$ alloy.

EB originates due to the interfacial exchange interaction between the ferromagnetic and antiferromagnetic layers present in the system [19]. In the case of

Heusler alloys, this interaction generates between the Mn-Mn, Mn-Ni inter-site and Mn-Mn intra-site orderings. Due to the polycrystalline nature of the sample, the total H_{EB} which comes from each crystallites get averaged out and only the contribution from the sample's surface remains measurable. Fig. 6.5 represents the temperature dependence of H_{EB} and H_C within the temperatures between 5 K and 120 K. As the temperature increases, the thermal agitation weakens the magnetic correlations and the interfacial interaction also, which leads to a decrease in H_{EB} and its blockage at T_{EB} (~ 70 K).

6.3.3. Isofield M - T curves and MCE

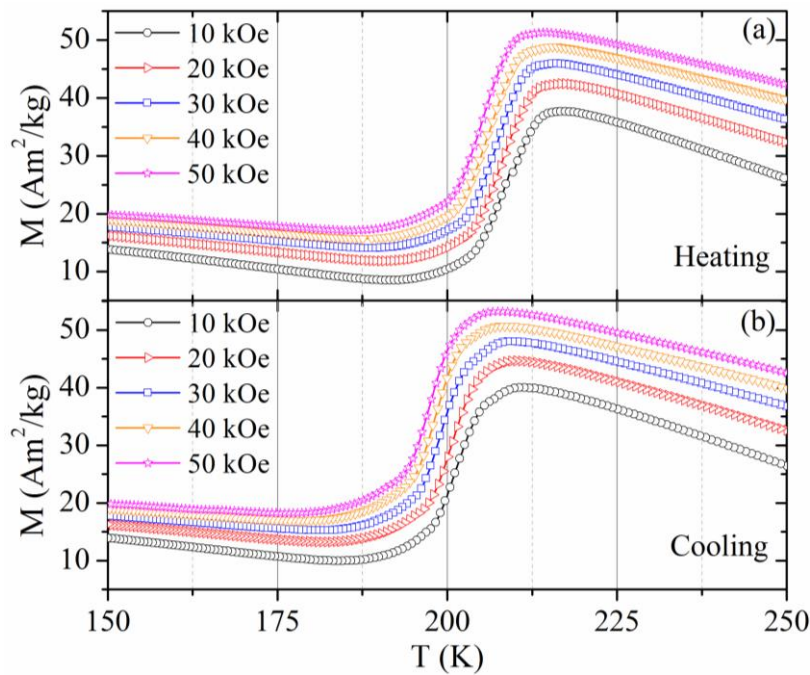


Fig. 6.6: M - T curves in the vicinity of the martensitic transition for $Mn_{46}Ni_{39.5}Sn_{10}Si_{4.5}$ alloy during (a) heating and (b) cooling in the presence of 10, 20, 30, 40 and 50 kOe magnetic field.

Figs. 6.6(a and b) represent respectively, the heating and cooling M - T curves in the presence of 10, 20, 30, 40 and 50 kOe magnetic field within the temperatures between 150 K and 250 K. A shift in the structural transition can be seen under the application of higher magnetic field. This originates from the field induced metamagnetic nature of the structural transition. The shift is ~ 0.08 K/kOe. We have calculated the ΔS_M across the structural transition using these high field M - T data. A simple approach has been taken using one of the Maxwell's thermodynamic

relations, where we have first calculated $(\partial M/\partial T)_H$ from these M - T curves and then multiplied it by the applied field ($\Delta S_M = (\partial M/\partial T)_H \times H$). The temperature dependent entropy change curves are plotted in Fig. 6.7. A maximum ΔS_M of 18.26 J/kg K and 20.04 J/kg K are obtained at 205 K and 197 K due to a field change of 50 kOe during heating (Fig. 6.7(a)) and cooling (Fig. 6.7(b)) respectively. Values are also given in table 6.1. These ΔS_M values can differ from the results that can be obtained from the isothermal field dependence of magnetization data (M - H curves). The reason is that the ΔS_M is not a linear function of H . So, the obtained results can either overestimate or underestimate the MCE values. In the next part of this chapter, we will be discussing about the results obtained from M - H measurements and then compare with the results as obtained from these M - T measurements.

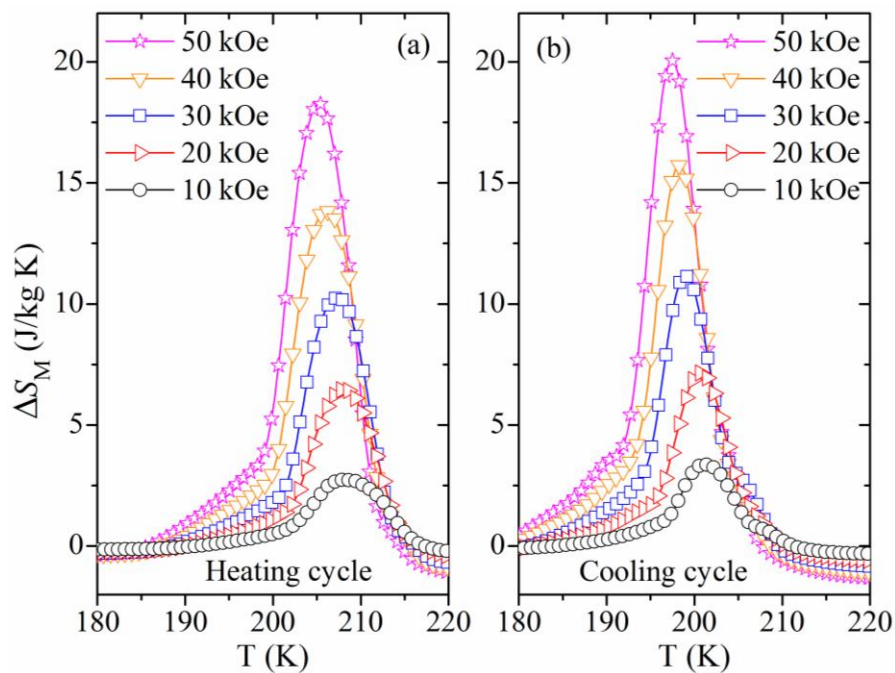


Fig. 6.7: Temperature dependence of magnetic entropy change for $\text{Mn}_{46}\text{Ni}_{39.5}\text{Sn}_{10}\text{Si}_{4.5}$ alloy during (a) heating and (b) cooling as calculated from the isofield M - T data.

6.3.4. Field dependent magnetic properties in heating and cooling protocol

The isothermal M - H curves of the Mn-rich Mn-Ni-Sn-Si alloy across its structural transition point are plotted in Fig. 6.8. The field sweeping is done as follows: $0 \rightarrow 50 \text{ kOe} \rightarrow 0$. The M - H measurements have been carried out in two different protocols: discontinuous heating and discontinuous cooling protocol [34,

35]. In the first protocol, the sample was first cooled to 150 K (well below the M_f of the sample) and then heated back to near its A_s without overshooting. A $M-H$ curve was measured at that temperature and after the completion of measurement, the sample was again cooled to 150 K. This time the sample was heated to a temperature 2 K higher than the last measurement temperature without any overshoot and then another $M-H$ curve was measured. This method was repeated for all the $M-H$ curves taken within the temperatures between 191 K and 215 K (across the martensite to austenite transition) as shown in Fig. 6.8(a). In the case of cooling protocol, the same method was used but the only differences are; before each measurement the sample was heated to 250 K (well above the A_f of the sample) and then cooled back to a temperature 2 K lower than the previous set point. This protocol has been used to measure the $M-H$ curves of this sample within the temperatures between 216 K and 192 K (across the austenite to martensite transition) as shown in Fig. 6.8(b).

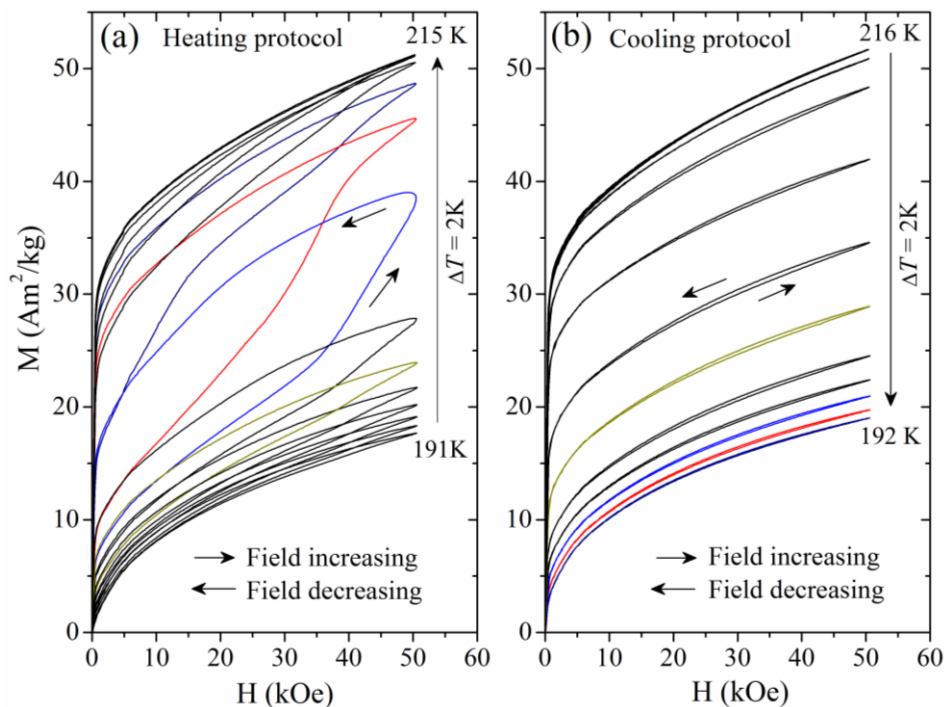


Fig. 6.8: Isothermal magnetization vs magnetic field ($M-H$ curves) curves for $\text{Mn}_{46}\text{Ni}_{39.5}\text{Sn}_{10}\text{Si}_{4.5}$ across the (a) martensite to austenite transition during heating and (b) austenite to martensite transition during cooling. Detail measurement protocol is given in the text written above this figure.

Almost all the curves in the heating protocol show the field induced hysteresis. This gives a signature of metamagnetic transition where the structural transition gets

influenced by the application of external magnetic field and shifts toward the weakly magnetic phase so that the highly magnetic phase becomes more stable. During heating, both the temperature and the magnetic field stabilize the same phase (austenite phase). The same indication has been found in the high field $M-T$ curves also (Fig. 6.6), where the structural transition temperature decreases with increasing the magnetic field. This hysteresis increases as the temperature reaches towards the transition temperature and then it decreases. Unlike heating protocol, the cooling protocol shows almost negligible hysteresis. The field induced shift in the structural transition is also present here, but the temperature induced irreversible reverse transition opposes the field induced transition [10, 11]. During cooling protocol, the magnetic field tries to stabilize the austenite phase but, temperature drags it to the martensite phase. This is why the magnetization does not increase non-linearly in the high field region during the cooling protocol. This protocol dependent nature of $M-H$ curves across the magneto-structural transition can affect the magnetocaloric properties also, which is discussed in the next parts of this chapter.

6.3.5. Isothermal magnetic entropy change

The ΔS_M of $Mn_{46}Ni_{39.5}Sn_{10}Si_{4.5}$ alloy has been estimated from the isothermal $M-H$ curves using the Maxwell's relations (equation (1.18)) [6] and plotted against temperature in Fig. 6.9. Data have been plotted for 10 kOe to 50 kOe field changes. These results are also given in table 6.1. One can notice that both the isofield and isothermal measurements lead to almost closer ΔS_M^{Peak} values. Figs. 6.9(a and b) show the $\Delta S_M - T$ curves under heating protocol during field increasing and decreasing respectively. Except for 10 kOe, the nature of the curves and the values of ΔS_M^{Peak} are not similar for field increasing and decreasing under the same field changes. This originates due to the field induced non-linear change in the isothermal $M-H$ curves as measured under the heating protocol in the high field region (Fig. 6.8(a)). Figs. 6.9(c and d) represent the $\Delta S_M - T$ curves under cooling protocol during field increasing and decreasing respectively. Here, we can see that the nature of the curves and as well as the values of ΔS_M^{Peak} are almost independent of the field sweeping conditions (heating or cooling) under the same field change. The $M-H$

curves across the austenite to martensite transition as taken in cooling protocol do not show any significant difference between their field increasing and decreasing periods (Fig. 6.8(b)). This in turn presents such consistent $\Delta S_M - T$ curves under the cooling protocol (Figs. 6.9(c and d)).

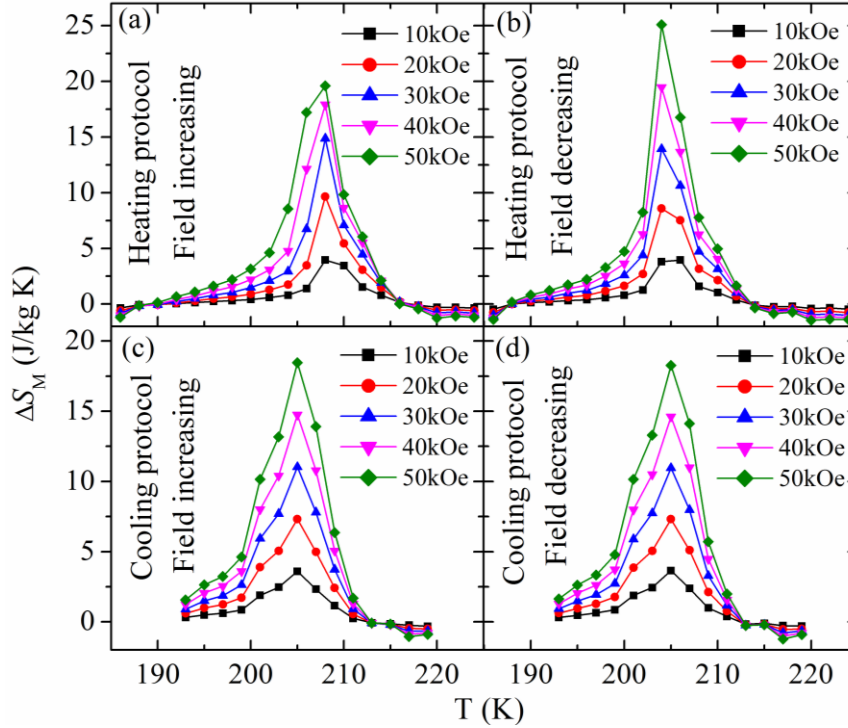


Fig. 6.9: Isothermal magnetic entropy change as a function of temperature for $\text{Mn}_{46}\text{Ni}_{39.5}\text{Sn}_{10}\text{Si}_{4.5}$ alloy under heating protocol during (a) field increasing, (b) field decreasing and cooling protocol during (c) field increasing, (d) field decreasing as estimated from the isothermal $M-H$ curves.

Table 6.1: Magnetic entropy changes under different measurement protocols ($H \uparrow$ for field increasing and $H \downarrow$ for field decreasing).

ΔH kOe	ΔS_M^{Peak} (J/kg K)					
	Isofield study		Isothermal study			
	Heating	Cooling	Heating protocol		Cooling protocol	
			$H \uparrow$	$H \downarrow$	$H \uparrow$	$H \downarrow$
10	2.78	3.37	3.95	3.95	3.6	3.65
20	6.47	7.12	9.66	8.58	7.32	7.32
30	10.23	11.15	14.87	13.93	11.03	10.96
40	13.83	15.72	17.91	19.48	14.75	14.62
50	18.26	20.04	19.59	25.1	18.45	18.27

6.3.6. Universal curve fitting of MCE

In order to compare the aforementioned two measurement protocols, we have taken a simple approach to construct phenomenological universal curves which can be obtained by normalizing all the $\Delta S_M - T$ curves by their respective ΔS_M^{Peak} values ($\Delta S' = \Delta S_M(T)/\Delta S_M^{\text{Peak}}$) and rescaling the temperature axis across the phase transition point (T_C). The rescaled parameter, θ is defined as [36]

$$\theta = - (T - T_C)/(T_1 - T_C) \text{ for } T \leq T_C \quad (6.1)$$

$$= (T - T_C)/(T_2 - T_C) \text{ for } T \geq T_C \quad (6.2)$$

where T_1 and T_2 are two reference temperatures selected from the FWHM of the respective $\Delta S_M - T$ curves. Fig. 6.10 shows the θ dependence of $\Delta S'$ across the FOMST of $\text{Mn}_{46}\text{Ni}_{39.5}\text{Sn}_{10}\text{Si}_{4.5}$ alloy. Figs. 6.10(a and b) represent the same for heating protocol (field increasing and decreasing respectively). The data points of different field change curves are found to merge only near the transition point for the same θ values during both the times of field increasing and decreasing at the forward transition from martensite to the austenite. But, below T_1 and above T_2 , data are largely scattered. In the case of reverse transition from austenite to the martensite phase (cooling protocol) as shown in Figs. 6.10(c and d), almost all the data points under different field values and corresponding to a single θ merge satisfactorily. This in turn confirms the universality of MCE curves in this Mn-rich Mn-Ni-Sn-Si alloy across its reverse structural transition during cooling.

We have tried to fit these normalized entropy change vs rescaled temperature curves universally by using a Lorentz function [36]

$$\Delta S' = \frac{a}{b + (\theta - c)^2} \quad (6.3)$$

Where a , b and c are the free parameters. If we consider the asymmetry of the $\Delta S' - \theta$ curves, two set of constants are required to use (one set for $T \leq T_C$ and another one for $T \geq T_C$). All the parameters' values for the two protocols (heating and cooling) are given in table 6.2. The red lines in Fig. 6.10 represent the fitted curves. All the field change curves for a particular measurement protocol and field sweeping method are fitted globally using the aforementioned two sets of the free

parameters' values. It can be noticed that only the fitting of the curves under cooling protocol (during both the field increasing and decreasing) collapse (Figs. 6.10(c and d)). But, for the heating protocol, only the region within $-1 \leq \theta \leq +1$ ($T_1 \leq T \leq T_2$) a reasonable fitting has been achieved. By looking at the parameters' values and their standard errors (as given in table 6.2) it can be seen that the best fitting has been achieved only under the cooling protocols.

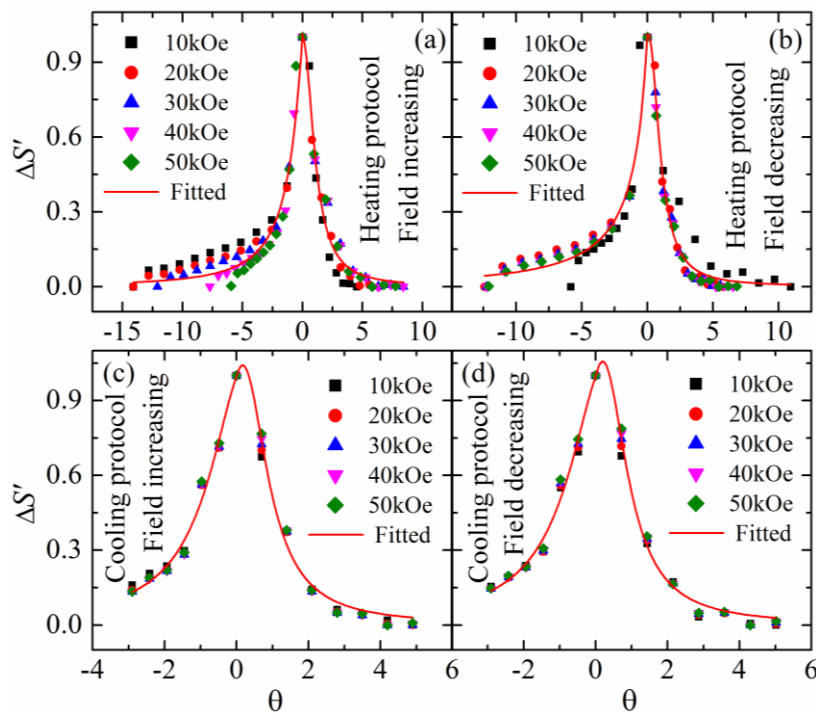


Fig. 6.10: Normalized entropy change ($\Delta S'$) as a function of rescaled temperature (θ) for $\text{Mn}_{46}\text{Ni}_{39.5}\text{Sn}_{10}\text{Si}_{4.5}$ alloy under heating protocol during (a) field increasing, (b) field decreasing and cooling protocol during (c) field increasing, (d) field decreasing as estimated from the isothermal M - H curves.

There are many reports in the literature regarding this phenomenological universal curve fitting of ΔS_M across the SOMT of MCE materials [9, 36, 37]. In the case of FOMST, the fitting does not converge because of the field induced effect on the same phase transition. We have come to a very similar finding for the heating protocol, where the effect of high magnetic field on the sample's forward transition from martensite to the austenite phase can easily be visualized from the M - T curves under different magnetic field (Fig. 6.6) and isothermal M - H curves (Fig. 6.8(a)). Now, there is a debate regarding the validity of Maxwell's relation for calculating

the MCE across any first order phase transition. Generally, it gives overestimated result and spikes in the $\Delta S_M - T$ curves due to the unwanted non linearity in the $M-H$ curves across the saturation region because of the metamagnetic transition [28, 29].

Table 6.2: Values of the free parameters and their standard error.

Parameters	Field increasing				Field decreasing			
	$T \leq T_C$		$T \geq T_C$		$T \leq T_C$		$T \geq T_C$	
	Value	Error	Value	Error	Value	Error	Value	Error
Heating protocol								
a	4.35	± 1.05	1.22	± 0.18	15.12	± 7.99	0.95	± 0.1
b	1.69	± 1.04	1.22	± 0.18	-36.54	± 53.49	0.95	± 0.1
c	1.61	± 0.62	0.07	± 0.09	7.17	± 4.36	0.08	± 0.05
Cooling Protocol								
a	1.54	± 0.17	0.7	± 0.06	1.65	± 0.17	0.69	± 0.05
b	1.46	± 0.12	0.67	± 0.06	1.55	± 0.11	0.65	± 0.05
c	0.3	± 0.1	0.17	± 0.02	0.33	± 0.1	0.2	± 0.02

A valuable treatment for this is to use the discontinuous heating protocol, which can indeed remove the history effect from the $M-H$ curves across the FOMST of a material [34, 35]. Along with this, we need to verify the average field induced hysteresis loss across the FOMST and then subtract it from the total RC [30]. Although, the aforementioned procedures may be helpful under low field region, the measurements of MCE under high magnetic field (beyond 20 kOe) still suffer from the aforementioned difficulties. But, the $M-H$ measurements under the cooling protocol do not show any noticeable field induced effect and therefore, its chance to overestimate the results is negligible. So, from all these study we can predict that the use of discontinuous cooling protocol as mentioned earlier can be very helpful. However, the dependence of RC on these measurement protocols is required to be verified, which is discussed in the later part of this chapter.

6.3.7. Refrigerant capacity

The RC of this Mn-rich Mn-Ni-Sn-Si alloy has been calculated using equation (1.20) under 50 kOe field change for all the measurement procedures and given in

table 6.3. The isofield study shows the maximum RC among all other methods. But, these data can be overestimated because of its calculation procedures, which roughly estimates the ΔS_M . In the case of isothermal measurements, we can see that the discontinuous cooling protocol shows larger and more consistent RC values than the heating protocol under different field sweeping methods. Moreover, heating protocol suffers from large field induced loss which diminishes the net RC to nearly the half of the RC_{avg} ($(RC_{H\uparrow} + RC_{H\downarrow})/2$) value. The same loss under the cooling protocol is negligible and thus, totals RC_{avg} and net RC for cooling protocol are almost the same. Now, if we summarize all the results, it can be concluded that the discontinuous cooling protocol can provide a better and more accurate outcomes in MCE study for those materials having field induced transition. In the sample of our present study, the transition temperature shifts towards the lower temperatures with the application of high magnetic field. If the same moves towards the higher temperatures, then the protocols are needed to be switched, which may be applicable for the materials those have first order magnetic transition from ferromagnetic to a paramagnetic phase on heating [1, 7, 9, 36, 37].

Table 6.3: Refrigerant capacity under different measurement protocols ($H\uparrow$ for field increasing and $H\downarrow$ for field decreasing).

RC (J/kg)											
Isofield study		Isothermal study									
Heating	Cooling	Heating protocol					Cooling protocol				
		$H\uparrow$	$H\downarrow$	RC_{avg}	HL_{avg}	Net RC	$H\uparrow$	$H\downarrow$	RC_{avg}	HL_{avg}	Net RC
122.1	108.8	89.2	83.3	86.3	43.1	43.2	105.1	104.3	104.7	1.1	103.6

6.3.8. Magnetoresistance

Fig. 6.11 represents the temperature dependent resistivity for $Mn_{46}Ni_{39.5}Sn_{10}Si_{4.5}$ alloy during heating and cooling in the presence of 0 and 80 kOe magnetic field. The characteristic transition temperatures as estimated from the temperature dependent ac susceptibility data and $M-T$ curves (Figs. 6.2 and 6.3) agree well with the values as estimated from these $\rho - T$ curves. Nearly 30% drop in

resistivity is found during the structural transition from martensite to the austenite phase on heating. The field induced shift of the FOMST has been observed under 80 kOe field, which we have already seen in the high field M - T curves (Fig. 6.6). The martensite phase of the sample show semi-metallic behavior as its resistivity decreases monotonically with increasing the temperature. In the case of austenite phase the nature is metallic, where the same increases as the temperature increases further after the completion of the forward FOMST on heating. Very similar results have been obtained in the previous chapter also [24]. The inset of Fig. 6.11 shows the temperature dependence of MR during heating and cooling under the field of 80 kOe. Nearly 20% and 25% MR_{\max} has been observed across the martensitic transition during heating and cooling respectively. Across the FOMST, a very small amount of contribution in MR comes out from the s - d scattering mechanism and the rest of the amount is contributed by the structural transition and its field induced shift.

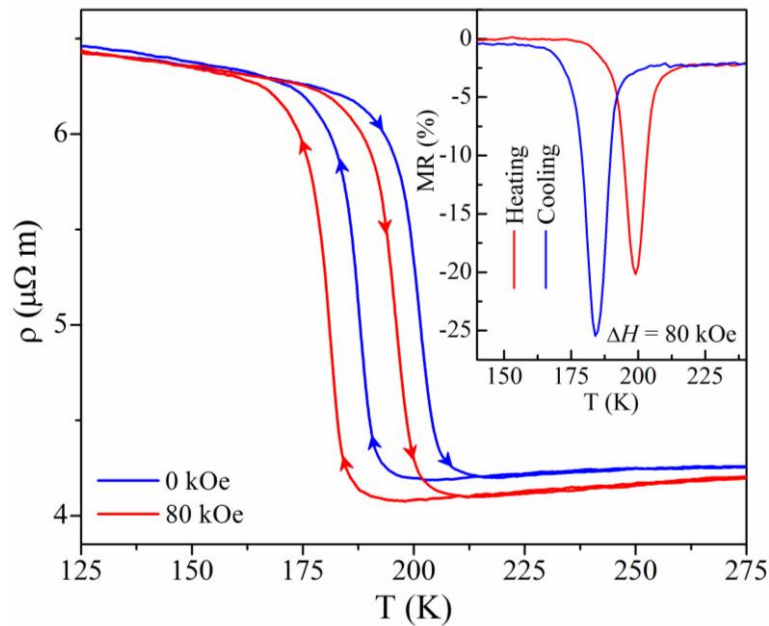


Fig. 6.11: Temperature dependence of electrical resistivity in the presence of 0 and 80 kOe magnetic field for Mn₄₆Ni_{39.5}Sn₁₀Si_{4.5}. Inset: Temperature dependent magnetoresistance.

The field dependent MR are plotted in Fig. 6.12. The field sweeping is done as follows: 0 \rightarrow 80 kOe \rightarrow 0 \rightarrow -80 kOe \rightarrow 0. At 30 K (inhomogeneous martensite phase), MR \sim 1% is obtained whereas almost 3% of MR is achieved at 230 K (ferromagnetic austenite phase). A strong antiferromagnetic interaction persists in the martensite

phase which in turn diminishes the possibility of decreasing the s - d scattering in presence of magnetic field. Therefore, the same phase exhibits smaller MR. In the case of austenite phase (below T_C^A), a dominating ferromagnetic interaction reduces the s - d scattering largely and thus the MR increases. At 300 K, about 1.5% of MR is obtained in the paramagnetic austenite phase. At 200 K, the sample resides very close to the FOMST. Application of large magnetic field has induced the phase transition and as a result, the MR started to increase enormously with increasing the field. The MR changes negligibly during the decrease of magnetic field and also during its further increase. The FOMST of the sample becomes completely irreversible under the application of high magnetic field. Only the temperature sweeping can restore the previous phase of the sample.

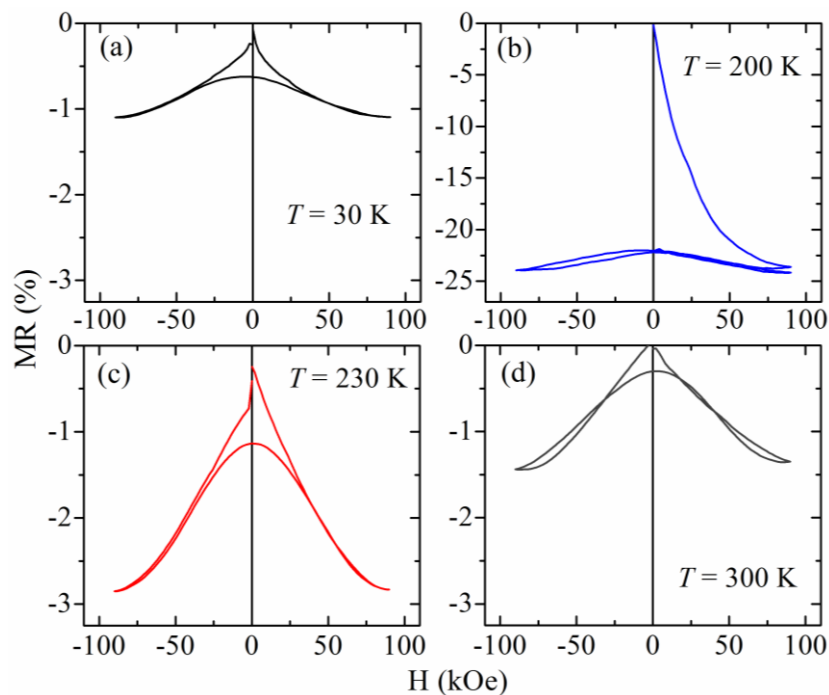


Fig. 6.12: Field dependence of magnetoresistance for $\text{Mn}_{46}\text{Ni}_{39.5}\text{Sn}_{10}\text{Si}_{4.5}$ alloy at (a) 30 K, (b) 200 K, (c) 230 K and (d) 300 K.

6.4. Conclusions

In summary, we have systematically studied the magnetocaloric properties in a Ni-Mn based Mn-rich $\text{Mn}_{46}\text{Ni}_{39.5}\text{Sn}_{10}\text{Si}_{4.5}$ off-stoichiometric Heusler alloy under different measurement protocols. Addition of Si has decreased the ferro-para Curie

temperature significantly, which might be a problem in the light of the practical application. A large isothermal magnetic entropy change has been achieved in this alloy in the vicinity of its martensitic phase transition. The estimation of entropy change using the high field $M-T$ curves does not overestimate noticeably and thus can be a handy tool for MCE study. The MCE parameters across the martensitic transition of the sample are found to be very sensitive to the measurement method under the application of high magnetic field.

The discontinuous heating protocol can overestimate the entropy change values in the high field region and decrease the cooling power of the material due to the metamagnetic transition and the hysteresis losses associated with it. In the case of discontinuous cooling protocol, the MCE values are more stable and consistent. Along with this, it shows almost negligible field induced hysteresis losses, which helped the material to exhibit a very large net value of the refrigerant capacity. The universal phenomenological curve fitting of the normalized entropy changes that are plotted against the rescaled temperature axis has converged only under the cooling protocol during both the times of increasing and decreasing the magnetic field. All these results collectively indicate that the use of discontinuous cooling protocol to study the MCE in materials with first order magneto-structural phase transition (like Heusler alloys) can provide a better and more accurate result.

The exchange bias effect has been found to exist in this material under zero field cooled mode, which develops during the time of initial magnetization. Although, the same effect has large practical application, the working temperature in this sample for such effect is not suitable. A magnetoresistance of 25% has been achieved also. Such value of magnetoresistance across the magneto-structural transition of this type of materials mainly originates from the field induced effect on the aforementioned transition. At the remote temperatures from the structural transition point, the magneto-transport properties of the same material are controlled by the $s-d$ scattering mechanism.

Bibliography

- [1] K. A. Gschneidner Jr., V. K. Pecharsky and A. O. Tsokol, *Rep. Prog. Phys.* 68, 1479 (2005).
 - [2] B. F. Yu, Q. Gao, B. Zhang, X. Z. Meng and Z. Chen, *Int. J. Refrig.* 26, 622 (2003).
 - [3] K. A. Gschneidner Jr. and V. K. Pecharsky, *Annu. Rev. Mater. Sci.* 30, 387 (2000).
 - [4] C. Zimm, A. Jastrab, A. Sternberg, V. K. Pecharsky, K. A. Gschneidner Jr., M. Osborne and I. Anderson, *Adv. Cryog. Eng.* 43, 1759 (1998).
 - [5] V. K. Pecharsky, K. A. Gschneidner Jr., *Phys. Rev. Lett.* 78, 4494 (1997).
 - [6] K. A. Gschneidner Jr. and V. K. Pecharsky, *Int. J. Refrig.* 31, 945-961 (2008).
 - [7] M. H. Phan and S. C. Yu, *J. Magn. Magn. Mater.* 308, 325 (2007).
 - [8] A. Planes, L. Manosa and M. Acet, *J. Phys.: Condens. Matter* 21, 233201 (2009).
 - [9] V. Franco, J. S. Blazquez, B. Ingale and A. Conde, *Annu. Rev. Mater. Res.* 42, 305 (2012).
 - [10] V. Basso, C. P. Sasso, K. P. Skokov and O. Gutfleisch, *Phys. Rev. B* 85, 014430 (2012).
 - [11] P. J. Shamberger and F. S. Ohuchi, *Phys. Rev. B* 79, 144407 (2009).
 - [12] B. Hernando, J. L. S. Lamazares, J. D. Santos, V. M. Prida, D. Baldomir, D. Serantes, R. Varga and J. González, *Appl. Phys. Lett.* 92, 132507 (2008).
 - [13] V. D. Buchelnikov and V. V. Sokolovskiy, *Phys. Met. Metallog.* 112, 633 (2011).
 - [14] Z. D. Han, D. H. Wang, C. L. Zhang, H. C. Xuan, B. X. Gu and Y. W. Du, *Appl. Phys. Lett.* 90, 042507 (2007).
 - [15] T. Krenke, E. Duman, M. Acet, E. F. Wassermann, X. Moya, L. Manosa, and A. Planes, *Nature Mater.* 4, 450 (2005).
 - [16] H. C. Xuan, Y. Deng, D. H. Wang, C. L. Zhang, Z. D. Han and Y. W. Du, *J. Phys. D: Appl. Phys.* 41, 215002 (2008).
 - [17] K. Koyama, H. Okada, K. Watanabe, T. Kanomata, R. Kainuma, W. Ito, K. Oikawa and K. Ishida, *Appl. Phys. Lett.* 89, 182510 (2006).
 - [18] M. Wang, Y. Liu, B. Xia, P. Ren and L. Wang, *J. Appl. Phys.* 111, 043912 (2012).
 - [19] S. Giri, M. Patra and S. Majumdar, *J. Phys.: Condens. Matter* 23, 073201 (2011).
-

- [20] S. E. Muthu, N. V. R. Rao, M. M. Raja, D. M. R. Kumar, D. M. Radheep and S. Arumugam, *J. Phys. D: Appl. Phys.* 43, 425002 (2010).
- [21] S. Paul and S. Ghosh, *J. Phys.: Condens. Matter* 23, 206003 (2011).
- [22] L. Ma, S. Q. Wang, Y. Z. Li, C. M. Zhen, D. L. Hou, W. H. Wang, J. L. Chen and G. H. Wu, *J. Appl. Phys.* 112, 083902 (2012).
- [23] Q. Tao, Z. D. Han, J. J. Wang, B. Qian, P. Zhang, X. F. Jiang, D. H. Wang and Y. W. Du, *AIP Adv.* 2, 042181 (2012).
- [24] A. Ghosh and K. Mandal, *J. Phys. D: Appl. Phys.* 46, 435001 (2013).
- [25] A. Ghosh and K. Mandal, *J. Appl. Phys.* 117, 093909 (2015).
- [26] H. C. Xuan, Y. X. Zheng, S. C. Ma, Q. Q. Cao, D. H. Wang and Y. W. Du, *J. Appl. Phys.* 108, 103920 (2010).
- [27] Z. Han, J. Chen, B. Qian, P. Zhang, X. Jiang, D. Wang and Y. Du, *Scripta Mater.* 66, 121 (2012).
- [28] N. A. de Oliveira and P. J. von Ranke, *Phys. Rev. B* 77, 214439 (2008).
- [29] G. J. Liu, J. R. Sun, J. Shen, B. Gao, H. W. Zhang, F. X. Hu and B. G. Shen, *Appl. Phys. Lett.* 90, 032507 (2007).
- [30] T. L. Phan, P. Zhang, N. H. Dan, N. H. Yen, P. T. Thanh, T. D. Thanh, M. H. Phan and S. C. Yu, *Appl. Phys. Lett.* 101, 212403 (2012).
- [31] A. Ghosh and K. Mandal, *J. Alloys Compd.* 579, 295 (2013).
- [32] A. Ghosh and K. Mandal, *Eur. Phys. J. B* 86, 378 (2013).
- [33] A. Ghosh and K. Mandal, *Appl. Phys. Lett.* 104, 031905 (2014).
- [34] L. Caron, Z. Q. Ou, T. T. Nguyen, D. T. C. Thanh, O. Tegus and E. Bruck, *J. Magn. Magn. Mater.* 321, 3559 (2009).
- [35] G. J. Liu, J. R. Sun, J. Shen, B. Gao, H. W. Zhang, F. X. Hu and B. G. Shen, *Appl. Phys. Lett.* 90, 032507 (2007).
- [36] Q. Y. Dong, H. W. Zhang, J. R. Sun, B. G. Shen and V. Franco, *J. Appl. Phys.* 103, 116101 (2008).
- [37] C. M. Bonilla, F. Bartolomé, L. M. García, M. Parra-Borderías, J. Herrero-Albillos and V. Franco, *J. Appl. Phys.* 107, 09E131 (2010).
-

Chapter 7 | **Conclusion and scope for future work**

In this chapter we have made an overall conclusion of the work described in this thesis and also discussed about the scope for further work in the related fields.

7.1. Epilogue

In this thesis we have studied the magnetocaloric properties in Ni-Mn-Sn Heusler alloys by varying their elemental ratios and substituting other agents. These materials have also exhibited exchange bias and large magnetoresistive properties. The core findings of the thesis is discussed in this final chapter and compared with the other materials reported in the literature.

We have prepared Co-doped Ni-rich (Ni ~ 50 at%) $\text{Ni}_{48.5-x}\text{Co}_x\text{Mn}_{37}\text{Sn}_{14.5}$ ($x = 0, 1$ and 2) and $\text{Ni}_{47.5-y}\text{Co}_y\text{Mn}_{37.5}\text{Sn}_{15}$ ($y = 0, 1, 2$ and 3.5) alloys and systematically studied their magnetic, magnetocaloric and magneto-transport properties. Our results have shown that the substitution of Co lowers the magneto-structural transition temperature with larger width and thermal hysteresis. The exchange bias behavior decreases with the increase in Co content due to the enhancement in ferromagnetic part which indeed suppresses the interfacial exchange interactions between the ferromagnetic and antiferromagnetic layers. The magnetic entropy change increases monotonically with increasing the Co concentration, but field induced hysteresis losses become a major problem, which minimizes the net refrigerant capacity of these materials. A lower concentration of Co doping is found to be effective in that context. For the first series, the undoped material have shown negligible field induced effect and thus negligible hysteresis loss, which helped the first order martensitic transition to become competitive with the second order magnetic transition for magnetocaloric applications. One of the Co-doped samples of the later series has shown large magnetoresistance (~ 70%) within a broad working temperature limit.

Next, we have prepared and studied a Ni-rich off-stoichiometric $\text{Ni}_{50}\text{Mn}_{36.5}\text{Sn}_{13.5}$ Heusler alloy by varying its annealing time. The atomic ordering increases due to the heat treatment and the exchange bias effect get improved with the same. Significant changes in the magnetic properties have been observed due to the increase in structural ordering. In the martensite phase, strong antiferromagnetic interaction has been achieved by annealing. Although, the magnetic entropy change is found to increase with increasing the ordering, the refrigerant capacity becomes

the maximum for a partially disordered sample. This originates due to a relatively broadened transition width for the aforementioned disorder. Therefore, a certain degree of disorder can be very helpful to achieve a better magnetic cooling as compared to the ordered similar materials.

We have also studied the magnetocaloric properties in Mn-rich (Mn ~ 50 at%) Ni-Mn based Heusler alloys. The Mn-rich $\text{Mn}_{50.5-x}\text{Ni}_{41}\text{Sn}_{8.5+x}$ ($x = 0, 1$ and 2) alloys have shown enormous improvement in the magnetocaloric properties across the martensitic phase transition. These materials dissipate only a small amount of energy due to their smaller thermal hysteresis and exhibit a large refrigerant capacity, which is almost 50% higher as compared to the similar Ni-rich systems. A magnetoresistance of up to 33% is also available from these alloys. Afterwards, we doped this Mn-rich system with Fe independently in the place of Ni and Mn, and found that the martensitic transition temperature follows the conventional e/a ratio dependence (proportional). The ferromagnetic correlations in the austenite phase increase when Ni is replaced by Fe, but the same decrease when Mn is replaced by the same element. This is because of the weakening of ferromagnetic interaction in the austenite phase due to the decrease in Mn-content. In the case of martensite phase, the antiferromagnetic interaction becomes unstable with increasing the Fe concentration in both the series. Large values of magnetic entropy change have been observed with high refrigerant capacities in these Fe-doped samples only for the low concentration of doping (~ 1-2 at%). The highly doped samples suffer from the large field induced losses and thus found not so effective. The enhanced magnetocaloric properties in these Mn-rich systems can make them good magnetic refrigerant for the possible use in environment friendly refrigeration technology.

At last, we have prepared a Mn-rich $\text{Mn}_{46}\text{Ni}_{39.5}\text{Sn}_{10}\text{Si}_{4.5}$ off-stoichiometric Heusler alloy and studied its magnetocaloric properties under different measurement protocols. The estimation of magnetic entropy change from the temperature dependent magnetization measurements carried out in presence of high field can be a handy tool for MCE study. Detail study shows that the discontinuous heating protocol can overestimate the entropy change values in the high field region

and decrease the cooling power of the material due to large field induced losses that arise because of the metamagnetic transition. In the case of discontinuous cooling protocol, the MCE values are more stable and consistent. Along with this, it shows almost negligible field induced hysteresis losses, which helps the material to exhibit a very large net value of the refrigerant capacity. The universal fittings of the temperature dependent normalized entropy change curves also indicate that the use of discontinuous cooling protocol to study the MCE in materials with first order magneto-structural phase transition (like Heusler alloys) can provide a better and more accurate result.

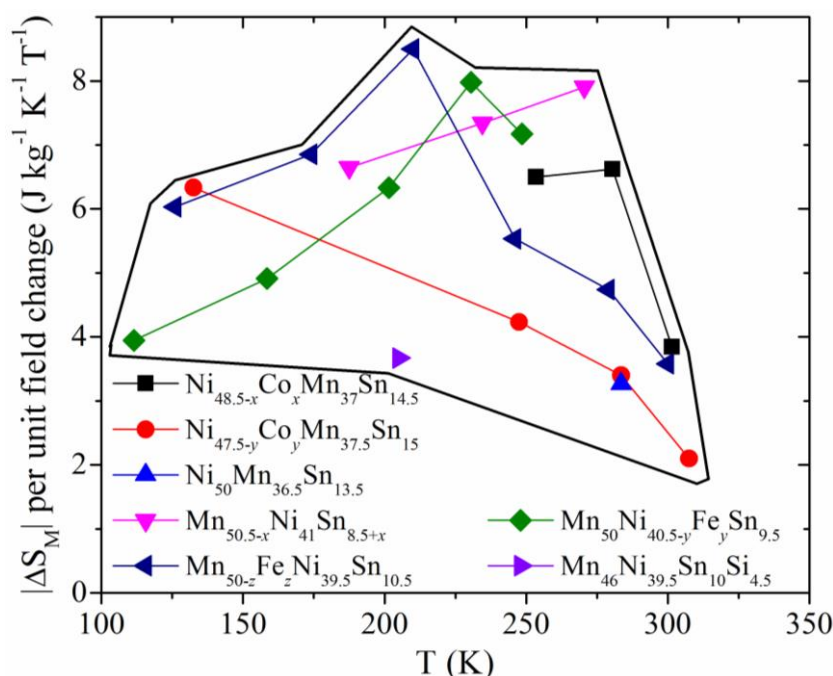


Fig. 7.1: Temperature dependent peak value of the normalized magnetic entropy change (divided by the respective field changes) for all the samples that are reported in this thesis work.

Fig. 7.1 represents the peak value of normalized entropy change (divided by the field change values) as a function of temperature for all the samples we have reported in this thesis. These materials altogether have exhibited large MCE along with a large window of working temperature. In the chapter 1 (introduction), we have discussed about the other magnetocaloric materials and compared them with the help of a normalized master curve (Chapter 1; subsection 1.7; Fig. 1.5). In Fig. 7.2, we have plotted the same curve and added our results in it. One can clearly observe

that we have been able to enhance the MCE in Ni-Mn based Heusler alloys to the giant values within a broad range of working temperature which resides around the room temperature (~ 300 K). Moreover, these alloys are much cheaper in cost as compared to the rare earth based highly expensive MCE materials. A suitable device fabrication by using the above mentioned Heusler alloys as refrigerant may open a way to make energy efficient and environmentally clean cooling technology possible for our daily life usage.

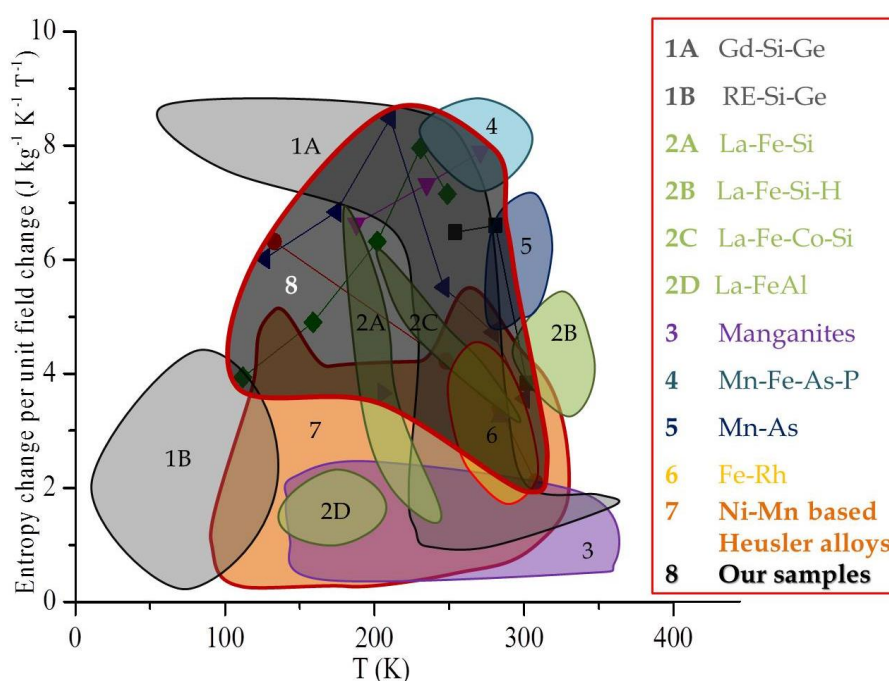


Fig. 7.2: Normalized magnetic entropy change (divided by the respective field changes) of the reported magnetocaloric materials and the samples that are reported in this thesis work.

7.2. Scope for future work

The Ni-Mn based Heusler alloys have been explored extensively during the last decade. In the context of magnetocaloric applications, these materials have shown significant potential, but their sharp transition, structural irreversibility under high magnetic field and its corresponding large hysteresis losses come out as some of the major limitations. We have found some ways to deal with these problems and discussed elaborately in this thesis. The Mn-rich (Mn ~ 50 at%) Ni-Mn based Heusler alloys are found to be very interesting and can be studied further to enhance their magnetocaloric properties. Their sharper structural transition can be made broader

by inducing structural disorder. For undoped such alloys, the ferro-para Currie temperature resides around 280 K. Therefore, a few at% of Co or Fe doping is required to increase the Currie temperature along with the aforementioned disorder. In this way, the structural phase transition from a weakly magnetic martensite to the magnetically more sensitive austenite can be made to occur near room temperature (~ 300 K), which is desirable for various practical applications.

Moreover, the broadly used post transition elements like Ga, In, Sn, Sb etc. can be partially replaced by other similar agents with relatively smaller atomic radii. The magnetic interactions and structural properties in these materials largely depend on the inter-atomic spacing. Therefore, by changing the lattice parameter one can play with various interesting physical properties. In addition to the magnetic field, pressure can also be applied to change the structural and as well as calorimetric properties of multifunctional Heusler alloys. Although, a large number of prototypes have been demonstrated to achieve room temperature magnetic cooling, a considerable amount of efforts is still required to make it applicable commercially.

The exchange bias effect in these materials is usually found in the magnetically inhomogeneous martensite phase at low temperatures (< 100 K), which is required to investigate for its further improvements. For a polycrystalline Heusler alloy the interfacial exchange interactions between the atoms from different sites get averaged out and only contribution from the surface results in a smaller exchange bias field. Single crystalline such materials can resolve the problem and a large exchange bias effect may become obtainable. These materials are also found to show large negative magnetoresistance connected with their magneto-structural transition. The field induced effect, which is not beneficial for magnetic refrigeration, is desirable for obtaining large magnetoresistance. Therefore, considering all the above mentioned facts several treatments can be made on the Ni-Mn based Heusler alloys to functionalize them for multidimensional applications.
